

# LOAN DOCUMENT

PHOTOGRAPH THIS SHEET

AD-A262 019



DTIC ACCESSION NUMBER

LEVEL

INVENTORY

AFDSR-YR-93-0121

DOCUMENT IDENTIFICATION

Dec 92

## DISTRIBUTION STATEMENT 1

Approved for public release.  
Distribution Unlimited

DISTRIBUTION STATEMENT

### ACCESSION FOR

NTIS GRA&I  
DTIC TRAC  
UNANNOUNCED  
JUSTIFICATION

☒  
☐  
☐

BY

DISTRIBUTION/

AVAILABILITY CODES

DISTRIBUTION

AVAILABILITY AND/OR SPECIAL

A-1

DISTRIBUTION STAMP

DTIC  
ELECTE  
MAR 10 1993  
S C D

DATE ACCESSIONED

DATE RETURNED

98 3 10 014

~~98 3 4 067~~

DATE RECEIVED IN DTIC

93-04697



REGISTERED OR CERTIFIED NUMBER

PHOTOGRAPH THIS SHEET AND RETURN TO DTIC-FDAC

H  
A  
N  
D  
L  
E  
  
W  
I  
T  
H  
  
C  
A  
R  
E

1. AGENCY USE ONLY (Leave blank)

28 Dec 92

Annual 1 Sep 91 - 31 Aug 92

2. FUNDING NUMBERS

1992 Summer Faculty Research Program (SFRP)

Volumes 1 - 16

✓-11

F49620-90-C-0076

Mr Gary Moore

3. PERSONAL OR ORGANIZATION NAME(S) AND ADDRESS(ES)

Research & Development Laboratoeis (RDL)  
5800 Uplander Way  
Culver City CA 90230-6600

AFOSR/NI 01 91

4. MONITORING AGENCY NAME(S) AND ADDRESS(ES)

AFOSR/NI  
110 Duncan Ave., Suite B115  
Bldg 410  
Bolling AFB DC 20332-0001  
Lt Col Claude Cavender

5. SUPPLEMENTARY NOTES

6. DISTRIBUTION AVAILABILITY STATEMENT

UNLIMITED

7. ABSTRACT (Maximum 200 words)

The purpose of this program is to develop the basis for continuing research of interest to the Air Force at the institution of the faculty member; to stimulate continuing relations among faculty members and professional peers in the Air Force to enhance the research interests and capabilities of scientific and engineering educators; and to provide follow-on funding for research of particular promise that was started at an Air Force laboratory under the Summer Faculty Research Program.

During the summer of 1992 185 university faculty conducted research at Air Force laboratories for a period of 10 weeks. Each participant provided a report of their research, and these reports are consolidated into this annual report.

8. KEY WORDS

10. SECURITY CLASSIFICATION

UNCLASSIFIED

18. SECURITY CLASSIFICATION OF THIS PAGE

UNCLASSIFIED

19. SECURITY CLASSIFICATION OF ABSTRACT

UNCLASSIFIED

UL

11. ABSTRACT

UNITED STATES AIR FORCE  
SUMMER RESEARCH PROGRAM -- 1992  
GRADUATE STUDENT RESEARCH PROGRAM (GSRP) REPORTS

VOLUME 11

ARNOLD ENGINEERING DEVELOPMENT CENTER  
CIVIL ENGINEERING LABORATORY  
FRANK J. SEILER RESEARCH LABORATORY  
WILFORD HALL MEDICAL CENTER

RESEARCH & DEVELOPMENT LABORATORIES

5800 Uplander Way  
Culver City, CA 90230-6608

Program Director, RDL  
Gary Moore

Program Manager, AFOSR  
Lt. Col. Claude Cavender

Program Manager, RDL  
Billy Kelley

Program Administrator, RDL  
Gwendolyn Smith

Submitted to:

AIR FORCE OFFICE OF SCIENTIFIC RESEARCH

Bolling Air Force Base

Washington, D.C.

December 1992

## PREFACE

This volume is part of a 16-volume set that summarizes the research accomplishments of faculty, graduate student, and high school participants in the 1992 AFOSR Summer Research Program. The current volume, Volume 11 of 16, presents the final research reports of graduate student (GSRP) participants at Arnold Engineering Development Center, Civil Engineering Laboratory, Frank J. Seiler Research Laboratory, and Wilford Hall Medical Center.

Reports presented herein are arranged alphabetically by author and are numbered consecutively -- e.g., 1-1, 1-2, 1-3; 2-1, 2-2, 2-3. Research reports in the 16-volume set are organized as follows:

VOLUME	TITLE
1	Program Management Report
2	Summer Faculty Research Program Reports: Armstrong Laboratory
3	Summer Faculty Research Program Reports: Phillips Laboratory
4	Summer Faculty Research Program Reports: Rome Laboratory
5A	Summer Faculty Research Program Reports: Wright Laboratory (part one)
5B	Summer Faculty Research Program Reports: Wright Laboratory (part two)
6	Summer Faculty Research Program Reports: Arnold Engineering Development Center; Civil Engineering Laboratory; Frank J. Seiler Research Laboratory; Wilford Hall Medical Center
7	Graduate Student Research Program Reports: Armstrong Laboratory
8	Graduate Student Research Program Reports: Phillips Laboratory
9	Graduate Student Research Program Reports: Rome Laboratory
10	Graduate Student Research Program Reports: Wright Laboratory
11	Graduate Student Research Program Reports: Arnold Engineering Development Center; Civil Engineering Laboratory; Frank J. Seiler Research Laboratory; Wilford Hall Medical Center
12	High School Apprenticeship Program Reports: Armstrong Laboratory
13	High School Apprenticeship Program Reports: Phillips Laboratory
14	High School Apprenticeship Program Reports: Rome Laboratory
15	High School Apprenticeship Program Reports: Wright Laboratory
16	High School Apprenticeship Program Reports: Arnold Engineering Development Center; Civil Engineering Laboratory

## 1992 GRADUATE RESEARCH REPORTS

**Arnold Engineering Development Center  
Civil Engineering Laboratory  
Frank J. Seiler Research Laboratory  
Wilford Hall Medical Center**

<b><u>Report Number</u></b>	<b><u>Report Title</u></b>	<b><u>Author</u></b>
<b><u>Arnold Engineering Development Center</u></b>		
1	Experiences using Model-Based Techniques for the Development of a Large Parallel Instrumentation System	Theodore Bapty
2	An Overview of the Behavior of Aluminum in Solid Propellant Rocket Motors	Robert J. Geierman
3	Solid Particulate Dispersion in Turbulent Atmospheric Boundary Layers	William Kvasnak
4	CAD and Acoustic BEM Applied to the Modelling of the AEDC ASTF EGMS	Richard A. Marschall
5	A Multigraph Implementation of a Distributed Image Processing System	Michael S. Moore
6	A Cell Averaged Approach to the Solution of Integral Conservation Laws	Blair H. Rollin
7	Analysis of Acoustic Oscillations in Cavities with Spoiler Attachments	Daniel E. Schatt
8	Numerical Modelling of Mixing and Reacting Flowfields	Paul Vitt
9	Multidimensional Conjugated Heat Transfer Analysis for the Arnold Engineering Development Center Heat-H1 Test Unit Nozzle	Michael A. Weaver
<b><u>Civil Engineering Laboratory</u></b>		
10	Setting Criteria for Halon Replacement Agents	Timothy Keen
11	A Simplified Model for Predicting Jet Impingement Heat Transfer	Mark E. Kithcart
<b><u>Frank J. Seiler Research Laboratory</u></b>		
12	Velocity and Vorticity Measurements in Transient Oscillatory Separating Boundary Layer Flows	Paul K. Berg
13	(Report not received)	
14	Multivariable Transfer Functions and Optimal Passive Damping for a Slewing Piezoelectric Laminate Beam	Travis DuBois

**Report  
Number**

**Report Title**

**Author**

**Frank J. Seiler Research Laboratory (cont'd)**

- |    |  |                   |
|----|--|-------------------|
| 15 | A Neural Network Model of the Unsteady Aerodynamics on a Pitching Wing | William E. Faller |
| 16 | NMR Relaxation Studies of Microdynamics in Chloroaluminate Melts       | Pamela A. Shaw    |

**Wilford Hall Medical Center**

- |    |   |              |
|----|---|--------------|
| 17 | (Report not received)                                 |              |
| 18 | Enhanced Physiologic Monitoring of Closed Head-Injury | Brian Carter |

**ARNOLD ENGINEERING DEVELOPMENT CENTER**

EXPERIENCES USING MODEL-BASED TECHNIQUES  
FOR THE DEVELOPMENT OF A  
LARGE PARALLEL INSTRUMENTATION SYSTEM

Ben Abbott  
Csaba Biegl  
Research Faculty  
Theodore A. Bapty  
PhD. Candidate  
Department of Electrical Engineering

Vanderbilt University  
400 24th Ave. S.  
Nashville, TN 37235-1824

Final Report for:  
Summer Research Program  
Arnold Engineering Development Center

Sponsored by:  
Air Force Office of Scientific Research  
Bolling Air Force Base, Washington, D.C.

August 1992



EXPERIENCES USING MODEL-BASED TECHNIQUES  
FOR THE DEVELOPMENT OF A  
LARGE PARALLEL INSTRUMENTATION SYSTEM

Ben Abbott  
Csaba Biegl  
Research Faculty  
Theodore A. Bapty  
PhD. Candidate  
Department of Electrical Engineering  
Vanderbilt University

Abstract

Experience using a *model-based* approach to develop an 83 processor parallel instrumentation system for turbine engine aeromechanic stress analysis is described. The approach includes using a graphics based editor to describe the structure of the desired signal flow graph as well as the target hardware architecture. Program synthesis techniques are used to automatically transform these models into an executable system.

AN OVERVIEW OF THE BEHAVIOR OF ALUMINUM  
IN SOLID PROPELLANT ROCKET MOTORS

Robert J. Geierman  
Graduate Research Assistant  
Department of Aerospace Engineering

University of Tennessee Space Institute  
B. H. Goethert Parkway  
Tullahoma, TN 37388

Final Report for:  
Summer Research Program  
Arnold Engineering Development Center

Sponsored by:  
Air Force Office of Scientific Research  
Bolling Air Force Base, Washington, D.C.

August 1992

AN OVERVIEW OF THE BEHAVIOR OF ALUMINUM  
IN SOLID PROPELLANT ROCKET MOTORS

Robert J. Geierman  
Graduate Research Assistant  
Department of Aeronautical Engineering  
University of Tennessee Space Institute

Abstract

An extensive literature search was conducted in order to provide an adequate understanding of the processes which aluminum undergoes at several locations in a solid rocket motor. This paper describes the phenomena which occur at the propellant surface, the combustion chamber, the rocket motor nozzle, and the exhaust plume. These descriptions include a discussion of previous models and experiments that have been conducted. Although several of these models make very accurate performance predictions, much of their basis rests on empirical data instead of analytical models. Due to this fact, some of the previous models may have several shortcomings (in the analytical sense). Some of these shortcomings include: -1) the lack of an adequate analytical agglomeration model, -2) the neglect of agglomerate radiation heat transfer to the propellant surface, -3) the neglect of particle collisions and fragmentations, -4) no predictions of slag accumulation versus nozzle geometry, and -5) the lack of an accurate description of the particle distribution and nozzle ablation at the nozzle throat. An effort to remedy these shortcomings will be presented in a thesis at a later date.

## Introduction

Metal additives have long been used in solid rocket propellants in order to improve acoustic stability, control burn rate and, most importantly, to improve specific impulse. Due to its relatively low cost, availability, and high combustion temperature, aluminum is, by far, the most often used metal additive.

Although aluminum has been used in rocket motors for many years, its combustion processes are still not completely understood. An adequate understanding of the combustion of aluminum is necessary to accurately: -1) predict plume signatures and radiation heat transfer (due to the aluminum oxide particle radiation in the plume), -2) predict combustion stability due to acoustic damping of aluminum oxide particles, and -3) compute the specific impulse of the rocket motor by properly incorporating the two-phase flow losses of the aluminum oxide particles.

This paper attempts to describe the physical processes which occur throughout the aluminized solid propellant rocket motor. This is accomplished through the use of an extensive literature search which describes the physical phenomena for four locations throughout the motor. These locations include: -1) the propellant surface, -2) the area inside the combustion chamber, -3) the rocket motor nozzle, and -4) the rocket motor exhaust plume. Later, these processes will be described by partial differential equations, incorporated into numerical models and presented in a thesis in order to predict the characteristics of aluminum combustion in subscale HTPB/Al/AP propellant motors.

## Propellant Surface

An adequate understanding of the propellant surface phenomena is probably the most important aspect of aluminum combustion modeling. Its importance is due to the fact that the size of the aluminum and aluminum oxide particles released from the surface largely determines the chemical composition, physical properties, and the distribution of particles throughout the rocket motor and exhaust plume. The complexity of this process is mainly due to the fact that the aluminum first melts and then forms "agglomerates" that can become much larger than the initial particle size before they leave the propellant surface and ignite. Both the size and degree of agglomeration are some complicated function of the ballistic parameters and the propellant composition. There have been several attempts to model this phenomenon, both experimental and analytical.

Due to the harsh environment in the combustion chamber, small aluminum agglomerate sizes (typically < 100 microns), and relatively fast combustion times (typically 10 - 100 ms), the actual agglomerate sizes and properties are difficult, if not impossible, to observe directly during an actual motor firing (Ref. 1). Attempts have been made to measure particle sizes by collecting the quenched exhaust products from burning propellant strands in closed strand combustion bombs (Ref. 2-4). By collecting the exhaust products, scientists were able to measure the pertinent properties of the combustion products (i.e. size, composition, etc.). Although these firings should have produced accurate and consistent measurements, their data shows significant scatter. These

experimental methods have, however, produced some very accurate empirical models and some important qualitative information(Ref. 5).

Another experimental method that has been used to determine the combustion processes at the surface of the propellant is the use of strand burners combined with high speed photography(Ref. 6-8). These usually consist of burning a propellant strand in a pressurized combustion bomb. In order to observe the surface phenomenon, the propellant strand is sometimes fed into the combustion bomb at a rate equal to the burning rate of the propellant. In this way, the propellant surface is kept stationary relative to an observation window and high speed film is used to record the combustion processes occurring at the propellant surface. The use of these combustion bombs has also produced some qualitative information that is consistent with the exhaust product experiments. It should be noted, however, that care should be taken when trying to extrapolate the results of either of these experiments to actual rocket motors. This is due to the fact that many of these experiments are conducted at conditions that are not consistent with actual rocket motor environments(i.e. low chamber pressure, different species concentrations, etc.).

As noted earlier, both of these experimental methods do produce some important qualitative information. Some of these dependencies include:

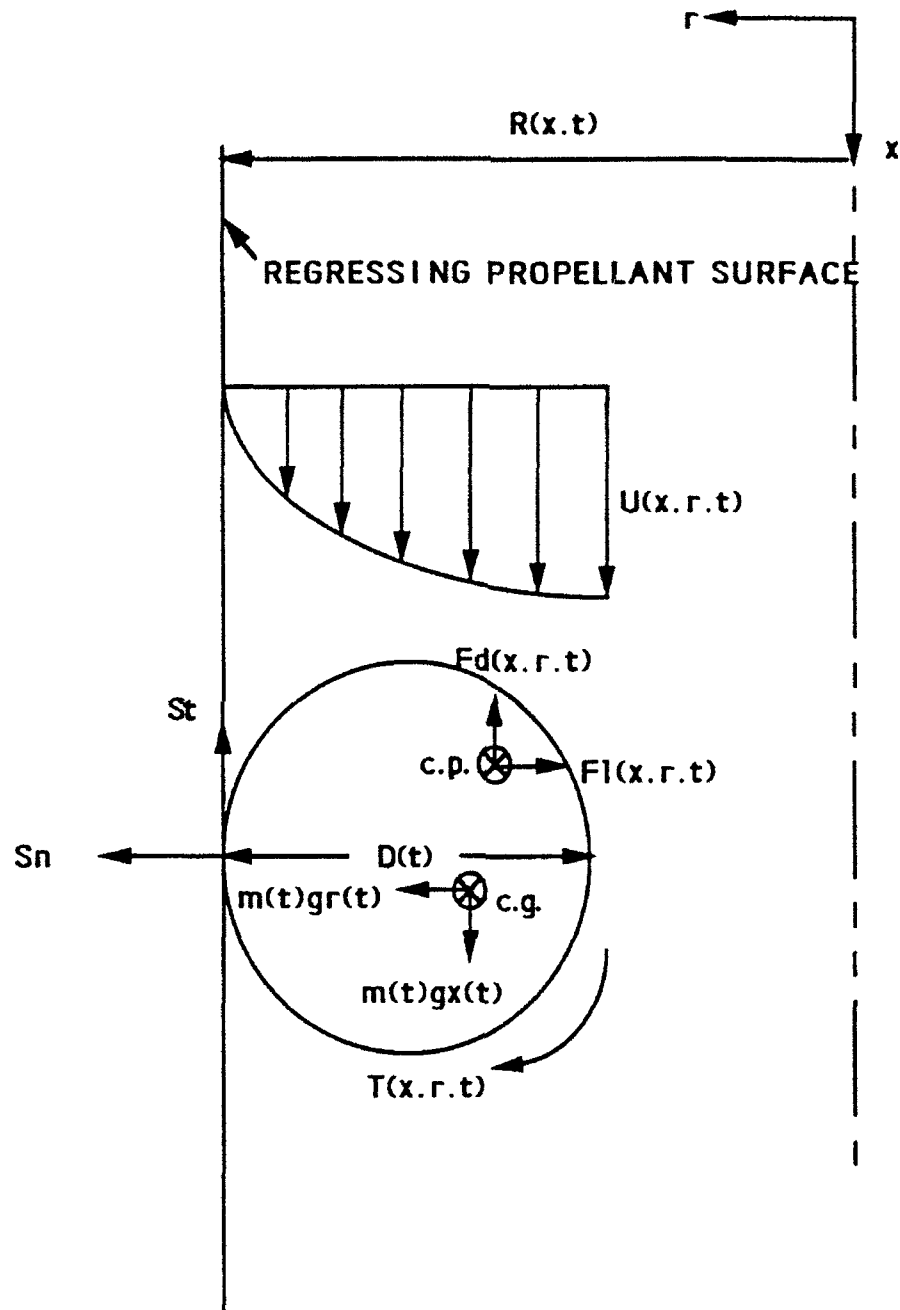
- 1) as chamber pressure increases, the agglomerate size decreases.
- 2) as the normal component of acceleration increases, agglomerate size increases.

- 3) as velocity of the gas increases, agglomerate size decreases.
- 4) as aluminum concentration increases (or oxidizer concentration decreases), agglomerate size increases.
- 5) as ammonium perchlorate (AP) particle size decreases, agglomerate size increases.

Another method that can be used to model the propellant surface phenomenon is to apply an analytical approach. One can immediately see the difficulty of employing an analytical model just by looking at the forces that occur on the individual agglomerates as they emerge from the propellant surface (see Figure 1 and Variable Definitions (Ref. 9)). The agglomerate is held to the propellant surface by surface tension and a normal acceleration term (for spin-stabilized rockets). The forces that attempt to "roll" the agglomerate down the propellant surface include the drag and axial acceleration while the lift term attempts to pull the particle away from the propellant surface. Since the diameter of the agglomerate is a function of time and the flow is assumed to be turbulent, all of the above mentioned forces also become time dependent. Add to this the fact that some of the aluminum may be converting to aluminum oxide and one can see that both the center of gravity and center of pressure of the particle can be at a variable location (causing additional moments). It should be noted that even this generalized force diagram has made several simplifying assumptions. These assumptions include: spherical agglomerate shape, smooth propellant surface and axial gas velocity.

# FIGURE 1: GENERALIZED FORCE DIAGRAM

(Ref. 9)





## VARIABLE DEFINITIONS

$A_e$  = nozzle exit area

$A(x,t)$  = area of nozzle or plume as a  
function of axial location  
and time

c.g. = center of gravity

c.p. = center of pressure

$D(t)$  = diameter as a function of time

$E(x,r,t,T)$  = particle emissivity as a  
function of location, time  
and temperature

$F_d(x,r,t)$  = drag force as a function of  
location and time

$F_l(x,r,t)$  = lift force as a function of  
location and time

$g_x(t)$  = axial acceleration as a  
function of time

$g_r(t)$  = radial acceleration as a  
function of time

$m(t)$  = droplet mass as a function of  
time

$R(x,t)$  = propellant surface location as  
a function of  $x$  and time

$R_t$  = radius of curvature for nozzle

$S_n$  = normal surface tension

$S_t$  = tangential surface tension

$T(x,r,t)$  = surface shear force as a  
function of location and time

$U_g(x,r,t)$  = gas velocity distribution as  
a function of location and  
time

$U_p(x,r,t,D)$  = particle velocity as a  
function of location, time  
and diameter

One type of analytical approach used to describe the propellant surface phenomenon involves using partial differential equations(Ref. 10-11). First, simplified assumptions about the propellant surface processes are made. Then, the necessary conservation equations with their appropriate boundary conditions are applied. Finally, the resulting partial differential equations are usually discretized and incorporated in a numerical model. The accuracy of this approach is subject to the initial assumptions made and the step size taken in the discretization scheme. Depending upon the simplifying assumptions, these methods can involve considerable computational time in order to produce accurate results.

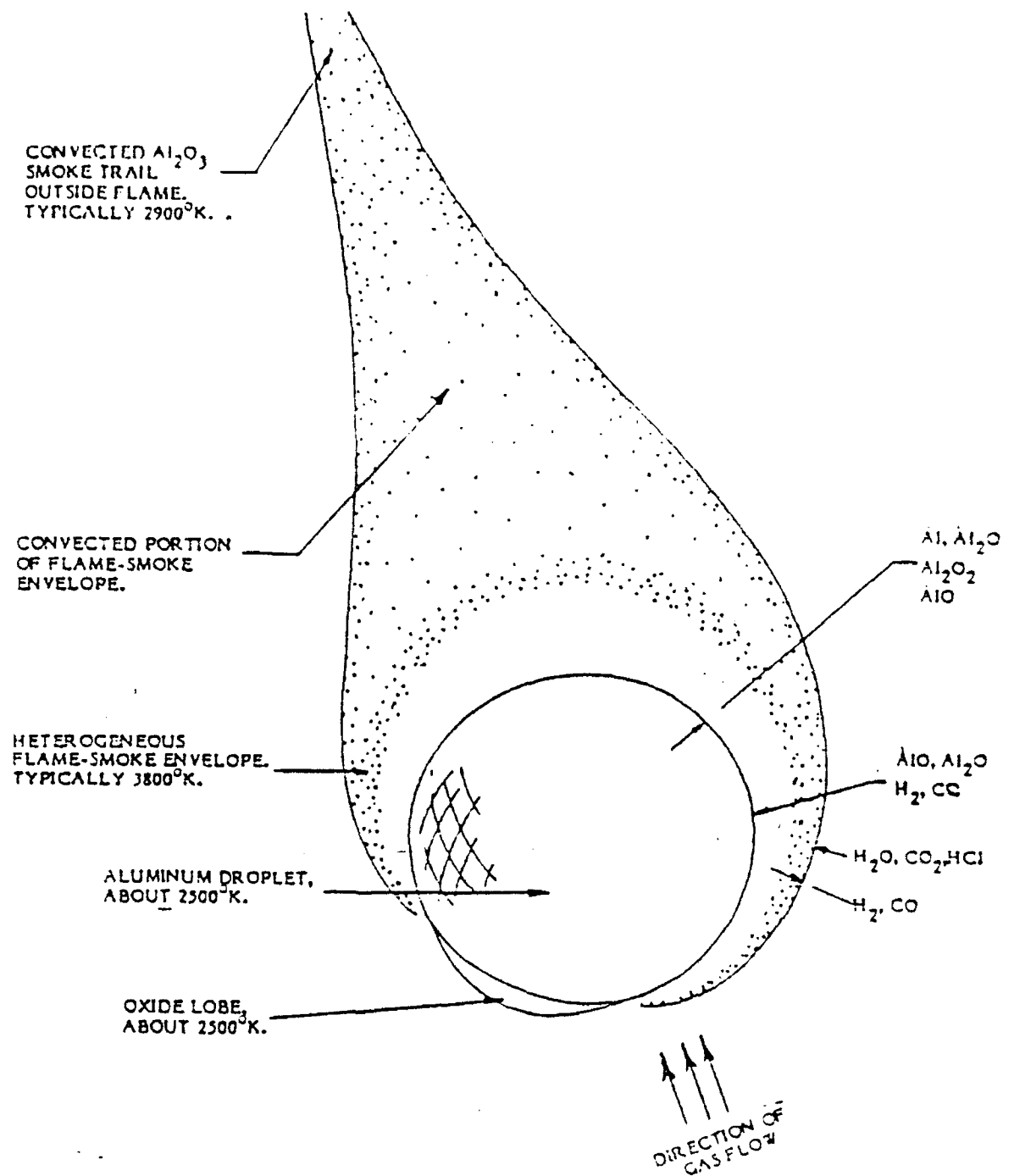
Another analytical method employs the use of a "pocket" model(Ref. 12-14). Here, the propellant is assumed to be made up of a series of "pockets" defined by increasing AP size with an aluminum particle in the center of the pocket. The size of the initial aluminum and AP determine if the aluminum will burn immediately or agglomerate and then burn in the next larger sized pocket. This method also seems to produce accurate qualitative results that agree with experimental data. Since this method allows for varying AP size and can be easily incorporated into a numerical model, it is probably quicker to obtain accuracy, and therefore, more preferable to the partial differential equation approach.

velocity lags, and thermal lags for that matter, they usually do not consider the amount of slag that has accumulated or the corresponding mass loss to the flow(Ref 19). This may be due to the fact that slag accumulation is largely geometry dependent. For this reason, only limited studies of slag accumulation in individual solid rocket motors have been conducted(Ref. 20).

As the particles enter the nozzle throat they go through a normal shock wave. This increase in pressure and temperature may cause many of the larger particles to break up into smaller particles. Some models incorporate this fragmentation by considering the particle's Weber number and comparing it to a critical value(Ref. 21). Whenever a particle reaches this critical value the particle is assumed to break up, but no size distribution of the fragments is calculated. In addition to the fragmentation, some of the throat material may ablate and thus add "contaminants" to the flow.

As the particles go from the throat to the exit plane, they encounter numerous oblique shock waves. The number of oblique shock waves is usually limited by careful selection of the nozzle contour. These oblique shocks may also act to shatter the larger particles. As the particles approach the exit, some of the smaller particles may begin to solidify. Once again, the smaller particles closely follow the streamlines of the gas while the larger particles lag behind.

**FIGURE 2: GENERAL NATURE OF ALUMINUM DROPLET COMBUSTION IN A SOLID ROCKET MOTOR ENVIRONMENT**  
(Ref. 1)



is recommended that further investigation of the combustion processes be conducted.

Combustion of agglomerates is not the only process that occurs in the combustion chamber(see Figure 3). Fine "smoke" particles(usually submicron in size) make up the majority of the combustion products. The agglomerates may break up due to internal and external forces or they may form larger agglomerates due to collisions. Both of these competing processes are usually considered to be equal and no net change in particle sizes is calculated. This assumption warrants further investigation. Also, as the burning particle leaves the propellant surface, it emits radiation back to the surface and to other cooler particles. This term, too, is usually neglected(even though it has been shown to contribute as much as twenty percent of the surface heating(Ref. 18)). In order to accurately model the combustion process, this radiation heat transfer must be included in both the surface model and the combustion chamber model.

#### Motor Nozzle

As the combustion products enter the nozzle they may or may not be completely burned(see Figure 4). As the agglomerates enter the inlet the smaller particles(and smoke) will follow the gas streamlines and velocities more closely. This lag in velocity and direction by the larger particles is due to their larger mass and inertia. For this reason and due to the geometry of the nozzle, some of the larger molten aluminum and aluminum oxide particles may accumulate as slag on the surface of the nozzle inlet. Although many models compensate for these

**FIGURE 3: COMBUSTION CHAMBER PHENOMENON**

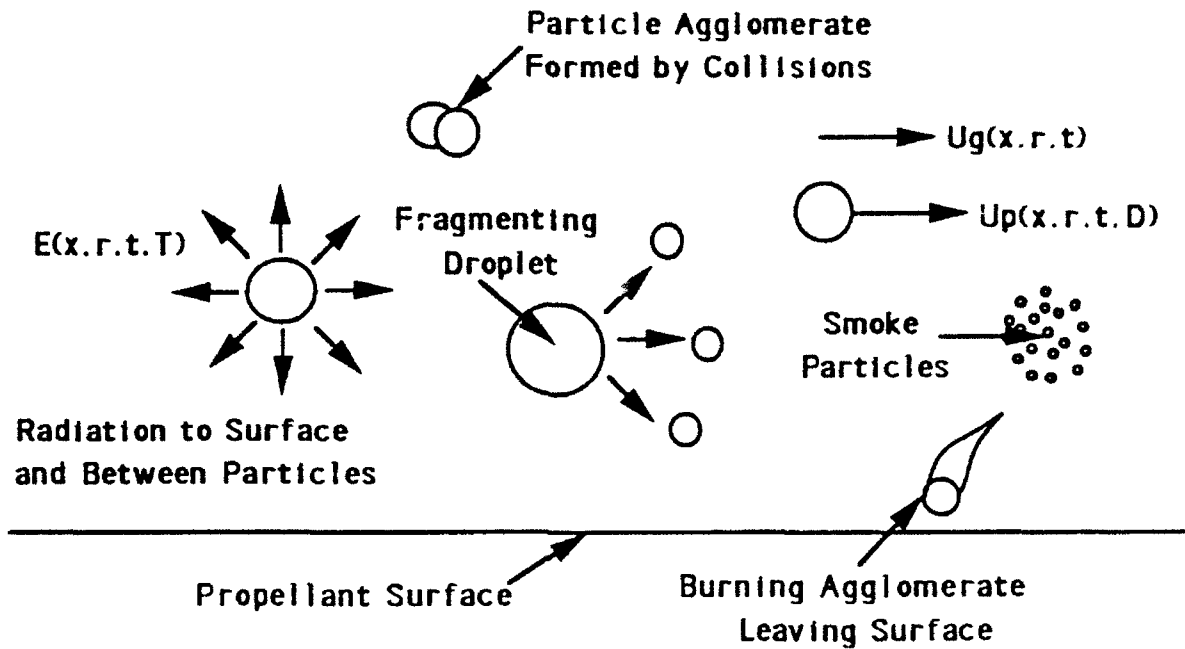
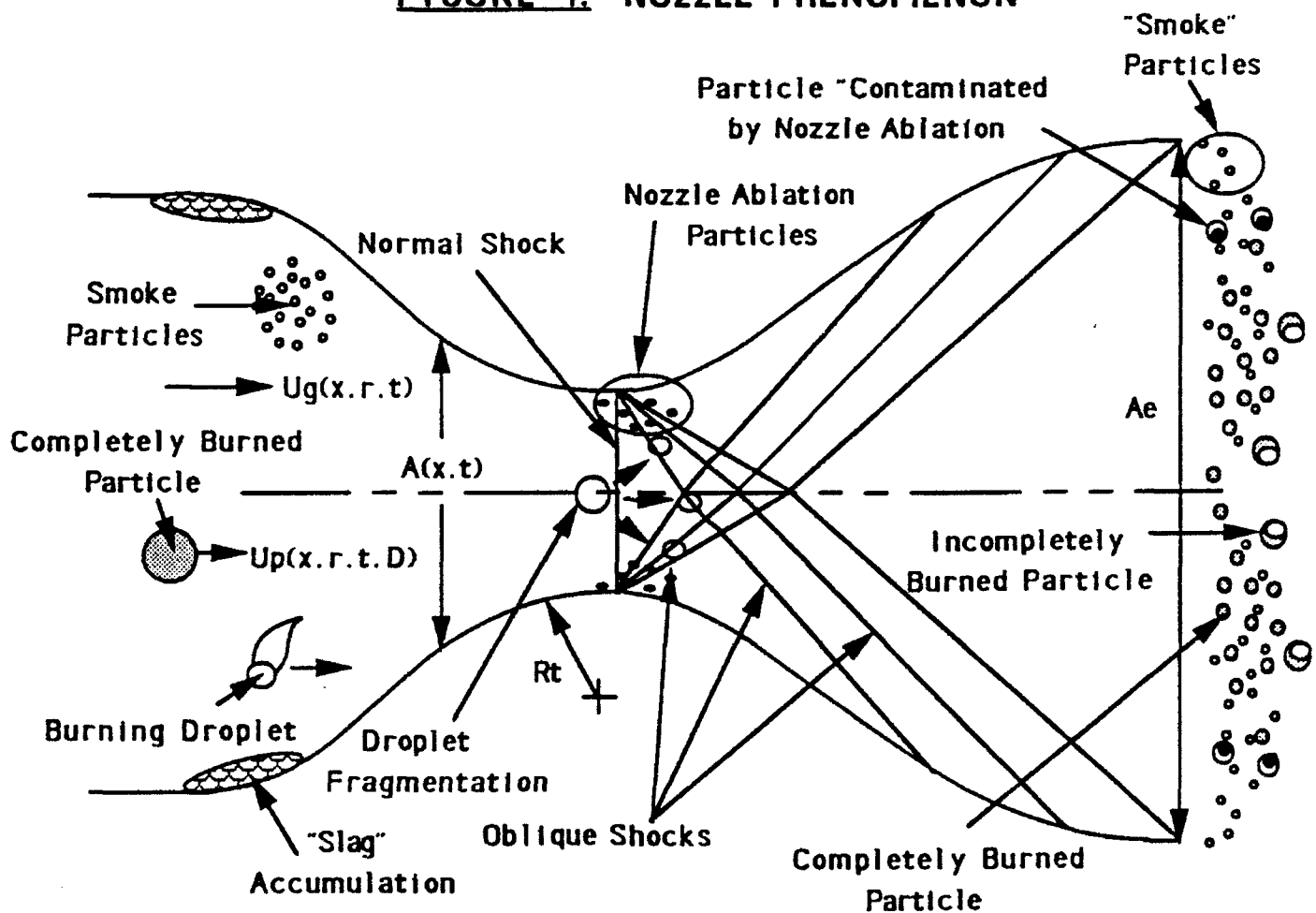


**FIGURE 4: NOZZLE PHENOMENON**



velocity lags, and thermal lags for that matter, they usually do not consider the amount of slag that has accumulated or the corresponding mass loss to the flow(Ref 19). This may be due to the fact that slag accumulation is largely geometry dependent. For this reason, only limited studies of slag accumulation in individual solid rocket motors have been conducted(Ref. 20).

As the particles enter the nozzle throat they go through a normal shock wave. This increase in pressure and temperature may cause many of the larger particles to break up into smaller particles. Some models incorporate this fragmentation by considering the particle's drag pressure and comparing it to a critical value(Ref. 21). Whenever a particle reaches this critical value the particle is assumed to break up, but no size distribution of the fragments is calculated. In this way, however, a maximum stable droplet size can be calculated. In addition to the fragmentation, some of the throat material may ablate and thus add "contaminants" to the flow.

As the particles go from the throat to the exit plane, they encounter numerous oblique shock waves. The number of oblique shock waves is usually limited by careful selection of the nozzle contour. These oblique shocks may also act to shatter the larger particles. As the particles approach the exit, some of the smaller particles may begin to solidify. Once again, the smaller particles closely follow the streamlines of the gas while the larger particles lag behind.

If one assumes a uniform particle distribution at the throat (which may not be an accurate assumption), as in most models, the particle distribution at the exit consists of larger particles near the center and smaller particles near the outside. However, the number of particles along the centerline at the exit is not a maximum. The maximum occurs at a small distance from the centerline. From the maximum, the number density tapers off to the exit radius value (Ref. 22).

#### Exhaust Plume

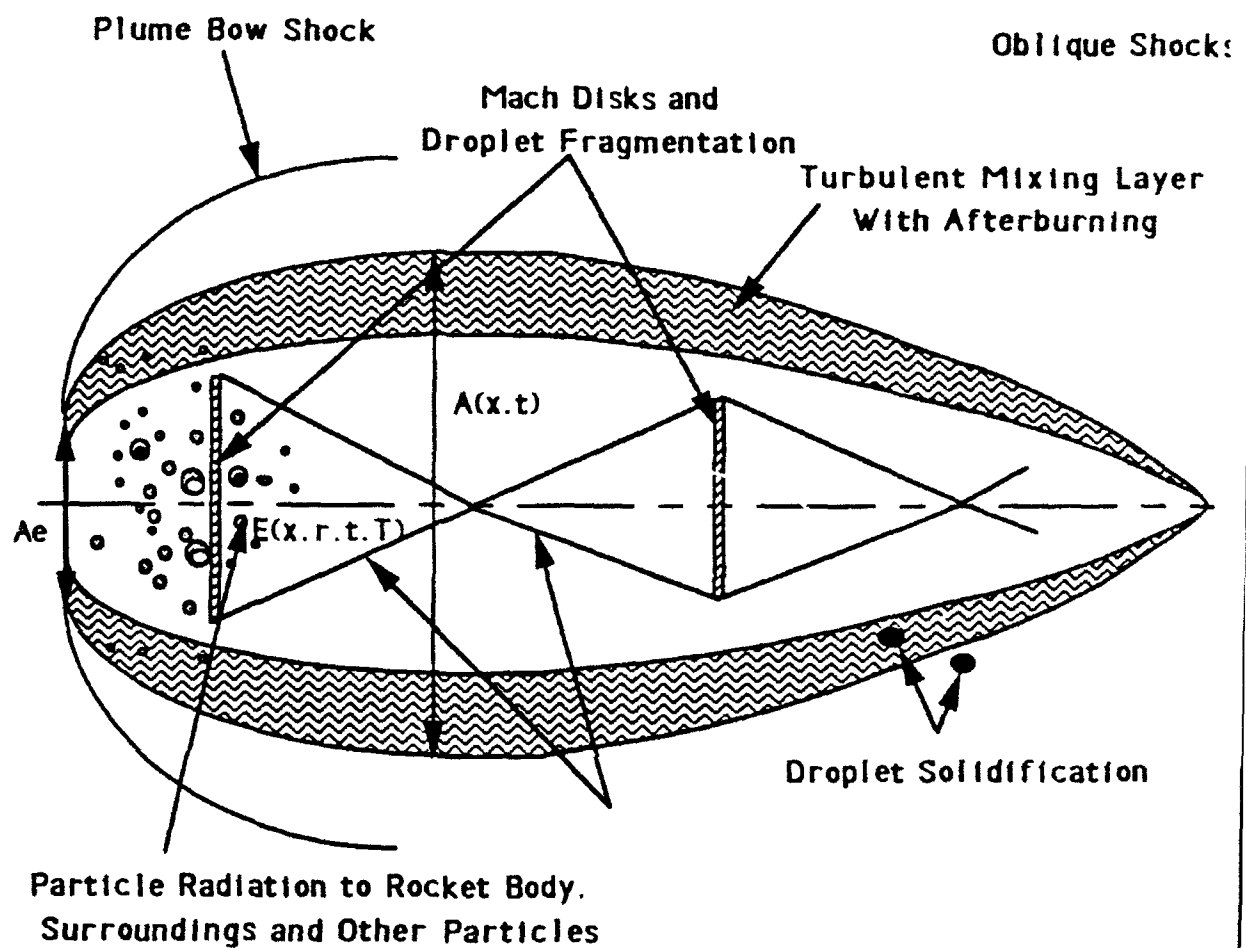
As the particles enter the plume, they again encounter a shock wave structure consisting of Mach disks (normal shocks) and oblique shocks (see Figure 5). In addition to these shocks, there may also be a bow shock at the edge of the plume depending upon the velocity and altitude of the rocket. The plume shape itself may vary drastically with altitude.

Another phenomenon which occurs in the plume is the existence of a turbulent mixing layer. This mixing layer may also include afterburning in which unburned aluminum particles are ignited. Also, some of the aluminum and aluminum oxide droplets will begin to solidify in the plume, with the larger droplets solidifying farther downstream (Ref. 23).

A large portion of the radiation heat transfer, and corresponding plume signature, comes from this cloud of liquid and solid aluminum oxide particles. Numerous models have been used to predict the plume



**FIGURE 5: ROCKET PLUME PHENOMENON**



radiation using Mie theory, Rayleigh scattering, and other methods(Ref. 24-26). The main limit to the use of these radiation models is an adequate description of the physical properties of the particles and an adequate representation of the size, composition, and distribution of the particles in the plume. The physical properties of interest include the emissivity, absorptivity, reflectivity, temperature, velocity, and density of the particles. Most of these properties are inter-related and some of them have been measured for actual rocket motor environments(Ref. 27-28). The composition of the particles can be greatly affected by nozzle ablation and afterburning. In turn, the composition of the particles has a tremendous influence on its physical properties. The distribution of these particles is mainly a function of the initial agglomerate size and the nozzle geometry.

#### Conclusions and Recommendations

Although some very accurate numerical models, such as the Solid Performance Program(SPP by Hermsen et. al.) and the One-Dimensional Reacting Three-Phase Flow with Mass Transfer Between Phases(OD3P by Kliegel et. al.), exist, it is recommended that some improvements should be implemented(Ref. 29). These improvements include: -1) the incorporation of an analytical pocket model, which includes the influence of ballistic parameters, to predict the size and extent of surface agglomeration.

-2) the inclusion of radiation heat transfer from the burning agglomerates to the propellant surface and other particles.

- 3) an adequate model to compute the size of particles formed by collisions of agglomerates in the combustion chamber.
- 4) a description which includes the size distribution of fragmented droplets in the combustion chamber, the nozzle, and the exhaust plume.
- 5) a simplified relation between slag accumulation and nozzle geometry.
- 6) computation of the actual particle distribution at the nozzle throat.
- 7) a calculation of the nozzle ablation rate and its effect on plume radiation.

Due to the length constraints of this paper, it was not possible to describe any area of the rocket motor in a detailed, analytical manner. However, some of these models and their suggested improvements will be investigated further. Ideally, these improvements will be incorporated into a numerical model and presented in a thesis at a later date.

## References

1. Price, E. W., "Combustion of Metalized Propellants", Fundamentals of Solid Propellant Combustion, AIAA Progress Astronautics and Aeronautics, Vol. 90, New York, 1984, pp.479-513.
2. Mitani, T. and Izumikawa, M., "Combustion Efficiencies of Aluminum and Boron in Solid Propellants", Journal of Spacecraft and Rockets, Vol. 28, No. 1, 1991, pp.79-84.
3. Eisel, J. L., Brown, B. G. and Price, E. W., "Pressure, Velocity, and Geometry Effect on Aluminum Oxide Produced During Aluminized Propellant Combustion", AIAA Journal, Vol. 13, No. 7, July, 1975, pp. 913-917.
4. Price, E. W., et. al., "Combustion of Aluminum in Solid Propellant Flames", AGARD Propulsion and Energetics Symposium on Solid Rocket Motor Technology, April 1979.
5. Hermesen, R. W., "Aluminum Oxide Particle Size for Solid Rocket Motor Performance Prediction", Journal of Spacecraft and Rockets, Vol. 18, No. 6, 1981, pp. 483-490.
6. Willoughby, P. G., Crowe, C. T. and Baker, K. L., "A Photographic and Analytic Study of Composite Propellant Combustion in an Acceleration Field", Journal of Spacecraft and Rockets, Vol. 8, No. 4, April, 1971, pp. 310-317.
7. Povinelli, L. A. and Rosenstein, R. A., "Alumina Size Distributions from High-Pressure Composite Solid-Propellant Combustion", AIAA Journal, Vol. 2, No. 10, October, 1964, pp. 1754-1760.
8. Gany, A., Caveny, L. H. and Summerfield, M., "Aluminized Solid Propellants Burning in a Rocket Motor Flowfield", AIAA Journal, Vol. 16, No. 7, July, 1978, pp. 736-739.
9. Pruitt, D., Personal Communications, July, 1992.
10. Gany, A. and Caveny, L. H., "Agglomeration and Ignition Mechanism of Aluminum Particles in Solid Propellants", Seventeenth Symposium (International) on Combustion, August, 1978, pp. 1453-1461.
11. Tsuji, H. "An Aerothermochemical Analysis of Erosive Burning of Solid Propellant", Ninth Symposium (International) on Combustion, (Academic Press, New York, 1963) pp. 384-393.
12. Cohen, N. S., "A Pocket Model for Aluminum Agglomeration in Composite Propellants", AIAA Paper No. 81-1585, Presented at the AIAA/SAE/ASME Seventeenth Joint Propulsion Conference, July 27-29, 1981, Colorado Springs, Colorado.
13. Kovalev, O. B., "Physicomathematical Model of the Agglomeration of Aluminum in the Combustion of Mixed Condensed Systems", Novosibirsk, Translated from Fizika Goreniya i Vzryva, Vol. 25, No.1, January - February, 1989, pp. 39-48.
14. Babluk, V. A., et. al., "Investigation of the Agglomeration of Aluminum Particles During the Combustion of Metalized Composite Condensed Systems", Leningrad, Translated from Fizika Goreniya i Vzryva, Vol. 3, May - June, 1985, pp. 20-25.

### References (continued)

15. Price, E. W., "Combustion of Aluminum in Solid Propellant Flames", Proceedings of the Fifty-Third Meeting of AGARD Propulsion and Energetics Panel, AGARD-CP-259, 1979, pp. 14-1-14-15.
16. Larson, R. S., "Size Distribution of Unburned Aluminum Particles in Solid Propellant Rocket Motor Exhaust", Sandia National Laboratories, Livermore, California, SAND86-8224.
17. Prentice, J. L., "Aluminum Droplet Combustion: Rates and Mechanisms in Wet and Dry Oxidizers", Naval Weapons Center, China Lake, California, NWC-TP-5569
18. Brewster, M. Q. and Parry, D. L., "Radiative Heat Feedback in Aluminized Solid Propellant Combustion", Journal of Thermophysics and Heat Transfer, Vol. 2, No. 2, April, 1988, pp. 123-130.
19. Hoffman, J. D. and Lorenc, S. A., "A Parametric Study of Gas-Particle Flows in Conical Nozzles", AIAA Journal, Vol. 3, No. 1, July, 1975, pp. 918-923.
20. Boraas, S., "Modeling Slag Deposition in the Space Shuttle Solid Rocket Motor", Journal of Spacecraft and Rockets, Vol. 21, No. 1, 1984, pp. 47-54.
21. Bartlett, R. W. and Delaney, L. J., "Effect of Liquid Surface Tension on Maximum Particle Size in Two-Phase Nozzle Flow", Pyrodynamics, Vol. 4, 1966, pp. 337-341.
22. Hiers, R. S., Personal Communications, July, 1992.
23. Reed, R. A., Personal Communications, August, 1992.
24. Edwards, D. K. and Babikian, D. S., "Radiation from a Nongray Scattering, Emitting, and Absorbing Solid Rocket Motor Plume", Journal of Thermophysics and Heat Transfer, Vol. 4, No. 4, 1990, pp. 446-453.
25. Stockham, L. W. and Love, T. J., "Radiative Heat Transfer from a Cylindrical Cloud of Particles", AIAA Journal, Vol. 6, 1969, pp. 1935-1940.
26. Watson, G. H. and Lee, A. L., "Thermal Radiation Model for Solid Rocket Booster Plumes", Journal of Spacecraft and Rockets, Vol. 14, No. 11, pp. 641-647.
27. Parry, D. L. and Brewster, M. Q., "Optical Constants and Size of Propellant Combustion Aluminum Oxide ( $Al_2O_3$ ) Smoke", AIAA Paper No. 88-3350, Presented at the AIAA/ASME/SAE/ASEE Twenty-Fourth Joint Propulsion Conference.
28. Worster, B. W. and Kadomiya, R. H., "Rocket Exhaust Aluminum Oxide Particle Properties", ARI RR-30, August, 1973.
29. George, D., "Recent Advances in Solid Rocket Motor Performance Prediction Capability", AIAA Paper No. 81-0033, Presented at the AIAA Nineteenth Aerospace Sciences Meeting, January 12-15, 1981, St. Louis, Missouri.

**SOLID PARTICULATE DISPERSION IN TURBULENT ATMOSPHERIC BOUNDARY  
LAYERS**

**William Kvasnak**

**Department of Mechanical and Aeronautical Engineering  
Clarkson University, Potsdam, NY 13699**

**Final Report for:  
Summer Research Program  
Arnold Engineering Development Center**

**Sponsored by:  
Air Force Office of Scientific Research  
Arnold Air Force Base, Tullahoma, TN.**

**August 1992**

# **SOLID PARTICULATE DISPERSION IN TURBULENT ATMOSPHERIC BOUNDARY LAYERS**

**William Kvasnak**

**Department of Mechanical and Aeronautical Engineering  
Clarkson University, Potsdam, NY 13699**

## **Abstract**

The simulation of turbulent and Brownian dispersion of solid particles in an atmospheric boundary layer requires the analysis of a Lagrangian trace of particle trajectories. A computer program for analyzing the motion of solid particles in the turbulent atmosphere is developed. The code is capable of providing near-field or far-field mass concentrations of particles from continuous, finite duration, and instantaneous point source emissions. The fully implicit integration of the particle equation of motion provides particle velocities induced by Stokes drag, Saffman lift, Brownian diffusion, and gravity. A maximum particle concentration of less than 0.02% by weight ensures that there is no modification of the air flow conditions by particle motion. Concentrations of this order allow for the omission of all particle-particle interactions. Three sample test cases are presented for illustrative purposes.

## Introduction

Problems caused by particulate dispersion affect our lives in ways we hardly even realize. The ecological difficulties caused by acid rain, smog, oil spills, and forest fires, alter the environment in ways that we are only beginning to comprehend. In addition to these and numerous other natural phenomena involving particulate transport, there are many man-made and industrial processes for which particulate flows play an essential role. For instance, in the early 1980's, the microelectronics industry determined that the microcontamination from small particles is the leading cause of loss of yield in the manufacturing process. This discovery led to a massive research effort in the area of microcontamination control and clean room applications. In addition, it has been determined that particles deposited from the air flow in the card passages, limit the life of circuit boards. These and many other applications lead to much research in the area of aerosol particle dynamics.

Due to the earlier research efforts in the area of aerosol particle dynamics, a wealth of knowledge exists on the subject. Fuchs [1], Hidy and Brock [2], van de Hulst [3], Twomey [4], and Cadle [5] are just a few of the classic textbooks on the subject. Particle dispersion in turbulent flows was simulated by Ahmadi [6], Li and Ahmadi [7], and Ounis et. al. [8]. However, to the author's knowledge, no detailed Lagrangian simulations of atmospheric turbulent dispersion have been published. The goal of this study is to provide a large-scale simulation of atmospheric dispersion of fine particles.

The use of a supercomputer facilitates large scale simulations which may provide the needed insight into the processes that dominate the motion and dispersion of fine particles in the atmosphere. This report describes a simulation program currently underway at Arnold Engineering Development Center for simulating the dispersion of fine particles in the atmosphere with application to environmental compliance with the Clean Air Act of 1990.

## Methodology

In this simulation a steady-state flow field is taken from an incompressible Navier-Stokes equation solver. The Lagrangian equation of motion for a heavy particle is then solved in time for a release of particles. The concentration at every location in the flow is taken as a mass percent of particles in a given region. The distribution of particles is calculated on a local and global level. Thirty-thousand particles, with diameters ranging from 0 to 100 microns, are simulated for instantaneous, finite duration, and continuous releases.

## Mechanics of Aerosols

By definition, an aerosol is a suspension of solid or liquid particles in a gas. Common aerosols found in nature include: dust, smoke, fog, haze, and smog. Aerosols typically range in size from 0.001 to 100



microns in diameter. To place these dimensions in perspective, note that the mean free path of air is about 0.07 microns and that the wavelength of visible light is between 0.4 to 0.7 microns. Also, the diameter of 0.01 microns roughly corresponds to the transition limit between molecule and particle. Particles larger than 100 microns typically do not remain suspended in air for a significant time duration. Thus, the behavior of particles is significantly affected by their size.

### Aerosol Particle Motion

The Lagrangian equation of motion for a heavy aerosol particle can be written as

$$m \frac{du^p}{dt} = \frac{3\pi\mu d}{C_c} (u^f - u^p) + mg, \quad (1)$$

where  $m$  is the mass of the particle and  $C_c$  is the Cunningham correction factor given by

$$C_c = 1 + \frac{2\lambda}{d} \left[ 1.257 + 0.4 \exp \left( -\frac{1.1d}{2\lambda} \right) \right]. \quad (2)$$

Dividing Eq. (3.2) by  $3\pi\mu d/C_c$  yields

$$\tau \frac{du^p}{dt} + u^p = u^f + \tau g \quad (3)$$

where  $\tau$  is the particle relaxation time. This is defined by

$$\tau = \frac{mC_c}{3\pi\mu d} = \frac{d^2 \rho^2 C_c}{18\mu} \quad (4)$$

where

$$m = \frac{\pi d^3}{6} \rho^f. \quad (5)$$

For relatively large particles,  $C_c \approx 1$  and

$$\tau = \frac{d^3 \rho^f}{18\mu}. \quad (6)$$

### Brownian Motion

Small particles suspended in a fluid undergo random translational motion due to molecular collisions. This phenomenon is referred to as Brownian motion. The Brownian motion leads to the diffusion of particles in accordance with Fick's law

$$J_i = -D \frac{dc}{dx_i}. \quad (7)$$

In this formula,  $c$  is the concentration,  $J$  is the flux, and  $D$  is the diffusion coefficient. The diffusivity is given as

$$D = \frac{kT}{3\pi\mu d} C_c. \quad (8)$$

The diffusion coefficient can be obtained by directly substituting Fick's law into the equation for mass conservation. The Brownian forces acting on the particle may be modeled as a white noise process. The

Brownian motion of particles is modeled by

$$\frac{du}{dt} + \beta u = n(t) \quad (9)$$

with

$$\beta = \frac{3\pi\mu d}{C_c m} = \frac{1}{\tau}. \quad (10)$$

Also,  $n(t)$  is a Gaussian white noise process with a spectral intensity

$$S_{nn} = \frac{2kT\beta}{\pi m}, \quad (11)$$

where  $k$  is the Boltzmann constant and  $T$  is the temperature. From Eq. (9) it follows that the power spectrum of the particle velocity is given as

$$S_{uu}(\omega) = |H(\omega)|^2 S_{nn}(\omega). \quad (12)$$

Here the system function,  $H(\omega)$ , is defined by

$$H(\omega) = \frac{1}{i\omega + \beta}. \quad (13)$$

Thus,

$$S_{uu}(\omega) = \frac{2kT\beta}{\pi m(\omega^2 + \beta^2)}. \quad (14)$$

The particle autocorrelation function is defined as

$$R_{uu}(\tau) = \overline{u'(t)u'(t+\tau)}, \quad (15)$$

and may be found by taking the inverse Fourier transform of the power spectrum, i.e.,

$$R_{uu}(\tau) = \frac{kT}{m} e^{-\beta|\tau|}. \quad (16)$$

The diffusivity is then given by

$$D = \int_0^\infty R_{uu}(\tau) d\tau = \frac{kTC_c}{3\pi\mu d}. \quad (17)$$

### Algorithm Development

This section is concerned with the actual algorithm used in the LTM3D program. The LTM3D program was written as a stand alone post processor for the Lawrence Livermore National Laboratory FEM3A/B gas transport and dispersion code. The LTM3D code solves the equations of motion for solid particles undergoing turbulent and Brownian diffusion. The Stokes drag assumption used, limits the particle

Reynolds number to a maximum of 1. The program models the dispersion of randomly sized particles using a Lagrangian approach. The computer program consists of a main program and seven subroutines written in standard FORTRAN 77 for portability. The next nine sections deal with the specifics of the code.

### Implicit Integration

The main program performs the actual integration of the equations. The constants that are used and the subroutines that are called are described in this section. The general logic is as follows. The program first reads the nodal points and velocities from an external file. Typically, these files are output from the FEM3A/B code. The new particles for each time step are then initialized. For each particle, the mean and the fluctuation fluid velocities are found. The Brownian force is also evaluated. Finally, the concentration is calculated. The particle velocity and position are then updated. Explicitly the particle equations in Eq. (3.3) are given as

$$\tau \frac{du^p}{dt} + u^p = u^f + B_u, \quad (18)$$

$$\tau \frac{dv^p}{dt} + v^p = v^f - g + B_v - qE. \quad (19)$$

$$\tau \frac{dw^p}{dt} + w^p = w^f + B_w. \quad (20)$$

Here  $u^p, v^p, w^p$  are the particle velocities. The fluid velocities are denoted as  $u^f, v^f, w^f$ . The variables  $B_u, B_v, B_w$  are the Brownian forces,  $E$  is the electric field strength,  $q$  is the particle charge number,  $\tau$  is the particle relaxation time, and  $g$  is the gravitational acceleration. The fully implicit formulation uses a Crank - Nicholson discretization method given by

$$\frac{x^{n+1} - x^n}{\Delta t} = \frac{u^{n+1} + u^n}{2} \quad (21)$$

$$\frac{u^{n+1} - u^n}{\Delta t} = \frac{1}{\tau} \left[ \frac{u^{n+1} + u^n}{2} - \frac{v(x^{n+1}) + v(x^n)}{2} \right] + \frac{w^{n+1} + w^n}{2} \quad (22)$$

A Newton's iterative method is used for the solution of the coupled equations in  $u$  and  $x$ .

The same routine is used to solve for these quantities for the next particle. The trajectory of each particle is individually advanced. Because of the amount of CPU time that is needed, an upper limit of 30,000 particles is suggested. A multiplicative scale factor can then be employed to simulate a more realistic release

### Concentration Calculation

The percent by mass of the particle in the area surrounding each node is assigned as an indication of the concentration at that node. The effect of mass concentration of a particle on each node is inversely proportional to the distance of the particle from that node. Specifically, the distance of the  $n^{th}$

particle from the  $m^{th}$  node is given as

$$d_{nm} = \sqrt{(x_n - x_m)^2 + (y_n - y_m)^2 + (z_n - z_m)^2}, \quad (23)$$

where  $d_i$  is the sum of the distances from the  $n^{th}$  particle to its 8 surrounding nodes.  $m^p$  is the mass of the  $n^{th}$  particle, and  $m^a$  is the mass of the fluid in the element containing the  $n^{th}$  particle. The mass percent contribution of the  $n^{th}$  particle on the  $m^{th}$  node is given by

$$c_{mn} = \frac{m^p(d_i - d_{nm})}{m^a}. \quad (24)$$

### Turbulent Fluctuations

The turbulent velocity field is constructed by the superposition of a fluctuating velocity onto the steady velocity field. A Gaussian random variable with a strength  $u'$  is generated in each of the three directions. The instantaneous velocity at the position of the particle is given as

$$\vec{u} = \vec{U} + u' \quad (25)$$

where  $\vec{U}$  is given by the subroutine fluid. Then, a Gaussian random variable with strength equal to the rms velocity may be used as a fluctuating component. If the procedure is done correctly, an imaginary hot wire held at a specific location in the flow will see a signal like the one shown in figure 1. from Tennekes and Lumley [9].

### Trilinear Interpolation

A Newton's iteration method and a trilinear interpolation (Benek et al. [10]) is used to find the particle position in grid coordinates. Then, using this information, it interpolates the fluid velocity at the particle location. Specifically, suppose the  $n$ th particle located at the point  $x_0$ , is contained in the cell with vertices

$$x_{j+\Delta j, k+\Delta k, l+\Delta l}, \quad \Delta j, \Delta k, \Delta l = 0, 1$$

and suppose the function values

$$f(x_{j+\Delta j, k+\Delta k, l+\Delta l}), \quad \Delta j, \Delta k, \Delta l = 0, 1$$

are known. The value  $f(x_0)$  is then approximated as follows. First, to establish a relation between computational and rectangular coordinates throughout the cell, define the trilinear vector-valued function:

$$\begin{aligned} X(\eta, \beta, \zeta) &= \sum_{p,q,r=0}^1 \alpha_{pqr} \eta^p \beta^q \zeta^r \\ &= \alpha_{000} + \alpha_{100}\eta + \alpha_{010}\beta + \alpha_{001}\zeta + \alpha_{110}\eta\beta + \alpha_{101}\eta\zeta + \alpha_{011}\beta\zeta + \alpha_{111}\eta\beta\zeta. \end{aligned} \quad (26)$$

The coefficients  $\alpha_{pqr}$  are determined by constraining this function to agree with known coordinates at the cell vertices:

$$\sum_{p,q,r=0}^1 \alpha_{pqr} (\Delta j)^p (\Delta k)^q (\Delta l)^r = x_{j+\Delta j, k+\Delta k, l+\Delta l}, \quad \Delta j, \Delta k, \Delta l = 0, 1. \quad (27)$$

This is a linear set of equations which can be solved algebraically for the components of the vectors  $\alpha_{pqr}$ . Similarly, the function  $f(x)$  is represented throughout the cell with a trilinear function:

$$F(\eta, \beta, \zeta) = \sum_{p,q,r=0}^1 f_{pqr} \eta^p \beta^q \zeta^r \quad (28)$$

$$= f_{000} + f_{100}\eta + f_{010}\beta + f_{001}\zeta + f_{110}\eta\beta + f_{101}\eta\zeta + f_{011}\beta\zeta + f_{111}\eta\beta\zeta.$$

The coefficients  $f_{pqr}$  are determined by constraining this function to agree with known function values at the cell vertices:

$$\sum_{p,q,r=0}^1 f_{pqr} (\Delta j)^p (\Delta k)^q (\Delta l)^r = f(x_{j+\Delta j, k+\Delta k, l+\Delta l}), \quad \Delta j, \Delta k, \Delta l = 0, 1. \quad (29)$$

Again, this is a linear set of equations which can be solved algebraically for  $f_{pqr}$ . To find the computational coordinates of the point  $x_0$ , Newton's method is used to find  $(\eta_0, \beta_0, \zeta_0)$  such that  $X(\eta_0, \beta_0, \zeta_0) = x_0$ . Specifically, if  $\eta_k = (\eta_k, \beta_k, \zeta_k)$  denote successive Newton approximations to  $(\eta_0, \beta_0, \zeta_0)$ , then

$$\eta_{k+1} = \eta_k - [D\eta X(\eta_k)]^{-1} [X(\eta_k) - x_0] \quad (30)$$

where

$$D\eta X = \left[ \frac{\partial X}{\partial \eta}, \frac{\partial X}{\partial \beta}, \frac{\partial X}{\partial \zeta} \right]. \quad (31)$$

After this iteration converges to  $(\eta_0, \beta_0, \zeta_0)$ , these computational coordinates are used to approximate  $f(x_0)$  by  $F(\eta_0, \beta_0, \zeta_0)$ .

## Results

Each test case uses the steady-state flow field output of the FEM3A/B code. Figure 2 shows the three-dimensional grid, contours of the average u-component of velocity, and the contours of the average v-component of velocity used for each test case. The 45 x 12 x 15 grid spans a three-dimensional space of 300m x 60m x 120m. The grid is packed near the ground, and in the area of the release. It is noted here that the grid used in these cases was chosen for speed, not accuracy. A much finer grid is needed for resolution of all relevant scales. The acceleration of the flow by the ramp is a classic test case. The results of the velocity are in good agreement with intuition and previous data. This flow was chosen because intuition may be the best tool available for solid particulate dispersion concentrations without any experimental data for comparison.

### Instantaneous Release

In the first test case 30,000 particles are released simultaneously from a point source in the flow. Figures 3 and 4 depict the diffusion dynamics of the instantaneous release. Figure 3 shows the initial distribution of the particle diameters, the contours of initial concentration, and the spatial distribution of the particles. The linear distribution between 0 and 100 microns has an average of 50 microns and a standard deviation of 25 microns. Approximately 300 particles of a given size exist in the flow field. The initial concentration is centered at the point source. The concentration is highest at the source and decreases monotonically in a sphere surrounding the source. The average diameter of 50 microns reflects that the particles are not separated with size, but instead are well mixed.

Figure 4 shows the dust cloud 87.5 seconds after the release. The distribution is now truncated at 50 microns. This indicates that the larger particles have precipitated out of the flow. The mean diameter is now 23 microns and the standard deviation is 17 microns. The small particles are still suspended in the flow. The concentration 87.5 seconds after release shows that the mass percent is centered at the middle of the cloud because of the relatively large number of small particles as compared with the smaller number of large particles. The cloud has moved downstream, leaving only deposited particles on the ground. Almost no concentration is found in the wake of the instantaneous released cloud. The cloud has diffused somewhat in the vertical direction due to Brownian and turbulent fluctuations. The spatial distribution of the particles left in the flow show that the smaller particles are much further downstream than the larger particles. The larger particles have a greater relaxation time and take longer to respond to the fluctuations of the velocity. The larger particles also occupy the space only near the ground. Gravity acts strongly on these particles and forces precipitation. The smaller particles extend quite further from the ground because of the reduced effect of gravity.

### Finite Duration Release

In the second test case, 400 particles are released every half-second for 37.5 seconds from a point source in the flow. This gives a total release of 30,000 particles analogous to test case 1. Figures 5 and 6 depict the diffusion dynamics of the finite duration release. Figure 5 shows the initial distribution of the particle diameters, the initial concentration contours, and the spatial distribution of particles at time  $t_0$ . The linear distribution between 0 and 100 microns has an average of 50 microns and a standard deviation of 25 microns. Approximately 15 particles of a given size exist in the flow field initially. The relative scatter of the diameters has now increased because of the lower number of samples. The initial concentration is centered at the point source. The concentration is highest at the source and decreases monotonically in a sphere surrounding the source. For the initial condition, the particles occupy the region surrounding the source. The average

diameter of 50 microns reflects that the particles are not separated with size, but instead are homogeneously mixed.

Figure 6 shows the dust cloud 87.5 seconds after the release. This figure indicates that the distribution is now constant for the first 50 microns then decreases to 80 microns. The largest particle left in the flow field is shown to be 80 microns. This indicates that the larger particles have precipitated out of the flow. The smaller particles, however, are still suspended in the flow even from the initial release. The concentration variation shows the cloud extending far downstream of the initial release. The mass percent is centered near the trailing edge of the cloud because of the relatively large number of large particles still in the flow as compared with the instantaneous release. The cloud of the finite duration release is much longer than the cloud of the instantaneous release. The cloud has moved downstream leaving only deposited particles on the ground. Almost no concentration is found in the wake of the finite duration cloud. The cloud has diffused somewhat in the vertical direction due to Brownian and turbulent fluctuations. Here, we also see that the smaller particles are much further downstream than the larger particles. The smaller particles released initially have now traveled far downstream and the larger particles released at the end of the finite duration have not yet precipitated out.

### Continuous Release

In the third test case, 150 particles are released every half-second for 100 seconds, from a point source in the flow. This gives a total release of 30,000 particles which is analogous to test cases 1 and 2. Figures 7 and 8 depict the diffusion dynamics of the continuous release. Figure 7 shows the initial distribution of the particle diameters, the initial concentration, and the spatial distribution of the particles at time  $t_0$ . The linear distribution between 0 and 100 microns has an average of 50 microns and a standard deviation of 25 microns. Approximately 5 particles of a given size exist in the flow field initially. The relative scatter of the diameters has again increased because of the number of samples. The initial concentration is centered at the point source. The concentration is highest at the source and decreases monotonically in a sphere surrounding the source. For the initial condition, the particles occupy the region surrounding the source. The average diameter of 50 microns reflects that the particles are not separated with size, but instead are homogeneously mixed. This is again very similar to both the instantaneous and finite duration releases.

Figure 8 shows the dust cloud 87.5 seconds after the initial release. This figure indicates that the distribution is now constant for the first 50 microns then decreases to 100 microns. The largest particle left in the flow field is shown to be 100 microns. The large particles still exist in the flow because they are released with every time step. The relative number of large particles indicates that the larger particles have precipitated out of the flow. The small particles, however, are still suspended in the flow even from

the initial release. The concentration shows the cloud extending far downstream of the initial release. The mass percent is centered near the trailing edge of the cloud because of the relatively large number of large particles still in the flow. The continuous release cloud is now very long because of the particles in the flow field from every time step. The concentration decreases rapidly with downstream distance. Here, we see that the smaller particles are much further downstream than the larger particles. The small particles released initially have now traveled far downstream and the larger particles released at the last time step have not yet precipitated out. The monotonic decrease in the average particle diameter is almost logarithmic with downstream distance.

### Conclusions

The main conclusion drawn here is the availability of a usable tool for the simulation of solid particulate diffusion and transport in atmospheric turbulent flow. Instantaneous, finite duration, and continuously released particles have been simulated for randomly dispersed particles. This indicates great hope for the eventual pollution predictive capability.

### Future Work

A logical improvement for future capability is to integrate the LTM3D program and the FEM3A/B program to solve for gaseous, liquid, and solid particulate dispersion simultaneously. The inclusion of temperature and density variations could also be integrated. The combustion and chemical reaction of solid particles also may need to be accounted for.

### References

1. Fuchs, N. A., *The Mechanics of Aerosols*, 1964, Pergamon Press Ltd., Oxford, Eng.
2. Hidy, G.M., and Brock, J.R., *The Dynamics of Aerocolloidal Systems*, 1970, Pergamon Press Ltd., Eng.
3. van de Hulst, H.C., *Light Scattering by Small Particles*, 1957, Wiley, New York, N.Y.
4. Twomey, S., *Atmospheric Aerosols*, 1977, Elsevier Scientific Publishing Co., New York, N.Y.
5. Cadle, H.D., *Particles in the Atmosphere*, 1966, Reinhold Publishing Co., New York, N.Y.
6. Ahmadi G., Motion of Particles in a Turbulent Fluid - On the effect of rotation on the dispersion coefficient, 1973, Second Int. Conf. on Pneumatic transport of Solids in Pipes, BHRA, Bedford, U.S.
7. Li, A., and Ahmadi, G., Deposition of Small Particles in a Turbulent Channel, 1991, *Aerosol Science and Technology*.



- 8. Ounis, H., Annadi, G., and McLaughlin, J., Brownian Diffusion of Submicron Particles in the Viscous Sublayer, 1991, J. of Colloid and Interface Science.
- 9. Tennekes and Lumley, A First Course in Turbulence, 1989, MIT Press
- 10. Benek, J.A., Steger, J.L., Dougherty, F.C., and Buning, P.G., Chimera: A Grid-Embedding Technique, AEDC - TR - 85 - 64, April 1986.

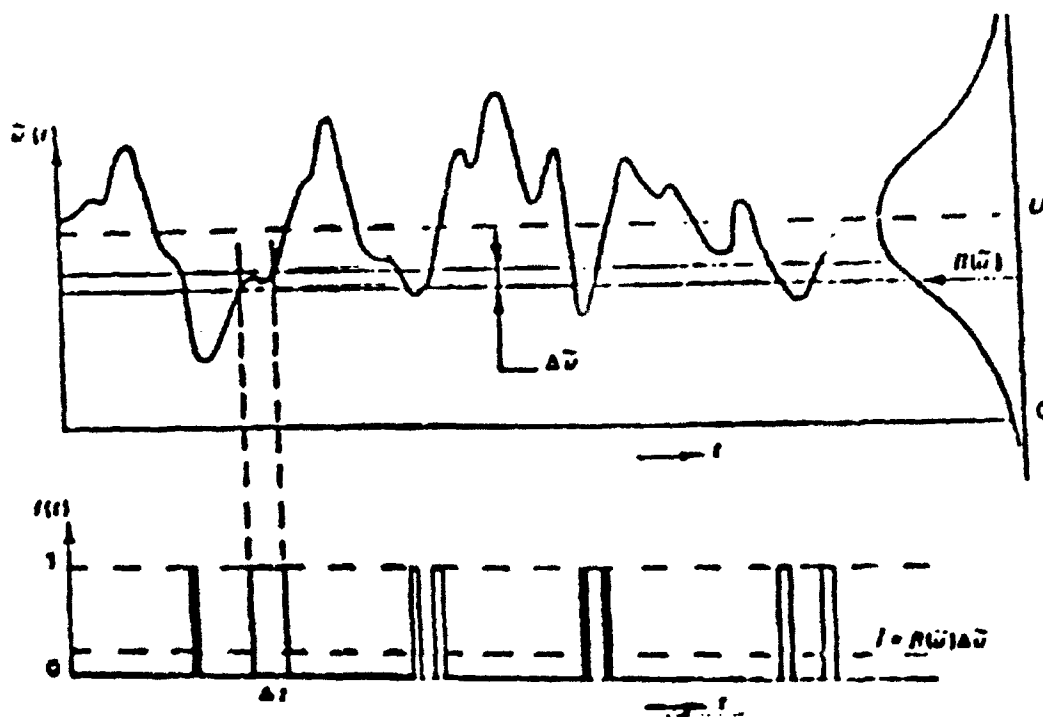


Figure 1: Gaussian Distributed Random Variable

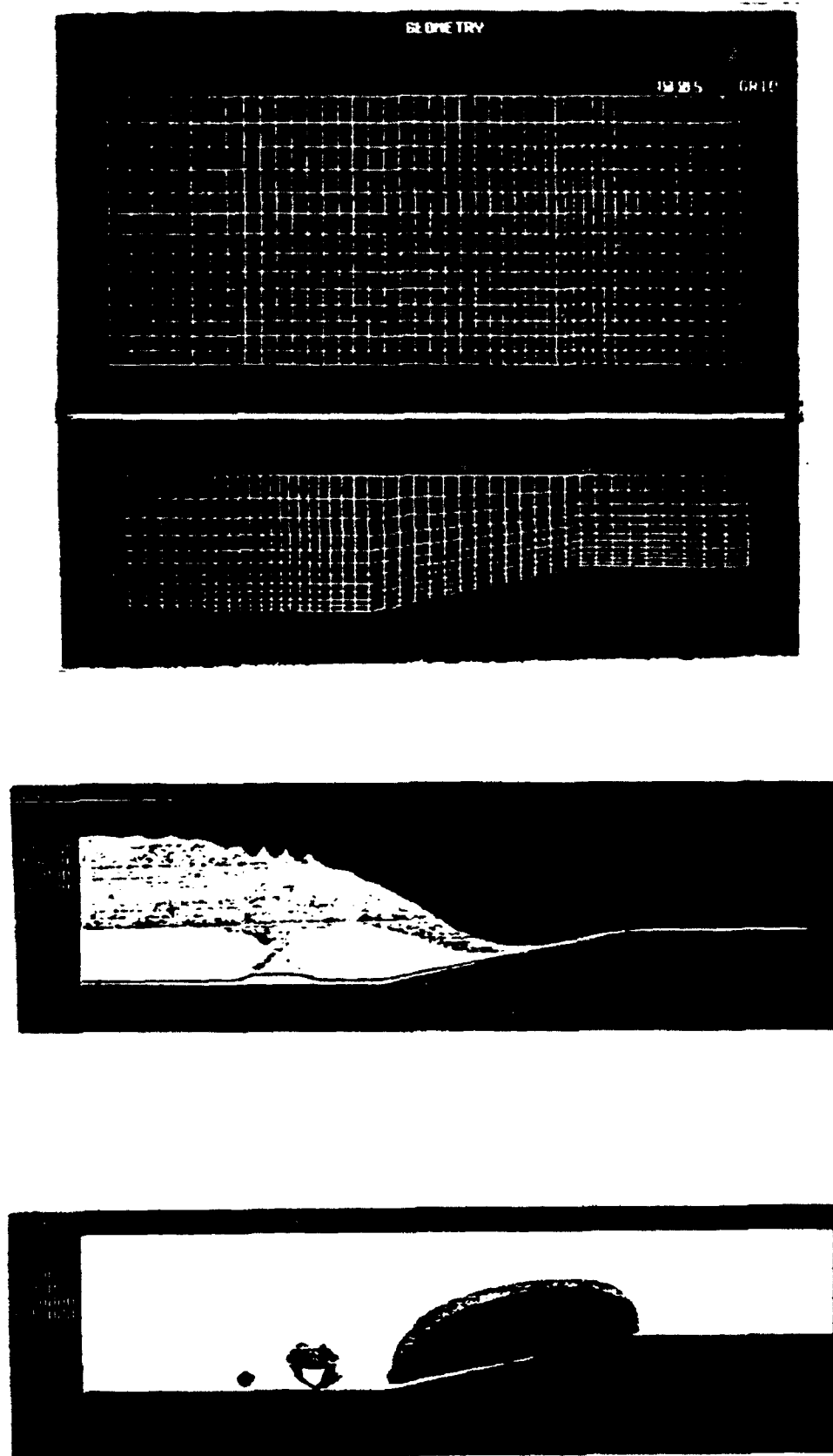
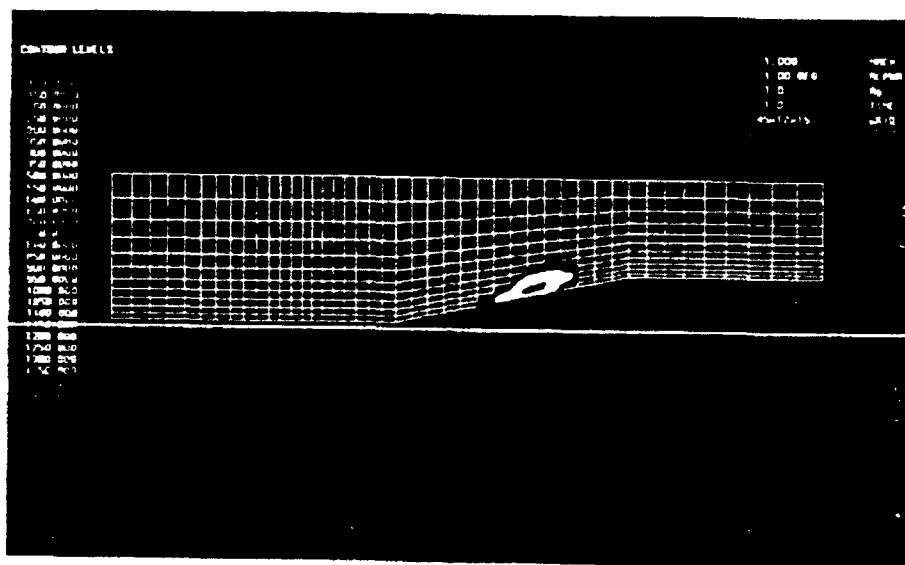
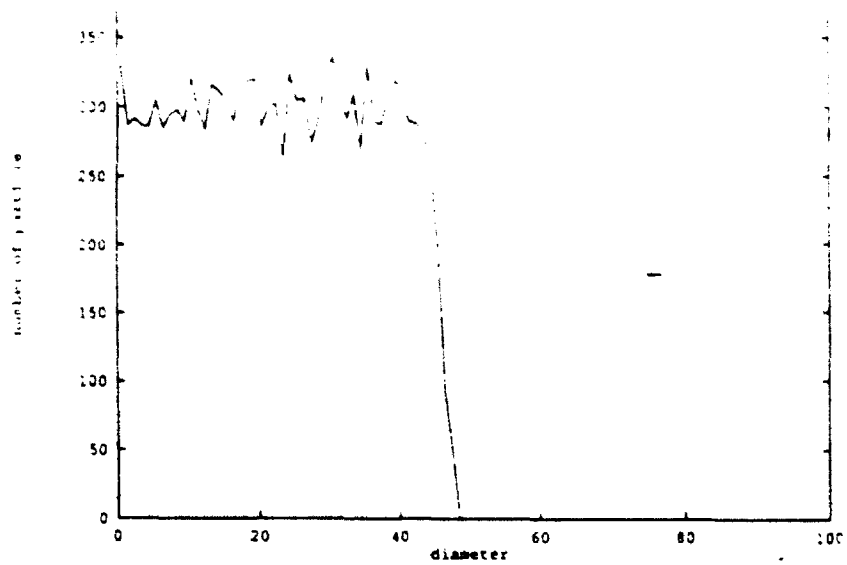


Figure 2: Flow Geometry and Velocities for Test Cases





Concentration

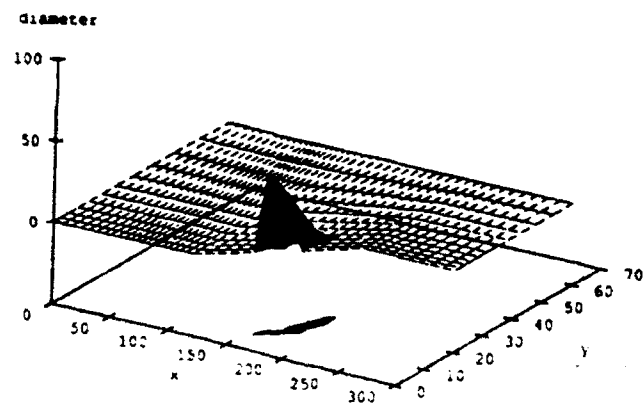
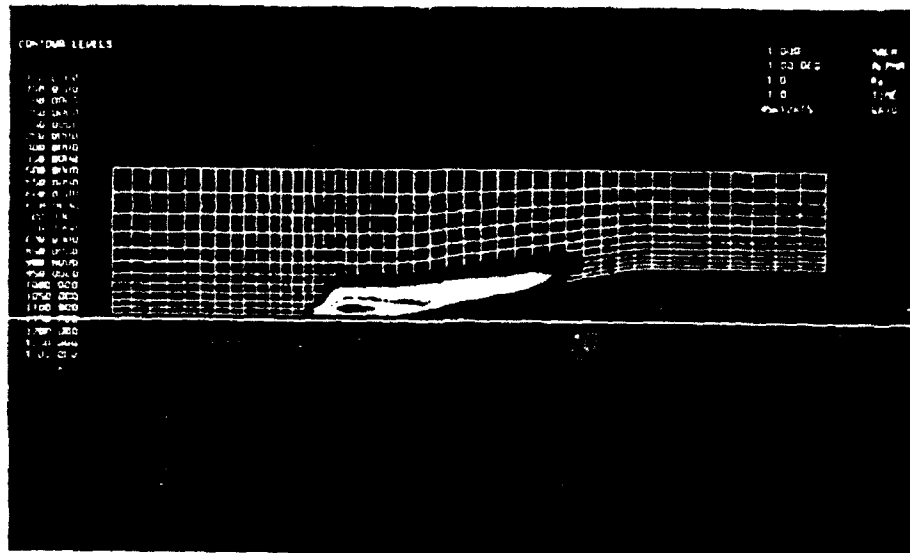
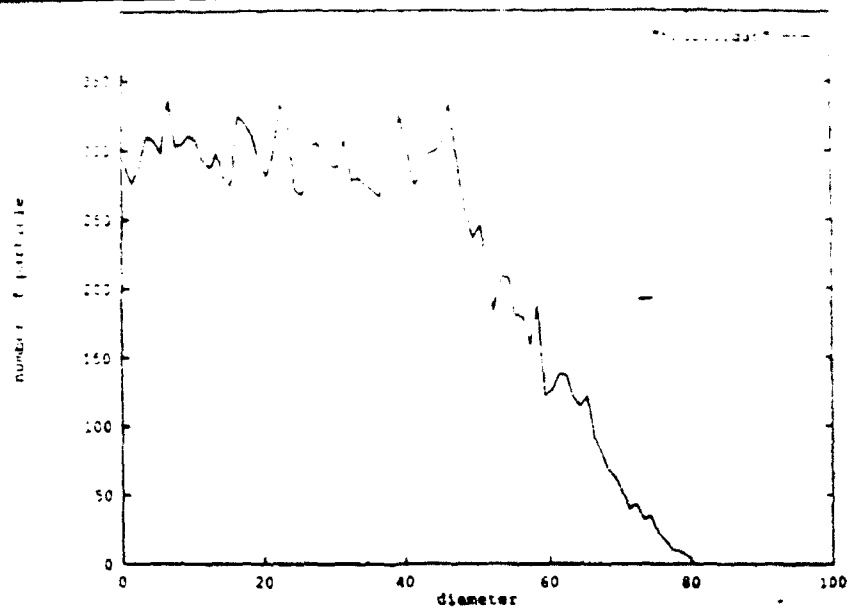


Figure 4: Conditions after 87.5 Seconds for Instantaneous Release





Concentration

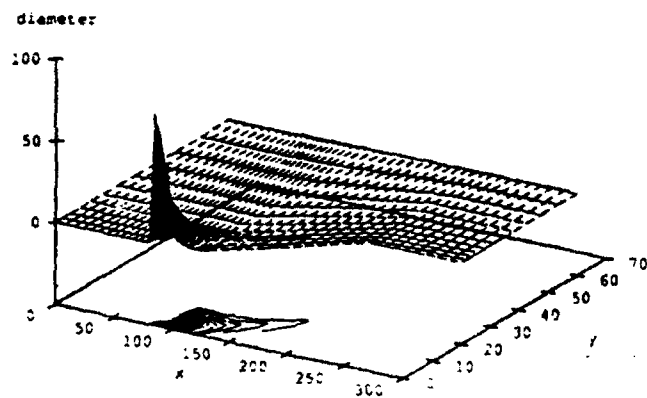
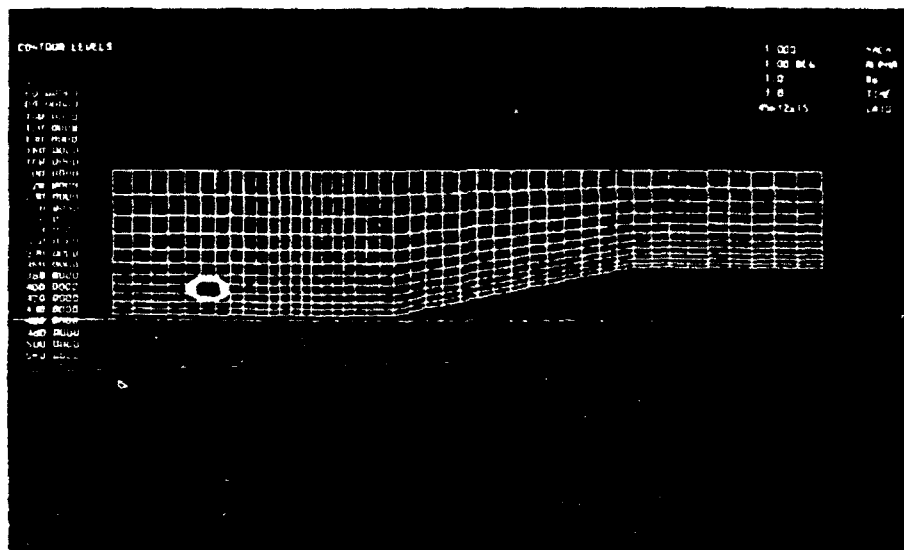
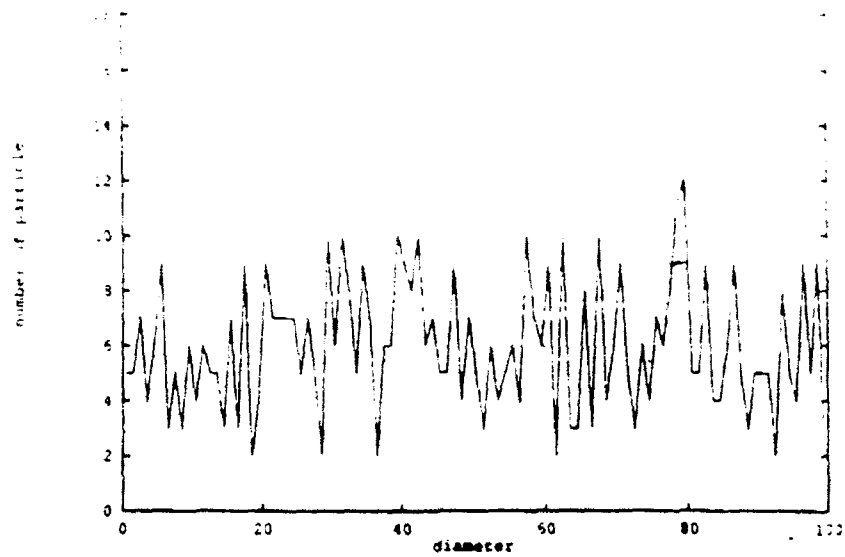


Figure 6: Dust Cloud 87.5 Seconds After Initial Release



Concentration

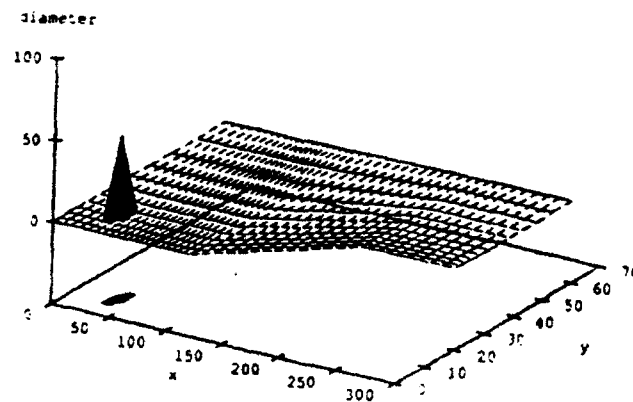
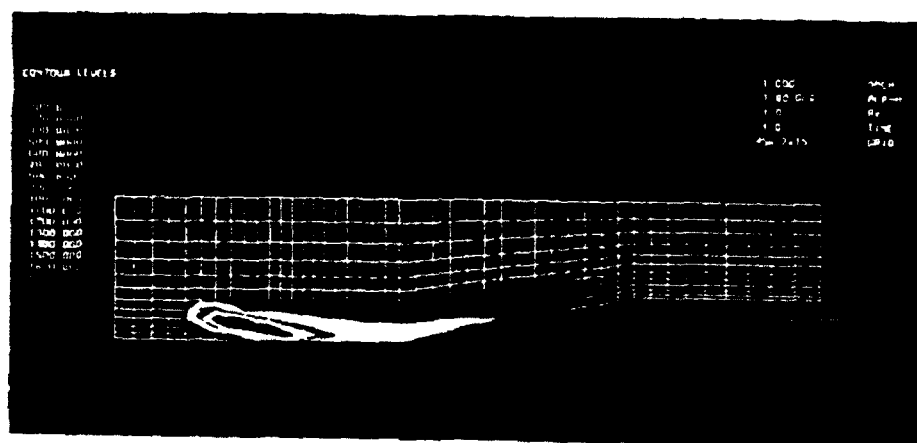
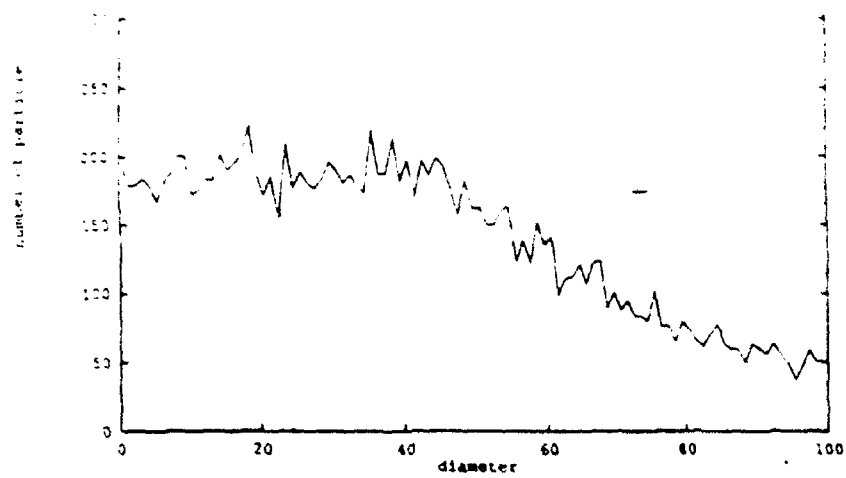


Figure 7: Initial Conditions for Continuous Particle Release





Concentration

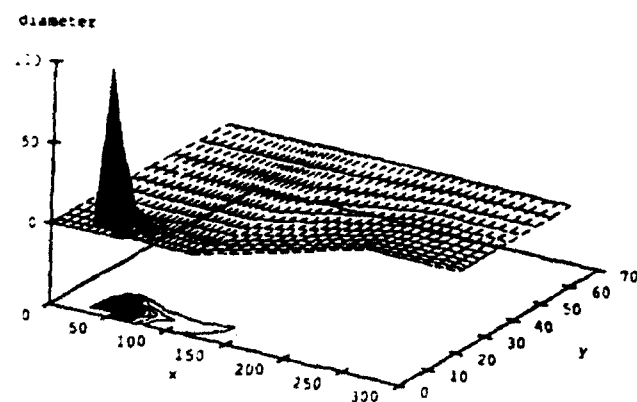


Figure 8: Cloud Orientation 87.5 seconds After Initial Release

**CAD AND ACOUSTIC BEM APPLIED TO THE MODELLING OF THE AEDC ASTF EGMS**

**Richard A. Marschall  
Ph.D. Candidate  
Department of Engineering Science and Mechanics**

**University of Tennessee  
Knoxville, TN 37006-0220**

**Final Report for:  
Summer Research Program  
Arnold Engineering Development Center**

**Sponsored by:  
Air Force Office of Scientific Research  
Bolling Air Force Base, Washington, D.C.**

**August 1992**

## **CAD AND ACOUSTIC BEM APPLIED TO THE MODELLING OF THE AEDC ASTF EGMS**

**Richard A. Marschall  
Ph.D. Candidate  
Department of Engineering Science and Mechanics  
University of Tennessee**

### **Abstract**

CAD input and display packages were interfaced to acoustic boundary element codes. These codes were examined with respect to accuracy of amplitude, phase, and frequency, as well as the rates of convergences as functions of element resolution. Sound pressure level distributions were calculated at two resolution levels for geometries and boundary conditions corresponding to certain AEDC ASTF EGMS diffusers. A full-scale acoustic boundary element model of the AEDC ASTF segment containing the EGMS was constructed.

# **CAD AND ACOUSTIC BEM APPLIED TO THE MODELLING OF THE AEDC ASTF EGMS**

**Richard A. Marshall**

## **INTRODUCTION**

In 1991, under the guidance of R. R. Jones III of the Sverdrup Technology Inc./AEDC Group, M. A. Weaver [1] began to investigate the feasibility of using a three-dimensional acoustic boundary element code to predict the acoustic response of the Arnold Engineering Development Center's (AEDC) Aeropropulsion Systems Test Facility (ASTF) Exhaust Gas Management System (EGMS). A description of the AEDC ASTF EGMS can be found in the report by Weaver [1] as well as a history of the problem which will not be repeated here. Weaver [1] reported that for geometries similar to the EGMS diffuser section, an acoustic boundary element method (BEM) using isoparametric elements seemed to predict resonant frequencies and modal amplitude distributions, at least along the boundaries. This report describes a continuation and extension of the previous study. In particular, this study, also under the direction of R. R. Jones III, attempted with some degree of success to scale up the use of an acoustic boundary element method to realistic full-size problems.

## **OBJECTIVES ACHIEVED**

1. Interfaced a three-dimensional computer-aided drawing package to the construction of the acoustic boundary element code (BEMAP) input data files. Now both the acoustic boundary element and field point inputs can be graphically prepared and displayed.
2. Interfaced a three-dimensional high resolution color CAD data display package to the outputs of the acoustic boundary element code BEMAP.
3. Examined boundary element acoustic codes HELM2D1 (developed at the University of Tennessee) and BEMAP (developed at the University of Kentucky) with respect to accuracies of amplitude, phase, and frequency, as well as the rates of convergence as functions of element resolution.
4. Examined BEMAP behavior at two resolution levels for geometries and boundary conditions with known analytical results. In particular, computed sound pressure level (SPL) distributions over a 150 Hz frequency range, were compared to theoretical and experimental results.
5. Constructed a full-scale acoustic boundary element model of the AEDC ASTF segment containing the EGMS with a cylindrical diffuser section. This model contained 1968 linear acoustic boundary elements and over 1700 field points.

## **OBJECTIVE NOT ACHIEVED**

Difficulties with the BEMAP code and/or its interaction with the computational platform on larger problems prevented the computation of a full-scale model over the frequency bands of interest during the short duration of this contract.

## **FIGURES AND DISCUSSION**

Figures 1-21 follow on page 4, discussion begins on page 19.

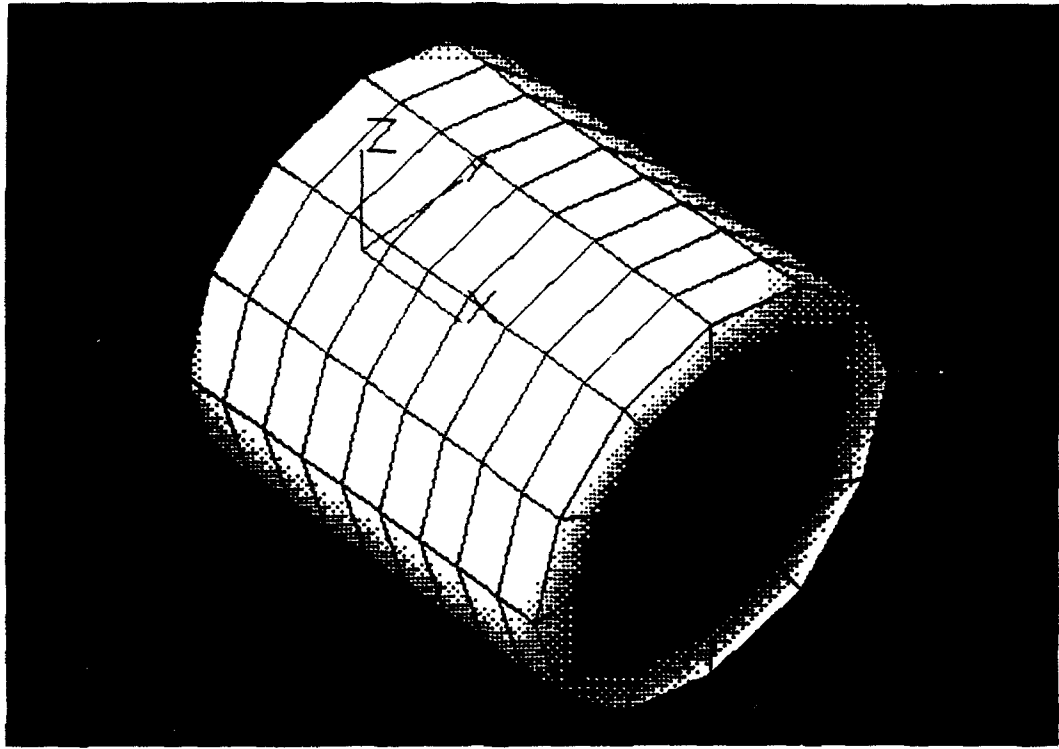


Figure 1: Exterior lighted view of coarse acoustic boundary element discretization of a cylindrical model of the Arnold Engineering Development Center (AEDC) Aeropropulsion Systems Test Facility (ASTF) Exhaust Gas Management System (EGMS). The axis is along the  $x$ -axis. The center of the left endcap is at the origin. Various boundary conditions were applied at the endcaps, the circumference of the cylinder was taken as perfectly rigid. Acoustic sources were modelled both within the interior and on the left endcap for various configurations. The coarse models used 198 linear acoustic boundary elements.

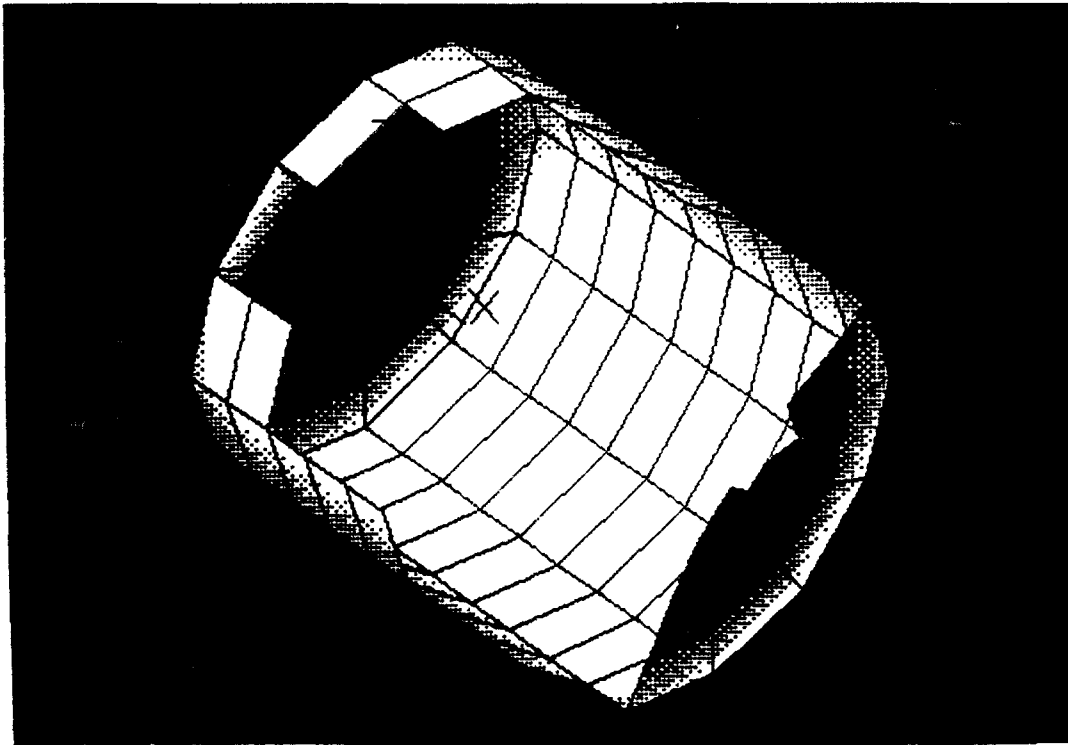


Figure 2: Cutaway interior lighted view of the coarse acoustic boundary element discretization of the cylindrical model of the AEDC ASTF EGMS. For the cases where an offset endpanel source was used, it was modelled by specifying a velocity on the "middle" panel of the first quadrant ( $y-z$  plane) of the left endcap. This view particularly shows how rough an approximation a 12-sided polygon is to a cylindrical surface. Not surprisingly, these models had difficulty reproducing circumferential modes.

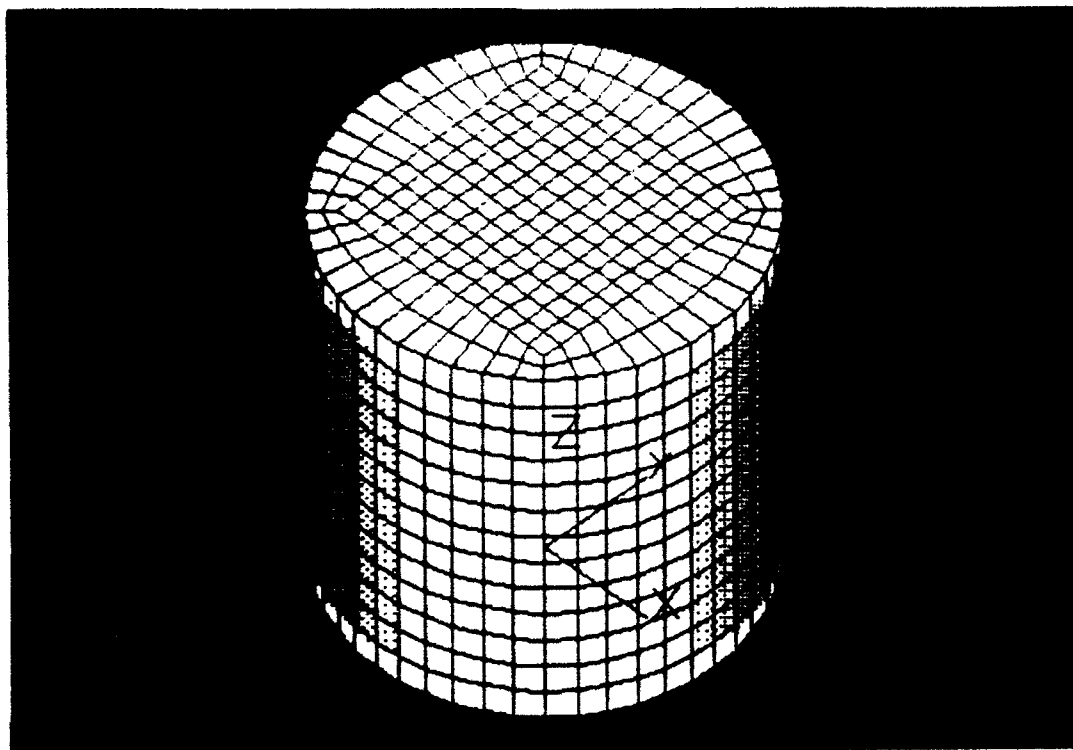


Figure 3: Exterior lighted view of the fine acoustic boundary element discretization of the cylindrical model of the AEDC ASTF EGMS. Note that compared to the coarse model displayed in Figures 1 and 2, the role of the  $x$  and  $z$  axes are reversed. Here, the  $z$ -axis is in the axial direction. This was to facilitate boundary condition editing in the fine model setups. These models consisted of 1104 linear acoustic boundary elements. Using the BEMAP code, each frequency need about 10 hours to compute on a 1.2 MFLOP computer.

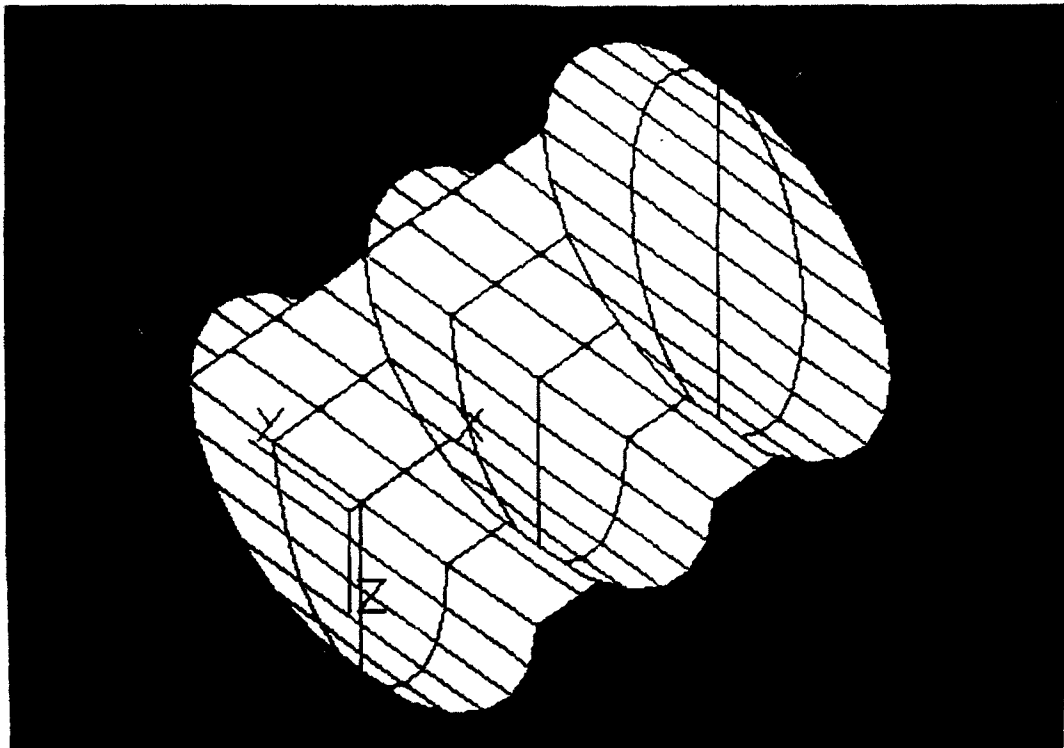


Figure 4: Surface view of the planes of interior field node points used in both the coarse and fine cylindrical acoustic models of the AEDC ASTF EGMS. The axes orientation shown here corresponds to the coarse boundary element models. The fine model field points are the same, except the  $x$  and  $z$  axes are reversed. The interior field point nodes are at the intersections of the grid lines. The number of field points computed was the same for both the coarse and fine models (195 points). The field point "endcap" planes were inset 3.05% of the cylinder length from the boundary element model endcaps. The inset distance in the radial direction was similar.



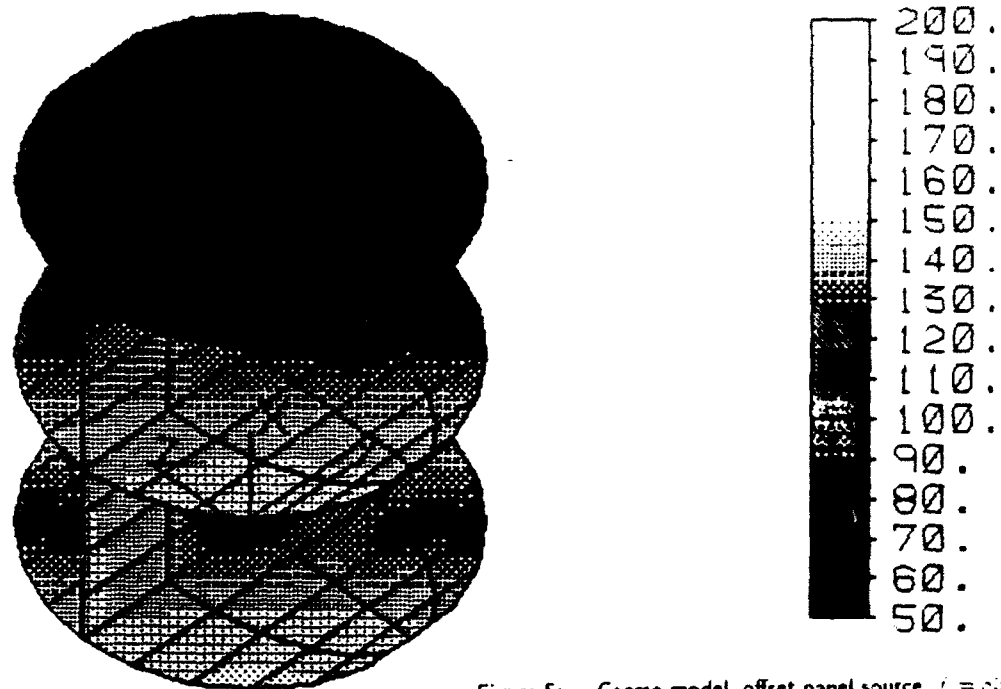


Figure 5: Coarse model, offset panel source.  $f = 63$  Hz.

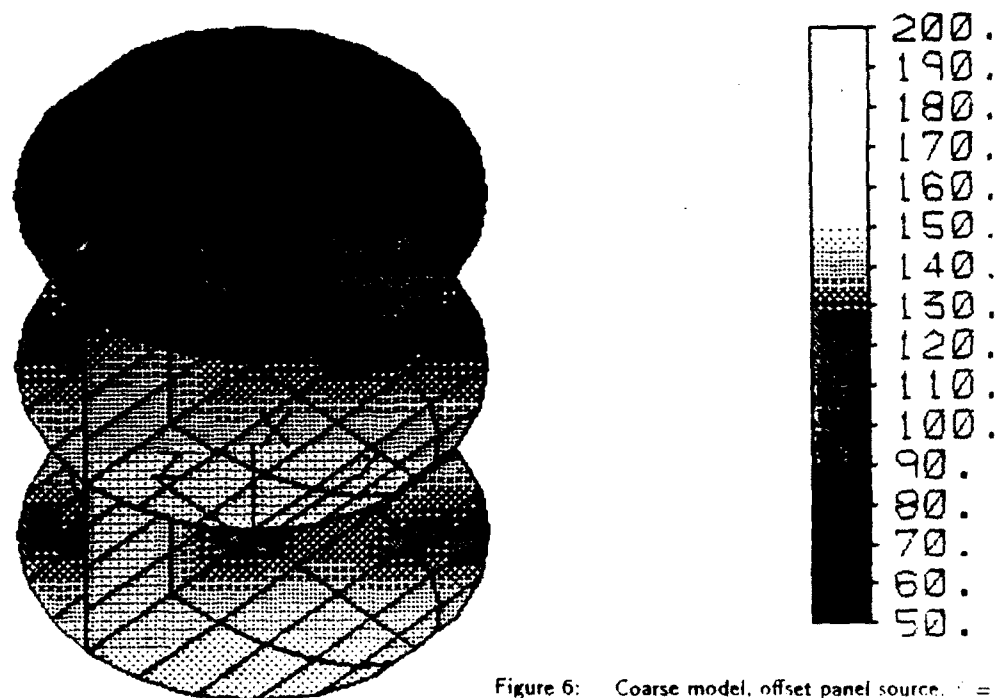


Figure 6: Coarse model, offset panel source.  $f = 127$  Hz.

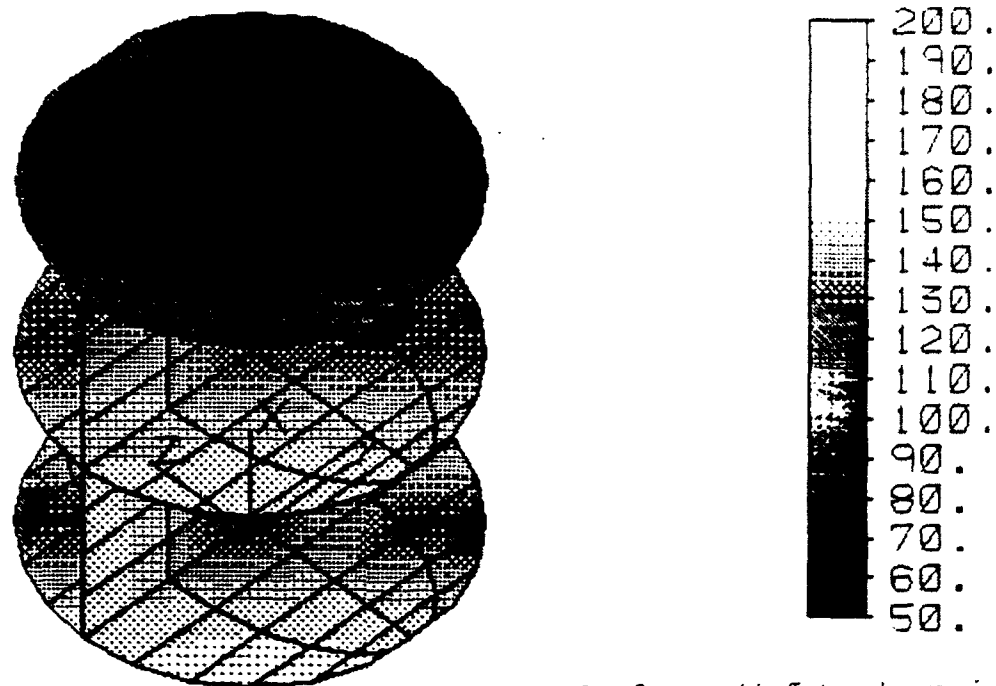


Figure 7: Coarse model, offset panel source,  $f = 85.2$   
 Closest to exact resonant  $f = 85.2$  Hz.

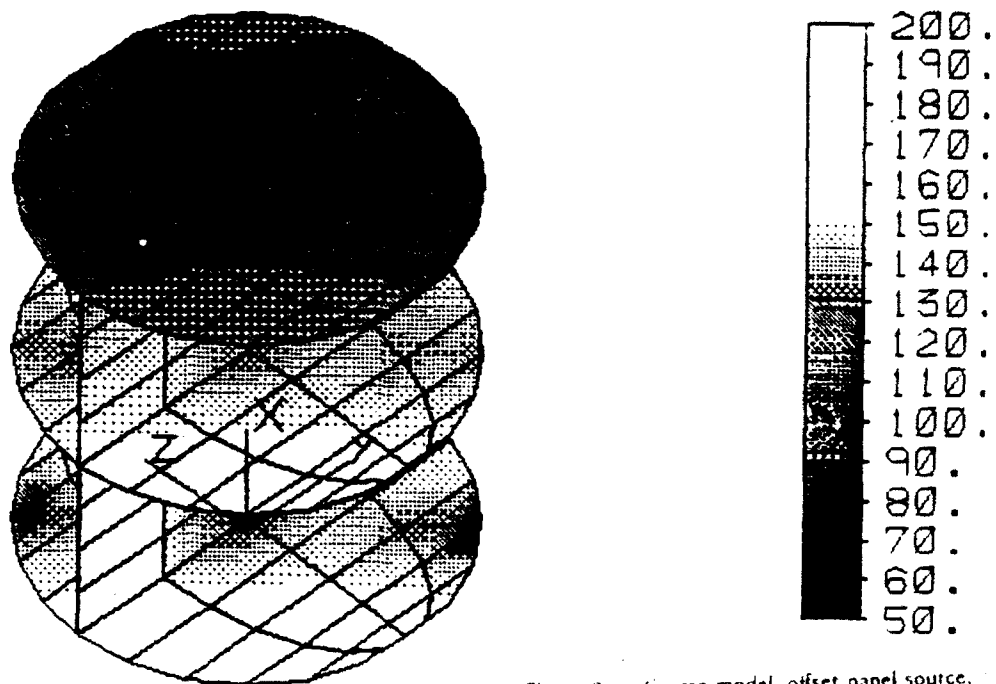


Figure 8: Coarse model, offset panel source,  $f = 100$   
 Shows start of resonance somewhat high.

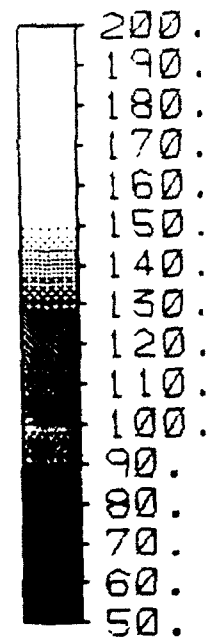
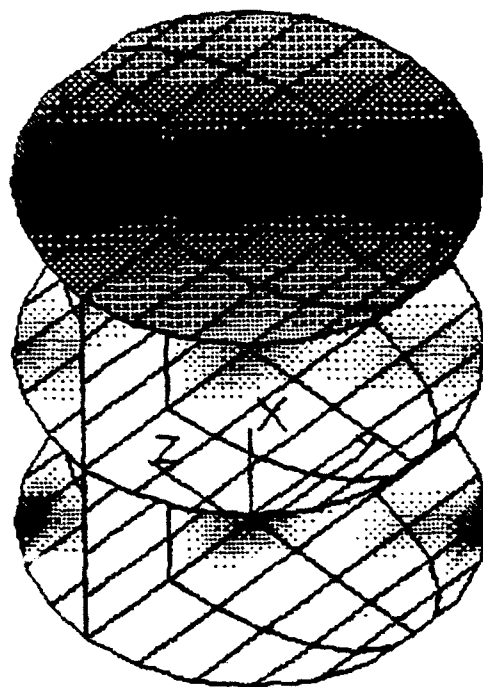


Figure 9: Coarse model, offset panel source,  $f = 57$  Hz  
Peak of computed resonance.

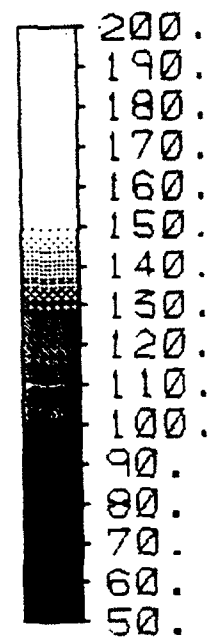
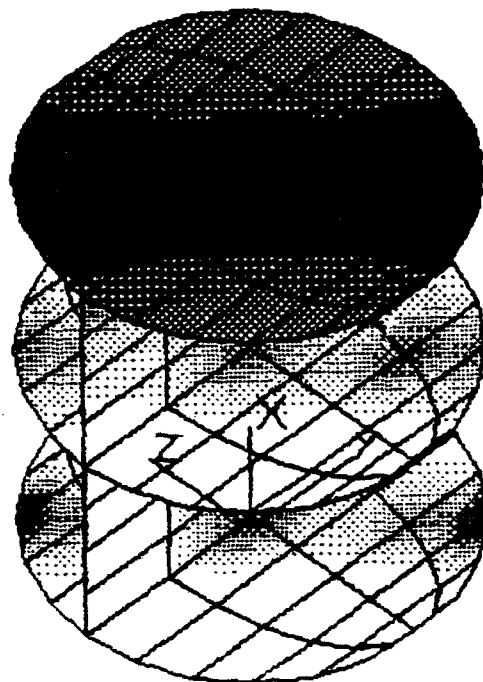


Figure 10: Coarse model, offset panel source,  $f = 58$  Hz  
Slightly off peak, 2.8 Hz away from exact.

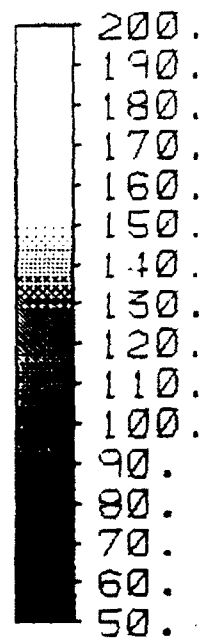
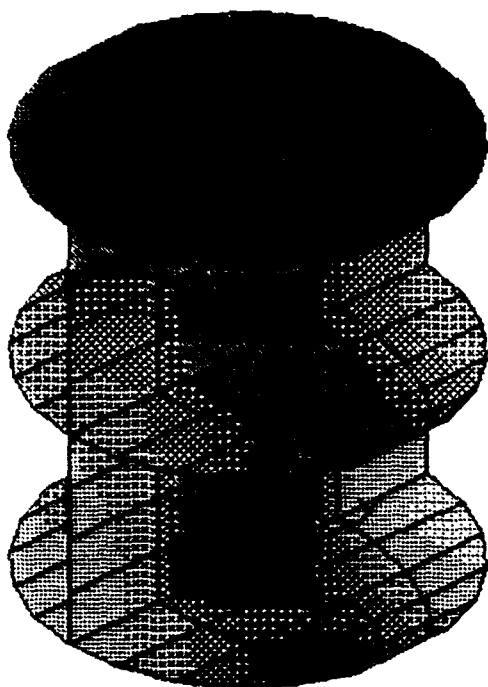


Figure 11: Fine model, offset-panel source,  $f = 83$  Hz.

Little indication of near resonance.

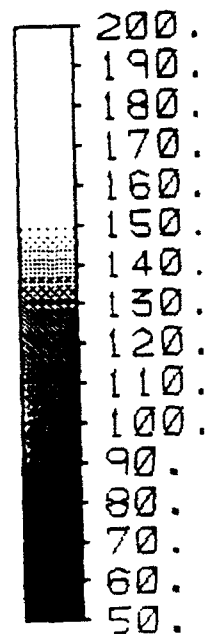
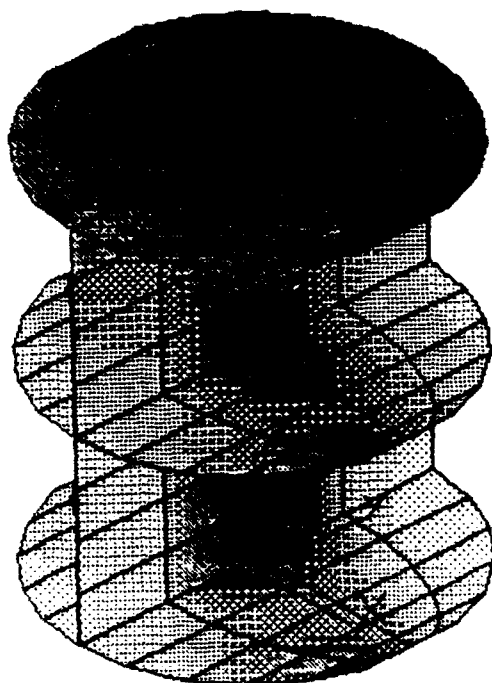


Figure 12: Fine model, offset panel source,  $f = 84$  Hz.

Slight indication of near resonance.

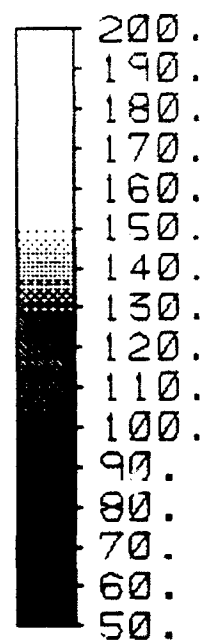
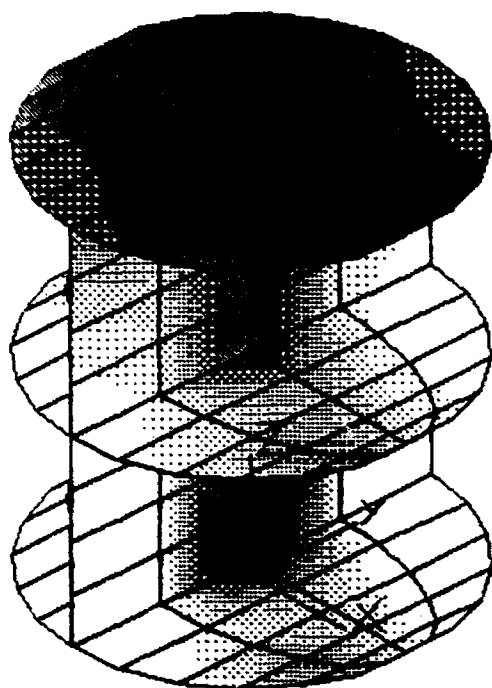


Figure 13: Fine model, offset panel source,  $f = 85$  Hz.

Clearly defined resonance.

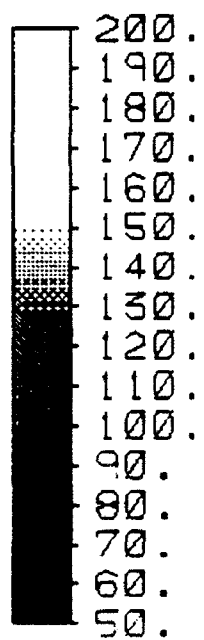
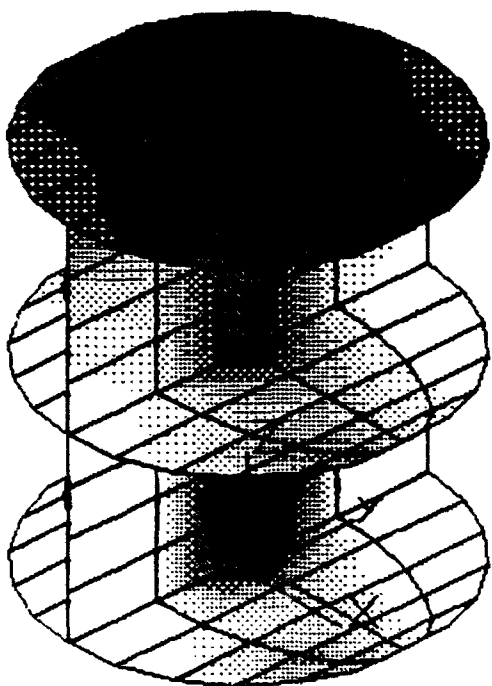


Figure 14: Fine model, offset panel source,  $f = 85$  Hz.

Also on resonant peak.

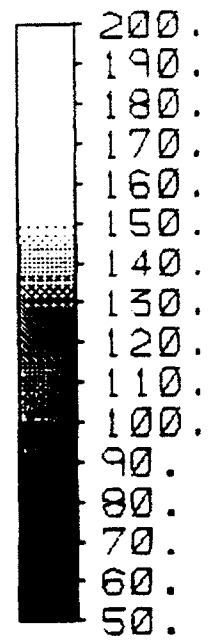
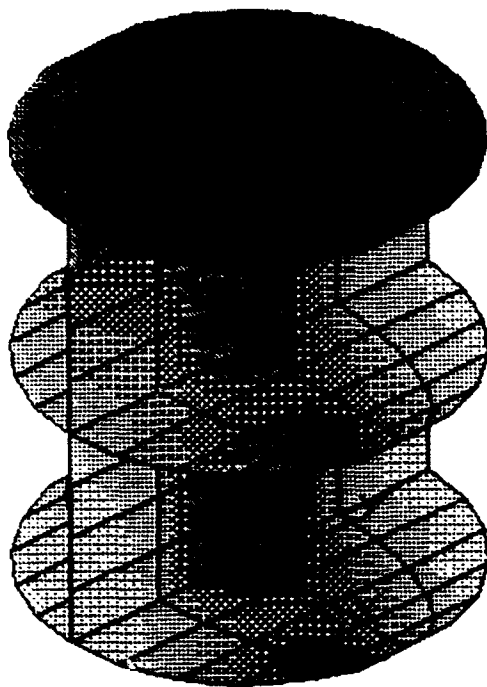


Figure 15: Fine model, offset panel source,  $f = 57$  Hz

Clearly off resonance.

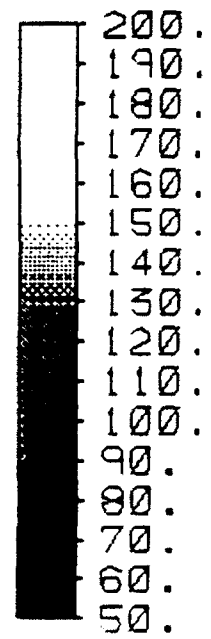
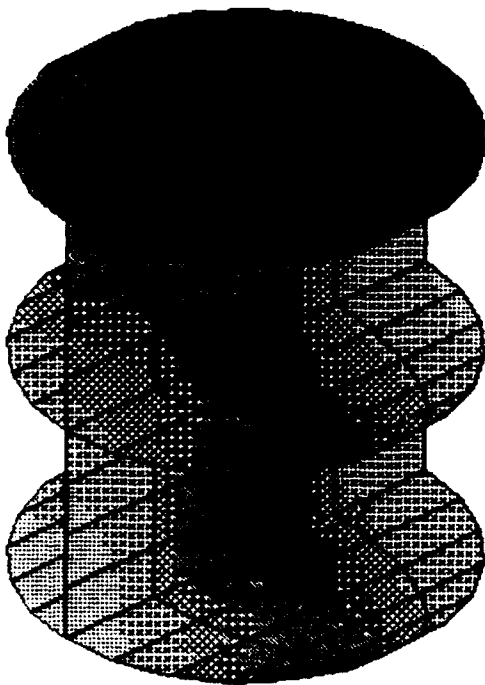


Figure 16: Fine model, offset panel source,  $f = 58$  Hz

Well off resonance.

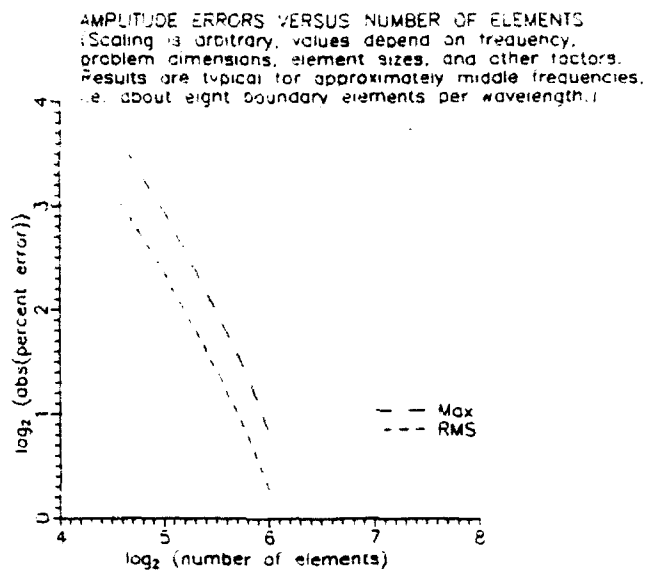
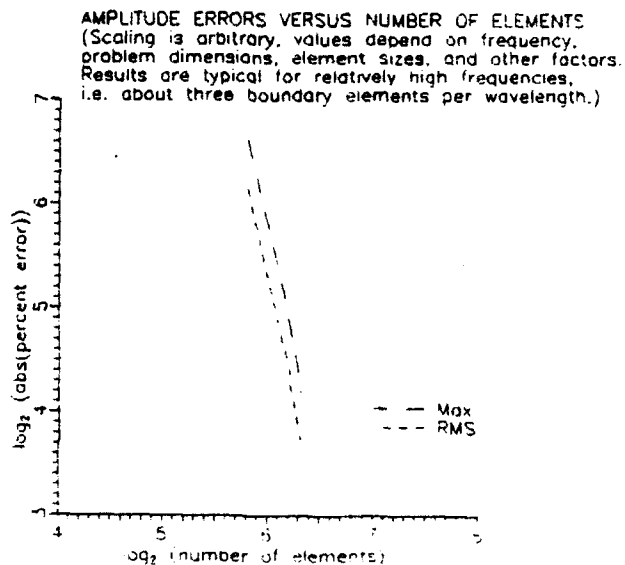


Figure 17a-17b : The order of linear acoustic boundary element methods increases with frequency, although the error itself becomes larger. That is, relative to the dimensions of the problem, at low frequencies increasing the number of elements improves on an already good solution only slightly, at mid-frequencies the improvement becomes quite significant (about 2nd order), and at high frequencies the improvement is dramatic (4th order or higher).



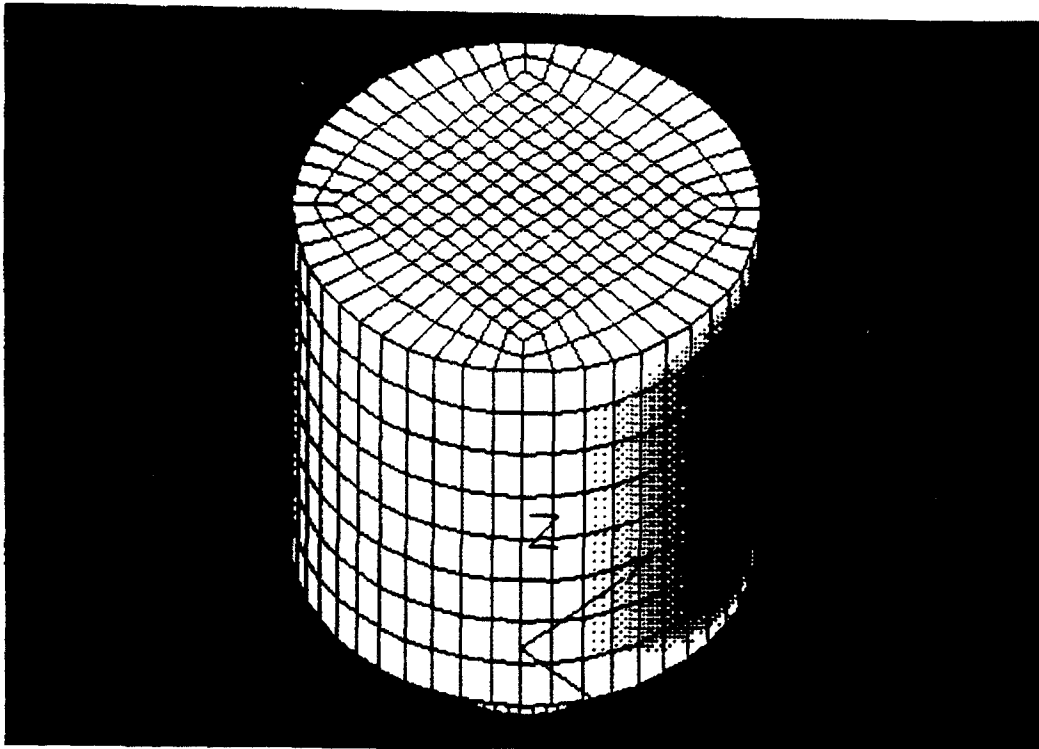


Figure 10: Exterior lighted view of the CHAMBER1 acoustic boundary element model of the AEDC ASTF segment containing the EGMS. This view shows the downstream location at the top of the page, i.e. flow is in the  $+z$ -direction. The exit endcap shown has an acoustic impedance boundary condition corresponding to perfectly absorbing to normally incident waves. The two circumferential rings of elements nearest the exit endcap also have this boundary condition. This model consists of 1968 linear acoustic boundary elements.



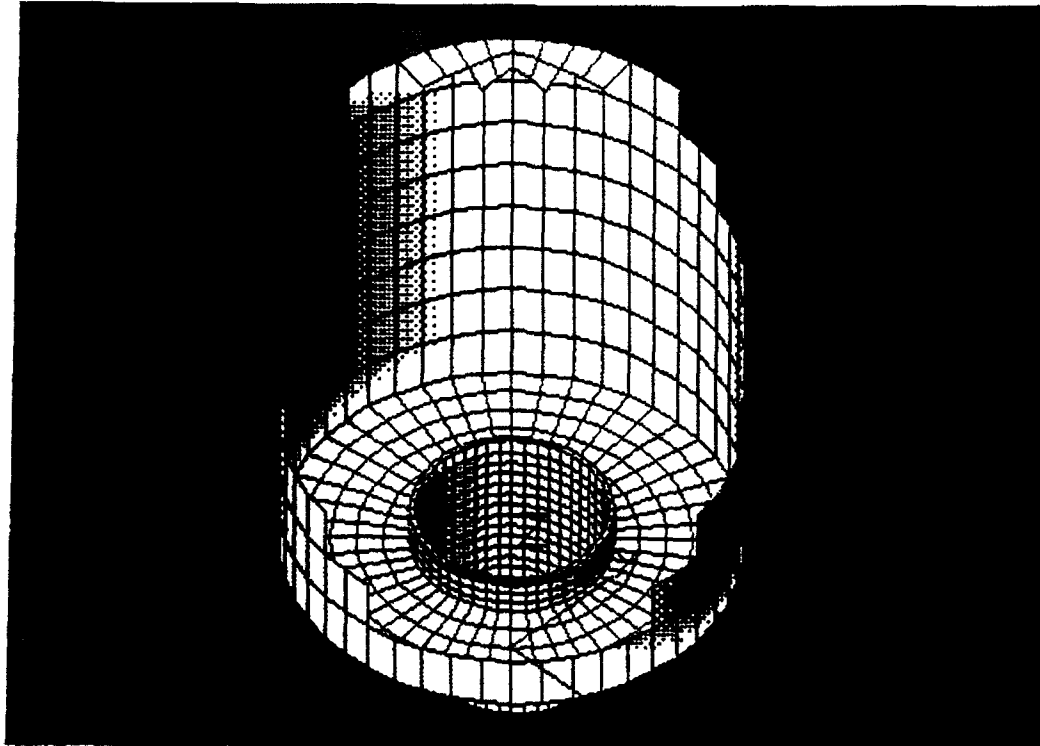


Figure 19: Cutaway lighted view of the CHAMBER1 acoustic boundary element model of the AEDC .5TF segment containing the EGMS. The diffuser region opening into the main tunnel, and the bulkhead region are clearly shown. The interior cylindrical diffuser region has the same dimensions and element resolution as the fine resolution cylinder model.

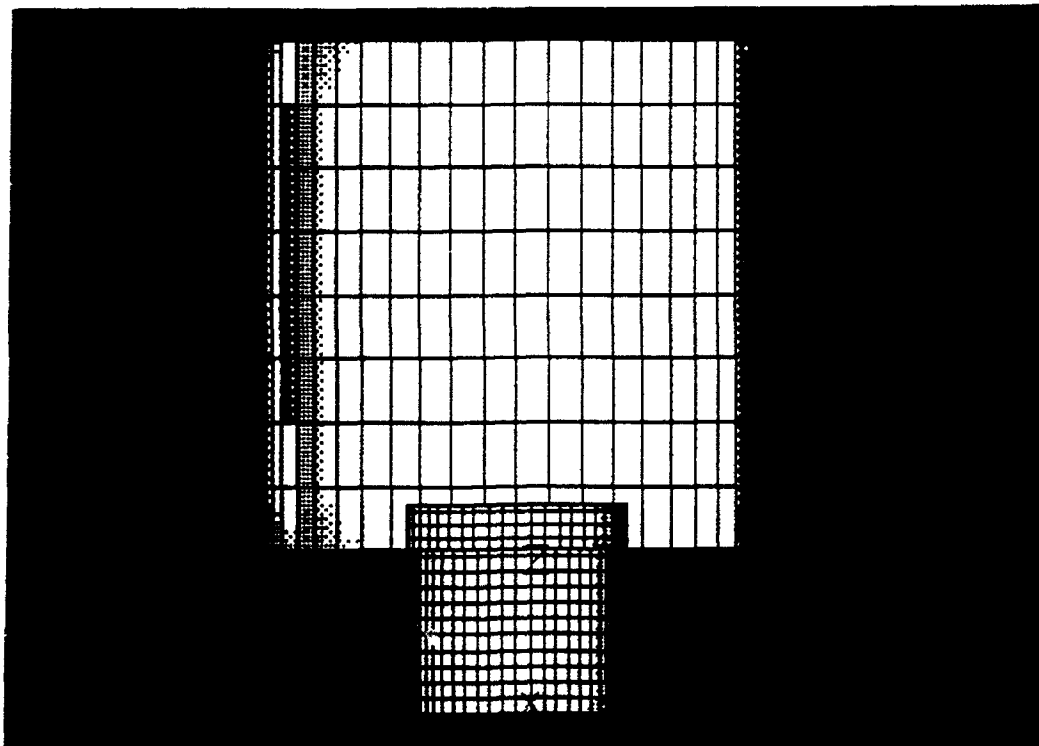


Figure 20: Cutaway lighted  $y$ - $z$  view of the CHAMBER1 acoustic boundary element model of the AEDC ASTF segment containing the EGMS. The cylindrical diffuser has a relatively high boundary element resolution in order to capture interior resonance frequencies and modal amplitude distributions accurately. The coarser downstream tunnel segment discretization is believed to be adequate for modelling the diffuser exit acoustic impedance.

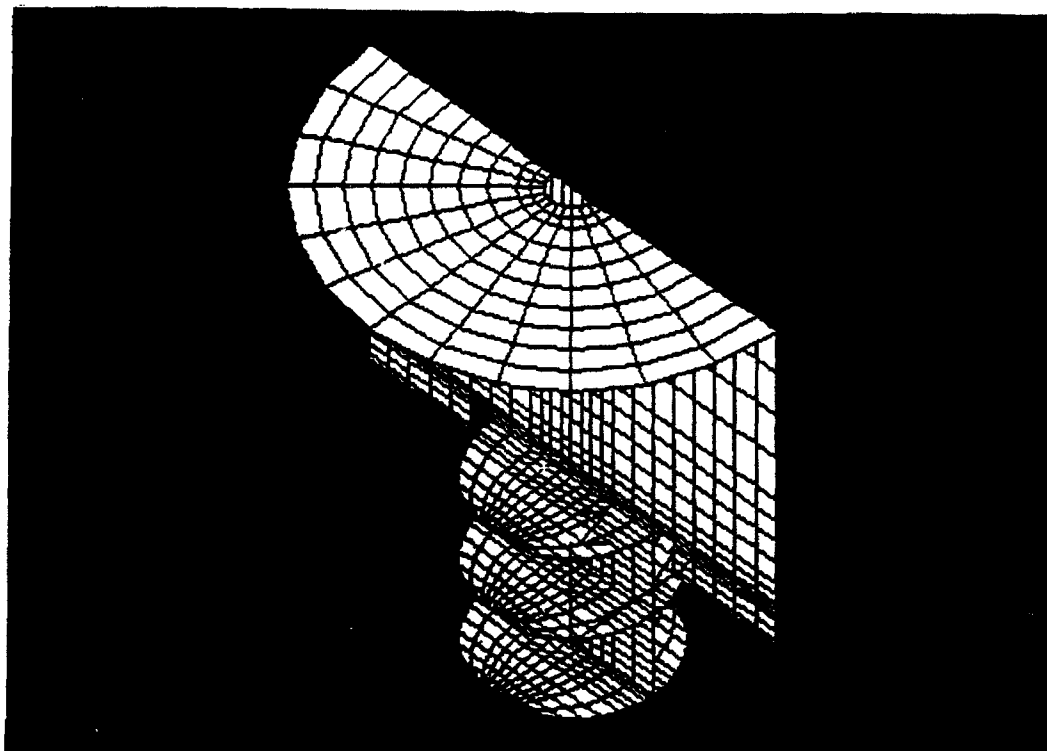


Figure 21: Field point planes for the CHAMBER1 acoustic boundary element model depicted in Figures 18-20. Field points are at the intersections of grid lines. As in the cylindrical models, the field point planes are inset a small distance from the boundary element surfaces. The field point resolution here is higher than the cylindrical models with over 1748 field points.

### *CAD Interface*

Although perhaps more accurate than linear acoustic boundary elements, the isoparametric acoustic boundary elements of the earlier study [1] have the rather severe disadvantage of being almost impossible to interface to CAD drawing and display packages. In order to use acoustic boundary element methods as a practical design tool for modelling realistic geometries, such CAD interfaces are a necessity. Linear acoustic boundary elements are not only much easier to interface, the models are also easier to debug since all nodes are at the vertices of the elements, i.e. all nodes are at the grid line intersections. For these reasons, this study used linear acoustic boundary elements exclusively.

### *Acoustic Boundary Element Low Resolution Models*

An acoustic boundary element model of a cylindrical diffuser section of the AEDC ASTF EGMS with a minimal number of elements was constructed to test BEMAP with linear quadrilateral elements and to compare to the earlier results by Weaver [1]. The low resolution, or coarse model, had about three elements per wavelength in all directions at the highest frequencies of interest. The coarse model geometry is shown in Figures 1 and 2. Note that the coarse model here has about the same number of elements as the "fine" element model of the earlier study [1]. The fine or high resolution model of this study, Figure 3, would have been very difficult to enter into BEMAP without the use of a CAD input interface.

The source location and boundary conditions (hardwall everywhere) were repeated and similar results were obtained, although here the resonant peaks were less well defined. That is, the isoparametric elements used by Weaver [1] produced sharper resonances somewhat closer to the exact analytical frequencies. The present study solved for interior field points, whereas the previous study examined the boundaries only. The field point locations are depicted in Figure 4.

In addition to the comparisons with earlier study results, computer runs were made with:

- Weaver's source location, but zero pressure endcap boundary conditions.
- Source point at the center with zero pressure endcap conditions.
- Offset wall panel source with the remainder of that endcap having a zero velocity or hardwall condition, and the other endcap having a zero pressure boundary condition.

A comparison of this last set of conditions at low and high resolutions is presented in this report.

### *Acoustic Boundary Element High Resolution Models*

The high resolution or fine acoustic boundary element geometry used to model the cylindrical diffuser portion of the AEDC ASTF EGMS is shown as Figure 3. These models with 1104 linear quadrilateral acoustic boundary elements and the field point geometries of Figure 4 were run for a variety of boundary conditions. Principal among these boundary conditions were:

- Source point in the center with zero pressure endcaps.
- Source point in the center with one endcap velocity (hardwall) and the other zero pressure.
- Offset wall panel source with the remainder of that endcap having a zero velocity (hardwall) condition, and the other endcap having a zero pressure boundary condition.

### *Comparison of the Two Resolutions*

As an illustrative example of the character of results obtained at the two resolutions, the sound pressure level (SPL) distributions were computed around a known analytical resonance at 85.2 Hz for the case of the offset wall panel source and boundary conditions of one hardwall endcap, the other zero pressure.

Figures 5-10 show the SPL distribution in dB for the resolution model around the exact 85.2 Hz resonance. The corresponding results for the high resolution model are displayed as Figures 11-16. Briefly comparing the two sets of results show that the high resolution model has its resonance closer to the exact value, and that it is much sharper. The low resolution model displays the resonance, but at a higher in frequency than predicted analytically. These results are typical when the low resolution model does in fact capture the resonance. Often, however, the low resolution model misses resonances entirely. This effect was noted by Weaver [1] for isoparametric elements and is true for linear quadrilateral elements. It appears that six or more linear acoustic boundary elements per wavelength in all directions are needed to reliably capture resonances.

### *Further Effects of Element Resolution*

Examination of the literature revealed almost no published results on the element resolutions required to solve various actual acoustic problems. Reference [3] recommended at least four elements per wavelength, and advised increasing the number of elements until the "error" was sufficiently small. An extensive investigation of the effects of element resolution on the amplitude and phase errors in boundary element methods was undertaken using the code HELM2D1 for the two-dimensional Helmholtz equation. Trends observed in two-dimensions were then examined in three-dimensions using BEMAP to see if they held true in general. Except for an absolute scale factor which was dependent on the various other aspects of the code implementations and problem particulars, a number of traits seemed to generalize. Among the most interesting were those shown in Figures 17a and 17b, that is, the order of linear acoustic boundary element methods increases with frequency, although the error itself becomes larger. In other words, relative to the dimensions of the problem, at low frequencies increasing the number of elements improves on an already good solution only slightly, at mid-frequencies the improvement becomes quite significant (about 2nd order), and at high frequencies the improvement is dramatic (4th order or higher).

### *Conclusions*

Acoustic boundary element methods continue to hold promise to be able to model the interior sound distribution and resonances of the AEDC ASTF EGMS. A code written specifically for this purpose could take advantage of particular characteristics of the geometry, frequency ranges, and accuracy requirements in order to arrive at results within realistic wall-clock times.

### *REFERENCES*

1. MICHAEL WEAVER 1991 *U.S. Air Force Summer Research Program, Graduate Student Research Program Reports* 8, 31-1-31-27. Boundary Element Acoustic Analysis of the Exhaust Gas Management System in the AEDC Aeropropulsion Systems Test Facility.
2. BENJAMIN SOENARKO 1983 *An Advanced Boundary Element Formulation for Acoustic Radiation and Scattering in Three Dimensions*. Lexington: University of Kentucky dissertation.
3. A.F. SEYBERT, T.W. WU and G.C. WAN 1990 *User's Manual Computer Program BEMAP Version 2.43* Lexington: Spectronics, Inc.

A MULTIGRAPH IMPLEMENTATION OF A  
DISTRIBUTED IMAGE PROCESSING SYSTEM

Michael S. Moore  
PhD. Candidate  
Department of Electrical Engineering

Vanderbilt University  
400 24th Ave. S.  
Nashville, TN 37235-1824

Final Report for:  
Summer Research Program  
Arnold Engineering Development Center

Sponsored by:  
Air Force Office of Scientific Research  
Bolling Air Force Base, Washington, D.C.

September 1992

# A MULTIGRAPH IMPLEMENTATION OF A DISTRIBUTED IMAGE PROCESSING SYSTEM

Michael S. Moore  
PhD. Candidate  
Department of Electrical Engineering  
Vanderbilt University

## Abstract

At Arnold Engineering Development Center, videos of rocket plumes are used in analysis. The videos are inherently noisy, so they must be digitally processed before they are useful. Processing the video frames on normal digital computers can require days or even weeks. Thus, there is a need for a high speed image processing system. It has been seen that the speed of image processing operations can be greatly increased by distributing the computational load over several workstations, PCs, or transputers using Multigraph. Multigraph, a system integration tool developed at Vanderbilt University, allows the building of complex algorithms from simpler processing blocks. Multigraph is capable of distributing processes over a network to a variety of computer architectures, and the network does not have to be homogeneous.

This report presents the results of the 1992 Graduate Summer Research Program: a Multigraph implementation of a distributed image processing system. The system utilizes a non-homogeneous network of workstations to gain a considerable increase in the execution speed of image enhancement, noise reduction, and analysis algorithms. The flexibility and speed of the system have been demonstrated. The overall results of the summer research are very promising.

## INTRODUCTION:

The engineers at Arnold Engineering Development Center (AEDC) routinely use rocket test videos to analyze rocket plumes. The videos are noisy, so digital image processing techniques are used to reduce noise and enhance the digitized video sequences. Due to the huge amount of data involved<sup>1</sup> and the complexity of the algorithms, it can take days or even weeks to process the video from one test firing. Thus, there is a need for a low cost, flexible, high speed image processing system with which the engineers can reduce greatly the computer time and man-hours needed to process the video data.

Another need is for a system with which engineers can rapidly develop new image processing algorithms. It is desirable that the user be able to build an algorithm from a library of small pre-coded operation blocks without knowing the internal details. The system should be based on models that allow the algorithms to be easily modified without recompiling of the source code.

This work represents a continuation of a research effort initiated by this author as a participant of the 1991 AFOSR-RDL summer research program [4]. The new distributed image processing system has been greatly improved and new functions have been added. The system is designed to speed up image processing routines by distributing the computational load across a network of Unix workstations. The machines used include Sun SPARC2, IBM RS6000, and 4d340 Silicon Graphics Iris stations. Since all of these machines are commonly used at AEDC, the distributed image processing system requires no new hardware. The Multigraph execution environment is used for data flow, process control, and communication. The HDL (hierarchically descriptive language) interface is used to define *graphs* of each of the processing algorithms and to communicate with the Multigraph kernel.

In the following text, an explanation of the objectives of the summer research is given. Then a brief description of the tools used in implementing the distributed image processing system is discussed. The image processing capabilities of the system are discussed next, with a brief description of each of the utility functions and processing algorithms that have been implemented to date. Then the performance of the system is analyzed and recommendations for future research are made.

---

<sup>1</sup>For example consider a standard 60 second video: 60 frames/sec interlaced (net 30 frames/sec), 512 by 480 pixels, one byte/pixel. That is more than 442 Mbytes of data to be processed per minute of video!



## OBJECTIVES OF THE RESEARCH EFFORT:

The basic research objectives were:

- Create image processing utilities to perform tasks such as reading, writing, and passing images. Create a basic image viewer for on line use.
- Establish protocol for system topology and image structure to be used in future additions to the library of image processing functions.
- Begin a library of general image processing routines. Create an interface between the new protocol and previously written Multigraph routines. [6]
- Improve upon image splitting and reconstruction techniques so as to reduce the effects of a non-homogeneous network.
- Demonstrate the speed and flexibility of the system with several examples of distributed implementations of image processing algorithms.

As will be described in the text, these objectives were met with the summer's work.

## THE MULTIGRAPH ENVIRONMENT:

Multigraph is a system integration tool developed at Vanderbilt University. It allows the construction of complex algorithms from smaller modules of code. Multigraph will automatically schedule, execute, and control the data flow of an algorithm. Since Multigraph supports distributed processes, any part of an algorithm can be executed remotely. The remote processes can be executed on workstations, PCs, or transputers, and the network need not be homogeneous.

The heart of Multigraph is the Multigraph kernel (MGK). It does the scheduling, process control, and the communication. It uses a model of the system called a *graph*. A graph represents all aspects of the algorithm to be implemented. Important components of the graph are given below.

1. *Actors* are the computational operators of the graph. To each actor is attached a state, which can be inactive, active, ready, or running. The state is used by the scheduler to decide when the actor's function will be performed [1].

An actor is made up of several components:

- (a) The *script* is the actual code that will be executed when the actor runs. The actor script can be in almost any language, and can be used by any number of unique actors in the same graph. Within the script, Multigraph kernel calls are used to receive the input data, propagate the output data, and manage memory.
  - (b) The *context* of the actor is an area of static memory allocated by the kernel that is not reset or cleared each time the actor is run. Thus, the actor can save its state between runs. Also, the context may be set when the graph is built to pass initial parameters to the script. This type of context allows the execution to be controlled by the specification of the graph with no need to recompile the script.
  - (c) The *input ports* are where data is passed to the actor by the kernel and the *output ports* are where data leaves the actor. The number of input and output ports of an actor is specified when the actor is created and cannot be changed without rebuilding.
  - (d) The *control principle* is the method by which the kernel decides when to schedule an actor for execution. An actor can be an *ifall* or an *ifany* actor. An *ifall* actor will be scheduled for execution when all of its input ports contain data. An *ifany* actor will be scheduled whenever one of more of its input ports have data available.
2. *Datanodes* are places in memory where data is queued between actornodes. They connect actor output ports to actor input ports. Since they are queued, they allow the kernel to provide dynamic scheduling for the graph. A datanode can be connected to any number of actor input ports, and any number of actor output ports can be connected to it. (Note that data cannot flow directly from an actor's output port to another's input port. It must flow through a datanode. This is because the input and output ports do not queue data.) Each datanode is assigned a type – either *scalar* or *stream*. When an actor receives data from an input port attached to a scalar

datanode, only the last piece of data propagated to the datanode will be received. However, data on a stream datanode will be received in FIFO order.

3. The *Environment* to which an actor is attached is a protected set of system resources that it uses. An environment has associated with it a priority, which the kernel uses in scheduling. Only one actor per environment can be executed at any time. Thus, for all actors associated with a particular environment, mutual exclusion is ensured on that environment's resources .
4. A *task* is an interface to the physical resources of the machine. In a multitasking environment tasks are the different processing threads available to the Multigraph kernel. In a multiprocessor system they are the individual processors themselves [1]. The system discussed in this work is a multiprocessor system, so the tasks represent the workstations that will actually do the computation. Each environment is attached to a task, and any task can have multiple environments. Also, multiple tasks can be associated with a machine.

The Multigraph kernel provides the interface to build, modify, monitor, and control the graph. <sup>2</sup> When constructing large graphs, though, the direct MGK interface calls can become cumbersome. To allow more elegant communication with the kernel, higher level tools exist. One such tool is the HDL (hierarchal descriptive language) interface. The HDL interface is described in the following section.

### THE HDL INTERFACE:

HDL (hierarchal descriptive language) is used to model the signal flow graph of the system. The language represents the processing system in terms of its structure. The HDL language is naturally analogous to a block diagram representation of the graph, and as such provides an easy method of describing the processing blocks and interconnections of complex systems. As its name infers, HDL is inherently hierarchal. Thus, any block of a graph can represent an arbitrary hierarchy of sub-blocks. This allows for high level abstraction and simpler data flow graphs. The simplest and lowest level blocks are called primitives. They

---

<sup>2</sup>For a complete description of the MGK interface, see [2].

are the blocks to which actual code is associated. Blocks made up of one or more sub-blocks are called compounds. The sub-blocks of a compound can be either primitives, compounds, or any mixture of each.

### The Semantics of HDL

The HDL language uses scripts with a specific syntax to interpret the structure of the system. Either a primitive or a compound is declared in each script. Examples of a primitive and a compound script are given in figures 1 and 2 respectively. Note that HDL ignores anything after a ";" on a line, so lines starting with ";" are comments. Referring to figure 1, note that the primitive is named *mclean primitive*. It is an IFALL actor with two inputs and one output. Its context consists of a static parameter called *mclean\_number*, which is an integer that defaults to 0 at build time if it is not otherwise set. The context could also have dynamic parameters, but does not. None of the actors in this image processing system use dynamic parameters. See [3] for a complete description of dynamic parameters. This actor is attached to the environment named "e", which is attached to the task named "t". The script that will be executed when "mclean primitive" is run is named "mclean". The script "mclean" must have been linked to the Multigraph kernel at compile time.

The compound definition shown in figure 2 contains the primitives *OpenRas primitive*, *SetParams primitive*, *mclean primitive*, and *WriteRas primitive*. It has no inputs, outputs, static parameters, or dynamic parameters. The datanodes of a graph are specified by the SIGNALS declaration in the script. The data nodes of the mclean compound are *mclean\_parameters*, *topology*, *raw\_image*, and *new\_image*. The meanings of the PARAMS, SHARED, VARS, and COMPUTE declarations can be found in the HDL manual [3], but are not important here. The STRUCT declaration is where the topology of the actor is defined. Each sub-actor has input and output ports which are attached to data nodes. Each sub-actor is also attached to an environment and a task. Note that in figure 2 no static parameter is passed to the mclean primitive (ie. NIL is in the static parameter position). In this situation, the graph builder will assign the default value, which is 0, to the mclean primitive's local static parameter *mclean\_number*.

To build the mclean graph, the HDL scripts for the mclean compound and all of the

```

;;; Definition for |mclean primitive|.
(DEFPRIMITIVE |mclean primitive| :IFALL
  ; input and output definitions
  (
    (|mclean_parameters| :STREAM) (|RasIn| :STREAM) -> (|RasOut| :STREAM)
  )
  ; static parameters
  ( ( |mclean_number| 0 :INT ) )
  ; dynamic parameters
  NIL
  ;environment/task mapping
  (|e|) (|t|)
  ; two unused graphics slots
  NIL NIL
  ;script name
  "mclean"
)

```

Figure 1: Example of an HDL Primitive

related primitives must be loaded using the HDL interface. For specific procedures for loading scripts, building graphs, and executing algorithms, see [3].

### TOPOLOGICAL CONSIDERATIONS:

For any distributed system special considerations must be addressed. A computational topology must be chosen for the algorithm. In other words, one must decide how the processing is to be broken up between the available resources. The best choice is highly dependent upon both the algorithm and the resources available.

One way to distribute the work load is to break the algorithm into steps, or computational blocks. Each computational block can be assigned to a processor, thus presumably

```

;;; hdl compound 'mclean'
(DEFCompound |mclean| ( -> ) NIL NIL

  ;no inputs, outputs, static or dynamic parameters
  ;environment/task mapping
  (|e|) (|t|)

  ; two unused graphics slots
  NIL NIL

  (SIGNALS    (|mclean_parameters| :STREAM) (|topology| :STREAM)
              (|raw_image| :STREAM) (|new_image| :STREAM) )

  (PARAMS) (SHARED) (VARS) (COMPUTE)

  (STRUCT    (|Open| (|OpenRas primitive|
                    ( -> |raw_image|
                      NIL NIL
                      (|e|) (|t|) ) )

              (|SetParams| (|SetParams primitive|
                            ( -> |mclean_parameters| |topology|
                              NIL NIL
                              (|e|) (|t|) ) )

              (|morphological cleaner| (|mclean primitive|
                                        ( |mclean_parameters| |raw_image| -> |new_image|)
                                        NIL NIL
                                        (|e|) (|t|) ) )

              (|Write| (|WriteRas primitive|
                      (|RasOut| -> )
                      NIL NIL
                      (|e|) (|t|) ) )

  )
)

```

Figure 2: Example of an HDL Compound

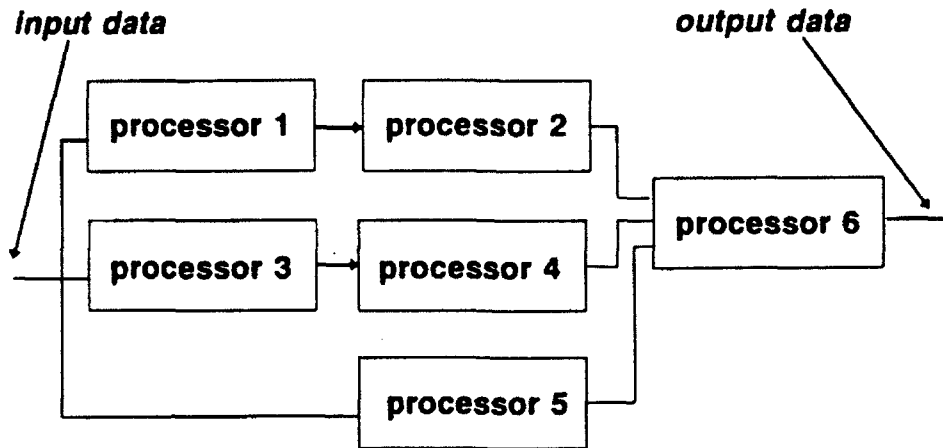
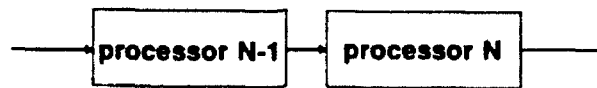


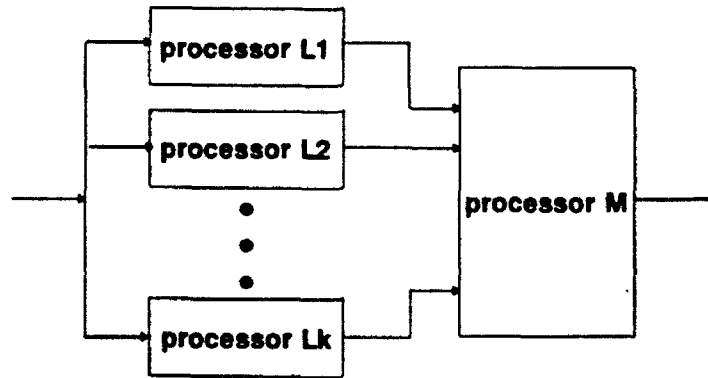
Figure 3: A Graph of a Decomposed Algorithm

causing a net speedup in processing. See figure 3. However, note that if one processing block's input data depends upon another block's output data, as in part *a* of figure 4, then the system is effectively a serial processor. Processor  $n$  will have to wait on processor  $n - 1$  to finish before it can run. This serial topology can still be effective if the data set is such that many "waves" of data will be propagated through the system one after the other. Then, if each of the serial processing blocks is assumed to have approximately the same execution time, then each processor "down the line" will be idle only until the first wave of data reaches it. After that, a continuous flow of data will be achieved. Note that the processing blocks are assumed to have similar execution times. The difficulties of this condition become clear in light of the fact that the processor assigned to block  $n$  could much faster or slower than the one assigned to block  $n - 1$ . Since most networks are non-homogeneous, this is a likely situation. Also, an algorithm's natural decomposition may not lead to blocks of similar complexity, which would similarly effect the system's speed.

Some algorithms may decompose naturally in a parallel manner, as show in part *b* of figure 3. Again, the successful speedup depends upon the condition that the parallel processing blocks  $l_1 \dots l_k$  are executed at nearly the same speed. Thus all of the inputs to block  $m$  arrive with approximate synchronicity. This will insure that block  $m$  does not waste time waiting on one or more input(s) while its others are already available. Again, non-homogeneity of the processor network becomes an issue.



**Part a: Serial Processing Topology**



**Part b: Parallel Processing Topology**

**Figure 4: Serial and Parallel Decomposition**

A different approach to parallelizing a system is to distribute the data instead of distributing the algorithm. In the image processing case, this means to split the image into pieces and send the pieces to remote processors. Each remote processor will perform the same operation on its sub-image. The processed sub-images are then put together to form the output image. This technique is commonly referred to as *farming*. Not all imaging algorithms are appropriate for farming because they do not use *neighborhood operations*. Neighborhood operations form the output at each pixel from pixels in a neighborhood around that position. Examples of neighborhood operators are the median filter, the morphological opening and closing operations, and linear convolution with a short duration FIR filter. By choosing sub-images with slightly overlapping edges, a distributed implementation of a neighborhood operation can have the same outcome as the non-distributed case. (ie. Neighborhood operations can be considered invariant under this type of farming process.)

Farming was the process distribution method used in implementing all of the algorithms presently supported by the distributed imaging system. However, the other methods can easily be applied where appropriate. An example of an applicable algorithm is the 2-dimensional wavelet transformation. The planned approach to parallelizing the Daubechies wavelet transform for images includes a combination of farming and process decomposition methods.



## IMAGE PROCESSING UTILITIES:

Several utility actors were developed that are used by almost all of the implemented algorithms. Basic I/O, system topology control, and image viewing capabilities were needed. The following Multigraph actors were written to fit these needs.

1. *OpenRas* is the actor that opens an image file, reads it into Multigraph memory, and propagates it to an output port. The type of memory structure it allocates is called *RasImg*. The *RasImg* structure is described in [4] and is declared in the file *include.h*. *OpenRas* is always capable of reading compressed or uncompressed Sun rasterfiles, whether or not compression is specified in the filename. If PBMplus is available on the computer where *OpenRas* is executed, it can read any PBM supported image format, compressed or uncompressed. In its present state, *OpenRas* runs once and then deactivates itself. This property can be easily modified to accommodate the processing of image batches.
2. *WriteRas* receives an image buffer and puts it into a *RasImg* type structure if it recognizes the incoming buffer type <sup>3</sup>. It then writes an uncompress Sun rasterfile.
3. *SplitRas* receives an image and a two data structures containing information describing the topology of the process distribution and the size of the neighborhood that will be used. From this information it decides how to cut the image and how much overlap to allow along the cuts. It then propagates the sub-images from its outputs.
4. *ConstructRas* receives the topology information, the width and height of the original image, and the sub-images. It reconstructs an output image of the same size as the original image, throwing away the overlapping edges. The result is propagated to an output port. An interesting feature of *ConstructRas* is that it is an IFANY actor. Each time one of its inputs becomes available, its script is executed. The output image buffer, which is stored as context, is updated whenever a sub-image becomes available. The partially filled out image is propagated from an output port called

---

<sup>3</sup>A magic number specifies each supported buffer type. Each actor in the system checks the magic number of the image buffer it receives and tries to convert the image to its format. These conversions are built into the image receiving functions, so they need not be apparent to the script writer

*display\_update* to the image displayer. Thus, the user can evaluate the results as the output image is still being formed.

5. *SetTopology* allows control of the image splitter. The operator can choose the number of slices to be made in the horizontal and vertical directions. At the present time, the maximum total number of sub-images is 10. This constraint is set only by the HDL scripts, not by the actor scripts. It can easily be made as large as desired by editing the HDL code.
6. *DisplayUpdate* receives an image and displays it in an X-window. The displayer was adapted from *xloadimage*, which is a standard X-windows image viewer.

Along the way, an image structure protocol was adopted so that future efforts will be compatible with the present system. Interfaces between already existing structures and the new protocol were developed. The supported formats are IMAGE <sup>4</sup>, *RasImg*, and AEDC\_EL3 <sup>5</sup>. Any actor that uses one of these image data structures internally can receive a generic image by calling its interface function. (For example *ReceiveRasImg* receives an image and puts it into a *RasImg* type buffer.)

#### IMAGE PROCESSING LIBRARY:

The following is a brief description of the algorithms presently available on the distributed image processing system. These algorithms were chosen to be implemented first because they are computationally expensive and thus usually require large amounts of processing time. Many other algorithms can easily be added in the future.

1. *Mclean* is a morphological noise reduction technique developed by R. A. Peters of Vanderbilt University [5]. It is based on the morphological operations *open* and *close*. *Mclean* is extremely effective in removing noise from images while leaving edges and small grained features intact. This algorithm was implemented during the 1991 RDL summer research program by this author [4]. Slight changes have been made to the

---

<sup>4</sup>The IMAGE data structure is defined in *image.h*

<sup>5</sup>The AEDC\_EL3 was adopted by the EL3 group at AEDC as the standard Multigraph image format to be used in the future. It is defined in *el3\_image.h*

software since then, but the algorithm is still as described in [4] and [5]. The *mclean* actor receives a data structure called *mclean\_parameter\_list*, which is created by another actor called *SetParameters*. The *mclean\_parameter\_list* contains the structuring element specifications and other information that *mclean* needs (see [4]). The *mclean* parameters can be set to default or edited at run-time, so the algorithm can be adjusted without recompiling the code.

2. The *adaptive histogram equalization* (AHE) algorithm is usually used for edge and detail enhancement. The algorithm rescales the intensity map for each pixel based on the *histogram* of a neighborhood around it. Note that the effect of the AHE operation is highly dependent upon the neighborhood size. In general, large neighborhoods will tend to bring out details such as edges very well. The actor was written by Rich Souder, and uses the *IMAGE* data structure [6]. Only minor adjustments were made to the code, including the installation of the data structure conversion interface previously discussed. The AHE actor receives width and height of the neighborhood via a data structure called *neighborhood\_info*, which is created by the actor *SetTopology*.
3. The *median filter* script, which was also written by Rich Souder, implements a neighborhood based image smoothing technique. The algorithm makes a list of intensities that occur in a window around each pixel. It sorts the list, and sets the pixel in the center of the window equal to the median value. The effect is similar to that of an averaging, or *rolling ball* filter. The noise is reduced in proportion to the window area. However, unlike the *mclean* filter, the edges and small grained features are significantly degraded. The median filter algorithm receives the same *neighborhood\_info* data structure that the AHE actor does, so the window size is easily changed.

#### SYSTEM PERFORMANCE:

The parallel image processing system was tested extensively. As an example, the results of the parallel *mclean* system test will be given here. Note that the other algorithms implemented have graphs very similar to the *mclean* graph shown in figure 5, and they performed similarly in tests.

A graphical model of the parallel mclean system is shown in figure 5. It uses a compound called *10\_mcleans*, which contains 10 unique mclean actors. Each of these mclean actors could be assigned to a separate processor, but they do not have to be. Two or more of them can be executed on the same processor if desired.

The mclean system was developed and tested on a network of seven Unix workstations. A diagram of the network is given in figure 6.<sup>6</sup> Note that each station has attached to it at least one task, and that each task has an associated environment. The *master* machine, named *nemo*, has two tasks-environment pairs. The *master* environment performs the image I/O, splitting, and reconstruction. The *io.win* environment sets the parameters and runs the display. The *slave* environments are attached to the mclean actors and therefore do most of the computation.

The speedup data shown in figure 7 were taken during the 1991 Summer Research Program. See [4]. The system was implemented on a network of Sun SPARC1 workstations. The algorithm tested was a parallel version of the mclean filter which used from one to three remote processes. Note that the execution time of the mclean algorithm is highly dependent upon the structuring element size. Thus, the structuring element size (actually structuring element width) was varied as well as the number of remote processes. Each test was performed on a 512 by 512, 8-bit greyscale image. Note that when the structuring element size varies, the execution time seems to increase in a quadratic fashion. This is because of the number of operations involved in mclean is proportional to the area of the structuring element, which is the square of the parameter we are calling structuring element size.

The speedup due to the parallelization was considerable. As an example, refer to the second plot of figure 7. The speedup figures for the curve marked  $X = 23$  are given by

$$Speedup[2] = \frac{465seconds}{265seconds} = 1.75 \quad (1)$$

$$Speedup[3] = \frac{465seconds}{205seconds} = 2.27 \quad (2)$$

where  $Speedup[n]$  is the speedup ratio observed with  $n$  remote processes. Note that the speedup ratio is less than  $n$  due to the overhead associated with data communications and

---

<sup>6</sup>Other configurations were tested that used from two to ten workstations. The diagram shows the most commonly used configuration.

## MCLEAN SYSTEM SCHEMATIC (version 2)

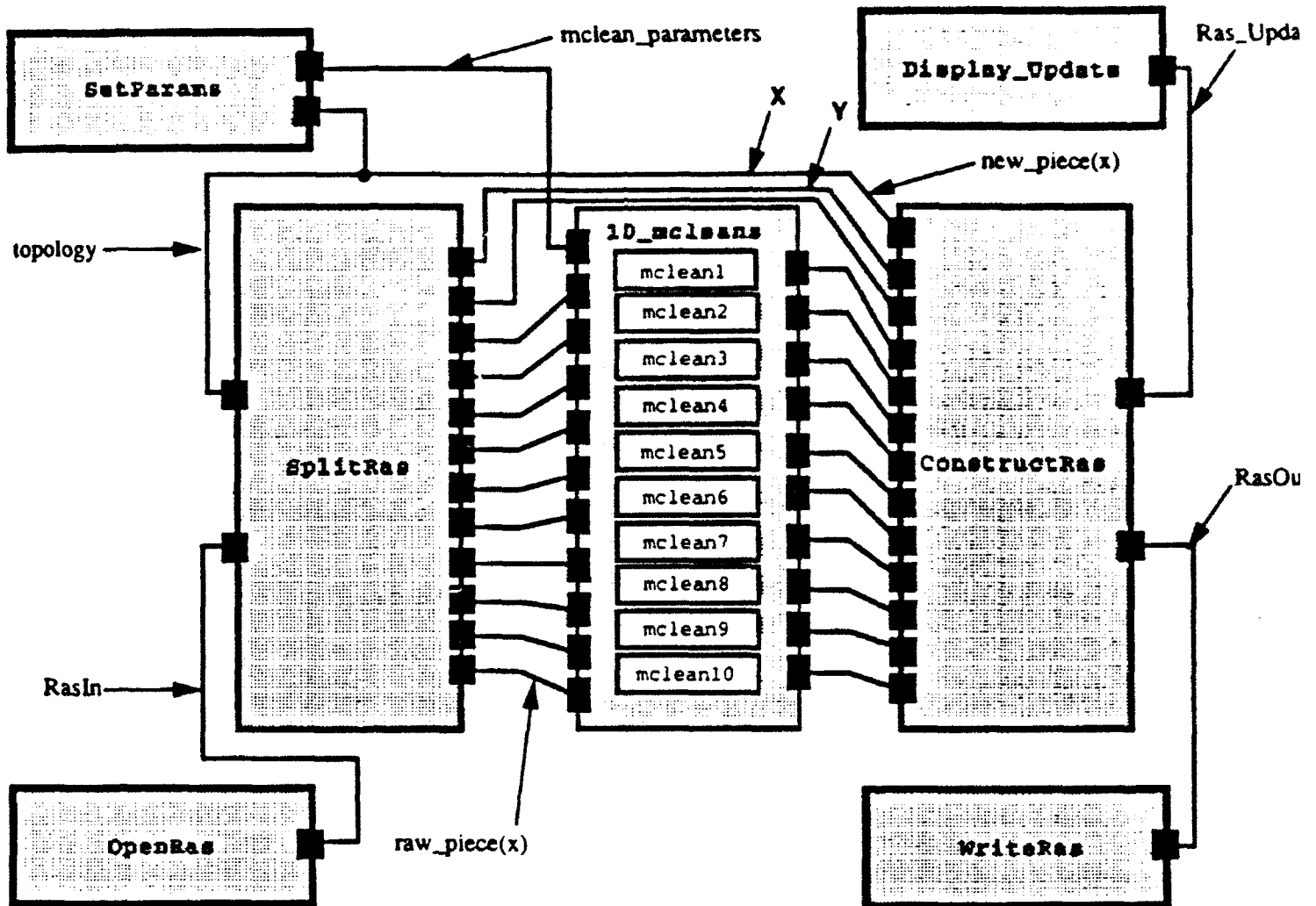


Figure 5: Graphical Model of the Parallel mclean System

the non-homogeneity of the network. The speedup ratios are expected to improve with a future modification of the splitting and reconstruction actors. These actors will soon be improved to adaptively route data based on the apparent performance of the processing nodes. This will reduce the effects of using a non-homogeneous network.

#### RECOMMENDATIONS FOR FUTURE RESEARCH:

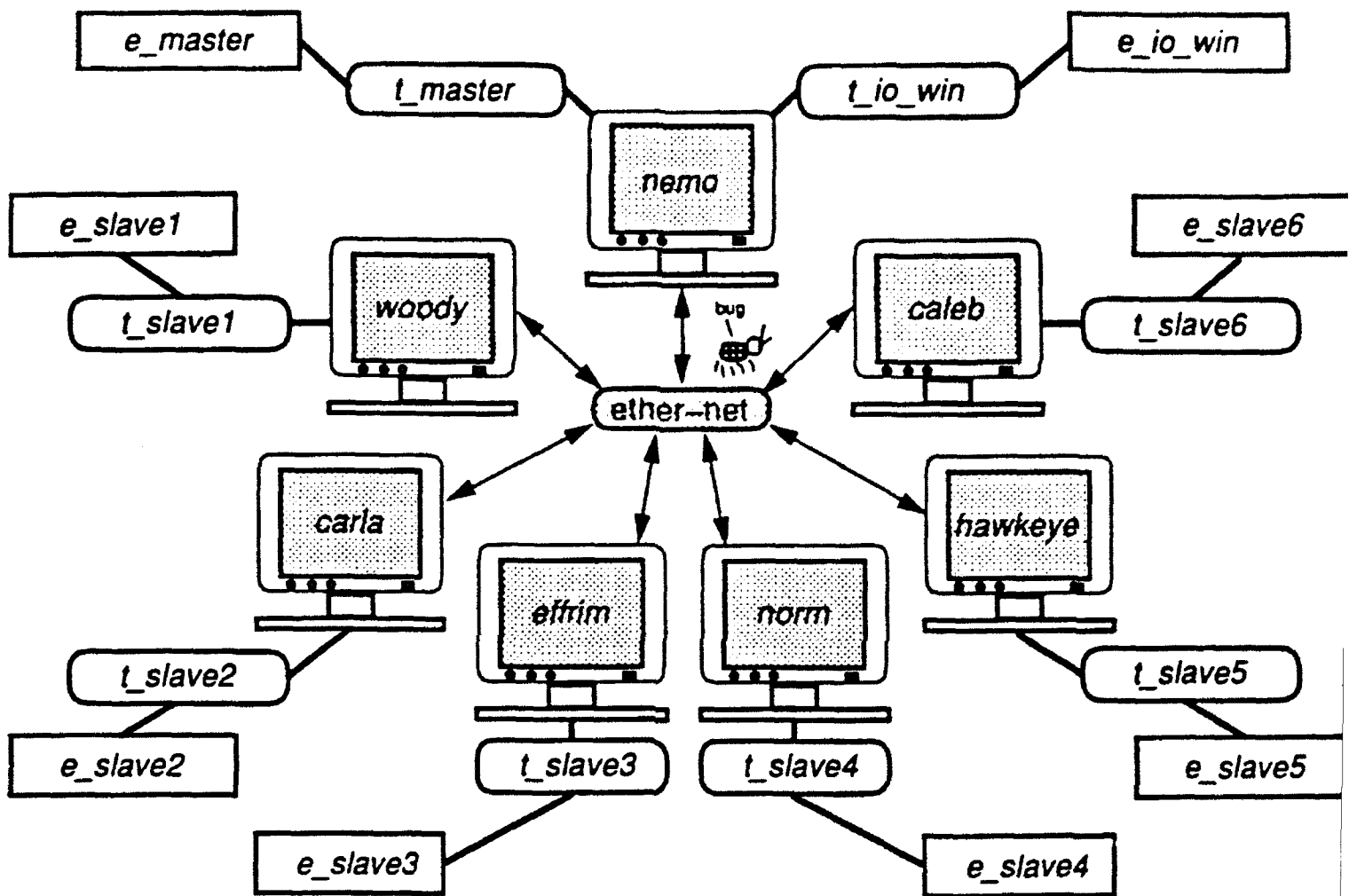
In the future much work should be done to improve the Multigraph distributed image processing system. The recommended improvements and areas of study include:

- Additions to the library of image processing routines to include a broad range of common applications.
- Improvement of the image data distribution technique to include adaptive routing of data.
- A general study of topology and algorithm parameterization. This study should consider the problem of matching processing topologies to a classes of image processing problems. The goal should be to develop an analytic method matching the optimal system configuration to a given algorithm.

#### ACKNOWLEDGEMENTS:

I would like to acknowledge the United States Air Force for making it possible for me to perform this research. The AFOSR summer research program has been an enriching and rewarding experience.

I would also like to acknowledge Ben Abbott, Ted Bapty, and Csaba Biegl, who helped with the development of the HDL code, the structure of the system, and many other facets of the project. People at AEDC who should be acknowledged are Rick Reopke, Hal Martin, and Jim Nichols. All of the support I received allowed the summer research to be a success.



The rounded off rectangular boxes connected to the machines represent tasks. The rectangular boxes represent environments. Each machine is a either a Sun SPARC, an IBM RS600, or a 4d340 Silicon Graphics workstation.

Figure 6: System Development and Test Network

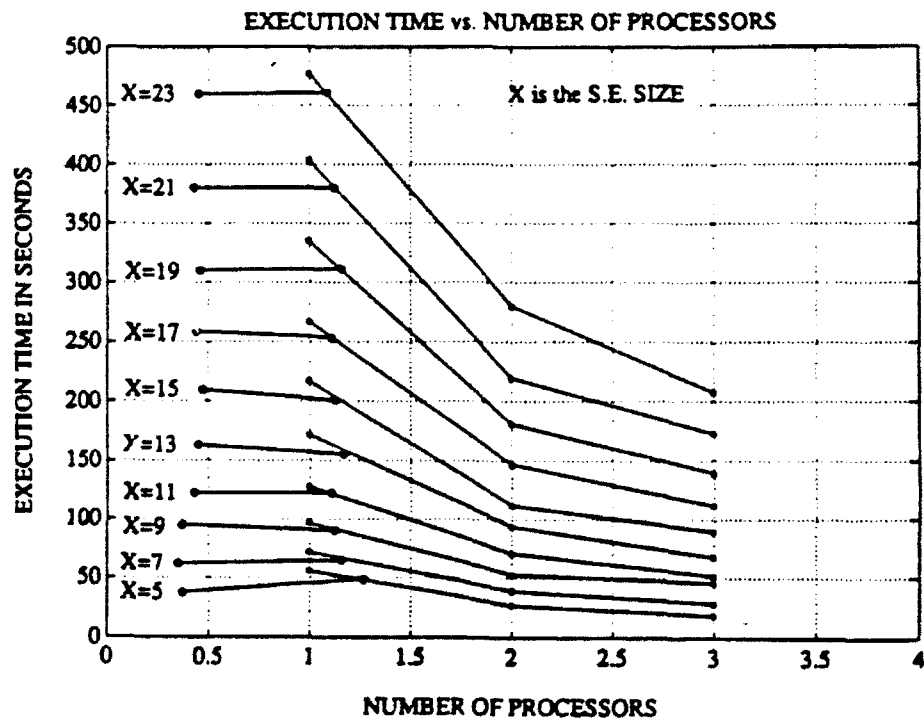
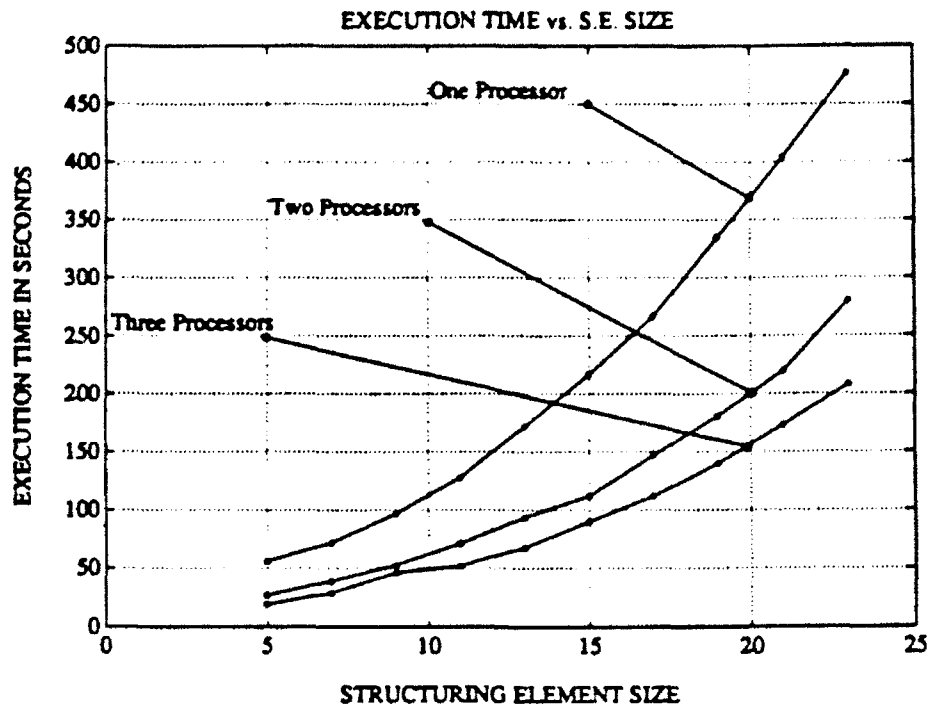


Figure 7: Speedup Data For the Parallel mclean System



## References

- [1] Abbott, B.A., Bapty, T.A., Biegl, C.: "Experiences Using Model-Based Techniques For The Development Of A Large Parallel Instrumentation System", Final Report for the 1992 USAF-RDL summer research program, 1992.
- [2] Biegl, Csaba.: "Multigraph Kernel (MGK) User's Manual", Dept. of Electrical Engineering, Vanderbilt University, 1988.
- [3] Karsai, G.: "Hierarchical Description Language (HDL) User's Manual" Dept. of Electrical Engineering, Vanderbilt University, Technical Report #87-004, 1987.
- [4] Moore, Michael S.: "Multigraph Implementation of Image Morphology", Final report for the 1991 USAF-RDL summer research program, 1991.
- [5] Peters, Richard Alan.: "Image Sequence Noise Reduction using Morphological Filters", Final report for the AFOSR. Research Initiation Program, 1991.
- [6] Souder, Richard S.: "Parallel Distributed Image Processing", Master's Thesis Submitted to the Faculty of the Graduate School of Vanderbilt University, 1989.

A CELL AVERAGED APPROACH TO THE SOLUTION  
OF INTEGRAL CONSERVATION LAWS

Blair H. Rollin  
Graduate Research Assistant  
Department of Mathematics

The University of Tennessee  
Space Institute  
Tullahoma, TN 37388

Final Report for:  
Summer Research Program  
Calspan Corporation/AEDC Operations  
Arnold Engineering Development Center  
Arnold Air Force Base  
Tullahoma, TN

Sponsored by:  
Air Force Office of Scientific Research  
Boiling Air Force Base, Washington, D.C.

August 1992

# A CELL AVERAGED APPROACH TO THE SOLUTION OF INTEGRAL CONSERVATION LAWS

Blair H. Rollin  
Graduate Research Assistant  
Department of Mathematics  
The University of Tennessee Space Institute

## Abstract

An analytical cell averaging approach is applied to the Local Lagrangian Finite Volume method developed for computing solutions to the compressible flow equations. This approach eliminates the need for pointwise evaluation of fluxes and coupled with nonoscillatory interpolating functions yields a highly accurate, conservative, stable scheme. This is done without the addition of any terms not present in the original equations, such as artificial dissipation terms. Nor are the equations split into characteristic fields. The scheme is derived and then demonstrated on two different fluid flow problems.

# A CELL AVERAGED APPROACH TO THE SOLUTION OF INTEGRAL CONSERVATION LAWS

Blair H. Rollin

## Introduction

The purpose of this paper is to formally document a new computational algorithm and demonstrate its viability for fluid flow applications.

It can be shown [1] that the Euler equations, describing the flow of an inviscid perfect gas, can be written in the form of a homogeneous coupled system of nonlinear ordinary differential equations. From this formulation it is seen that the domain of dependence of the system is symmetrically distributed about streamlines of the flow (in a differential sense). This fact makes a Lagrangian formulation of the equations a natural choice for the basis of numerical discretization.

Since late 1990, K. C. Reddy of The University of Tennessee Space Institute and the author have been developing a novel approach to solving the compressible flow equations based on a Lagrangian finite volume in space-time on fixed grids [2] [3]. The algorithm is particularly elegant in that, unlike most popular schemes used today, it includes no additional terms not discretized from the original equations to provide stability.

Recently, by adopting a cell averaged approach to the equations, great strides in accuracy and stability have been made. This paper focuses on the new cell averaged approach.

I will summarize, in brief, the development of the Local Lagrangian Finite Volume (LLFV) method since [2] was submitted. Then the present form of the algorithm will be derived and applied to several test cases.

## Discussion

Consider the one-dimensional Euler equations, a coupled system of PDE's.

$$(1) \quad \nabla \circ (Q, E) = 0 \quad \nabla = \left( \frac{\partial}{\partial t}, \frac{\partial}{\partial x} \right)$$

$$Q = \begin{pmatrix} \rho \\ \rho u \\ e \end{pmatrix}, E = \begin{pmatrix} \rho u \\ \rho u^2 + p \\ (e + p)u \end{pmatrix}, p = (\gamma - 1)(e - \rho u^2/2).$$

We wish to integrate these equations on a fixed, uniform, space-time grid over cells that are bounded spatially by particle paths and temporally by time levels  $n$  and  $n+1$  as shown in figure 1. Define

$$h = x_{j+1/2} - x_{j-1/2}, \quad \Delta t = t^{n+1} - t^n.$$

Integrating  $\nabla \circ (Q, E) = 0$  over volume  $V$  yields  $\oint_{\partial V} (Q, E) \circ n ds = 0$  or

$$\int_{x_{j-1/2}}^{x_{j+1/2}} Q(x, t^{n+1}) dx - \int_{x_{j-1/2}(x_j)}^{x_{j+1/2}(x_j)} Q(x, t^n) dx + \int_{\tau_{j+1/2}(t^n)}^{\tau_{j+1/2}(t^{n+1})} \frac{F(\tau_{j+1/2}(t), t)}{\|(u, 1)\|} d\tau_{j+1/2} - \int_{\tau_{j-1/2}(t^n)}^{\tau_{j-1/2}(t^{n+1})} \frac{F(\tau_{j-1/2}(t), t)}{\|(u, 1)\|} d\tau_{j-1/2} = 0$$

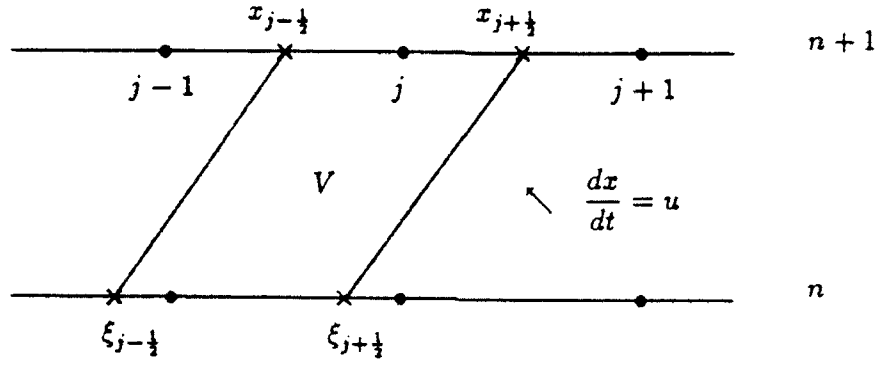


Figure 1: A Lagrangian Finite Volume in space-time.

with

$$(2) \quad F = -Qu + E = \begin{pmatrix} 0 \\ p \\ pu \end{pmatrix}$$

where  $x = \tau_{j\pm 1/2}$  are solutions to the differential equation

$$\frac{dx}{dt} = u, \quad \text{with} \quad \tau_{j\pm 1/2}(t^{n+1}) = x_{j\pm 1/2}.$$

Backward integration in time gives

$$\tau_{j\pm 1/2}(t^n) = \xi_{j\pm 1/2}.$$

Since

$$d\tau = (dx^2 + dt^2)^{1/2} = \left(\frac{dx}{dt}^2 + 1\right)^{1/2} dt = (u^2 + 1)^{1/2} dt,$$

we may rewrite the previous equation as

$$(3) \quad \int_{x_{j-1/2}}^{x_{j+1/2}} Q(x, t^{n+1}) dx - \int_{\xi_{j-1/2}(x_j)}^{\xi_{j+1/2}(x_j)} Q(x, t^n) dx +$$

$$\int_{(t^n)}^{(t^{n+1})} F(\tau_{j+1/2}(t), t) dt - \int_{(t^n)}^{(t^{n+1})} F(\tau_{j-1/2}(t), t) dt = O.$$

From the definition of  $\tau$

$$\begin{aligned} \int_{t^n}^{t^{n+1}} \tau' dt &= \int_{t^n}^{t^{n+1}} u(\tau(t), t) dt \\ \Rightarrow \xi_{j\pm 1/2} &= x_{j\pm 1/2} - \int_{t^n}^{t^{n+1}} u(\tau_{j\pm 1/2}(t), t) dt. \end{aligned}$$

Once this has been integrated,

$$\frac{d}{dt} \int_{\tau_{j-1/2}(t)}^{\tau_{j+1/2}(t)} \rho dx = 0.$$

In this way the Lagrangian formulation effectively transforms the system of three PDE's to that of three ODE's.

Approximating the integral on the right by the trapezoidal rule yields

$$(4) \quad \xi_{j\pm 1/2} = x_{j\pm 1/2} - \bar{u}_{j\pm 1/2} \Delta t.$$

$$\bar{u}_{j\pm 1/2} = (u_{j\pm 1/2}^{n+1} + u(\xi_{j\pm 1/2}, t^n))/2.$$

With this approximation we are assuming the characteristics  $\tau_{j\pm 1/2}$  to be straight lines of slope  $\frac{dx}{dt} = \bar{u}_{j\pm 1/2}$ . Integrating the second two terms in equation 3 similarly, we have,

$$(5) \quad \int_{x_{j-1/2}}^{x_{j+1/2}} Q(x, t^{n+1}) dx - \int_{\xi_{j-1/2}(x_j)}^{\xi_{j+1/2}(x_j)} Q(x, t^n) dx + \bar{F}_{j+1/2} \Delta t - \bar{F}_{j-1/2} \Delta t = O,$$

where

$$\bar{F}_{j\pm 1/2} = (F_{j\pm 1/2}^{n+1} + F(\xi_{j\pm 1/2}, t^n))/2.$$

and the so called flux vector  $F$  is defined by equation 2.

To preserve conservative properties in time and space for discrete equations we choose a solution space at each time step on a fixed spatial grid for approximating our solution to the PDE, and use this solution space consistently throughout each stage of the computation for integral evaluation [3] .

We choose a solution space that is piecewise constant within each interval  $(x_{j-1/2}, x_{j+1/2})$  for integration purposes and use linear interpolation of quantities between nodes. This choice yields a conservative stable scheme which can be shown to be dissipative of order 2 on the scalar equation  $u_t + au_x = 0, a = \text{constant}$ . Also, this provides only  $\mathcal{O}(h)$  accuracy.

To increase accuracy to  $\mathcal{O}(h^2)$ , a piecewise linear continuous solution space was chosen for both integration and interpolation purposes. This method proved highly accurate, but unstable for some initial conditions on the vector equations. Following ideas of the so-called MUSCL and flux-limited schemes, the previous two results suggested that a piecewise linear slope-limited approximation might provide stability along with high accuracy. However, this method also proved to be unstable for certain initial conditions, presumably due in part to the following.

It was observed that when the piecewise constant solution space was used for both integration and interpolation the method was also unstable (recall that this choice is stable if linear interpolation is used). When a discontinuous solution space is used for interpolation an ambiguity arises in determining a function value at a discontinuity. Moreover,



precise location of the argument is critical in the sense that a very small change in the argument could produce a very large change in the corresponding ordinate. This is clearly undesirable in an iterative process.

With these thoughts in mind we now develop the present form of the algorithm.

Let  $x \in (x_{j-1/2}, x_{j+1/2})$  and form a LLFV bounded by  $x - h/2$  and  $x + h/2$  at  $t^{n+1}$ . We have

$$(6) \quad \int_{x-h/2}^{x+h/2} Q(y, t^{n+1}) dy - \int_{\xi_L(x)}^{\xi_R(x)} Q(y, t^n) dy + \int_{\tau_R(t^n)}^{\tau_R(t^{n+1})} \frac{F(\tau_R(t), t)}{\|(u, 1)\|} d\tau_R - \int_{\tau_L(t^n)}^{\tau_L(t^{n+1})} \frac{F(\tau_L(t), t)}{\|(u, 1)\|} d\tau_L = O.$$

with  $\tau_R$  the solution to

$$\frac{dx}{dt} = u \quad \tau_R(t^{n+1}) = x + h/2.$$

where we define

$$\xi_R(x) = \tau_R(t^n),$$

with similar equations for  $\tau_L, \xi_L$ . Since

$$\int_{\tau_{R,L}(t^n)}^{\tau_{R,L}(t^{n+1})} \frac{F(\tau_{R,L}(t), t)}{\|(u, 1)\|} d\tau_{R,L} = \int_{t^n}^{t^{n+1}} F(\tau_{R,L}(t), t) dt,$$

we rewrite equation 6 and average over cell  $j$  to get,

$$(7) \quad \frac{1}{h} \int_{x_{j-1/2}}^{x_{j+1/2}} \int_{x-h/2}^{x+h/2} Q(y, t^{n+1}) dy dx - \frac{1}{h} \int_{x_{j-1/2}}^{x_{j+1/2}} \int_{\xi_L(x)}^{\xi_R(x)} Q(y, t^n) dy dx + \frac{1}{h} \int_{x_{j-1/2}}^{x_{j+1/2}} \int_{t^n}^{t^{n+1}} F(\tau_R(t), t) dt dx - \frac{1}{h} \int_{x_{j-1/2}}^{x_{j+1/2}} \int_{t^n}^{t^{n+1}} F(\tau_L(t), t) dt dx = O.$$

Using the midpoint rule we have the following results for the first two terms

$$\frac{1}{h} \int_{x_{j-1/2}}^{x_{j+1/2}} \int_{x-h/2}^{x+h/2} Q(y, t^{n+1}) dy dx = \int_{x_{j-1/2}}^{x_{j+1/2}} Q(x, t^{n+1}) dx + \mathcal{O}(h^2)$$

$$\frac{1}{h} \int_{x_{j-1/2}}^{x_{j+1/2}} \int_{\xi_L(x)}^{\xi_R(x)} Q(y, t^n) dy dx = \int_{\xi_L(x_j)=\xi_{j-1/2}(x_j)}^{\xi_R(x_j)=\xi_{j+1/2}(x_j)} Q(x, t^n) dx + \mathcal{O}(h^2)$$

provided  $Q$  is sufficiently smooth.

Consider the remaining term

$$\frac{1}{h} \int_{x_{j-1/2}}^{x_{j+1/2}} \int_{t^n}^{t^{n+1}} F(\tau_R(t), t) dt dx$$

and its counterpart with  $\tau_L$  replacing  $\tau_R$ . When

$$x = x_{j-1/2}, \begin{cases} \tau_R(t^{n+1}) = x_{j-1/2} + h/2 = x_j \\ \tau_L(t^{n+1}) = x_{j-1/2} - h/2 = x_{j-1} \end{cases}$$

and

$$x = x_{j+1/2}, \begin{cases} \tau_R(t^{n+1}) = x_{j+1/2} + h/2 = x_{j+1} \\ \tau_L(t^{n+1}) = x_{j+1/2} - h/2 = x_j \end{cases}$$

So, for example, the first term signifies the double integral of  $F$  over the region in the  $x-t$  plane bounded in time by the lines  $t = t^n$  and  $t = t^{n+1}$  and bounded spatially by streamlines intersecting  $t = t^{n+1}$  at  $x_j$  and  $x_{j+1}$ . Notice that this formulation eliminates the need for pointwise evaluation of fluxes. As we shall see, these approximations lead to discrete equations which will be solved iteratively.

Recall the result  $\xi_{j\pm 1/2} = x_{j\pm 1/2} - \bar{u}_{j\pm 1/2} \Delta t$ , equation 4. This result may be achieved through another interpretation which will prove useful in our current pursuit; namely, to

eliminate pointwise evaluation of quantities. We reinterpret the result in the following manner. Redefining

$$\xi_{j\pm 1/2} = x_{j\pm 1/2} - \frac{1}{\int_{\tau_{j\pm 1/2}(t^n)}^{\tau_{j\pm 1/2}(t^{n+1})} d\tau_{j\pm 1/2}} \int_{\tau_{j\pm 1/2}(t^n)}^{\tau_{j\pm 1/2}(t^{n+1})} u(\tau_{j\pm 1/2}(t), t) d\tau_{j\pm 1/2} \Delta t.$$

$\xi_{j\pm 1/2}$  may be interpreted as  $x_{j\pm 1/2}$  minus the average value of  $u$  along the curve of integration of the flux,  $\tau_{j\pm 1/2}$  multiplied by  $\Delta t$ . Then

$$\xi_{j\pm 1/2} = x_{j\pm 1/2} - \frac{1}{\int_{t^n}^{t^{n+1}} (u^2(\tau_{j\pm 1/2}(t), t) + 1)^{1/2} dt} \int_{t^n}^{t^{n+1}} u(\tau_{j\pm 1/2}(t), t) (u^2 + 1)^{1/2} dt \Delta t$$

since  $d\tau = (u^2 + 1)^{1/2} dt$ . Choosing some numerical approximation to  $u$  along  $\tau_{j\pm 1/2}$ , say  $\hat{u}$  where the subscripts on  $\hat{u}$  are suppressed for convenience,

$$\int_{t^n}^{t^{n+1}} (u^2(\tau_{j\pm 1/2}(t), t) + 1)^{1/2} dt = \delta\tau_{j\pm 1/2} = \|(\hat{u}, 1)\| \Delta t$$

and

$$\int_{t^n}^{t^{n+1}} u(\tau_{j\pm 1/2}(t), t) (u^2 + 1)^{1/2} dt \Delta t = \hat{u} \|(\hat{u}, 1)\| \Delta t^2$$

since  $\frac{dx}{dt} = \hat{u} = \text{constant}$ . The notation  $\delta\tau_{j\pm 1/2}$  simply means the distance between the two points  $(\xi_{j\pm 1/2}, t^n)$  and  $(x_{j\pm 1/2}, t^{n+1})$  in the  $x-t$  plane. So

$$\xi_{j\pm 1/2} = x_{j\pm 1/2} - \frac{1}{\|(\hat{u}, 1)\| \Delta t} \hat{u} \|(\hat{u}, 1)\| \Delta t^2 = x_{j\pm 1/2} - \hat{u}_{j\pm 1/2} \Delta t$$

in agreement with equation 4.

With this motivation, we define

$$\xi_{j\pm 1/2} = x_{j\pm 1/2} - \bar{u}_{j\pm 1/2} \Delta t.$$

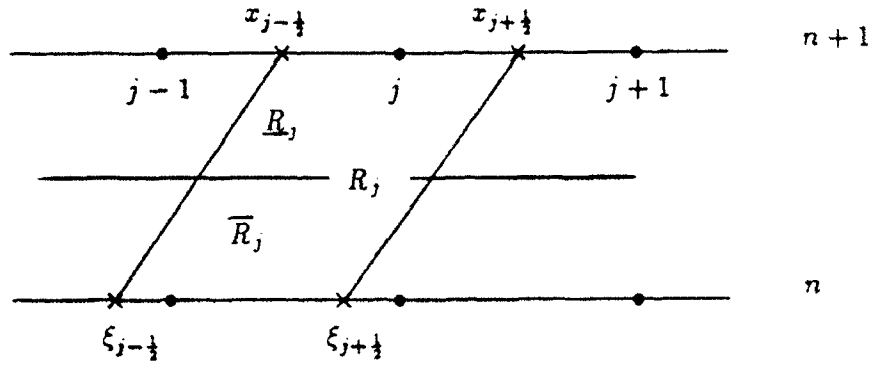


Figure 2: Region of flux integration.

where  $\bar{u}$  is taken to be the average value of  $u$  in the region of integration of the fluxes  $R_{j\pm 1/2}$  shown in figure 2. We may now formally define

$$R_{j+1/2} = \int_{x_{j-1/2}}^{x_{j+1/2}} \int_{\tau_R(t^n)}^{\tau_R(t^{n+1})} d\tau_R dx,$$

$$R_{j-1/2} = \int_{x_{j-1/2}}^{x_{j+1/2}} \int_{\tau_L(t^n)}^{\tau_L(t^{n+1})} d\tau_L dx.$$

It is now a simple extension to include a source term in our equation. For  $Q_t + E_x = S$ .

we have

$$\frac{\partial}{\partial t} Q + \frac{\partial}{\partial x} (E - \int_{x_0}^x S d\eta) = 0,$$

where  $x_0$  is some fixed point in our domain<sup>1</sup>. Before averaging, our surface integral expansion will now include the new term

$$- \int_{t^n}^{t^{n+1}} \int_{x_0}^{\tau_R(t)} S(\eta, t) d\eta dt + \int_{t^n}^{t^{n+1}} \int_{x_0}^{\tau_L(t)} S(\eta, t) d\eta dt.$$

<sup>1</sup>It may be noted that leaving the source term on the right side of the original equation, integrating over a LLFV centered at  $x$ , averaging this term and applying the midpoint rule produces the same result.

Moving these terms to the right side of equation 6, averaging the equation over cell  $j$  and applying the midpoint rule to the resulting integral on the right leaves us with equation 7, with a nontrivial right side given by

$$(8) \quad RHS = \int_{t^n}^{t^{n+1}} \int_{x_0}^{\tau_{j+1/2}(t)} S(x, t) dx dt - \int_{t^n}^{t^{n+1}} \int_{x_0}^{\tau_{j-1/2}(t)} S(x, t) dx dt.$$

This is simply the integral of  $S$  over a LLFV centered at  $x_j$ ; i.e., region  $R_j$  in figure 3.

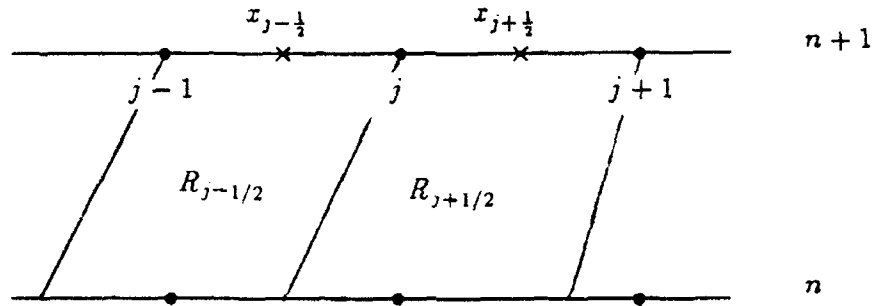


Figure 3: Region of source integration.

It is now clear that we will need to integrate various dependent variables over the regions shown in figures 2 and 3. For simplicity we consider the integration of the generic dependent variable  $f$  over the region  $R_j$  in figure 3. At any stage of the iteration we have an estimate of the solution at time  $t^{n+1}$  and we know the solution at  $t^n$ . Because of the Lagrangian formulation it is evident that assuming the solution to be constant along any given  $\tau$  in  $((n - 1/2)\Delta t, (n + 1/2)\Delta t)$  would be a better assumption than assuming it constant along  $x = \text{constant}$  in the same time interval. Therefore, we divide the region  $R_j$

into two parts shown in figure 3.  $\overline{R}_j$ , that region of  $R_j$  in  $((n + 1/2)\Delta t, (n + 1)\Delta t)$  and  $\underline{R}_j$ , that region of  $R_j$  in  $(n\Delta t, (n + 1/2)\Delta t)$ . We now make the approximations

$$\int \int_{\overline{R}_j} f d\overline{R}_j \approx \frac{1}{\Delta \tau(t^{n+1})} \int_{\tau_L(t^{n+1})}^{\tau_R(t^{n+1})} f dx \overline{R}_j = \frac{1}{h} \int_{x_{j-1/2}}^{x_{j+1/2}} f(x, t^{n+1}) dx \overline{R}_j$$

$$\int \int_{\underline{R}_j} f d\underline{R}_j \approx \frac{1}{\Delta \tau(t^n)} \int_{\tau_L(t^n)}^{\tau_R(t^n)} f dx \underline{R}_j = \frac{1}{\delta \xi_j} \int_{\xi_{j-1/2}}^{\xi_{j+1/2}} f(x, t^n) dx \underline{R}_j$$

$$\Delta \tau(t) = \tau_R(t) - \tau_L(t)$$

i.e.:  $f$  is assumed constant in the regions  $\overline{R}_j$  and  $\underline{R}_j$  with value equal to the average value of  $f$  at  $t^{n+1}$  in  $(x_{j-1/2}, x_{j+1/2})$ , and the average value of  $f$  in  $(\xi_{j-1/2}, \xi_{j+1/2})$  at  $t^n$ , respectively.

The integral of  $f$  over the regions  $\overline{R}_{j\pm 1/2}$ ,  $\underline{R}_{j\pm 1/2}$  is defined entirely similarly.

The preceding discussion has now led us to the following approximation to equation 7 including the source terms given by equation 8.

$$(9) \quad \int_{x_{j-1/2}}^{x_{j+1/2}} Q(x, t^{n+1}) dx - \int_{\xi_{j-1/2}}^{\xi_{j+1/2}} Q(x, t^n) dx + \\ \frac{1}{h} \left\{ \frac{\underline{R}_{j+1/2}}{\delta \xi_{j+1/2}} \int_{\xi_j}^{\xi_{j+1}} F(x, t^n) dx + \frac{\overline{R}_{j+1/2}}{h} \int_{x_j}^{x_{j+1}} F(x, t^{n+1}) dx \right\} - \\ \frac{1}{h} \left\{ \frac{\underline{R}_{j-1/2}}{\delta \xi_{j-1/2}} \int_{\xi_{j-1}}^{\xi_j} F(x, t^n) dx + \frac{\overline{R}_{j-1/2}}{h} \int_{x_{j-1}}^{x_j} F(x, t^{n+1}) dx \right\} - \\ \left\{ \frac{\underline{R}_j}{\delta \xi_j} \int_{\xi_{j-1/2}}^{\xi_{j+1/2}} S(x, t^n) dx + \frac{\overline{R}_j}{h} \int_{x_{j-1/2}}^{x_{j+1/2}} S(x, t^{n+1}) dx \right\} = O,$$

where  $\delta \xi_{j+1/2} = \xi_{j+1} - \xi_j$  and  $\delta \xi_j = \xi_{j+1/2} - \xi_{j-1/2}$ . Note that the  $R$ 's can be written in terms of the  $\xi$ 's as follows.

$$\overline{R}_{j+1/2} = \frac{3h\Delta t}{8} + \frac{\Delta t}{8}(\xi_{j+1} - \xi_j) \quad \overline{R}_j = \frac{3h\Delta t}{8} + \frac{\Delta t}{8}(\xi_{j+1/2} - \xi_{j-1/2}).$$

$$\underline{R}_{j+1/2} = \frac{h\Delta t}{8} + \frac{3\Delta t}{8}(\xi_{j+1} - \xi_j) \quad \underline{R}_j = \frac{h\Delta t}{8} + \frac{3\Delta t}{8}(\xi_{j+1/2} - \xi_{j-1/2}).$$

Equation 9 is the LLFV method. We now have everything sufficiently defined so that the iterative process may begin.

We need only choose a solution space on which to perform the integration required in equation 9 and a method of integration.

For the solution space we choose interpolating functions devised by Harten and Osher[4]. These are piecewise linear slope-limited in each cell, constructed from the cell averages of  $Q$ , and provide  $\mathcal{O}(h^2)$  approximation to the components of  $Q$ . Moreover, they have the additional property that the cell averages of the interpolating functions are an  $\mathcal{O}(h^3)$  approximation to the cell averages of the components of  $Q$ . These interpolating functions can be shown to be nonoscillatory in the sense that the number of local extrema in the solution to the scalar equation will not increase.

Because of the form of the interpolants, the first two terms in equation 9 can be evaluated exactly.

The remaining terms are integrated by two point Gaussian quadrature in each subinterval in which  $Q$  is continuous. This provides  $\mathcal{O}(h^5)$  accuracy for sufficiently smooth flux and source functions[5].

As stated previously, because of the coupling of the solution at time level  $n+1$  and the location of the  $\xi$ 's at time level  $n$ , it is necessary to solve the resulting implicit equations iteratively. The Locally Implicit Method (LIM) developed by Reddy and Benek[6] was

chosen as the method of solution.

## Results

The algorithm was applied to two test cases, the familiar shock-tube problem[1] and the quasi-one-dimensional nozzle flow problem[7], both of which have analytical solutions.

### Shock Tube:

We wish to solve the Euler equations, equation 1, on an infinite domain with initial conditions of two constant states separated by a discontinuity in the components of  $Q$ . In equation 9  $F$  is given by equation 3 and  $S = 0$ . Rather than present the details, I merely state that sweep dependent coefficients for the LIM were derived through a lengthy analysis. The coefficients used were

$$\Delta x + \frac{|2\bar{R}_{j+1/2} - \bar{R}_{j-1/2}|}{2\Delta x} c_j \quad \text{left to right sweeps}$$

and

$$\Delta x + \frac{|\bar{R}_{j+1/2} - 2\bar{R}_{j-1/2}|}{2\Delta x} c_j \quad \text{right to left sweeps}$$

where  $c$  is the speed of sound.

The density solution for initial conditions  $p_L = 10^5$ ;  $\rho_L = 1$ ;  $p_R = 10^3$ ;  $\rho_R = 0.01$ ;  $u_L = u_R = 0$ , is shown in figure 4. Note that the solution is highly accurate but virtually nonoscillatory. The contact discontinuity is particularly well resolved.



Shock Tube Flow: NGRD=100 CFL=2.0 TIME=3.9msec

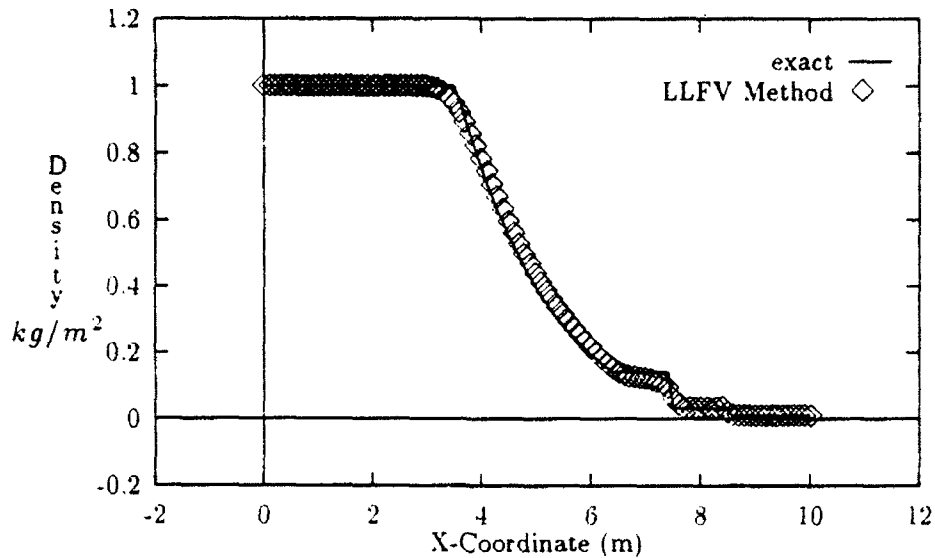


Figure 4: Density in the shock tube.

Nozzle Flow:

The quasi-one-dimensional nozzle flow equations can be written as  $Q_t + E_x = S$  where

$$Q = \alpha \begin{pmatrix} \rho \\ \rho u \\ e \end{pmatrix}, E = \alpha \begin{pmatrix} \rho u \\ \rho u^2 + p \\ (e + p)u \end{pmatrix}, S = \begin{pmatrix} 0 \\ p\alpha' \\ 0 \end{pmatrix}$$

and  $\alpha(x)$  is the crosssectional area of the nozzle. The equations were solved in a diverging duct with domain  $x \in [0, 10]$  and the area of the duct given by  $\alpha(x) = 1.398 + 0.347 \arctan[0.8(x - 4)]$ . Empirical knowledge has indicated that the same coefficients used for the shock tube problem are appropriate and work well for the nozzle flow problem. These were used and indeed did provide convergence. Figure 5 shows the steady state

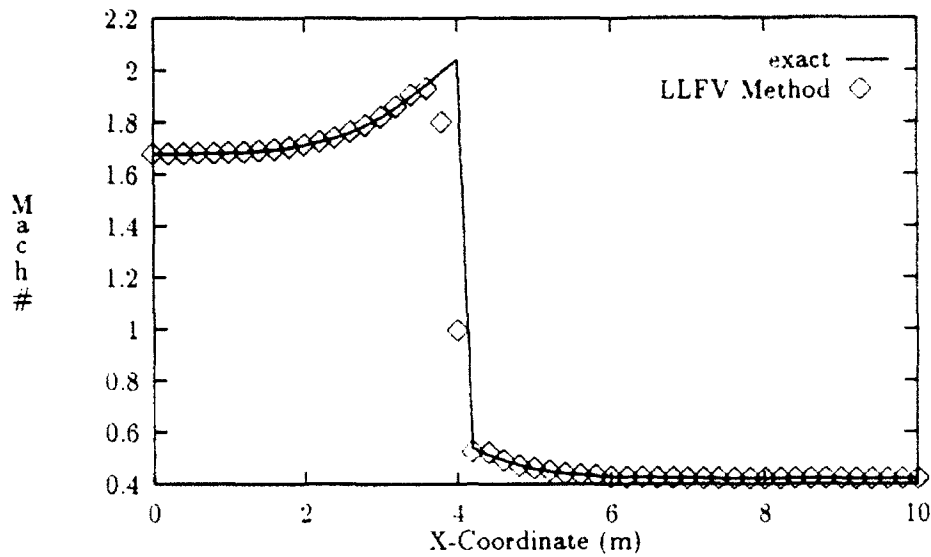


Figure 5: Mach number in diverging duct.

Mach number distribution for inlet conditions  $T_0 = 300K$ ;  $p_0 = 1bar$ ;  $A^* = 0.8$  with outlet boundary conditions to locate a shock at  $x = 4$ . No convergence studies were undertaken. It was necessary to use a CFL number less than or equal to 1 due to the difficulty in imposing boundary conditions with large time steps. Again the solution is highly accurate.

## Conclusions

The purpose of this research was to formalize the new cell averaged algorithm and investigate its viability on some fluid flow applications.

The new cell averaged approach applied to the LLFV method provides a mathematically

elegant, highly accurate, numerically stable method of solution for conservation laws. In order for it to be applied to realistic flow problems, future work must concentrate on implementing boundary conditions in conjunction with large time steps and extensions to multiple dimensions.

## Acknowledgments

I wish to thank AFOSR and RDL for financial support of this research. I also wish to express my gratitude to all those at CALSPAN Corp./AEDC Operations who have assisted me over the last two summers, in particular Stephen L. Keeling and Robert W. Tramel for insightful discussions. Finally I wish to thank K. C. Reddy, without whose ideas none of this research would have been possible.

## References

- [1] Hirsch, C., *Numerical Computation of Internal and External Flows, Volume 2*, John Wiley and Sons, West Sussex, England, 1990
- [2] Rollin, B. H., *A Local Lagrangian Model for the Infinite Domain Shock Tube Problem*, AFOSR Summer Research Program, Final Report, 1991
- [3] Reddy, K. C., Rollin, B. H., *A Local Lagrangian Method for Conservation Laws*, Developments in Theoretical and Applied Mechanics, Volume XVI, Proceedings of

- the Sixteenth Southeastern Conference on Theoretical and Applied Mechanics, eds.  
B. N. Antar, R. Engels, A. A. Prinaris, T. H. Moulden, The University of Tennessee  
Space Institute, 1992
- [4] Harten, A., Osher, S., *Uniformly High-Order Accurate Nonoscillatory Schemes*, SIAM  
Journal of Numerical Analysis, Vol. 24, No. 2, April 1987
- [5] Davis, P. J., Rabinowitz, P., *Methods of Numerical Integration*, Academic Press, New  
York, 1975
- [6] Reddy, K. C., Benek, J. A., *A Locally Implicit Scheme for 3-D Compressible Viscous  
Flows*, AIAA-90-1525, June 1990
- [7] Zucker, R. D., *Fundamentals of Gas Dynamics*, Matrix Publishers, Chesterland, OH,  
1977

ANALYSIS OF ACOUSTIC OSCILLATIONS IN CAVITIES  
WITH SPOILER ATTACHMENTS

Daniel E. Schatt  
Master of Science Candidate  
Department of Aerospace Engineering  
University of Tennessee Space Institute

Final Report for:  
Summer Research Program  
Arnold Engineering Development Center

Sponsored by:  
Air Force Office of Scientific Research  
Bolling Air Force Base, Washington, D.C.

August 1992

# ANALYSIS OF ACOUSTIC OSCILLATIONS IN CAVITIES WITH SPOILER ATTACHMENTS

Daniel E. Schatt  
Master of Science Candidate  
Department of Aerospace Engineering  
University of Tennessee Space Institute

## Abstract

An attempt was made to predict the amplitude of acoustic oscillations in cavities with various types of spoilers being used as suppression devices. A computer code was written for this purpose. The basic approach was to represent the spoiler as a thicker initial boundary layer, which would have the same effect in suppressing the acoustic oscillations. With this equivalent boundary layer, each spoiler configuration could be assigned a certain drag coefficient, which served as the primary input device for the code. The prediction was made over a wide range of Mach numbers, from subsonic to supersonic. The results of the computer code were compared with experimental data, and also with empty cavity cases (no spoiler).

# ANALYSIS OF ACOUSTIC OSCILLATIONS IN CAVITIES WITH SPOILER ATTACHMENTS

Daniel E. Schatt

## INTRODUCTION

Aeroacoustic oscillations in flow over cavities have been studied since the 1950's. Investigation of this phenomenon has great importance because cavities are encountered in a wide variety of applications. A cavity is defined as a cutout in a surface. A typical example is a weapons bay in a bomber aircraft. In my own work, this application was the primary consideration.

Essentially, the oscillations are due to excitation of the instabilities of the shear layer which develops over the cavity. Interaction of the shear layer with the leading and trailing edges creates resonance at certain frequencies, which intensifies the response of the shear layer at those frequencies. The oscillations occurring in the cavity (weapons bay) can be so intense that they cause damage to sensitive instrumentation in or on the stores. In some cases, they can even excite the main structural modes of the aircraft. Therefore, it is very important to be able to predict, at least approximately, the characteristics of the oscillations (i.e. frequency and amplitude). In my research work in the 1991 Summer Research Program, I assisted in the development of a computer code (known as the Cavity Acoustic Prediction Code, or CAP Code) that could give rough predictions of the frequency-amplitude spectrum up to Mach 1.5.

The objective of my current work was to extend to the code to different flow configurations. Frequently, suppression devices are used in an attempt to reduce the intensity of the oscillations. These suppression devices are normally spoilers which are positioned upstream, or at the leading edge, of the cavity. By interfering with the initial development of the cavity shear layer, the magnitude of the oscillations is drastically reduced. My objective was to incorporate into the existing computer code a method for predicting the magnitude of the oscillations for cases where spoilers are used. Several different types of spoilers were tested experimentally, and these results were compared with the computer code results.

## METHODOLOGY

Before discussing my work in detail, it is necessary to briefly review the fundamentals of the CAP Code. The code is based on the principle that the so-called "edgetone" frequencies, first introduced by Rossiter, largely determine the characteristics of the oscillations. These frequencies are the frequencies at which vortices are shed from the leading edge of the cavity. These vortices propagate downstream within the shear layer and interact with the trailing edge. This generates pressure pulses which travel upstream, interact with the leading edge, and generate the vortices. Thus, we have a continuous, self-sustaining feedback loop. Rossiter devised an empirical formula based on this model, to determine the edgetone frequencies:

$$f_e = \frac{V_\infty (m - \gamma)}{L \left( M_\infty \frac{a_\infty}{a_t} + \frac{1}{\phi_d} \right)}$$

where  $m = 1, 2, 3, \dots$  = the frequency mode number of the edgetone.

$\gamma, \phi_d$  = empirical parameters

$a_\infty$  = speed of sound based on freestream static temperature

$a_t$  = speed of sound based on freestream total temperature

As can be seen, the edgetone frequencies occur in integral modes, similar to harmonics. The frequencies observed in cavity oscillations occur invariably on the edgetones, with the first three or four modes dominating, and the higher modes fading into the background noise.

The basic assumption of the CAP Code, justified by experimental observation, is that when the edgetone frequencies are at or near the natural acoustic frequencies of the cavity, resonance occurs and the edgetones are greatly amplified. Frequencies away from the edgetones are damped out, with the degree of damping determined empirically. Specifically, the damping is determined by the so-called damping ratio. Each edgetone frequency, for a given case, has associated with it a damping ratio, which is expressed as a function of Mach number and damping factor. The damping factor, in turn, depends on the edgetone frequency. In order to determine the frequency-



amplitude spectrum, frequencies through the spectrum are tested at set intervals. For each frequency that is tested, the amplitude is determined using the first ten damping ratio corresponding to the first ten edgetone frequencies, and the maximum is extracted as the amplitude for that spectrum frequency. The amplitude is determined by calculating a response coefficient  $R_i$  and then multiplying by a reference pressure.

The details of this analysis can be found in last year's report. What I wish to focus on now is how the initial boundary layer thickness affects the calculated amplitudes for the various frequencies. The parameter  $\phi_d$  in Rossiter's equation was expressed empirically as:

$$\phi_d = (0.6163 + 0.0178 M_\infty) \left( 1 - e^{-\frac{0.8}{\eta_p}} \right)$$

where  $\eta_p = \sigma \frac{\delta}{L}$ , a turbulent mixing position parameter

and  $\sigma$  = the similarity parameter for turbulent mixing, after Bauer

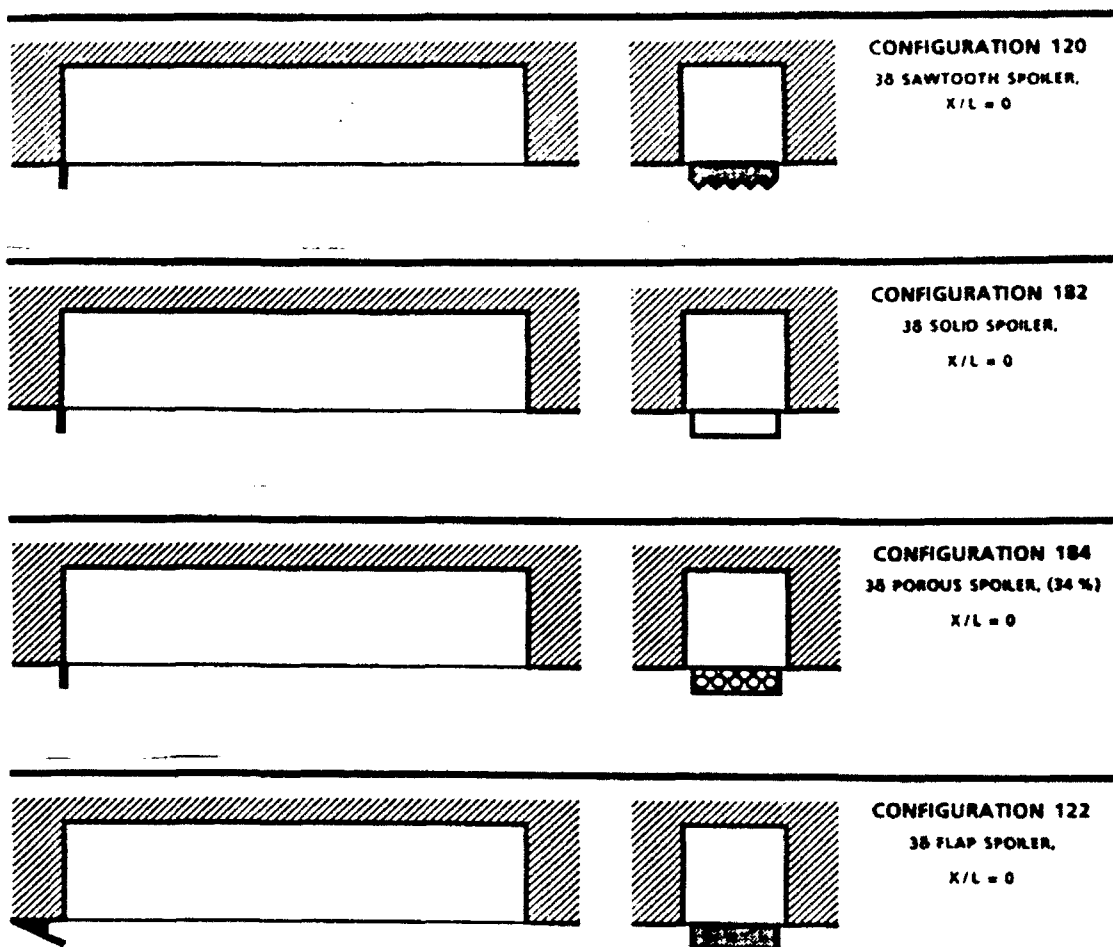
Therefore, the boundary layer thickness affects the edgetone frequencies, which in turn affects the amplitude (sound pressure level).

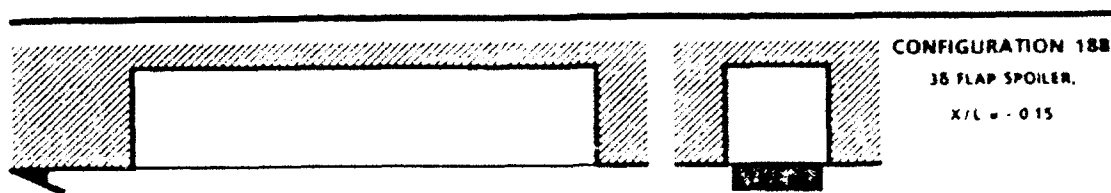
This fact was used in the analysis of the spoiler cases. First, the initial boundary layer thickness approaching the cavity is assumed to be the turbulent boundary layer thickness according to the results of Whitfield and Tucker. This thickness is a function of Mach number. These values are inputted into the CAP Code, which computes the sound pressure levels of the empty cavity case (no spoiler) for various Mach numbers. It is important to point out that here, and henceforth, we are referring to the overall sound pressure level, which is essentially a root-mean-square of all the amplitudes corresponding to all the frequencies, for a particular case. These computed sound pressure levels (SPLs) are compared with the experimental values, for each Mach number. This allowed the difference between the CAP Code and experimental values to be calculated, for each Mach number.

These empty cavity results were then used for the spoiler cases. The differences in sound pressure level, for the various Mach numbers, were subtracted from the experimental spoiler results to obtain an equivalent SPL for the CAP Code. Then, boundary layer thicknesses were

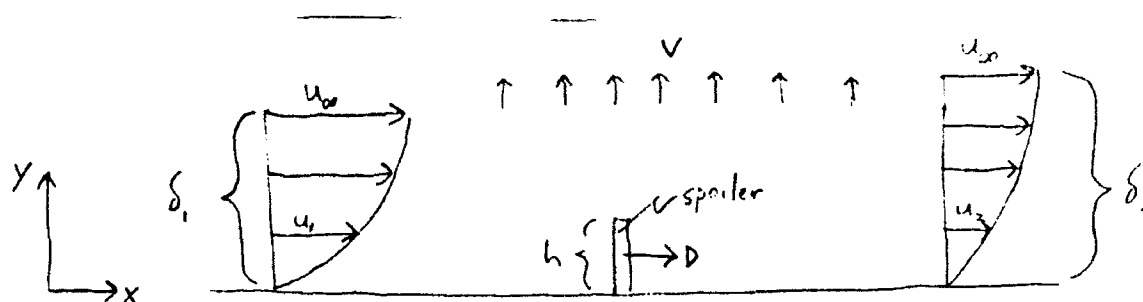
inputted in an iterative fashion until the CAP Code SPL matched this equivalent SPL. This boundary layer thickness was taken as an equivalent thickness; in other words, the spoiler can be considered to have the same effect on the SPL as a greater initial boundary layer thickness, as calculated by the CAP Code.

It is appropriate at this stage to briefly review the various spoiler types used in the analysis (and compared with experiment). Two spoilers with sawtooth edges were used: one with coarser sawtooth and one with finer sawtooth. A solid spoiler and porous spoiler were also used. Finally, a flap configuration was tried in two different streamwise positions. All of these configurations are illustrated below:





It will be seen shortly that height of the spoiler is an important parameter. All configurations have the same height, although the sawtooth spoilers and the porous spoiler used an equivalent height due to the geometry.



MOMENTUM:  $\int_0^{\delta_1} \rho u_1^2 dy + \rho_\infty u_\infty^2 (\delta_2 - \delta_1) + p_\infty \delta_2 = p_\infty \delta_2 + \frac{D}{\text{unit width}} + \int_0^{\delta_2} \rho u_2^2 dy + \rho_\infty v u_\infty \quad (2)$

Multiply (1) by  $u_\infty$ , subtract (2) :

$$u_\infty \int_0^{\delta_1} \rho u_1 dy - \int_0^{\delta_1} \rho u_1^2 dy = -\frac{D}{W} + u_\infty \int_0^{\delta_2} \rho u_2 dy - \int_0^{\delta_2} \rho u_2^2 dy$$

By definition :

$$\rho_\infty u_\infty (\delta - \delta^*) = \int_0^\delta \rho u dy$$

$$\rho_\infty u_\infty^2 (\delta - \delta^* - \theta) = \int_0^\delta \rho u^2 dy$$

where  $\delta^*$  = displacement thickness  
 $\theta$  = momentum thickness

Then :

$$\rho_\infty u_\infty^2 (\delta_1 - \delta_1^*) - \rho_\infty u_\infty^2 (\delta_1 - \delta_1^* - \theta_1) = -\frac{C_D \rho_\infty u_\infty^2}{2} \frac{A}{W} + \rho_\infty u_\infty^2 (\delta_2 - \delta_2^*) - \rho_\infty u_\infty^2 (\delta_2 - \delta_2^* - \theta)$$

Simplifying :

$$\theta_1 = -\frac{C_D h}{2} + \theta_2 \xrightarrow{\text{assume } \frac{\theta_1}{\delta_1} = \frac{\theta_2}{\delta_2}} \frac{\theta_1}{\delta_1} (\delta_2 - \delta_1) = \frac{C_D h}{2} \longrightarrow \boxed{C_D = \frac{2(\frac{\theta_1}{\delta_1})}{h} (\delta_2 - \delta_1)}$$

These drag coefficients are based on the dynamic pressure of the freestream,  $q_\infty$ , according to:

$$D = C_D q_\infty A$$

Since  $q = 0.5 \rho U^2$ , the  $q$  is obviously changing over the height of the spoiler. In order to calculate a more accurate  $C_D$ , it is necessary to correlate it to an average  $q$  ( $\bar{q}$ ) over the height of the spoiler. Once  $\bar{q}$  is known, the new adjusted  $C_D$  can be determined because drag remains constant and, therefore, the product  $C_D q$  remains constant. Thus:

$$(C_D)_1 q_\infty = (C_D)_2 \bar{q} \longrightarrow (C_D)_2 = (C_D)_1 \frac{q_\infty}{\bar{q}}$$

The difficulty arises in calculating an average  $q$ . This was accomplished by integrating  $q = 0.5 \rho U^2$  over the height of the spoiler using a typical 1/7 power turbulent boundary layer profile, and dividing by the spoiler height. This procedure resulted in an analytical expression for the ratio of  $\bar{q}$  to  $q_\infty$ . In turn, these results were used to adjust the drag coefficients for all the cases computed previously. The derivation, carried out with the help of Blair Rollin, another Summer Program participant, is shown below:

$$\left\{ q = \frac{1}{2} \rho u^2 \longrightarrow \text{find } \int_0^{\delta} \rho u^2 dy \right\}$$

$$c_p T + \frac{1}{2} u^2 = c_p T_0$$

$$T = T_0 - \frac{u^2}{2 c_p}$$

$$\rho = \frac{p}{RT} = \frac{p}{R(T_0 - \frac{u^2}{2 c_p})} = \frac{2 c_p p}{R(2 c_p T_0 - u^2)}$$

for turbulent boundary layer:  $\frac{u}{u_1} = \left( \frac{y}{\delta} \right)^{1/7}$

$$\left( \frac{u}{u_1} \right)^7 = \frac{y}{\delta}$$

$$y = \delta \left( \frac{u}{u_1} \right)^7 = \frac{\delta}{u_1^7} u^7$$

$$dy = \frac{7\delta}{u_1^7} u^6 du$$

in limits: as  $y(0 \rightarrow \delta) \Rightarrow u(0 \rightarrow u_1)$

$$\text{so: } \int_0^{\delta} \rho u^2 dy = \int_0^{u_1} \frac{2 c_p p}{R(2 c_p T_0 - u^2)} u^2 \frac{7\delta}{u_1^7} u^6 du = \frac{14 \delta p c_p}{u_1^7 R} \int_0^{u_1} \frac{u^8}{2 c_p T_0 - u^2} du$$

$$\text{solve } \int_0^{u_1} \frac{x^5}{c-x^2} dx = - \int_1^{\frac{u_1}{\sqrt{c}}} \frac{u^5}{x^2-c} dx$$

$$\begin{array}{r} x^6 + 0 + cx^4 + c^2x^2 + c^3 \\ x^2-c \overline{) x^6 + 0x^5 + 0x^4 + 0x^3 + 0x^2 + 0x + 0} \\ \underline{-(x^6 - cx^4)} \phantom{+ 0x^3 + 0x^2 + 0x + 0} \\ cx^4 + 0x^3 + 0x^2 + 0x + 0 \\ \underline{-(cx^4 - c^3x^2)} \phantom{+ 0x + 0} \\ c^3x^2 + 0x + 0 \\ \underline{-(c^3x^2 - c^5)} \phantom{+ 0} \\ c^5 + 0 - cx^6 \\ \underline{-(cx^6 - c^4x^4)} \phantom{+ 0} \\ c^4x^4 + 0x^3 + 0x^2 + 0x + 0 \\ \underline{-(c^4x^4 - c^6x^2)} \phantom{+ 0} \\ c^6x^2 + 0x + 0 \\ \underline{-(c^6x^2 - c^8)} \phantom{+ 0} \\ c^8 \end{array}$$

$$\text{then } \frac{x^5}{x^2-c} = x^6 + cx^4 + c^2x^2 + c^3 + \frac{c^4}{x^2-c}$$

$$- \int_0^{u_1} \frac{x^5}{x^2-c} dx = - \left[ \int_0^{u_1} (x^6 + cx^4 + c^2x^2 + c^3) dx + \int_0^{u_1} \frac{c^4}{x^2-c} dx \right]$$

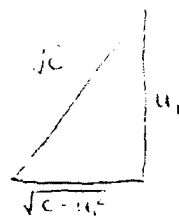
$$\text{set } y = \frac{x}{\sqrt{c}}, dy = \frac{1}{\sqrt{c}} dx : = - \int_0^{u_1/\sqrt{c}} (x^6 + cx^4 + c^2x^2 + c^3) dx - \frac{c^4}{c} \int_0^{u_1/\sqrt{c}} \frac{1}{y^2-1} \sqrt{c} dy$$

$$- \int_0^{u_1} \frac{x^5}{x^2-c} dx = - \int_0^{u_1} (x^6 + cx^4 + c^2x^2 + c^3) dx + c^{7/2} \int_0^{u_1/\sqrt{c}} \frac{1}{1-y^2} dy$$

$$\begin{aligned} \text{let } y = \sin v : \quad - \int_0^{u_1} \frac{x^5}{x^2-c} dx &= - \int_0^{u_1} (x^6 + cx^4 + c^2x^2 + c^3) dx + c^{7/2} \int_0^{\sin^{-1}(\frac{u_1}{\sqrt{c}})} \frac{\cos v}{\cos^2 v} dv \\ &= \quad \quad \quad + c^{7/2} \int_0^{\sin^{-1}(\frac{u_1}{\sqrt{c}})} \sec v dv \\ &= \quad \quad \quad + c^{7/2} \ln |\sec v + \tan v|_0^{\sin^{-1}(\frac{u_1}{\sqrt{c}})} \end{aligned}$$

$$\text{Evaluate } c^{7/2} \ln |\sec v + \tan v|_0^{\sin^{-1}(\frac{u_1}{\sqrt{c}})} :$$

$$c^{7/2} \ln |\sec v + \tan v|_0^{\sin^{-1}(\frac{u_1}{\sqrt{c}})} = c^{7/2} \ln \left[ \sec \left\{ \sin^{-1} \left( \frac{u_1}{\sqrt{c}} \right) \right\} + \tan \left\{ \sin^{-1} \left( \frac{u_1}{\sqrt{c}} \right) \right\} \right]$$



$$\theta = \sin^{-1}\left(\frac{u_1}{\sqrt{c}}\right)$$

$$\sec \theta = \frac{\sqrt{c}}{\sqrt{c - u_1^2}} = \sqrt{\frac{c}{c - u_1^2}}$$

$$\tan \theta = \frac{u_1}{\sqrt{c - u_1^2}}$$

$$\text{then } c^{7/2} \ln|\sec \theta + \tan \theta| \Big|_{\sin^{-1}\left(\frac{u_1}{\sqrt{c}}\right)} = c^{7/2} \ln \left[ \frac{\sqrt{c} + u_1}{\sqrt{c - u_1^2}} \right]$$

$$\text{Therefore } - \int_0^{u_1} \frac{x^5}{x^2 - c} = - \left[ \frac{x^7}{7} + \frac{cx^5}{5} + \frac{c^2x^3}{3} + c^3x \right]_0^{u_1} + c^{7/2} \ln \left[ \frac{\sqrt{c} + u_1}{\sqrt{c - u_1^2}} \right]$$

$$\text{Recall: } \int_0^s f u^2 dy = \frac{148 p c_p}{R u_1^7} \int_0^{u_1} \frac{u^5}{2 c_p T_0 - u^2} du$$

$$\begin{aligned} \frac{148 p c_p}{R u_1^7} \int_0^{u_1} \frac{u^5}{2 c_p T_0 - u^2} du &= \frac{148 p c_p}{R u_1^7} \left\{ - \left[ \frac{u^7}{7} + \frac{2 c_p T_0 u^5}{5} + \frac{4 c_p^2 T_0^2 u^3}{3} + 8 c_p^3 T_0^3 u \right] \right. \\ &\quad \left. + (2 c_p T_0)^{7/2} \ln \left| \frac{\sqrt{2 c_p T_0} + u}{\sqrt{2 c_p T_0 - u^2}} \right| \right\} \\ &= \frac{148 p c_p}{u_1^7 R} \left\{ (2 c_p T_0)^{7/2} \ln \left[ \frac{\sqrt{2 c_p T_0} + u_1}{\sqrt{2 c_p T_0 - u_1^2}} \right] - \frac{u_1^7}{7} - \frac{2 c_p T_0 u_1^5}{5} \right. \\ &\quad \left. - \frac{4 c_p^2 T_0^2 u_1^3}{3} - 8 c_p^3 T_0^3 u_1 \right\} \end{aligned}$$

$$q_\infty = \frac{\rho M^2}{2} \rightarrow p = \frac{2 q_\infty}{\rho M_\infty^2}$$

substitute for  $p$  in previous result and divide by  $2h$ .

$$\bar{q} = \frac{1}{2h} \int_0^s f u^2 dy,$$

assume  $\delta = h$  (height of spoiler):

$$\bar{q} = q_{\infty} \left\{ \frac{14 c_p}{\gamma M_{\infty}^2 u_{\infty}^2 R} \left[ (2 c_p T_{\infty})^{7/2} \ln \left( \frac{\sqrt{2 c_p T_{\infty}} + u_{\infty}}{\sqrt{2 c_p T_{\infty}} - u_{\infty}} \right) - \frac{u_{\infty}^2}{\gamma} - \frac{c_p T_{\infty}}{\gamma} \right] \right.$$

$$\left. - \frac{4 c_p^2 T_{\infty}^2 u_{\infty}^2}{3} - 8 c_p^2 T_{\infty}^2 \right\}$$

use Crocco number:  $C_r^2 = \frac{u_{\infty}^2}{2 c_p T_{\infty}}, \quad \frac{c_p}{R} = \frac{\gamma}{\gamma-1}$

$$\boxed{\bar{q} = q_{\infty} \left\{ \frac{14}{(\gamma-1) M_{\infty}^2} \left[ \frac{1}{C_r^2} \ln \left\{ \frac{\frac{1}{C_r^2} + 1}{\sqrt{\frac{1}{C_r^2} - 1}} \right\} - \frac{1}{\gamma} - \frac{1}{5 C_r^2} - \frac{1}{3 C_r^2} - \frac{1}{C_r^2} \right] \right\}}$$

To my knowledge, this is the first time an analytical solution has been presented for the total momentum in a turbulent boundary layer. In order to verify this analytic solution, the results were compared to the results obtained from the following derivation by Bob Bauer:

$$\text{For } h \geq \delta: \quad \bar{q} = \frac{1}{2h} \int_0^{\delta} \rho u^2 dy + \frac{1}{2h} \rho_{\infty} u_{\infty}^2 (h - \delta)$$

$$\rho_{\infty} u_{\infty}^2 (\delta - \delta^* - \theta) = \int_0^{\delta} \rho u^2 dy$$

$$\text{Substituting: } \bar{q} = \frac{\rho_{\infty} u_{\infty}^2}{2h} (\delta - \delta^* - \theta + h - \delta)$$

$$\bar{q} = q_{\infty} \left( \frac{h - \delta^* - \theta}{h} \right)$$

$$\bar{q} = q_{\infty} \left[ \frac{\frac{h}{\delta} - \frac{\delta^*}{\delta} - \frac{\theta}{\delta}}{\frac{h}{\delta}} \right]$$

$$\text{if } \frac{h}{\delta} = 1: \quad \boxed{\bar{q} = q_{\infty} \left( 1 - \frac{\delta^*}{\delta} - \frac{\theta}{\delta} \right)}$$

The parameters  $\frac{\delta^*}{\delta}, \frac{\theta}{\delta}$  can be found in standard tables for various  $1/n$  power profiles.

An example comparing results of the two methods is shown below:



$$C_p = 2000 \frac{\text{BTU}}{\text{lb} \cdot ^\circ\text{F}}$$

$$\delta = 1.4$$

$$M_\infty = 2$$

$$T_0 = 400^\circ\text{R} \rightarrow T = 222^\circ\text{R}$$

$$R = 1715$$

$$\mu = 1460.897 \frac{\text{lb}}{\text{s}}$$

$$1) \quad \bar{q} = q_\infty \left\{ \frac{14}{(r-1)M_\infty^2} \left[ \frac{1}{C_r^7} \ln \left\{ \frac{\frac{1}{C_r} + 1}{\sqrt{\frac{1}{C_r^2} - 1}} \right\} - \frac{1}{7} - \frac{1}{5C_r^2} - \frac{1}{3C_r^4} - \frac{1}{C_r^6} \right] \right\}$$

$$\text{Substituting: } \bar{q} = q_\infty \left\{ 97.222 \left[ 3373.7236 - \frac{1}{7} - 2.17664 - 23.7406 - 3240.7703 \right] \right\}$$

$$\boxed{\bar{q} = 0.6864 q_\infty}$$

$$2) \quad \bar{q} = q_\infty \left( 1 - \frac{\delta^*}{\delta} - \frac{\theta}{\delta} \right)$$

Look in tables for  $M=2.0$ ,  $\frac{1}{7}$  power profile

$$\frac{\delta^*}{\delta} = 0.23636$$

$$\frac{\theta}{\delta} = 0.07714$$

$$\bar{q} = q_\infty (1 - 0.23636 - 0.07714)$$

$$\boxed{\bar{q} = 0.6862 q_\infty}$$

This approach was integrated into the CAP Code. For each case, a  $C_D$  is inputted using the previous results as a guide ( $C_D$  based on  $q_\infty$ ). In addition, the turbulent boundary layer thickness

and the height of the spoiler are inputted. The sawtooth spoilers and the porous spoilers are given equivalent heights (total area divided by width). Then, an equivalent downstream boundary layer thickness is calculated. This formula was derived in the following manner:

$$\text{From previous derivation: } C_D = \frac{2 \left( \frac{h}{S_1} \right)}{1} (S_2 - S_1)$$

$$S_2 = \frac{C_D h}{2 \left( \frac{h}{S_1} \right)} + S_1$$

$$\text{But: } \frac{\bar{q}}{q_\infty} = \left( 1 - \frac{\delta^*}{S} - \frac{\delta}{S} \right)$$

$$\text{Then } \frac{\delta}{S} = 1 - \frac{\bar{q}}{q_\infty} - \frac{\delta^*}{S}$$

$$\text{Substitute: } S_2 = \frac{C_D h}{2 \left( 1 - \frac{\bar{q}}{q_\infty} - \frac{\delta^*}{S} \right)} + S_1$$

Multiply  $C_D$  by correction factor:

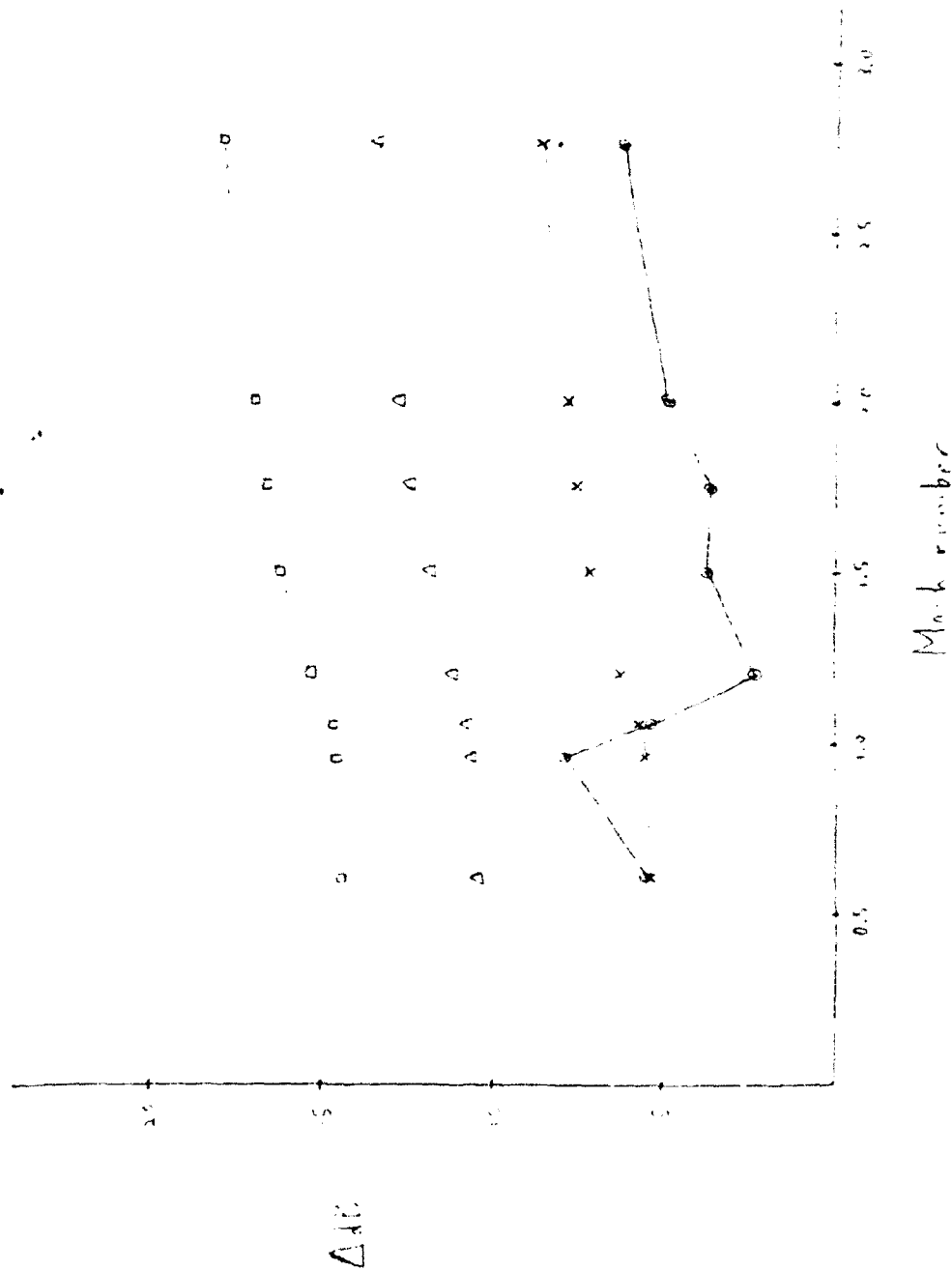
$$S_2 = \frac{C_D h \cdot \frac{\bar{q}}{q_\infty}}{2 \left( 1 - \frac{\bar{q}}{q_\infty} - \frac{\delta^*}{S} \right)} + S_1$$

As can be seen, the  $C_D$  is adjusted according to the aforementioned correction. Using this boundary layer thickness, the CAP Code goes on to calculate the overall SPL.

These results are, of course, highly dependent on the inputted  $C_D$ . It was decided that the difference in sound pressure level between the empty cavity case and the spoiler case, rather than the absolute sound pressure level, was of primary concern. Therefore, the change in sound pressure level was plotted as a function of Mach number. This was done for both the experimental and CAP Code cases. For each spoiler type, the CAP Code results were calculated for several different drag coefficient values. The plots are shown on the following pages.

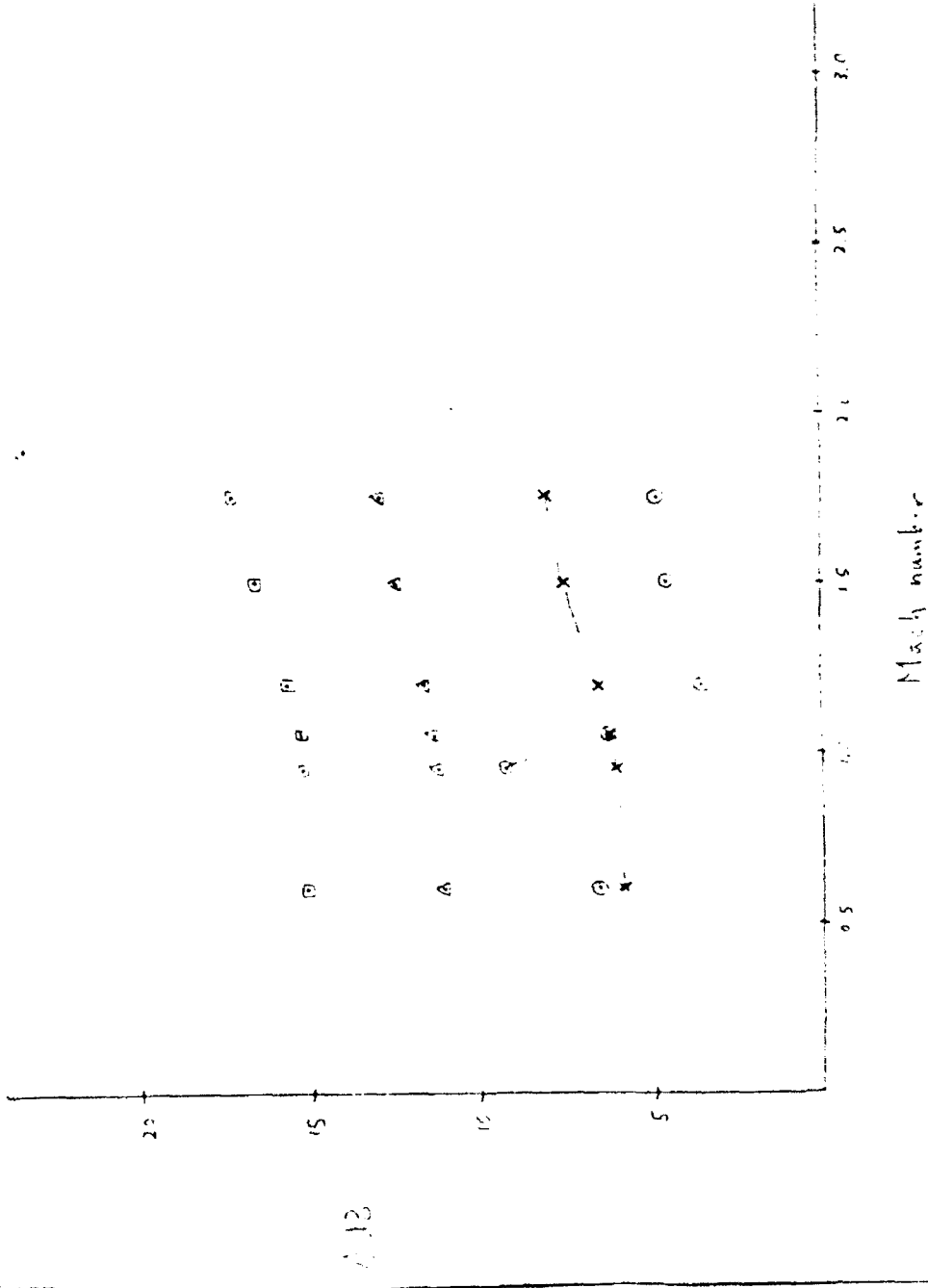
# FINE SAWTOOTH

$C_A = C_{2L}$   
 $C_3 = 1.0$   
 $C_2 = 0.5$   
 $C_1 = 0.2$

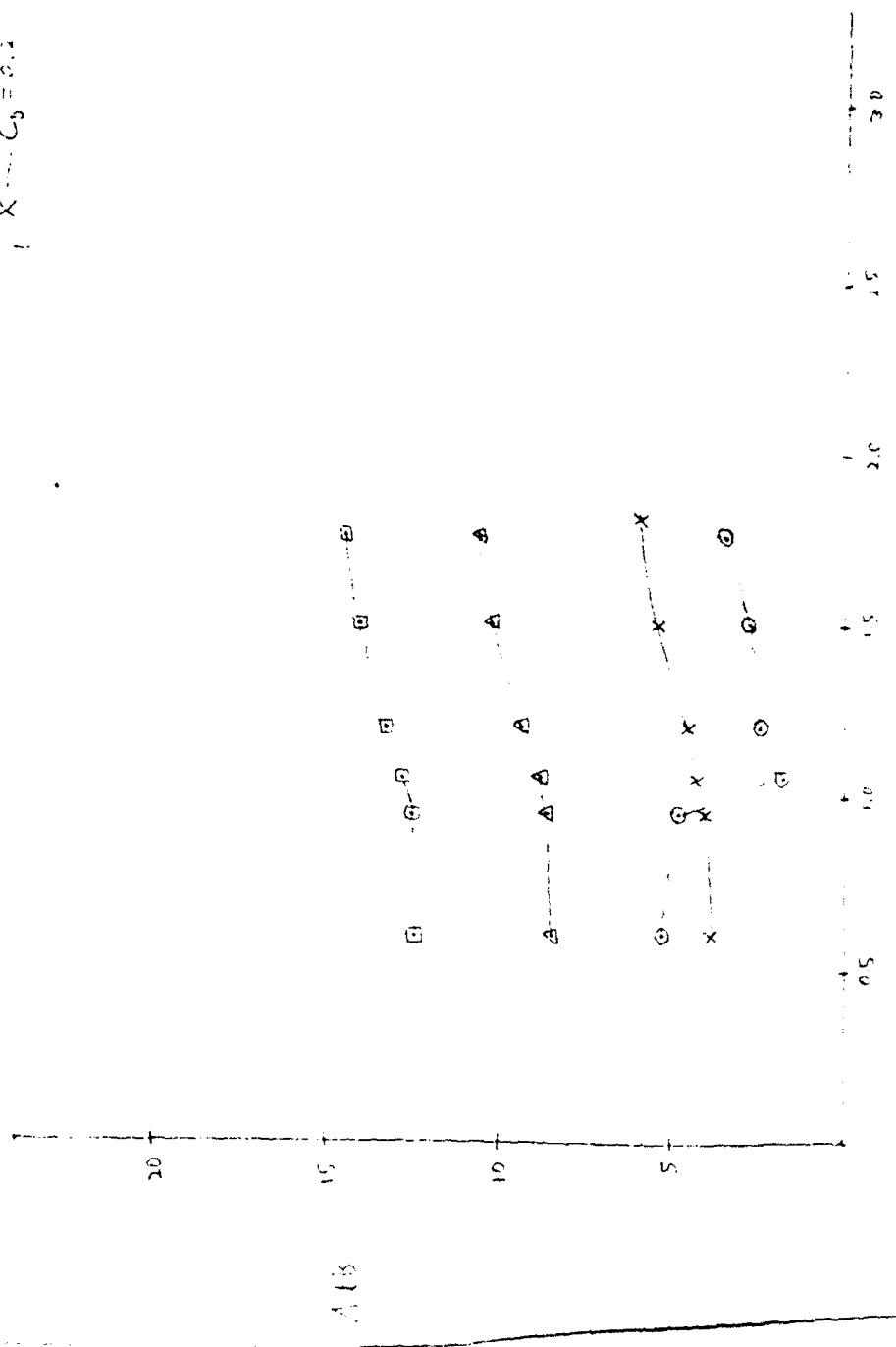


# SOLID

O — experimental  
 □ —  $C_L = 1.0$   
 Δ —  $C_D = 0.5$   
 X —  $C_D = 0.2$

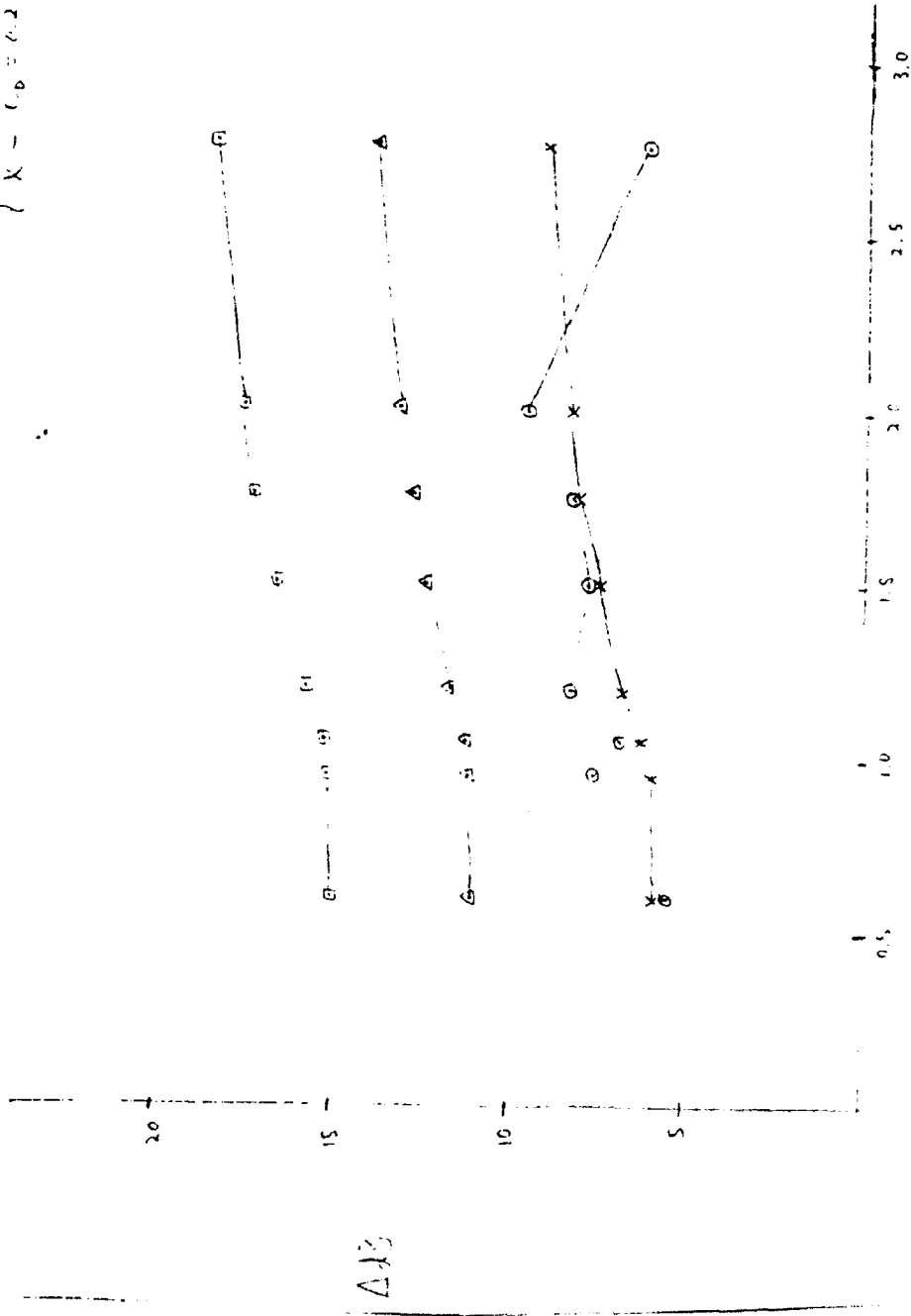


# POROUS (34%)



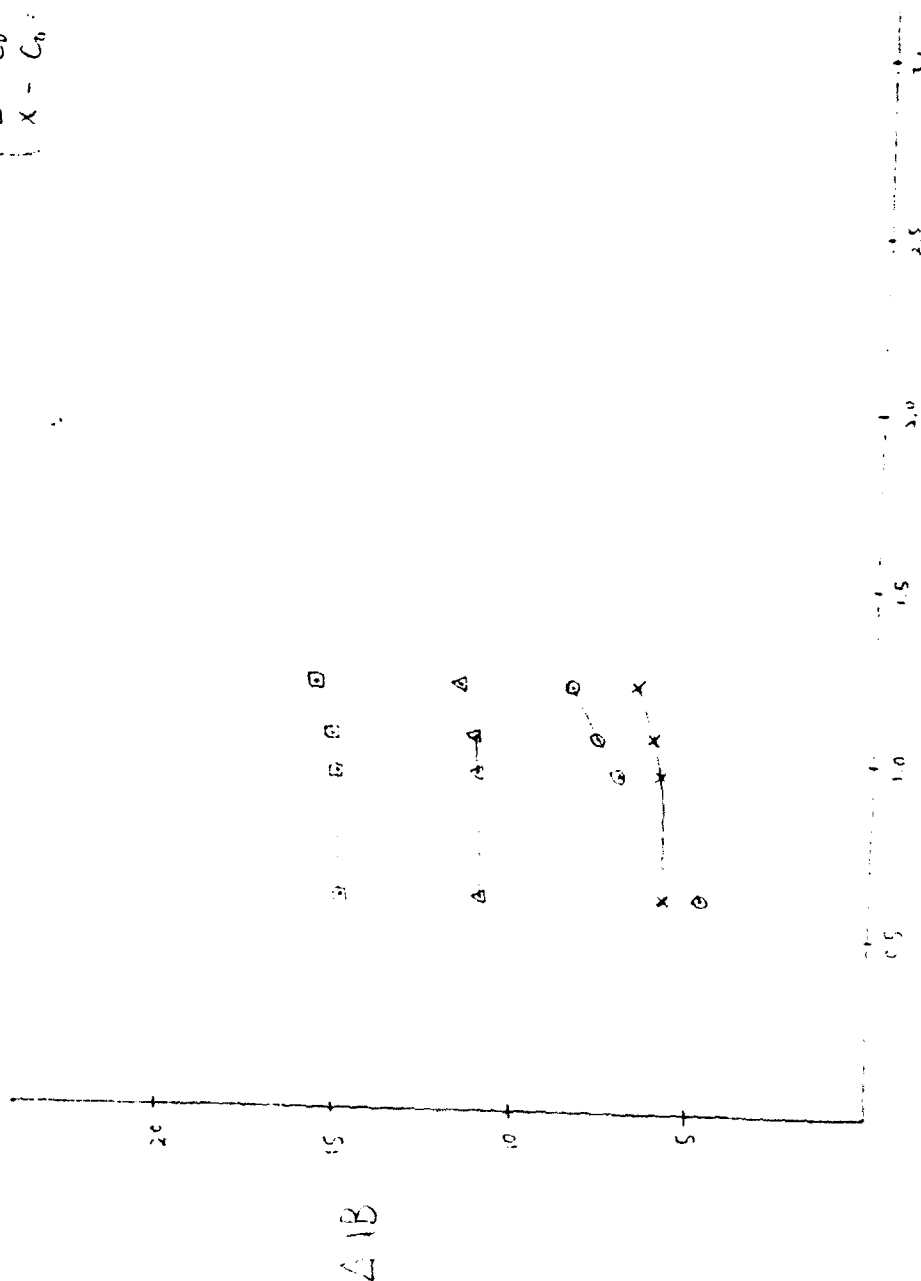
# FLAP

O -  $\sigma_{\text{eff}}$   $\sigma_{\text{eff}} = 1.0$   
 $C_{AP}$   $C_{10}$   $C_{10} = 1.0$   
 $\Delta$  -  $C_{10} = 0.5$   
 $\times$  -  $C_{10} = 0.2$



# FORWARD FLAP

$\square$  - experimental  
 $\square$  -  $C_D = 1.0$   
 $\Delta$  -  $C_D = 0.5$   
 $\times$  -  $C_D = 0.2$



## CONCLUSIONS

The following conclusions can be drawn:

- 1) From the preceding plots, it can be seen that the freestream  $C_D$  which is inputted should be higher than 0.2 for lower Mach numbers and lower than 0.2 for higher Mach numbers.
- 2) The suppression effectiveness is clearly a strong function of Mach number, and therefore the equivalent drag coefficient must change with Mach number.
- 3) With a sufficient experimental data base, the correct  $C_{Ds}$  to input could be estimated more precisely.



# **Numerical Modelling of Mixing and Reacting Flowfields**

**Paul Vitt  
Graduate Student  
Department of Mechanical and Aerospace Engineering and  
Engineering Mechanics**

**University of Missouri -- Rolla  
Rolla, MO 65401**

**Final Report For:  
Summer Research Program  
Arnold Engineering and Development Center**

**Sponsored By:  
Air Force Office of Scientific Research  
Bolling Air Force Base, Washington D.C.**

**August, 1992**

## Numerical Modelling of Mixing and Reacting Flowfields

Paul Vitt  
Graduate Student  
Department of Mechanical and Aerospace Engineering and Engineering Mechanics  
University of Missouri -- Rolla

### Abstract

The computational fluid dynamics (CFD) modelling of complex mixing and reacting flowfields is the goal of the current research. The mixing and reacting modelling has been broken up into several parts to evaluate their individual contributions to the solution. This fits into the general framework of evaluating the computational code GASP for engineering design purposes. The first part of the study involves qualitatively evaluating the effect of turbulence on chemical kinetics within the numerical modelling. A brief look at the effects of turbulent Schmidt number is also presented. The selection of an appropriate chemistry kinetics model is very important for flowfields where capturing the flame and ignition point are important, as is shown through a comparison of shock-induced combustion numerical experiments. The code is also used to predict the flowfield of premixed hydrogen air burner, which involves subsonic flow over a back step with an ignition torch. This case is to provide a comparison with another code which is modelling the same problem. The mixing part of the physics modelling is addressed through two low angle wall jet injectors, in which the GASP predictions were compared with experimental and other CFD results. The main conclusion from this part of the research is that the accuracy of the numerical simulation in GASP needs to be improved before more complex flowfields can be modelled with confidence. The chemistry turbulence interaction needs further attention, as does the selection of an efficient, accurate chemistry model. Finally, the turbulent diffusion model needs to be tuned before the modelling of swept ramp scramjet injectors (the final part of this research) is undertaken.

## 1. INTRODUCTION

The development of computational fluid dynamics (CFD) as a reliable tool for engineering analysis of aerodynamic and propulsive flowfields requires that the codes be validated against known physical results, i.e. experimental data. While the aerodynamic part of CFD modelling is fairly well represented, the modelling of propulsive flowfields (mixing and reacting) is still an area of uncertainty. To address this problem with regard to a single code, the General Aerodynamic Simulation Program, or GASP, several test cases have been developed. The final goal of the research is to determine if the code accurately models reacting flowfields well enough to be used as an analysis tool for designing the National Aerospace Plane (NASP) combustor. The design of the combustor is very important: with flight Mach numbers of 8 to 20, a supersonic combustor ramjet (scramjet) engine is a likely candidate. This engine is airframe integrated so that the forebody of the aircraft provides compression, as well as the cowl and injector struts. In order to minimize total pressure losses the combustion occurs supersonically (this also avoids the high static temperatures that would be associated with reducing the flow to subsonic conditions for combustion). The flow velocity varies only a few percent through the engine [1], but it is the high mass flow rate that allows only slight changes in velocity to generate thrust. Another consideration is that the combustor length must be minimized: 1. to minimize the extreme frictional losses at high flight Mach number velocities, and 2. to reduce structural weight and cooling requirements. All of these conditions lead to the fact that there is only a very short flow residence time in the combustor (on the order of milliseconds): hence mixing and combusting the fuel<sup>1</sup> quickly is a necessity. Since current ground facilities are limited in their range of hypersonic applicability, CFD modelling is important in the design of the combustor for the NASP.

This brings the discussion back to the reliability and accuracy of computational models. The test cases that have been analyzed in this research involve both mixing and reacting, for numerical experimentation as well as comparison with data. The first case examines the effect of turbulence modelling on reaction. A 10 degree compression ramp/expansion is used for this numerical experiment. The second test case looks at the Burrows and Kurkov test case, and the effect of turbulent Schmidt<sup>2</sup> number on the modelling of that problem. The third case looks at the computations of shock-induced combustion over a 10 degree compression ramp for different chemistry models. A fourth test case looks at subsonic combustion of premixed hydrogen. The fifth case looks at supersonic low angle helium injection into hypersonic flow, with the goal of validating the mixing predicted by GASP.

### *1.1 Mathematical Background*

GASP is an implicit solver of the finite-volume form of the Navier-Stokes equations. Approximate factorization routines solve either full Navier-Stokes (FNS) or the parabolized Navier-Stokes (PNS) form for space marching through largely supersonic domains. The chemistry is based on empirical

---

<sup>1</sup>probably hydrogen, because of its high specific impulse (low molecular weight)

<sup>2</sup>Sc(turb) controls turbulent mass diffusion

Arrhenius rates, with the properties supplied from the JANNAF (Gordon-McBride) curve fits. Turbulence is supplied from the Baldwin-Lomax algebraic model, [3], or from any of three two-equation models. The chemistry models chosen for study here are outlined in the Appendix in terms of species and reactions. Due to space limitations, for further numerical discussion of GASP, the reader is referred to Ref. [2] for the complete system details.

## 2. DISCUSSION OF RESULTS

### 2.1 Effect of Turbulence on Chemical Reactions

Turbulence-chemistry interactions are very important, since turbulence can control chemistry through mass diffusion, and chemistry should influence turbulence through flowfield gradients. In order to model complex problems, it is necessary to make the calculations with as few variables (equations) as possible, in order to minimize computational requirements. This numerical experiment is to determine whether the simpler Baldwin-Lomax algebraic turbulence model can interact with a chemistry model in a similar fashion to the 2-equation  $k-\epsilon$  model, and try to qualify the effect of turbulence modelling on chemical kinetics. The problem is a  $10^\circ$  ramp compression-expansion, with the inflow premixed stoichiometric hydrogen-air. The conditions at the inflow are shown in table 1.

Mach No.	T (K)	$T_{\text{wall}}$ (K)	$\rho$ (kg/m <sup>3</sup> )
6.0	1573.0	2000.0	0.0386

Table 1: Inflow conditions for reacting ramp-expansion problem

These conditions provided for shock-induced reaction. The results are summarized in the sketch presented in Figure 1. The locations of the maximum gradient in  $\text{H}_2\text{O}$  mass fractions are drawn on the flowfield geometry. All three cases used Drummond chemistry, as described in the Appendix. The first case used Baldwin-Lomax algebraic turbulence (which is very efficient computationally), the second and third used Chien's model low Reynolds number  $k-\epsilon$  turbulence (both cases add two new partial differential transport equations to the set which must be solved, Ref. [4]). The difference between the second and third cases is the amount of free-stream turbulence: the second case had  $0.02U_{\text{inflow}}$ , and case 3 had  $0.002U_{\text{inflow}}$ . The results are reflected in the flame speed (the location where reaction begins, which was taken here to be the maximum gradient in water mass fraction). The flame speed is driven by the mass diffusion rate, which is controlled by the turbulent viscosity through the Schmidt number. The flame would initiate at the high temperature wall and propagate out into the flow at the mass diffusion rate (of OH, the progenitor of  $\text{H}_2\text{O}$ ) until the temperature falls and reduces the reaction rates, halting the production of OH. The algebraic turbulence underpredicted the flame speed, as can be seen by the flame front being closer to the lower wall. In this case the flame was limited by the mass diffusion rate of OH. The high freestream turbulence case (2.0% case) had a flame speed that was faster than the flow velocity, and was limited only by the ignition source which was the shock wave. The third (low intensity: 0.2%)

case showed a flame speed that was located about half way between the first two cases, again being limited by the mass diffusion rate of OH. It can be seen that the freestream turbulence has a large influence on chemistry, and is a modelling problem for CFD simulations currently. The question is: how much freestream turbulence is there? Possibly, to improve the validity of the algebraic solution, if the amount of freestream turbulence is known, a constant  $\mu_t$  should be imposed on the flowfield, simulating the freestream turbulence of the  $k-\epsilon$  model.

## 2.2 Influence of Turbulent Schmidt Number

In order to qualify the effect of turbulent Schmidt number, which relates the turbulent momentum diffusion rate to the mass diffusion rate, the Burrows and Kurkov supersonic tangential  $H_2$  injection case was modelled (Figure 2a,b, [5]). This case was chosen because there was good experimental data on the chemistry compositions at the final plane, and it had been previously modelled with GASP, [2]. The case was first modelled with a turbulent Schmidt number of 0.7, which was the same as the published results, and came up with an identical solution (Figure 2c, square point).  $Sc_t$  was then changed to 0.5, and the case was rerun. The increased mass diffusion rate moved the flame front out slightly, but not enough to match the data. The reason for the flame front being closer to the wall than the experiment is that the incoming thick boundary layer is not modelled, and modelling this should increase the penetration of the mixing layer and flame front. The numerical experiment did qualify the amount of effect that the  $Sc_t$  has on the kinetics.

## 2.3 Influence of Modelling on Chemical Kinetics

The next stage in the investigation is the effect of the chemistry model on the results. Again, in terms of reducing the computational requirement, it is desired to use the least number of chemical species to capture the physics. The four chemistry models (detailed in the Appendix) are denoted by:

Chemistry Model	Number of Chemical Species	Number of Chemical Reactions
1. Drummond	7	7
2. Evans & Schexnayder 1	7	8
3. Evans & Schexnayder 2	12	25
4. NASP 4 ( $H_2/NO_x$ extension)	12	24

Table 2: Denotation of chemistry models

The problem is a  $10^\circ$  degree compression ramp<sup>3</sup>, with the inflow conditions shown in table 3.

Mach No.	T (K)	$T_{wall}$ (K)	P (Pa)	$\rho$ (kg/m <sup>3</sup> )	U (m/s)
6.0	1273.0	2000.0	19600.0	0.0386	4934.7

Table 3: Inflow conditions for the reacting ramp problem

<sup>3</sup>similar to the first part of section 2.1

These conditions were selected to produce shock-ignition of the premixed stoichiometric  $H_2$ -Air mixture. The chemistry models had a larger variation in the results than was expected or desired (Figures 3, 4, 5). The shock locations (as representative of the flowfield kinematics) are shown in Figure 3, a.-d. The Drummond chemistry model caused the shock location to be located further up the ramp but the other three cases were in good agreement for shock location. Figure 4 shows water mass fraction contours (representing the finite rate chemistry kinematics) for the different chemistry models. This is where the greatest disparity is shown between the models: the flame speed must be strongly influenced by the inclusion of the intermediary species in the larger models. This case is very close to the ignition point of the stoichiometric mixture, and the smaller models (7 species) are overpredicting the ignition delay in the flowfield. Line plots of the flowfield kinematics are shown in Figure 5 a. (velocity profiles) and b. (pressure profiles) at the end of the domain, which was intended to capture a cross-section of the flame front in the shock wave. OH mass fraction profiles (Figure 5c) and water mass fraction profiles (Figure 5d) at the same location portray the chemical kinetics. The models all have similar velocity profiles across the reacting shock layer (Figure 5a), indicating that the momentum physics is at least common to all of the models. The differing shock locations can be seen clearly in the pressure spikes (Figure 5b), with the last three models all showing a similar location. It is of note that the first Evans & Schexnayder model (7 species) predicts a shock location and strength that is halfway between the two larger (12 species) models. In terms of the chemical kinetics, the Evans & Schexnayder models predicted more reaction (more OH and  $H_2O$  production). The Drummond model and the NASP 4 model were in good agreement in terms of the amount of reaction that was present. The major difference between the models is the ignition delay, which is evidenced by the larger models by the reaction (OH and  $H_2O$ ) extending all of the way across the domain, whereas the 7 species models were limited by the shock location. One possibility for this discrepancy is the reactions rates, but the Evans & Schexnayder models use the same reaction rates for the basic 8 reactions in the 7 species model. Another interesting point is that the OH contours (not shown here) do not show a dramatic increase in  $\alpha_{OH}$  at the start of reaction -- note in Figure 4 c.-d. that the increasing water contours in the freestream are spread out axially<sup>4</sup>. This is indicative of there being only a weak flame front in this case. The presence of some of the intermediary species opening up new reactionary pathways (with perhaps lower activation energies) for OH and  $H_2O$  production in the 12 species models might be the cause of the increased reaction before the shock. The conclusion that can be drawn from this experiment is that the lower order models do not pick up the ignition delay well in comparison to 12 species model results, but from the compositions after the reaction, the 7 species models do calculate a correct equilibrium point.

---

<sup>4</sup>another note of interest for the kinetics is that the water mass fraction goes down inside the shock, as some of the water is turned back into OH, and then returns to its freestream equilibrium value after the shock.

#### *2.4 The Hydrogen-Torch Problem*

Another test case for the chemical reactions in GASP was designed around a hydrogen torch. The torch was an ignition source placed at the base of an axisymmetric backstep, and was to be used to light a premixed fuel-air mix. The problem was broken into three parts: 1. the air-only flowfield was established, 2. the hydrogen-air torch at the base of the backstep was established, and 3. the inflow was changed to a stoichiometric hydrogen-air mixture. Results for the second stage are shown in Figure 6a.-b. Temperature contours (a) show the limited influence of the torch (the torch exit was about 1/4 of the backstep, and the velocity vectors plot (b) shows why: the torch is buried at the bottom of the recirculation zone after the step, and the back flow is enough to confine the torch to the area adjacent to the step. Figure 7a.-c. shows the results after ignition of the premixed hydrogen-air inflow. The velocity vector/streamline plot (7a.) shows that most of the inflow is directed out through the unconfined top boundary. This is the expected result: earlier cases with the top boundary as a fixed wall thermally choked the flow at the inflow. Figure 7b. and 7c. show water mass fractions and temperature contours to be increasing at about the same location. The ignition has spread from the torch upwards towards the unconfined boundary. From the streamlines, only about 25% of the inflow actually proceeds into the combustion region shown in the plots: the rest is pushed out of the top of the domain by the pressure rise due to reaction. This result agrees with the expected physics for this problem, and is demonstrative of the ability of GASP to model these problems.

#### *2.5 Supersonic Helium Injection into a Supersonic Stream (Mixing Problem)*

Having addressed, qualitatively, the reacting flowfield, the other part of the computational model is correctly predicting the mixing. Mixing is driven by the modelling of the turbulence in two ways: 1. directly through mass diffusion and the Schmidt number, and 2. indirectly through the dissipation of any large structures in the flowfield, which induce large scale mixing through warping of the interface. In order to evaluate GASP, and its ability to predict flowfield mixing, a case with supersonic helium injection into a Mach 6 flowfield was chosen. This problem was selected due to the available experimental data, and the flowfield should approximate the conditions in a scramjet combustor. The helium was injected through a flush wall port at an angle of  $15^\circ$  to the plate. The computational model was initially broken up into three domains: 1. a flat plate entry length, 2. a nearfield injection region, and 3. the farfield mixing region. Experimental data is from Ref. [6], and GASP has previously modelled the problem in Ref. [7]. The earlier GASP results were not as accurate as they should be to confidently undertake more complex flowfield modelling, so this test program was undertaken to see if the accuracy could be improved.

Two separate cases were considered: an overpressurized injection case and a matched pressure case. These characterizations were based on the effective back pressure method of Schetz and Billig in Ref. [8], as modified by Fuller to angled injection in [6]. The effective back pressure is simply an estimate of the pressure that the jet will see in the flowfield: Fuller suggested that for this case a  $15^\circ$  cone be used

to represent the injection, and so the effective back pressure is based on the pressure after the shock over this cone. This is simply calculated using the cone-shock charts. The first case is that of matched injection pressure, and the second is for 5 times overpressure. The inflow and jet conditions are shown in table 5.

	P (Pa)	T (K)	V (m/s)	$\rho$ (kg/m <sup>3</sup> )
Freestream	4364.0	63.3	957.0	0.2405 (Air)
Matched P Jet	21380.0	150.0	1225.5 @ 15°	0.0686 (He)
5X P Jet	106898.0	150.0	1225.5 @ 15°	0.3430 (He)

**Table 5: Jet and freestream conditions for the 15 degree helium wall jet**

The turbulent Schmidt number was initially set to 0.5, and the algebraic turbulence model of Baldwin-Lomax was used. The Baldwin-Lomax model will not accurately capture nearfield turbulent structures, but by using a wake modification through the jet, it is hoped that the model will pick up the downstream turbulent mixing.

The results for this initial investigation with GASP proved to not be very accurate. Figure 8a.-b. is an axial plot of helium mass fraction, and shows the differences between the 1X matched pressure case (a) and the 5X overpressure case (b). The core penetration can be seen to be much more for the 5X case, as would be expected. In both the experiment and the computations, the core of the 1X jet stayed down along the wall for most of the domain. The mixing results are shown for crossflow planes of helium mass fraction. There were experimental measurements taken at four stations:  $X/D = 20, 40, 60$ , and  $80$ . The first three planes for the overpressure case are shown in Figure 9a.-c., for the experiment, the current computation (labelled GASP), and the previous computation with GASP, labelled *FULLER, et.al*<sup>5</sup>, respectively left to right. At  $X/D = 20$ , the experimental data is very asymmetric (only the left side of the data is shown), but seems to indicate that the core of the jet has been split by the overspill vortices. Neither of the CFD solutions display this effect and show considerably more diffusion and penetration. At  $X/D = 40$  and  $X/D = 60$ , the experimental core has rejoined into a single core, and the CFD solutions are still over-diffusing the jet. The Fuller solution is more diffusive than the current GASP solution. Figure 10 shows the helium crossflow contours for the matched pressure case: experiment and current computations. The CFD core is a little less transversely stretched, but overall the agreement is fairly good. Figure 11 shows the  $X/D = 80$  plane comparing the current CFD solution to the experimental contours. The core is well over-penetrated and over-diffused. For other types of CFD, a similar experiment to CFD comparison is shown for the finite-difference code SPARK [9], and also for the Fuller solution in Figure 12a.-b., respectively. The SPARK solution has fair agreement with the data, but the Fuller solution is as far off as the current solution. Figure 13 quantifies the observations above. Figure

<sup>5</sup>documented in Ref. [7] as the refined grid solution



13a -b. are conservation of mass plots (used for convergence criteria). The current domain is unconfined in the vertical direction: it is the bow shock wave turning the flow out of the domain that causes the large axial drop in total mass flux for both cases. The helium mass flux agreement is good for both overpressure and matched pressure cases. Figure 13c. shows the axial decay of the maximum concentration of helium mass fraction, comparing results for GASP CFD and experiment. The CFD solution overpredicts the decay rate, but this has been documented for this case for SPARK in Ref. [9]. Note that both the overpressure and matched pressure CFD solutions decay at the same rate, whereas the experimental decay is slightly faster for the matched pressure case. This is probably because the kinematic farfield is very similar for the two cases computationally, and since the turbulent diffusion is based on mean kinematic properties, the diffusion for both cases should be similar. This kinematic representation is probably the cause of some of the discrepancy between the solutions and the experimental data. Figure 13d. shows the penetration of  $\alpha_{He-max}$  with axial distance. The matched pressure case is in very good agreement with the data, in terms of the flowfield accurately predicting the core remaining along the wall until some downstream location before being lifted off. The penetration of the overpressure solution is grossly overpredicted by the CFD. There are several reasons for the poor performance of the CFD, and which continuing research is attempting to resolve. One major issue is the grid: the current grid is too coarse out in the main stream, in order to capture wall effects (which are not being studied here). This has been identified because the matched pressure case was fairly well represented: the core remained next to the wall for almost the entire domain, which was in the area where the grid density was highest. The overpressure solution core moved out into the low grid density region almost immediately. The grid is being regenerated to have better main flowfield resolution. The other adjustment that is being made is the return of  $Sc_t$  to 0.7, where binary theory indicates it should be. Also, grid blocking issues are being investigated.

### 3. CONCLUSIONS AND FUTURE RESEARCH

The ability of CFD solutions to accurately model complex mixing and reacting flowfields is the major issue that has been addressed here. The first two of three steps have been undertaken. The first step is to determine the effectiveness of GASP in modelling reacting flowfields. Here, the internal influences of modelling were examined. The effects of free stream turbulence (and also different models) was very dramatic on the flame speed observed in a shock-induced combustion problem. The effect of turbulent Schmidt number, which is the parameter which directly controls the amount of diffusion in the model, was examined for an experimental flowfield. The results, in terms of flame location, were improved with respect to the experimental results, but there were other modelling issues that need to be resolved for that problem. The turbulent Schmidt number does have a large impact on the diffusion in these high speed reacting cases, so that the models can be tuned for specific problems. A third comparison was done between different chemistry models in GASP, for a shock-induced combustion problem. The finite rate kinetics turned out to be very sensitive to the model chosen, especially for

problems near the ignition point. For a general combustion problem, GASP modelled the expected physics well.

Mixing in supersonic flowfields was also examined. Two 15 degree flush wall port injectors on a flat plate were modelled and the mixing results were compared to experimental data and other computational results. The current solution over-diffused the core and overpredicted the penetration of the core, especially for the overpressure injection case. The results were much better for the matched pressure case. This effect was also seen in other solutions for this problem with GASP. The SPARK code generated a good solution, illustrating that the problem can be modelled computationally. The major reason for the discrepancy, in this case, is postulated to be the grid. Future research will concentrate on improving the mixing solution.

The final part of this research is to model both mixing and reacting solutions for swept ramp injectors at a flight Mach number of 13, and evaluate the solution using experimental data. The final goal of this and future research, is to demonstrate GASP as a tool that can be used to predict the performance of scramjet combustors.

#### **REFERENCES**

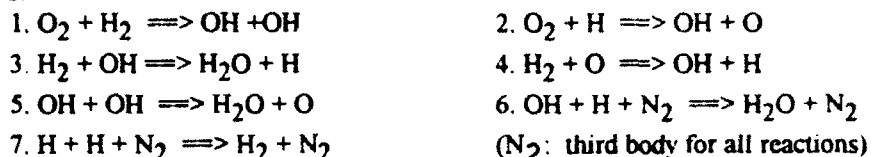
1. Swithenbank, J., Eames, I., Chin, S., Ewan, B., Yang, Z., Czo, J., Zhao, X., "Turbulent Mixing in Supersonic Combustion Systems", AIAA paper 89-0260, January, 1989.
2. Walters, R.W., Cinnella, P., Slack, D.C., Halt, D., "Characteristic-Based Algorithms for Flows in Thermochemical Nonequilibrium", AIAA Journal, Vol. 30, No. 5, May 1992, pp 1304-1313.
3. Baldwin, S., Lomax, H., "Thin Layer Approximation and Algebraic Models for Separated Turbulent Flows", AIAA paper 78-0257.
4. Chien, K.-Y., "Predictions of Channel and Boundary-Layer Flows with a Low Reynolds-Number Turbulence Model, AIAA Journal, Vol. 20, No. 1, January 1982, pp 33-38.
5. Burrows, M.C., Kurkov, A.P., "Analytical and Experimental Study of Supersonic Combustion of Hydrogen in a Vitiated Air Stream", NASA TM-X-2828, 1977.
6. Fuller, E., Mays, R., Thomas, R., Schetz, J., "Mixing Studies of Helium in Air at Mach 6", AIAA paper 91-2268.
7. Fuller, E.J., Walters, R.W., "Navier-Stokes Calculations for 3D Gaseous Fuel Injection with Data Comparisons", AIAA paper 91-5072.
8. Schetz, J.A., Billig, F.S., "Penetration of Gaseous Jets Injected Into a Supersonic Stream", Journal of Spacecraft and Rockets, Vol. 3, No. 11, November 1966, pp 1658-1665.
9. Riggins, D.W., McClinton, C.R. "A Computational Investigation of Mixing and Reacting Flows in Supersonic Combustors", AIAA paper 92-0626.

## APPENDIX: CHEMISTRY MODEL DETAILS

### 1. Drummond Chemistry Model: 7 species, 7 reactions.

Species:  $N_2$ ,  $O_2$ ,  $H_2$ ,  $OH$ ,  $H_2O$ ,  $O$ ,  $H$

Reactions:

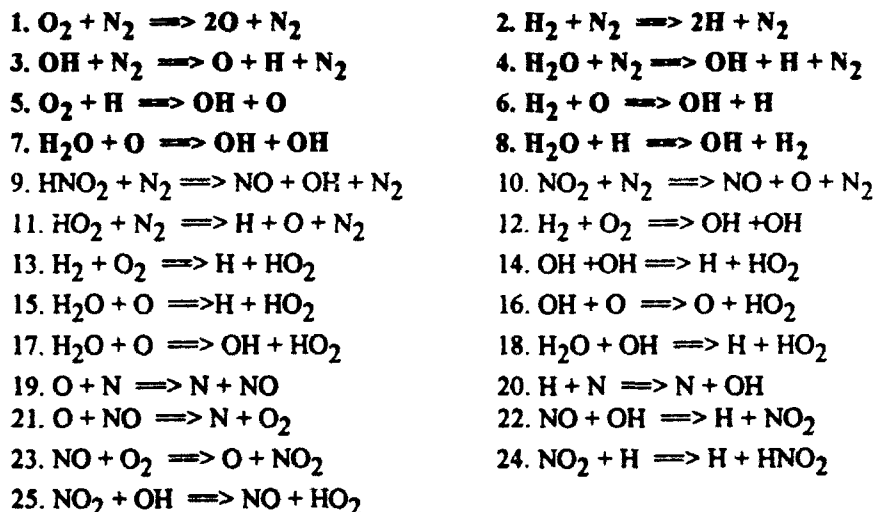


### 2. Evans and Schernayder 1 & 2 Chemistry Models:

Model 1: 7 species, 8 reactions (bold face), Model 2: 12 species, 25 reactions

Species:  $N_2$ ,  $O_2$ ,  $H_2$ ,  $OH$ ,  $H_2O$ ,  $O$ ,  $H$ ,  $NO$ ,  $NO_2$ ,  $HO_2$ ,  $HNO_2$ ,  $N$

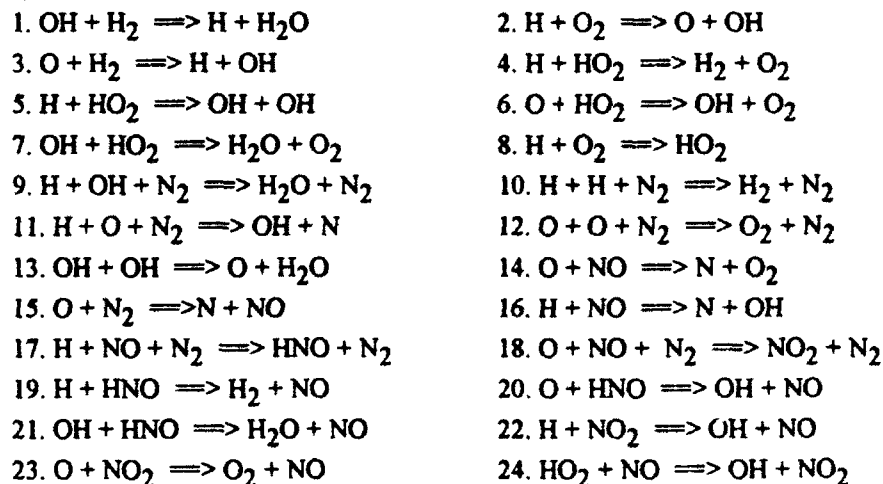
Reactions:



### 3. NASP 4 (Hydrogen/ $NO_x$ extension): 12 species, 24 reactions

Species:  $N_2$ ,  $O_2$ ,  $H_2$ ,  $NO$ ,  $OH$ ,  $NO_2$ ,  $HO_2$ ,  $HNO$ ,  $H_2O$ ,  $N$ ,  $O$ ,  $H$

Reactions:



## FIGURES

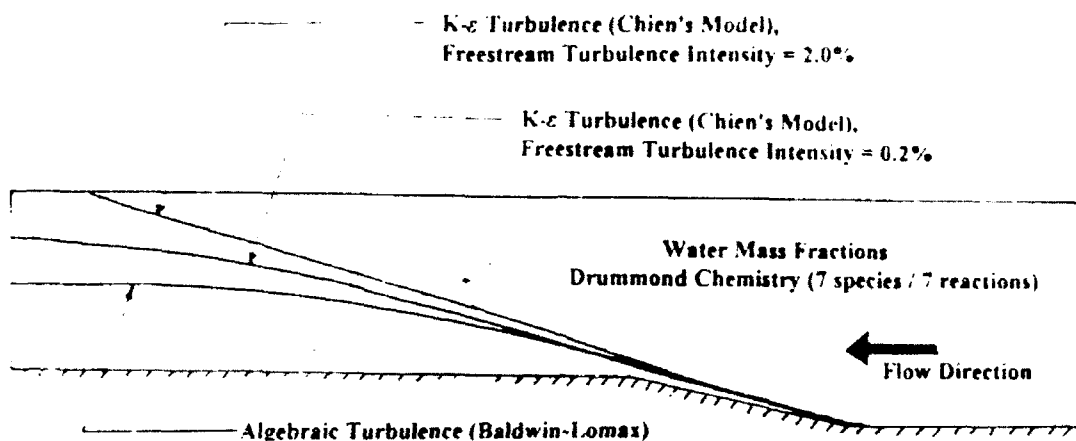


Figure 1: Sketch showing the flame fronts computed for different turbulence models and model geometry. The flame front is taken to be the location of maximum water mass fraction change.

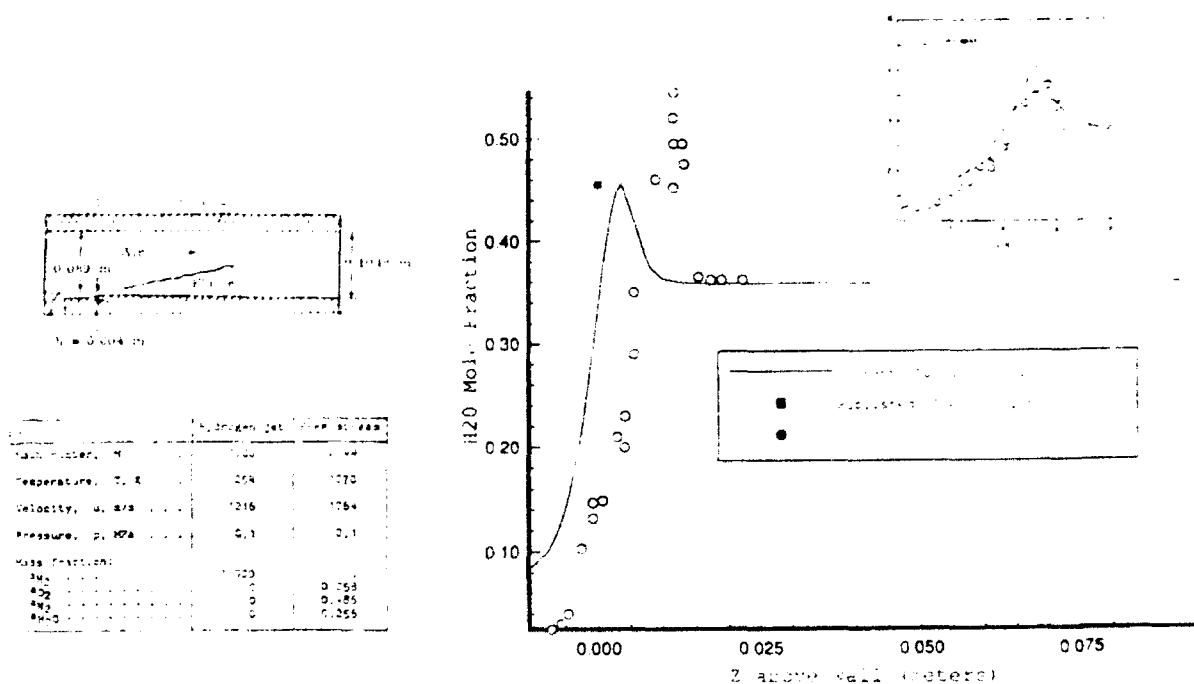
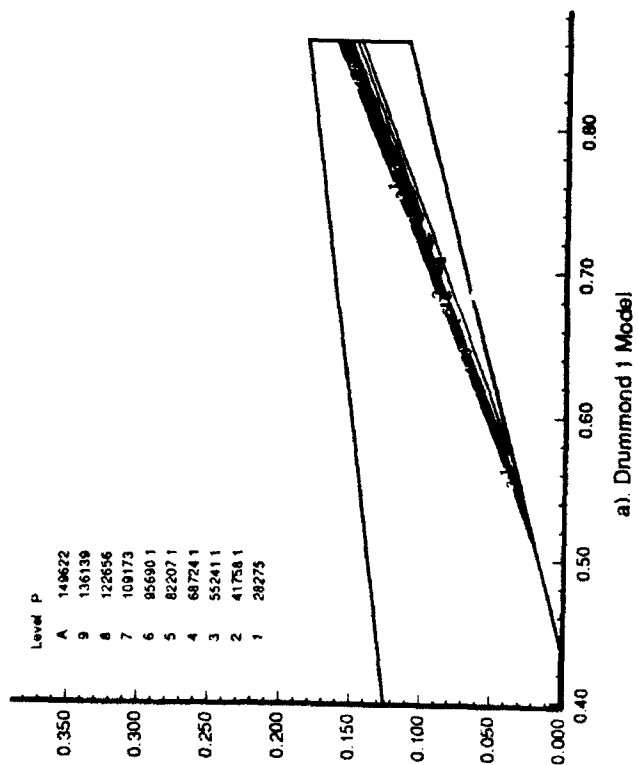


Figure 2: Burrows and Kurkov test case, computational and experimental results. a). geometry sketch, b). inflow conditions, c). current results for water mole fractions compared with data and a previously published CFD solution. Inset is the water mole fraction Figure published by Burrows and Kurkov, showing that the original analytical solution is as inaccurate as the current computation.



8-13

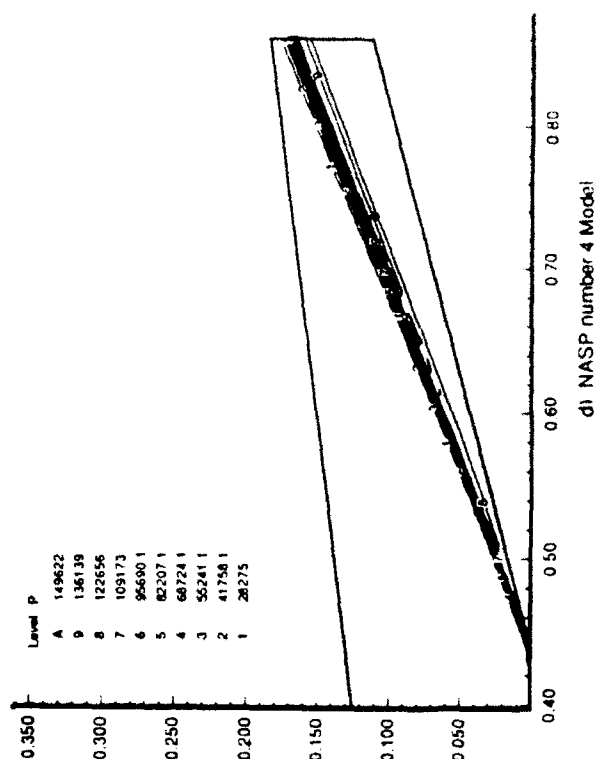
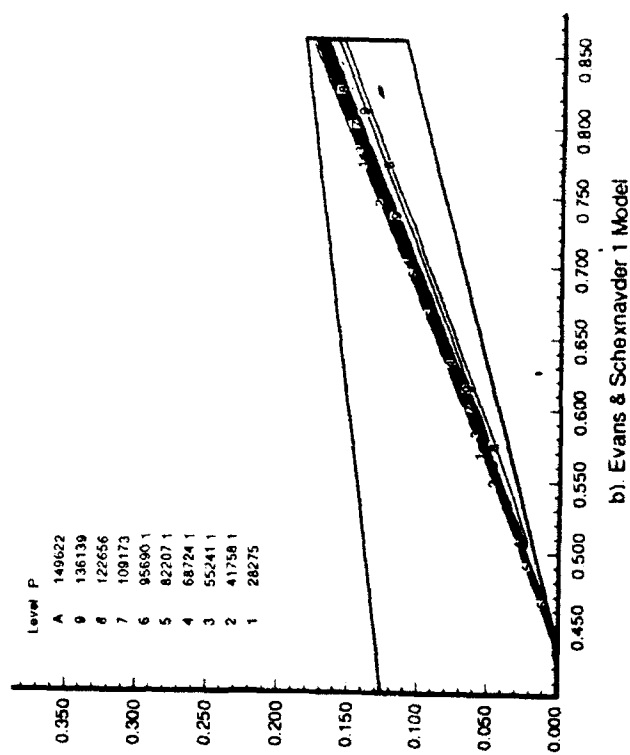
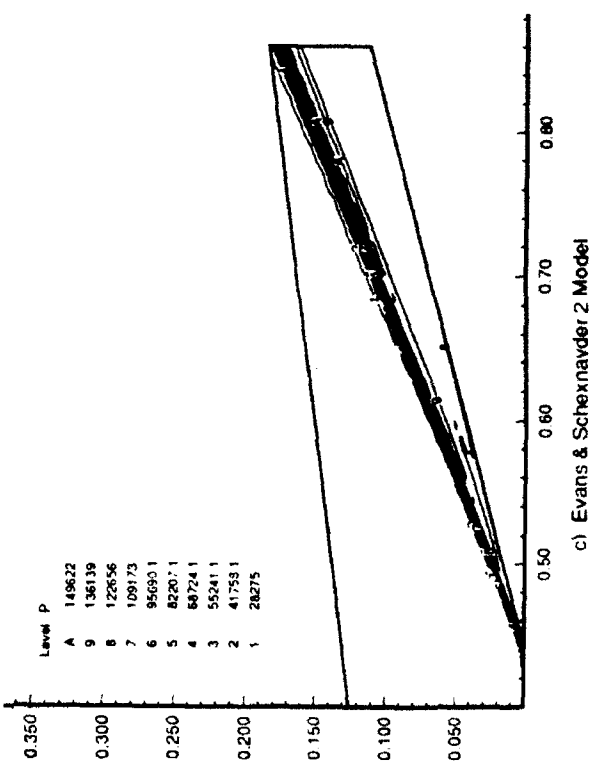
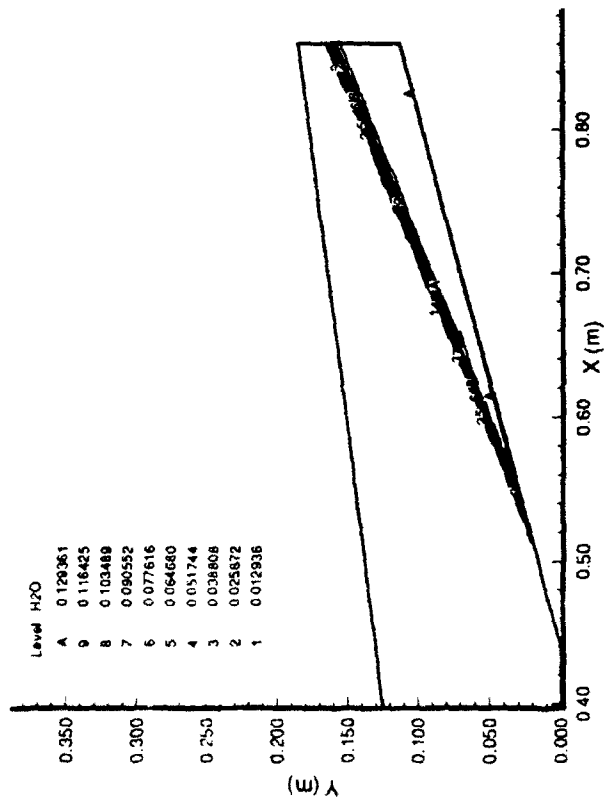
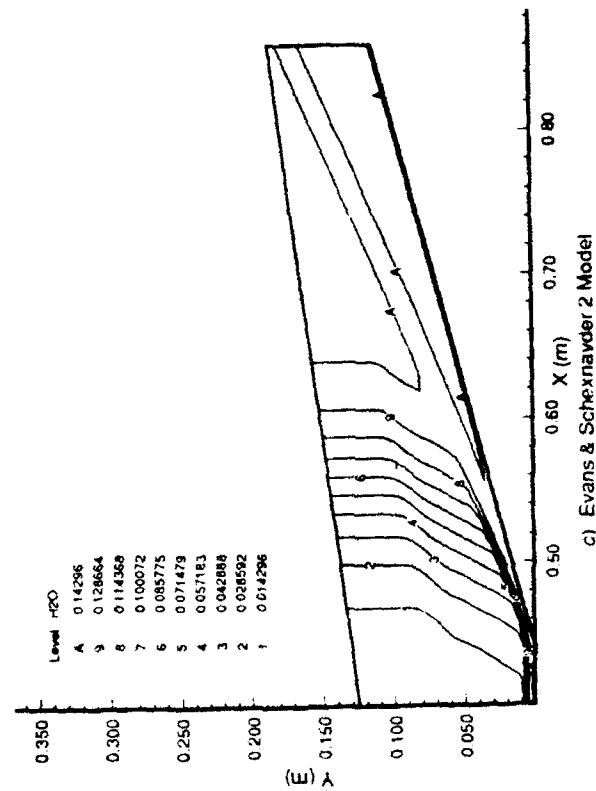


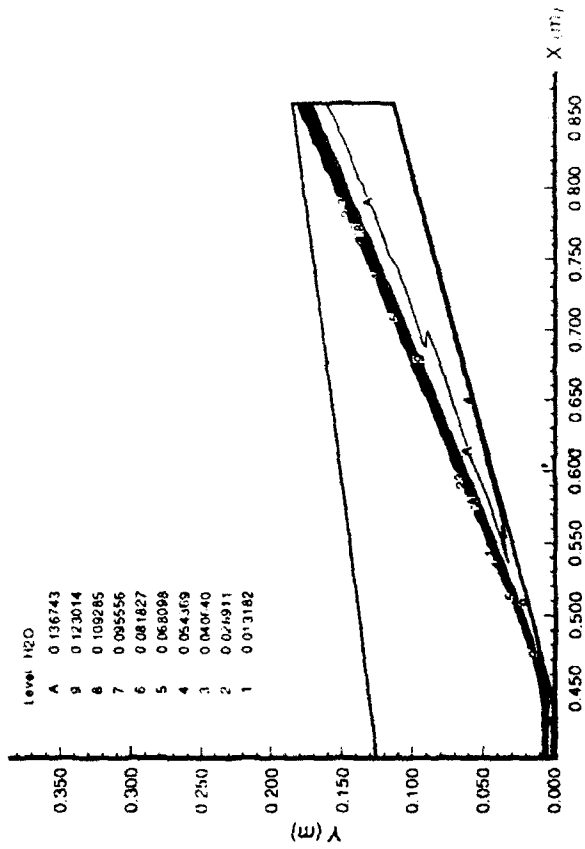
Figure 3: Pressure contours for a 10 degree ramp, for differing chemistry models.



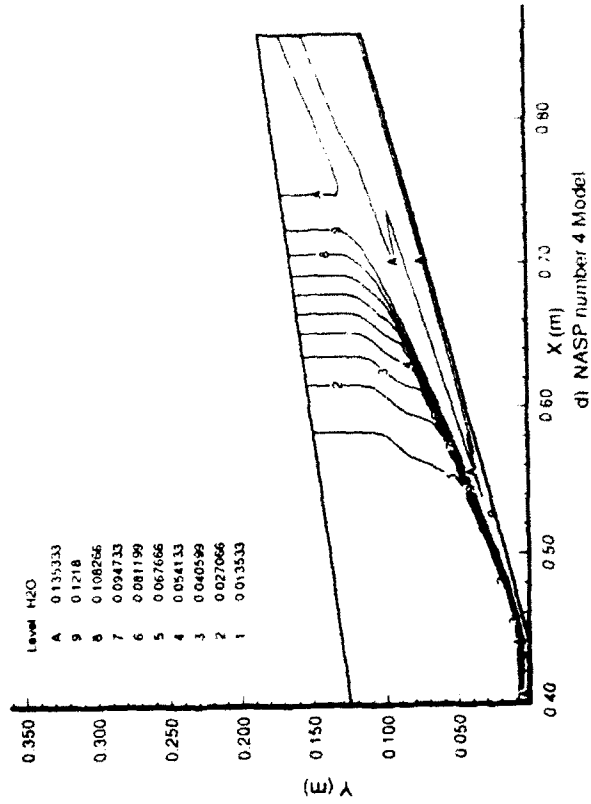
a) Drummond 1 Model



c) Evans & Schexnayder 2 Model



b) Evans & Schexnayder 1 Model



d) NASP number 4 Model

Figure 4: Water mass fraction contours for a 10 degree ramp, for differing chemistry models.

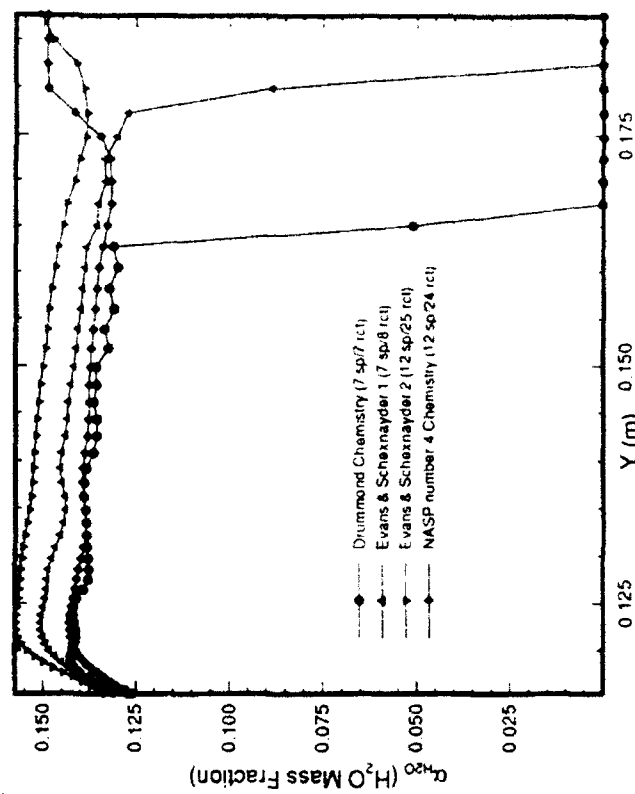
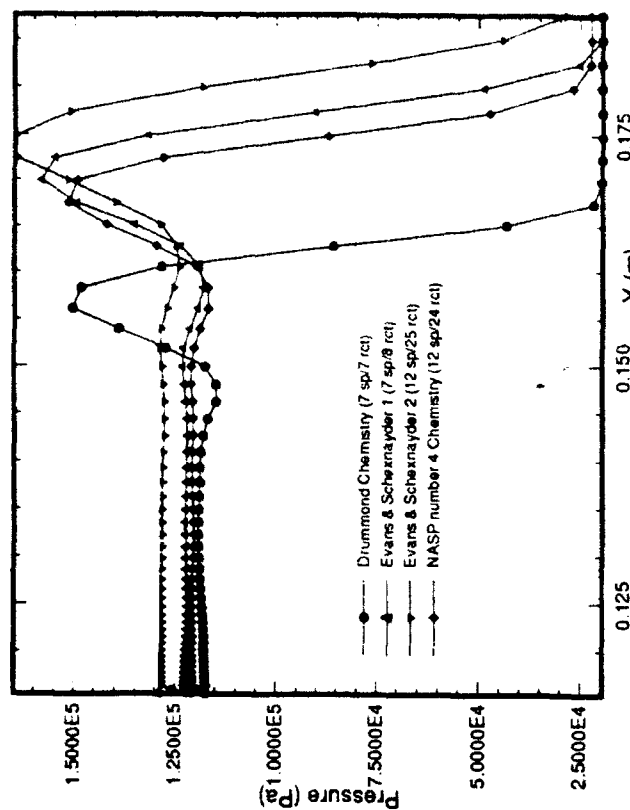
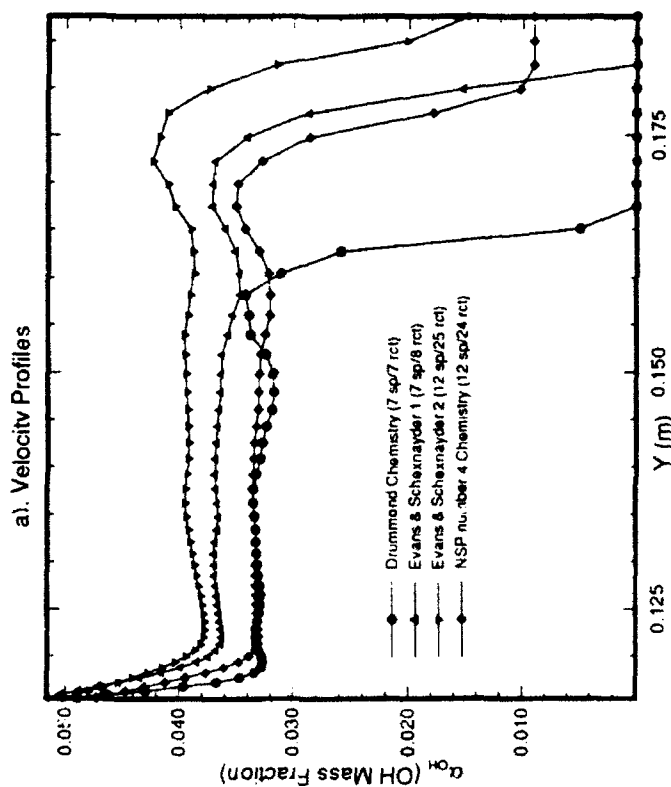
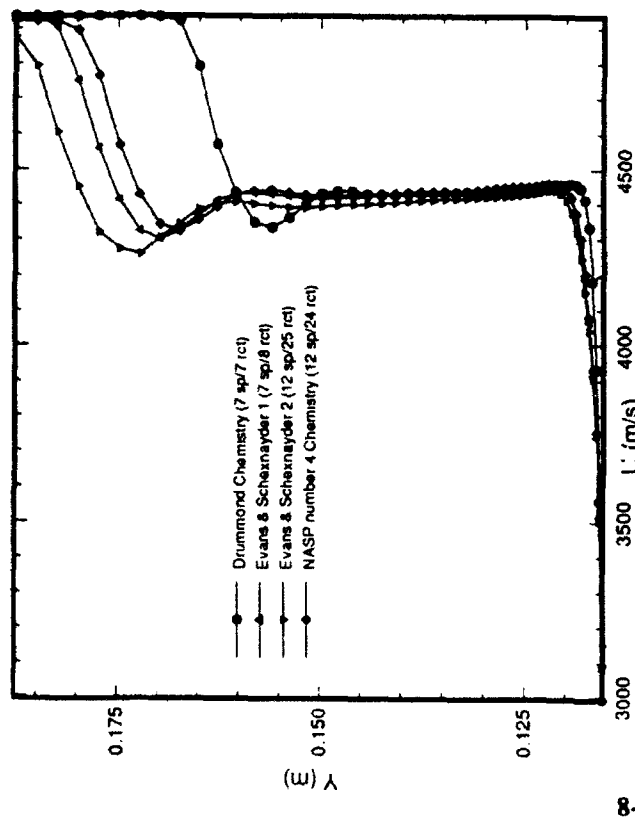
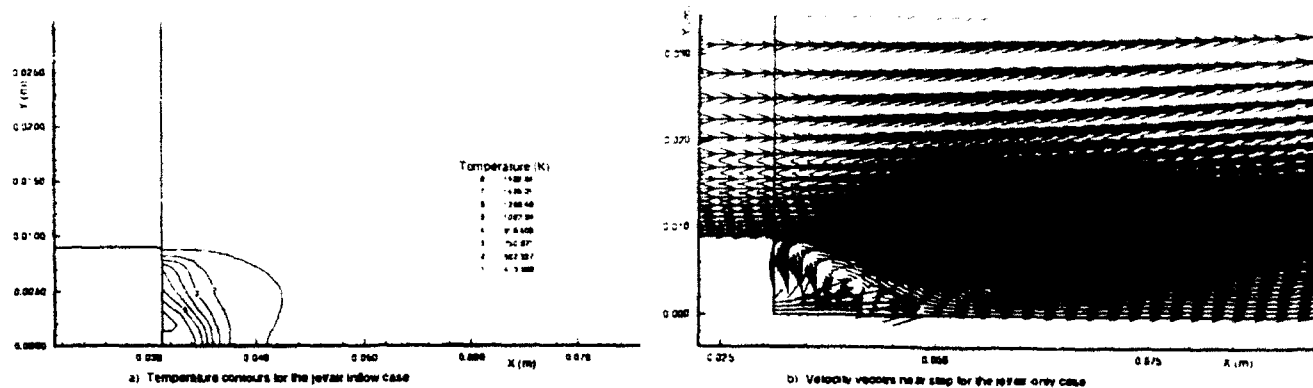
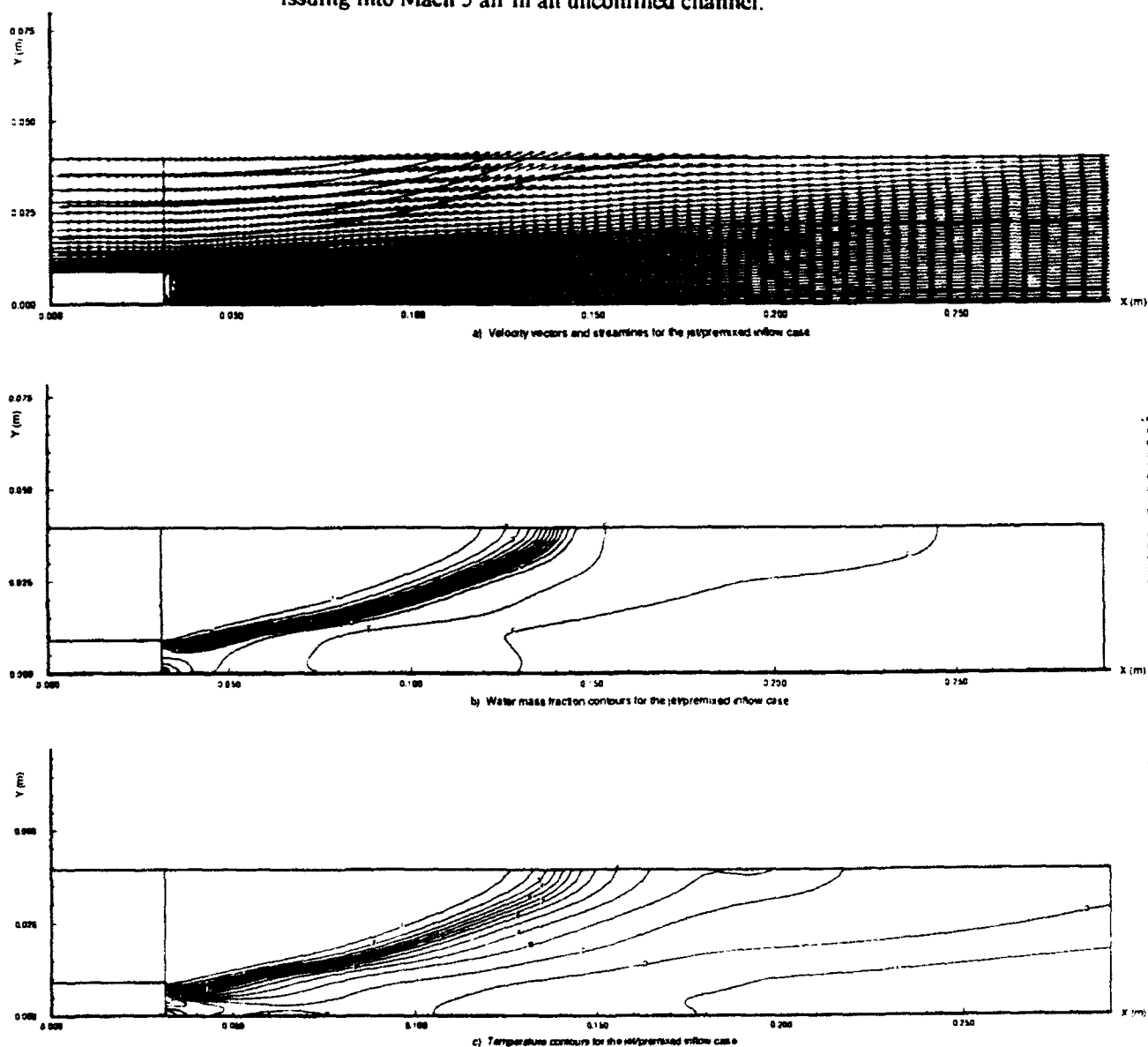


Figure 5: Quantitative results comparisons between the chemistry models.

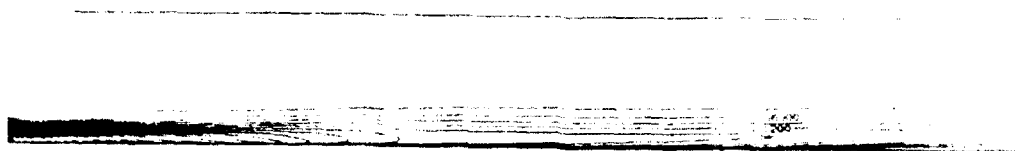


**Figure 6: Computational results for a hydrogen-air jet (or torch) at the base of a step issuing into Mach 5 air in an unconfined channel.**

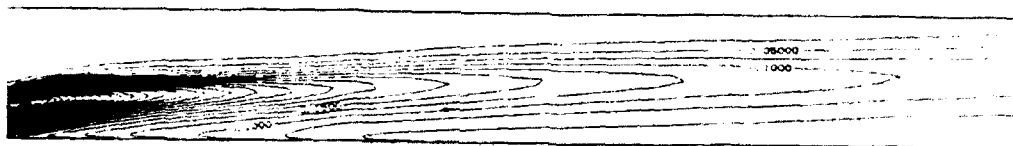


**Figure 7: Computational results for hydrogen-air reacting flowfield. Premixed hydrogen-air inflow at left, over a backstep, where it is ignited by the hydrogen-air jet illustrated in Figure 6. Upper boundary after backstep is unconfined.**



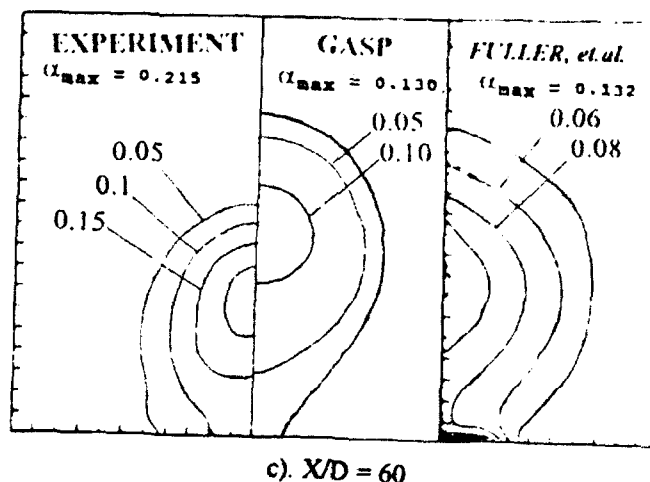
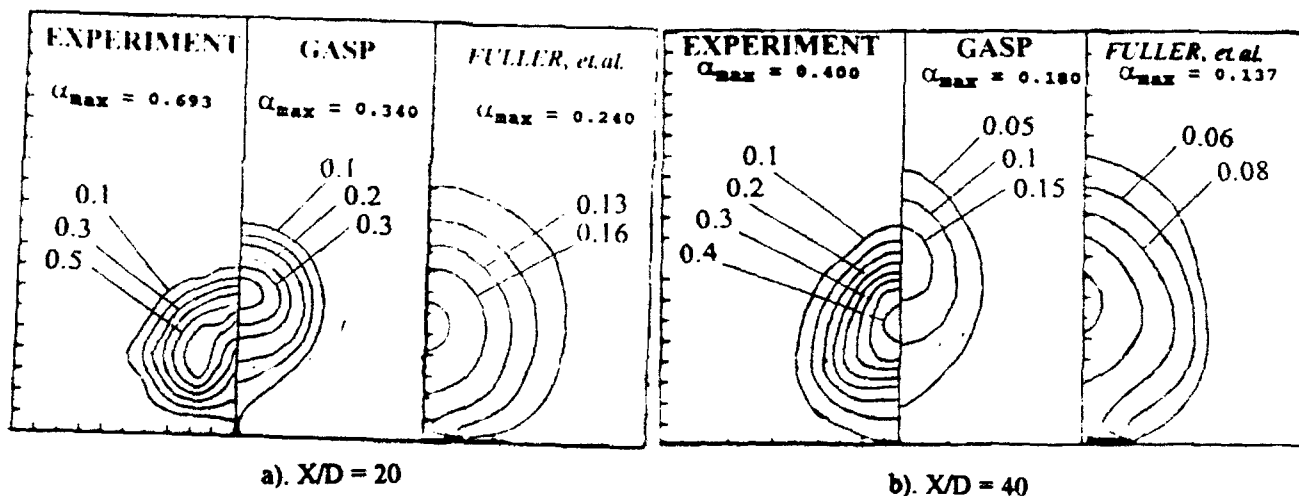


a). Matched pressure injection



b). 5X overpressure injection

Figure 8: Axial domain slices of helium mass fraction contours, showing the core penetration for the different injection pressures.



c). X/D = 60

Figure 9: Transverse slices of the downstream domain showing comparisons of experimental, computational, and previously published helium mass fraction contours. 5X case.

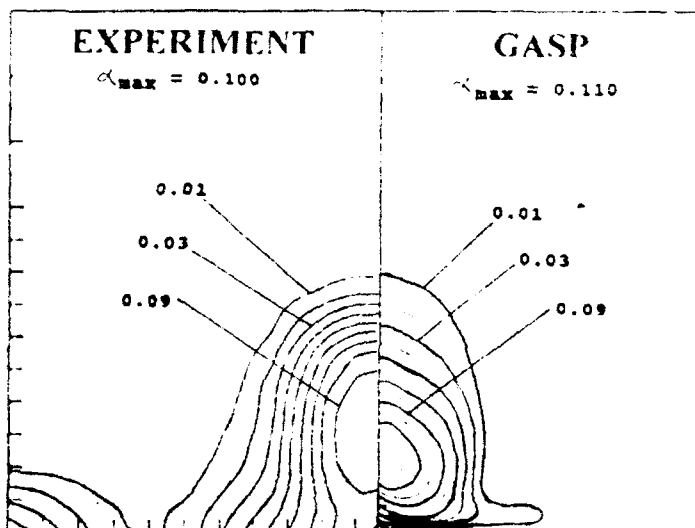


Figure 10: Matched pressure,  $X/D = 80$ , helium mass fraction contours.

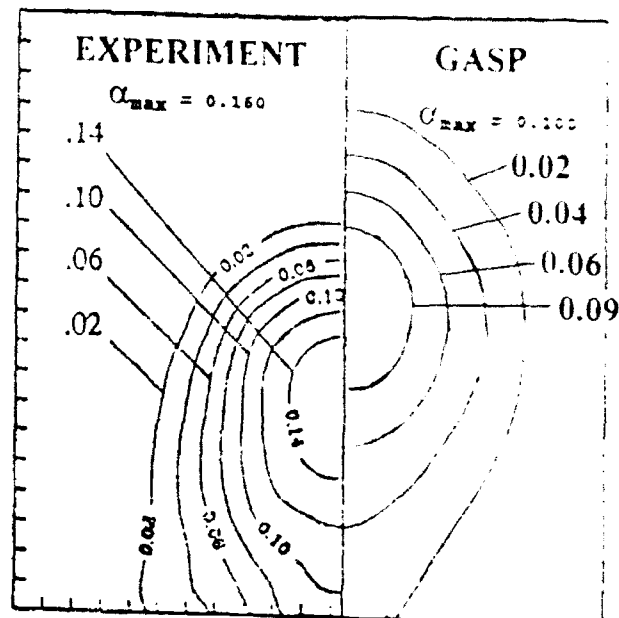
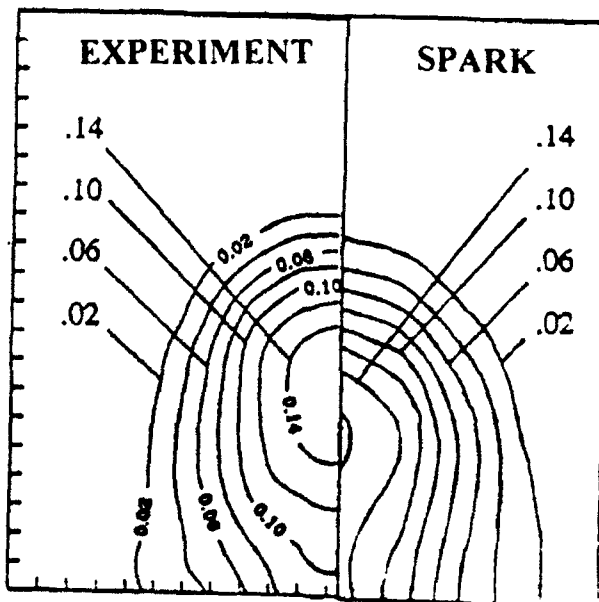
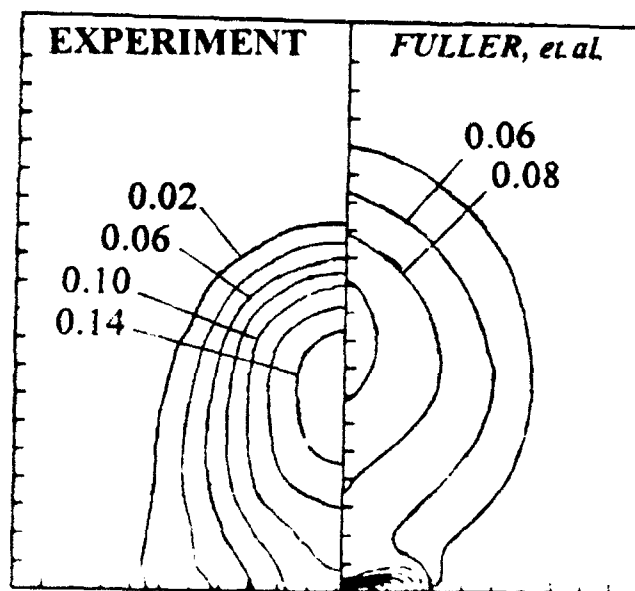


Figure 11: 5X overpressure,  $X/D = 80$ , helium mass fraction contours.



a) SPARK CFD solution/experiment comparison



b) previously published GASP solution comparison with experiment

Figure 12: 5X overpressure,  $X/D = 80$ , helium mass fraction contour comparison

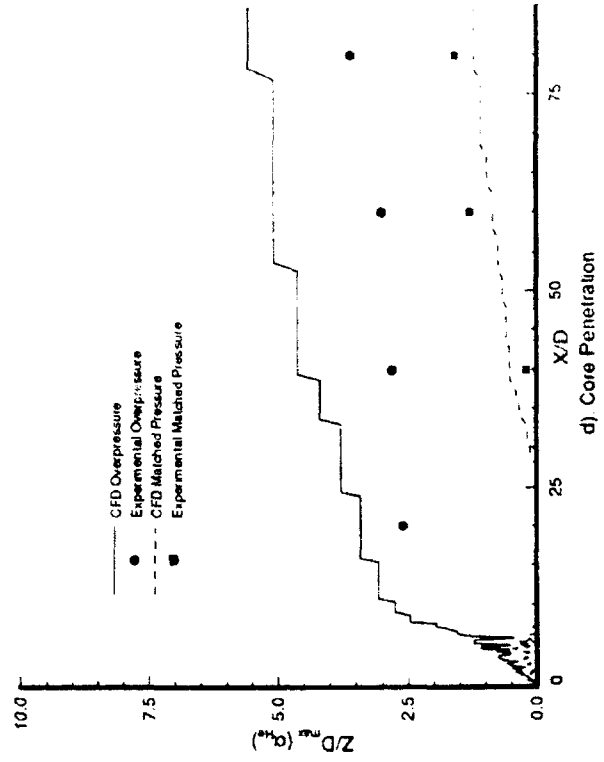
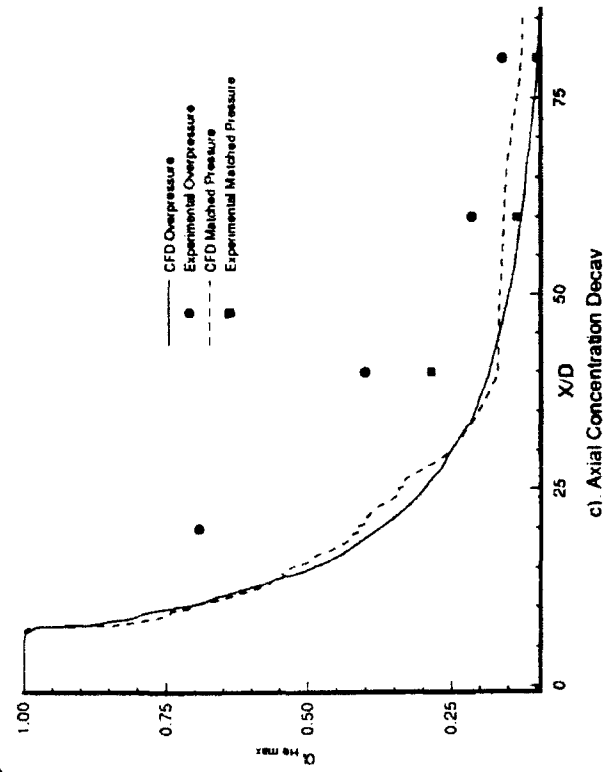
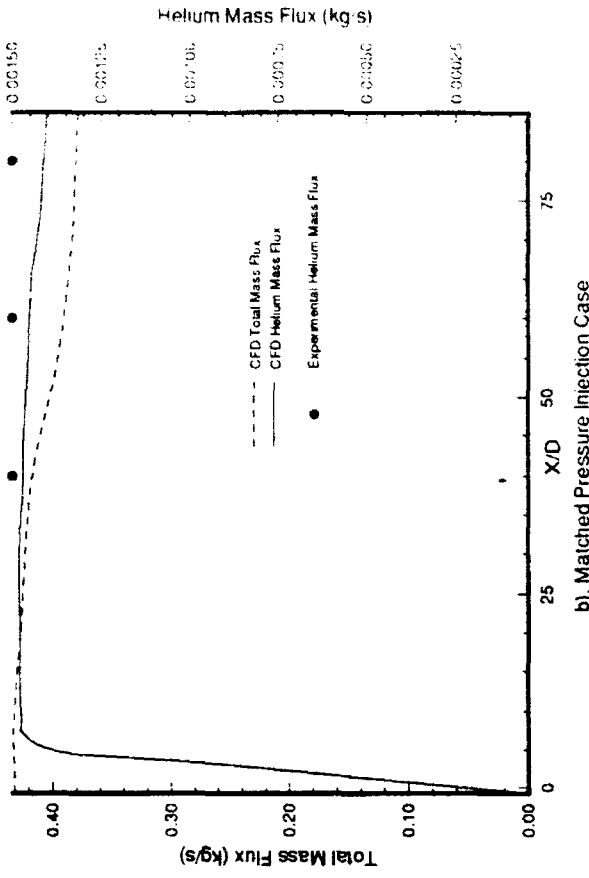
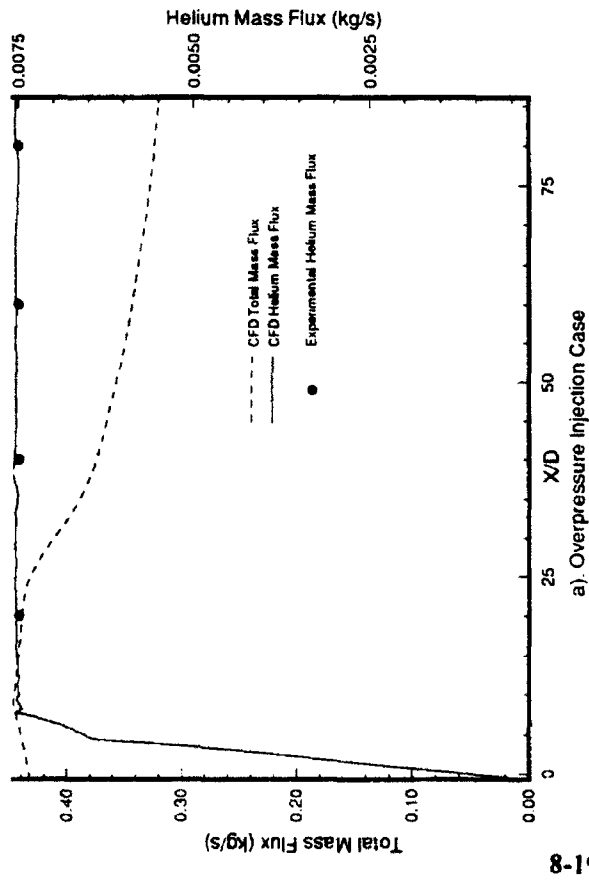


Figure 13: Quantitative comparison of the current computations for mixing and penetration of helium with experiment.

MULTIDIMENSIONAL CONJUGATE HEAT TRANSFER ANALYSIS  
FOR THE ARNOLD ENGINEERING DEVELOPMENT CENTER  
HEAT-H1 TEST UNIT NOZZLE

Michael A. Weaver, MSAE  
Graduate Student  
School of Aerospace Engineering  
Georgia Institute of Technology

Final Report for:  
AFOSR Summer Research Program  
Arnold Engineering Development Center

Sponsored by:  
Air Force Office of Scientific Research

11 September 1992

MULTIDIMENSIONAL CONJUGATE HEAT TRANSFER ANALYSIS  
FOR THE ARNOLD ENGINEERING DEVELOPMENT CENTER  
HEAT-H1 TEST UNIT NOZZLE

Michael A. Weaver, MSAE  
Graduate Student  
School of Aerospace Engineering  
Georgia Institute of Technology

Abstract

A method for unsteady, axisymmetric, conjugate heat transfer analysis was developed. The conjugate heat transfer domain comprises coflowing high temperature air and subcooled water coolant on opposite sides of a copper-zirconium, converging nozzle. Heat transfer through the nozzle wall is characterized by solid body conduction with convection boundary conditions along the air side and water side of the nozzle wall. The air side heat transfer is characterized by forced convection with a turbulent boundary layer. The water side heat transfer is characterized by forced convection, subcooled, nucleate boiling. Convective heat transfer coefficients on each side of the nozzle wall are functions of the wall temperature and the respective flow properties, thus coupling the three regions of the domain. The solution method marches in time, solving at each time step for the nozzle wall temperature distribution, the flow properties on each side of the nozzle wall, and for the convective heat transfer coefficients. The algorithm terminates when either the steady state is achieved or nozzle wall failure conditions are reached. Preliminary results are shown for run conditions at which nozzle wall survival has been experimentally verified.

MULTIDIMENSIONAL CONJUGATE HEAT TRANSFER ANALYSIS  
FOR THE ARNOLD ENGINEERING DEVELOPMENT CENTER  
HEAT-H1 TEST UNIT NOZZLE

Michael A. Weaver

Introduction

Within the context of this study, conjugate heat transfer describes the coupling between fluid flow over a structure and conductive heat transfer within the structure. Such coupling requires simultaneous consideration of both the convection and conduction phenomena. Conjugate heat transfer occurs, for example, in an actively cooled, high temperature wind tunnel nozzle. In this case, convective heat transfer through the working fluid boundary layer to the nozzle wall is coupled with the nozzle wall temperature. Convective heat transfer from the nozzle wall to the coolant is also coupled with the nozzle wall temperature. In turn, the conductive heat transfer within the solid nozzle material is coupled through convection boundary conditions to flow of the working fluid and coolant over the nozzle wall.

This study addresses conjugate heat transfer in the Arnold Engineering Development Center (AEDC) HEAT-H1 Test Unit nozzle. The HEAT-H1 Test Unit (hereafter referred to as HEAT-H1) is an arc-heated, free jet test facility, providing extremely high enthalpy air flow. Flows with enthalpies ranging from 2,000 to 8,500 Btu/lbm and pressures ranging from 20 to 115 atm are routinely produced [1]. Mach numbers ranging from 1.8 to 3.5 are achieved with interchangeable nozzles. Coflowing water with sub-cooled, nucleate boiling provides active, backside cooling for the nozzle wall.

Proposed future applications for HEAT-H1 require pressures up to 200 atm. Unfortunately, nozzle wall structural failure due to heat load occurs at pressures in the range 120 to 130 atm. The need exists to predict such heat

and failures, and then to recommend strategies for avoiding the failures.

The operating contractor at AEBC for the HEAT-H1 (Calspan Corporation AEBC Operations) has completed a failure analysis assuming one-dimensional conjugate heat transfer through the nozzle wall [2]. This approach gives good results in the limited region of applicability, which lies in the thin-walled section of the nozzle. Failure analysis of the complete nozzle must consider multidimensional conjugate heat transfer, and Calspan has begun such an analysis. The Air Force Office of Scientific Research sponsored work independently approaches the multidimensional conjugate heat transfer problem to complement the Calspan effort.

#### Discussion of Problem

The HEAT-H1 arc-heater configuration is shown in Fig. 1. Tangentially injected air flows between the anode and cathode for heating by the electric arc. The high temperature, subsonic air passes from the cathode, through a conical contraction, to the nozzle inlet, then expands through the nozzle to parallel, supersonic flow at the nozzle exit.

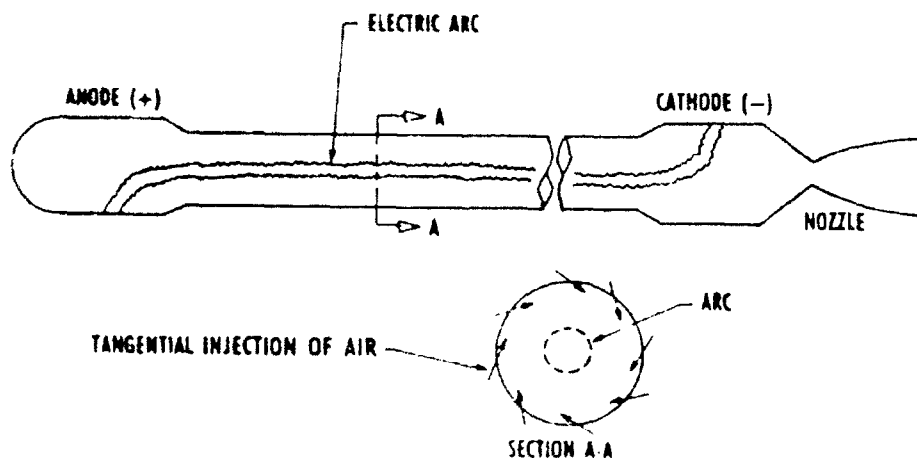


Fig. 1. Idealization of the HEAT-H1 arc-heated wind tunnel.

This and the previous studies focus on the HEAT-H1 Mach 1.8 nozzle. This axisymmetric nozzle is 2.3 in. long, with a throat diameter of 0.9 in. The material composition is copper-zirconium. The nozzle and surrounding cooling jacket are approximated in Fig. 2. Water flows between the nozzle and cooling jacket, providing backside cooling for the nozzle wall. Away from the end regions, heat transfer through the nozzle wall is approximately one-dimensional. Near the flanged ends of the nozzle, the solid body heat transfer becomes axisymmetric in nature.

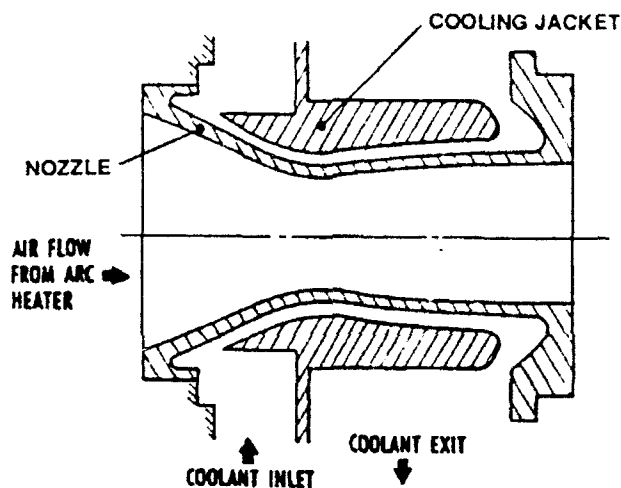


Fig. 2. Idealization of the HEAT-H1 nozzle and cooling jacket.

Air flow over the nozzle wall is assumed steady, compressible, and turbulent, with a high temperature boundary layer. Outside the boundary layer, flow is assumed to be steady, compressible, nonuniform, dissociated, equilibrium air, with decreasing stagnation temperature approaching the wall. Transport properties for the high temperature, high pressure air are strong functions of temperature and weak functions of pressure.

Water flow between the cooling jacket and nozzle wall is assumed steady,



incompressible, viscous, and turbulent. The water enters and exits the active cooling region in the subcooled state. Subcooled nucleate boiling is assumed to occur at the nozzle wall, while the outer cooling jacket wall is assumed adiabatic. Transport properties for the subcooled water are functions of temperature and pressure.

Heat load structural deformation and failure in the HEAT-H1 nozzles has been observed in the region between the nozzle inlet and the nozzle throat. Nozzle wall failure has not been observed downstream of the nozzle throat. For this reason, the current analysis is limited to the HEAT-H1 Mach 1.8 nozzle geometry from the nozzle inlet to the nozzle throat. This simplification leads to a nonphysical longitudinal boundary at the nozzle throat. Due to the approximately one-dimensional (radial) nature of heat transfer at the throat, this longitudinal throat boundary is assumed adiabatic. The three regions of the conjugate heat transfer domain (nozzle, air, and water) are summarized in Fig. 3 with the adiabatic boundary conditions indicated.

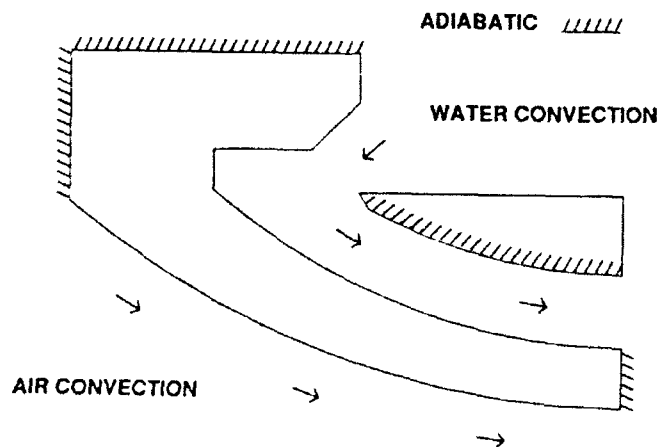


Fig. 3. Conjugate heat transfer domain for the HEAT-H1 nozzle.

### Method of Analysis

At least three modes of heat load failure exist for the nozzle wall. First, the temperature in the nozzle wall may reach the melting point of the material, causing immediate catastrophic failure. Second, the critical heat flux from the nozzle wall to the boiling coolant may be reached, leading to wall "burnout". Third, the time span and magnitude of the heat load may permit plastic deformation great enough to produce structural failure, even though wall temperatures remain below the melting point of the material.

The failure mode being examined determines the appropriate analysis method. The first two failure modes can be analyzed with either a steady or an unsteady approach. The steady conjugate heat transfer problem could be solved, and then the solution checked for nozzle wall temperatures exceeding the material melting point, or for the critical heat flux being reached. Alternatively, the unsteady conjugate heat transfer problem could be marched in time until either the nozzle wall temperatures exceed the material melting point, the critical heat flux is reached, or the steady state is obtained. The third failure mode, by its unsteady nature, must be analyzed with an unsteady approach. The unsteady method already described could be used for the third failure mode, with the inclusion of an additional step to determine structural deformation, and a check for structural yielding.

In the current study, only the first two failure modes are considered, but the unsteady approach has been adopted for its future applicability to plasticity analysis for the third failure mode. The algorithm developed is as follows:

- a) Assume an initially constant nozzle wall temperature distribution equal to the water inlet temperature.

- b) Calculate the initial water flow properties along the water side and the initial air flow properties along the air side of the nozzle.
- c) Calculate the initial heat transfer coefficients for the water side and the air side of the nozzle.
- d) Use the heat transfer coefficients and effective fluid temperatures for the air side and water side of the nozzle in the initial time step of an unsteady heat transfer analysis of the copper-zirconium nozzle to obtain the new temperature distribution.
- e) Calculate the new water flow properties along the water side and the new air flow properties along the air side of the nozzle.
- f) Calculate the new heat transfer coefficients for the water side and the air side of the nozzle.
- g) Use the heat transfer coefficients and effective fluid temperatures for the air side and water side of the nozzle in the next time step of an unsteady heat transfer analysis of the copper-zirconium nozzle to obtain the new temperature distribution.
- h) Return to step e), until either the steady state is reached, the critical heat flux is reached, or the nozzle wall temperature exceeds the copper-zirconium melting point.

At each time step, this algorithm calculates the steady state flow and heat transfer properties of air and water, assuming the wall temperature distribution is in thermal equilibrium after each time step. For this assumption to remain valid, the time step size must be less than or equal to

the characteristic time for heat transfer in the nozzle wall material.

This approach requires numerical models (based on either analytic methods or engineering mathematical correlations) for the unsteady solid body heat transfer in the copper-zirconium nozzle, the flow properties and heat transfer coefficients on the air side of the nozzle, and the flow properties and heat transfer coefficients on the water side of the nozzle. Each of these models will be described for the three regions of the conjugate heat transfer domain.

**(i) Copper-zirconium nozzle wall:**

Unsteady, axisymmetric, solid body heat conduction, with no internal heat generation, and with temperature dependent thermal conductivity is governed by

$$\rho c_p \frac{\partial T}{\partial t} = \frac{1}{r} \left[ \frac{\partial}{\partial r} \left( kr \frac{\partial T}{\partial r} \right) + \frac{\partial}{\partial y} \left( kr \frac{\partial T}{\partial y} \right) \right].$$

The adiabatic wall boundary condition is given by

$$\left. \frac{\partial T}{\partial n} \right|_{w,11} = 0.$$

The convection boundary condition is given by

$$-k \left. \frac{\partial T}{\partial n} \right|_{w,11} = h(T_{w,11} - T_{eff}).$$

Here,  $c_p$  = isobaric specific heat,

$k$  = thermal conductivity,

$h$  = heat transfer coefficient,

$n$  = boundary normal coordinate,

$r$  = radial coordinate,

$t$  = time,

$T$  = solid body temperature,

$T_{eff}$  = effective fluid temperature,  
 $T_{wall}$  = wall temperature,  
 $y$  = longitudinal coordinate,  
 $\rho$  = mass density.

The finite element program TRAX [3] is used to solve this problem. At each time step, the heat transfer coefficients and effective fluid temperatures are specified. The effective fluid temperature for the water side is the local static temperature. For the air side, the effective fluid temperature is the local adiabatic wall temperature. Using these values, program TRAX reads the nodal temperature distribution from the previous time step and calculates the new nodal temperature distribution. The finite element mesh in Fig. 4 shows the geometry for the HEAT-H1 Mach 1.8 nozzle.

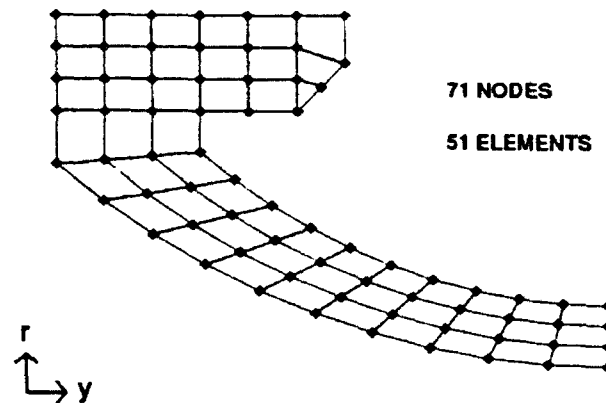


Fig. 4. Finite element model of the HEAT-H1 Mach 1.8 nozzle.

Material properties for elemental copper were used for the copper-zirconium nozzle. Values for  $c_p$ ,  $k$ , and  $\rho$  were linearly interpolated between values specified at 491.67° R and 2,500° R. The melting point for elemental copper is approximately 2,410° R.

(ii) Air side of the nozzle wall:

Steady state heat transfer through a turbulent, compressible boundary layer in accelerating, axisymmetric duct flow is given by the method of Ambrok [4],

$$St = \frac{0.0295}{Pr^{0.45}} \frac{R^{1/4} (T_{aw} - T_{wall})^{1/4} \mu^{1/5} (T_s/T_{wall})^{1/4}}{\left[ \int_0^x R^{3/4} (T_{aw} - T_{wall})^{3/4} G d\xi \right]^{1/5}} = \frac{h}{Gc_p}.$$

Here,  $c_p$  = isobaric specific heat,

$G$  = mass flux,

$h$  = heat transfer coefficient,

$Pr$  = Prandtl number,

$R$  = wall radius,

$St$  = Stanton number,

$T_{aw}$  = adiabatic wall temperature =  $T_s + Pr^{1/3}(T_o - T_s)$ ,

$T_o$  = stagnation temperature,

$T_s$  = static temperature,

$T_{wall}$  = wall temperature,

$x$  = wall arc length at position of interest,

$\mu$  = absolute viscosity,

$\xi$  = variable of integration (wall arc length).

This equation is based on solving the energy integral equation for the boundary layer [5]. It is valid for smoothly varying wall temperature and assumes a cooled wall. The boundary layer is assumed to originate at the lower limit of the integral. All properties are evaluated at the local static temperature.

The flow properties for dissociated, equilibrium air, as required for

the HEAT-H1 application, are obtained by mathematical correlation. An effective gas constant and specific heat ratio are used in the quasi-one-dimensional, isentropic flow equations to obtain mass flux, static temperature, and isobaric specific heat. The effective constants are chosen such that the correlated flow variables compare well with flow variables from a predetermined equilibrium gas solution. The boundary layer edge stagnation temperature from the real gas solution is used as the effective stagnation temperature in the isentropic flow equations. This value differs from the nominal HEAT-H1 run condition stagnation temperature due to nonuniformity of the flow. The nominal HEAT-H1 run condition stagnation pressure is used as the effective stagnation pressure in the isentropic flow equations.

The air transport properties are obtained from equilibrium gas tables [6]. Absolute viscosity and Prandtl number are bilinearly interpolated from values tabulated as functions of pressure and temperature. The local pressure and temperature used for interpolation are obtained from the flow properties correlation.

The heat transfer coefficients,  $h$ , and adiabatic wall temperatures,  $T_{aw}$ , are determined along the air side of the nozzle wall using these models. These values are then used to specify the air side boundary conditions for one time step of the finite element analysis.

**(iii) Water side of the nozzle wall:**

Steady state heat transfer during forced convection, subcooled nucleate boiling in an annular passage is predicted by the correlation of Shah [7,8,9]. This correlation assumes the total convective heat flux is the sum of the single-phase convection heat flux and the nucleate boiling heat flux,

$$q = q_{spc} + q_{nb},$$

where,  $q$  = two-phase convection heat flux,

$q_{spc}$  = single-phase convection heat flux,

$q_{nb}$  = nucleate boiling convection heat flux.

The single-phase heat flux, for turbulent flow, is determined from the Dittus-Boelter equation,

$$\frac{q_{spc}}{(T_{wall} - T_s)} = 0.023 \left( \frac{GD_{eq}}{\mu} \right)^{0.8} Pr^{0.4} \left( \frac{k}{D_{eq}} \right) = h_{sp},$$

where,  $D_{eq}$  = equivalent annulus diameter,

$G$  = mass flux,

$h_{sp}$  = single-phase convection heat transfer coefficient

$k$  = thermal conductivity,

$Pr$  = Prandtl number,

$T_s$  = static temperature,

$T_{wall}$  = wall temperature,

$\mu$  = absolute viscosity.

All quantities are evaluated at the local static temperature.

The nucleate boiling convection heat flux is determined from the correlation of experimental data for fully developed flow boiling. This follows the recommendation of Bergles and Rohsenow [10] when they demonstrated the nucleate boiling convection heat flux should not be determined with a pool boiling correlation.

The Shah correlation for forced convection, subcooled nucleate boiling in an annular passage is expressed as,

$$q = h_{sp} [(T_{wall} - T_{sat}) \text{Max}(230Bo^{1/2}, 1) + \sigma(T_{sat} - T_s)] = h_{tp}(T_{wall} - T_s),$$

where,  $Bo$  = boiling number =  $q/(i_{fg}G)$ ,

$i_{fg}$  = heat of vaporization,



$h_{tp}$  = two-phase convection heat transfer coefficient,

$T_{sat}$  = saturation temperature at local static pressure.

Also,

$$\sigma = \begin{cases} 0, & \text{for fully developed boiling} \\ 1, & \text{for local or partial boiling} \end{cases}$$

Here, local or partial boiling occurs when,

$$\frac{(T_{sat} - T_s)}{(T_{wall} - T_{sat})} > 2 \quad \text{or} \quad > 6.3 \times 10^4 Bo^{5/4},$$

otherwise, fully developed boiling is assumed.

If no boiling is present (i.e.  $T_{wall} < T_{sat}$ ), then the heat transfer coefficient is that for single-phase convection,  $h = h_{sp}$ . Otherwise, the heat transfer coefficient is that for two-phase convection from the Shah correlation,  $h = h_{tp}$ , which already includes a contribution from single-phase convection.

The nucleate boiling convection heat flux predicted by the Shah correlation (and subsequently used to obtain the two-phase convection heat transfer coefficient) must be compared to a predicted critical heat flux. The critical heat flux model used is derived from the Rousar-Chen model [11] for flat plates. Fred Shope at Calspan modified the Rousar-Chen critical heat flux by correlating data from curved plate flows to account for transverse flow acceleration effects due to the curvature. The Shope-Rousar-Chen correlation for critical heat flux in curved plate flows is given by

$$q_{chf} = [730 + 131.778(1 - e^{-0.000981082V})(T_{sat} - T_s)] \left[ 1 + 0.2(1 - e^{-0.003V^2/R/g}) \right],$$

where,  $g$  = gravitational acceleration ( $\text{ft s}^{-2}$ ),

$q_{chf}$  = critical heat flux ( $\text{Btu ft}^{-2} \text{ s}^{-1}$ ),

$R$  = radius of curvature ( $\text{ft}^{-1}$ ),

$T_s$  = static temperature ( $^{\circ}\text{R}$ ),

$T_{\text{sat}}$  = saturation temperature at local static pressure ( $^{\circ}\text{R}$ ),

$V$  = flow velocity ( $\text{ft s}^{-1}$ ).

The flow properties of water through the annular passage are determined by application of the steady state conservation laws to a one-dimensional control volume with area change. A control volume is assumed with the known quantities,

$A_{\text{in}}$  = inlet area,

$A_{\text{out}}$  = exit area,

$A_{\text{wet}}$  = wetted surface area,

$D_{\text{eq}}$  = equivalent annulus diameter,

$\dot{m}$  = mass flow rate,

$p_{\text{in}}$  = inlet static pressure,

$\dot{Q}$  = heat transfer rate into control volume,

$T_{\text{in}}$  = inlet static temperature,

$\mu$  = absolute viscosity,

$\rho$  = constant mass density.

Now, from conservation of mass in the control volume, the inlet and exit velocities must be

$$V_{\text{in}} = \frac{\dot{m}}{A_{\text{in}}\rho}, \text{ and } V_{\text{out}} = \frac{\dot{m}}{A_{\text{out}}\rho}.$$

The expression for conservation of momentum in the control volume is given by

$$p_{\text{in}}A_{\text{in}} - p_{\text{out}}A_{\text{out}} + \left( \frac{p_{\text{in}} + p_{\text{out}}}{2} \right) (A_{\text{out}} - A_{\text{in}}) - \tau A_{\text{wet}} = \dot{m}(V_{\text{out}} - V_{\text{in}}).$$

Here the turbulent wall shear stress  $\tau$  can be determined with Prandtl's universal law of friction for smooth pipes [12], and the known values  $D_{\text{eq}}$ ,  $V_{\text{in}}$ ,

$V_{out}$ ,  $\mu$ , and  $p$ . This leaves exit pressure as the only unknown in the momentum equation.

Conservation of energy for the control volume, assuming no work being done, is given by

$$\left( h_{out} + \frac{V_{out}^2}{2} \right) - \left( h_{in} + \frac{V_{in}^2}{2} \right) = \frac{\dot{Q}}{\dot{m}},$$

where,  $h_{in}$  = inlet specific enthalpy,

$h_{out}$  = exit specific enthalpy.

This equation is used in combination with the known values  $p_{in}$ ,  $p_{out}$ ,  $T_{in}$ , and the thermodynamic relations for water,

$$h_{in} = f(p_{in}, T_{in}) \text{ and } h_{out} = f(p_{out}, T_{out}),$$

to solve for the exit static temperature of the control volume.

Note that the Shah correlation and the method for determining local flow properties are coupled, due to the equivalence of the two-phase convection heat flux and the control volume heat transfer rate per unit heated area. For this reason, iteration between determining the local flow properties and determining the two-phase convection heat flux is required.

The water transport properties are obtained from the standard thermodynamic relations for subcooled water [13,14].

The heat transfer coefficients,  $h$ , and local static temperatures,  $T_s$ , are determined along the water side of the nozzle wall using these models. These values are then used to specify the water side boundary conditions for one time step of the finite element analysis.

## **Results**

Using this method of analysis, an axisymmetric conjugate heat transfer solution for the HEAT-H1 Mach 1.8 nozzle was obtained. The Mach 1.8 nozzle

has been shown to survive at the run conditions used in this analysis. These conditions are,

Air total pressure:	126.5 atm
Air total temperature:	9,000° R
Air total enthalpy:	3,480 Btu/lb <sub>m</sub>
Water mass flow rate:	11.54 lb <sub>m</sub> /s
Water inlet temperature:	557° R
Water inlet pressure:	1,000 psia

The effective properties for air were determined to be

Gas constant:	0.07400 Btu lb <sub>m</sub> <sup>-1</sup> °R <sup>-1</sup>
Specific heat ratio:	1.24
Total temperature:	7,513° R

Also, a constant Prandtl number of 0.72 was used for the air side. The effective total temperature corresponds to the boundary layer edge total temperature for the given run conditions in the Mach 1.8 nozzle. This effective total temperature (not the nominal total temperature of 9,000° R), was used for the determination of flow properties on the air side of the nozzle.

The algorithm was marched in time with a step size of 0.00001 seconds. After a solution time of 0.065 seconds (6,500 time steps), the 1-norm of the nodal temperature change dropped from 4.2% to 0.18%. The maximum nodal temperature change dropped from 0.54% to 0.0059%. At this point, neither the nozzle wall melting temperature, nor the critical heat flux along the water side of the nozzle had been reached.

Results from this solution are compared to results from the Calspan one-dimensional analysis. Nozzle wall temperature distributions for the air side

air and water side of the Mach 1.8 nozzle are shown in Fig. 5 and Fig. 6, respectively. Nozzle wall heat flux distributions for the air side and water side of the Mach 1.8 nozzle are shown in Fig. 7 and Fig. 8, respectively.

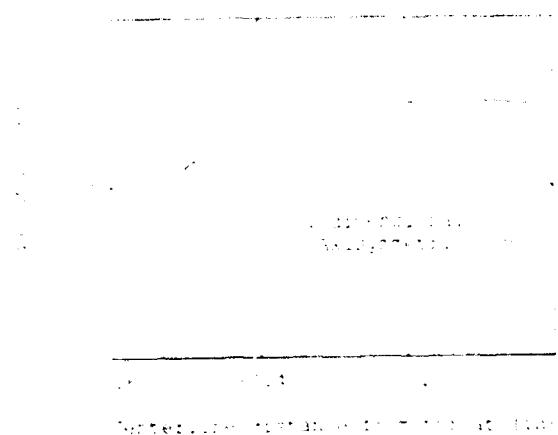


Fig. 5 Air side temperature distribution for the HEAT-H1 Mach 1.8 nozzle.

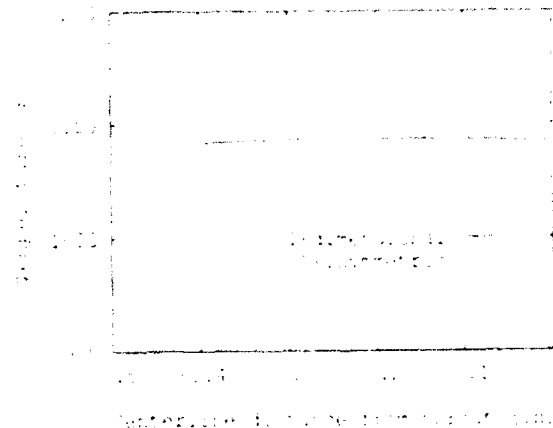


Fig. 6 Water side temperature distribution for the HEAT-H1 Mach 1.8 nozzle.

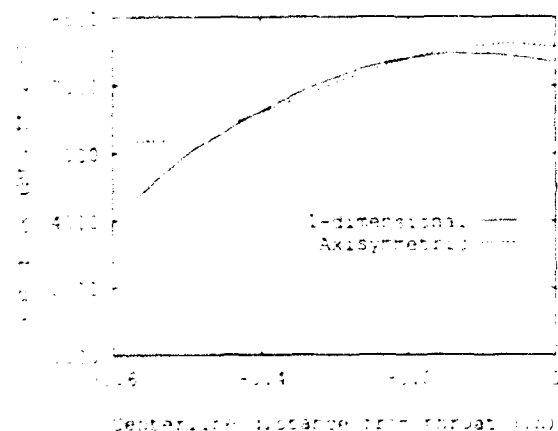


Fig. 7 Air side heat flux distribution for the HEAT-H1 Mach 1.8 nozzle.

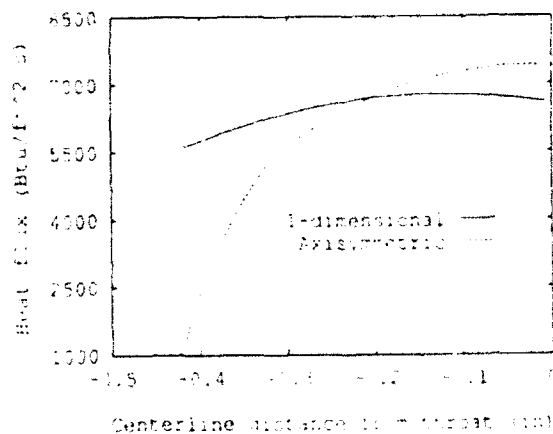


Fig. 8 Water side heat flux distribution for the HEAT-H1 Mach 1.8 nozzle.

The lower limit of centerline distance on these graphs corresponds to the upstream nozzle flange location. The effects of the flange were not

included in the one-dimensional analysis. The most striking differences between the one-dimensional analysis and the axisymmetric analysis occur near this region of the nozzle. The abrupt temperature change of the axisymmetric result in Fig. 6 demonstrates the influence of the multidimensional thermal effects which cannot be addressed by a one-dimensional approach. This rapidity of temperature change also indicates that the admittedly coarse finite element mesh should be refined in this region.

### Conclusion

The development of a method for unsteady, axisymmetric, conjugate heat transfer analysis has been accomplished, and preliminary results indicate its feasibility. However, useful application of this method requires refinement of its individual components, and further investigation of experimentally verifiable test cases. The space restriction of this report prevents mentioning more than a few potential improvements.

The current flow model for the water side of the nozzle should be replaced with an axisymmetric, incompressible, viscous flow solver. This is required to ascertain the degree of recirculation as the flow winds between the nozzle flange and cooling jacket at the water inlet. Refer back to Fig. 3 for the flow path of water in the HEAT-H1 Mach 1.8 nozzle.

The effects of finite element mesh refinement and solution time step size must be investigated. At present, only one finite element mesh (see Fig. 4) has been used. This mesh probably represents an upper limit on coarseness. Conjugate heat transfer solutions should be obtained with progressively finer meshes to understand the convergence behavior of the solution method. Also, a characteristic time for heat transfer in the nozzle geometry has not been adequately investigated.

## References

- [1] Horn, D. D. and Smith, R. T., "AEDC High-Enthalpy Ablation Test (HEAT) Facility Description, Development, and Calibration," AEDC-TR-81-10, July 1981.
- [2] Shope, F. L., "Conjugate Conduction/Convection/Nucleate-Boiling Heat Transfer with a High-Speed Boundary Layer," AIAA 3rd International Aerospace Planes Conference, Orlando, AIAA-91-5033, Dec. 1991.
- [3] Rochelle, J. K., Master's Thesis, University of Tennessee Space Institute, 1973.
- [4] Rohsenow, W. M., et al., *Handbook of Heat Transfer*, McGraw-Hill Book Company, 1973, pp. 7.151-7.154.
- [5] Ambrok, G. S., "Approximate Solution of Equations for the Thermal Boundary Layer with Variations in Boundary Layer Structure," *Soviet Physics/Technical Physics*, Vol. 2, No. 9, Sept. 1957, pp. 1979-1986.
- [6] Yos, J. M., "Revised Transport Properties for High Temperature Air and Its Components," Technical Release, Avco Systems Division, Nov. 1967, pp. 41-44.
- [7] Shah, M. M., "A General Correlation for Heat Transfer during Subcooled Boiling in Pipes and Annuli," *ASHRAE Transactions*, Vol. 83, Pt. 1, 1977, pp. 202-217.
- [8] Shah, M. M., "Generalized Prediction of Heat Transfer during Subcooled Boiling in Annuli," *Heat Transfer Engineering*, Vol. 4, No. 1, Jan.-Mar. 1983, pp. 24-31.
- [9] Cheremisinoff, I., et al., *Handbook of Heat and Mass Transfer, Volume 1: Heat Transfer Operations*, Gulf Publishing Company, 1986, pp. 387-391.
- [10] Bergles, A. E., and Rohsenow, W. M., "The Determination of Forced Convection Surface Boiling Heat Transfer," *Trans. ASME, Journal of Heat Transfer*, Aug. 1964, pp. 305-311.
- [11] Rousar, D. C., and Chen, F. F., "Cooling High Pressure Combustion Chambers with Super Critical Pressure Water," AIAA 24th Joint Propulsion Conference, Boston, AIAA-88-2845, July 1988.
- [12] Schlichting, H., *Boundary-Layer Theory*, McGraw-Hill Book Company, 1979, pp. 611-613.
- [13] *Supplementary Release on Transport Properties*, Sixth International Conference on the Properties of Steam, Nov. 1964.
- [14] *The 1967 IFC Formulation for Industrial Use*, International Formulation Committee of the International Conference on the Properties of Steam, Feb. 1967.

**CIVIL ENGINEERING LABORATORY**



**SETTING CRITERIA FOR HALON REPLACEMENT AGENTS**

Timothy Keen  
Graduate Student  
Fire Research and Testing Center

University of Florida  
FAC 101  
Gainesville, Florida 32611-2032

Final Report for:  
Summer Research Program  
Air Force Civil Engineering Support Agency

Sponsored by:  
Air Force Office of Scientific Research  
Bolling Air Force Base, Washington, D.C.

September 1992

## SETTING CRITERIA FOR HALON REPLACEMENT AGENTS

Timothy Keen  
Graduate Student  
Fire Research and Testing Center  
University of Florida

### Abstract

The program to replace CFC's in the U.S. Air Force inventory entails the examination of alternatives for the various major uses: refrigerants, solvents, and fire suppressants. Classic decision matrices allow a single evaluator to both rate and provide weights for each criterion against the various alternatives. The methodology described in this paper allows multiple evaluators to rank the criteria in order to generate criteria weights. A symbolic scheme to state the relative importance of the criteria and a system for "collapsing" the rankings are described.

## SETTING CRITERIA FOR HALON REPLACEMENT AGENTS

Timothy Keen

### INTRODUCTION

The Montreal Protocol of 1987 and the Clean Air Act Amendments of 1990 have dictated that the class of chemicals known as chlorofluorocarbons (CFC's) be banned from production by January 1, 1995 and from use by January 1, 2000. Largely used as refrigerants, CFC's also play an important role as firefighting agents where clean fire suppression is important. In computer and communications facilities it is desirable to extinguish the various classes of fires that may occur with minimal disruption to ongoing operations and without adding to the damage caused by the fire suppression method. Use of water sprinklers, foams, or dry chemicals necessitate extensive and expensive cleanup operations after a fire. A subset of CFC's known as Halons has provided clean fire suppression capability for over two decades. Halon 1301 has been the clean agent most frequently employed to protect computer/communications facilities from fire damage and collateral damage that would be a function of the fire suppression method. A replacement agent for Halon 1301 is being sought to meet the requirements of the Clean Air Act Amendments of 1990 and a set of criteria and a decision analysis matrix will be necessary to select the follow-on agent.

## DISCUSSION

In another U.S. Air Force program to select a replacement agent for Halon 1211, used in flightline firefighting and in facility and aircraft portable firefighting units, a decision analysis matrix was utilized rather late in the program to provide a framework to justify the selection of the replacement agent. Halon 1211 was compared to PFC-614 and HCFC-123 to determine which of the replacement agents should be selected for further testing. Criteria such as agent effectiveness, acute toxicity, system conversion costs, purchase cost, ozone depletion potential (ODP), and greenhouse warming potential (GWP) were used as the basis for agent evaluation. The decision analysis method used in this application had several undesirable features that need to be corrected for future programs such as the one that will replace Halon 1301 as the total flood agent for occupied facilities.

First, each criterion in the decision matrix was treated identically in terms of weight. Fire suppression efficiency received the same weight or emphasis as toxicity and cost. For all practical purposes it could be said that no weighting scheme was utilized.

Second, the scoring of each alternative was accomplished by awarding three points for the alternatives with the best performance against each criterion and one point against each criterion showing the worst performance. This spread of points is

not enough to significantly differentiate good performance from poor performance.

Third, several criteria are actually counted a number of times. The category entitled future regulatory phase-out is accounted for several times since ODP, GWP, HCFC's, EPA SNAP approval are all connected with this topic. Consequently out of 16 criteria, four are counted against possible phase-out.

This example illustrates several of the pitfalls associated with decision matrix methods. A set of clearly defined criteria are necessary in order to set up the decision matrix. Each criterion should appear once in the matrix and there should be no interdependence of criteria. This latter recommendation may not always be possible to implement. Nonetheless it should be utilized to the maximum extent possible. A weighting scheme should also be employed in order to indicate the relative priority of the criteria. The weights should be generated using input from several experts in the field in order to minimize the influence of any single rater on the final weights generated.

It is this latter point that is perhaps the most difficult to achieve. There is not at the present time any method that allows the opinions of several experts to be synthesized into a single outcome. In order to accomplish this synthesis, a method for aggregating the inputs of multiple experts is required.

## METHODOLOGY

The approach to solving the problem of allowing multiple experts to generate criteria weights was to create a system in which experts could provide their inputs in a symbolic fashion. The symbolic system consisted of listing the criteria from left to right with the most important criteria being in the leftmost position and the least important in the far right position. The following symbols are used to define the relationship of the left criterion to its right neighbor:

- = the criteria are of about equal importance
- > the left criterion is slightly more important
- >> the left criterion is more important
- >>> the left criterion is far more important

For a scheme with 12 criteria, the following is an example of how a single evaluator might rank the criteria:

5>6=4>>7>>>1=2>3>>8>>>9=10>11>>13=12

Note that each criterion is used only once and that all criteria are ranked.

The criteria that will be used in the Halon 1301 program are as follows:

- \* Fire Suppression Efficiency
- \* Low Residue Level
- \* Low Electrical Conductivity
- \* Low Metals Corrosion
- \* High Metals Compatibility
- \* Stability under Long Term Storage
- \* Low Toxicity
- \* ODP
- \* GWP
- \* Cost
- \* Production Availability
- \* Extinguishment Concentration
- \* Conversion Cost of Facility

In order to determine or create a suitable decision analysis system, these criteria must be analyzed and ranked by a number of experts. The rankings created by the "experts" will then be aggregated into a single expression of relative importance of the criteria. A weight will be generated for each criterion by virtue of the relative importance of the criterion. Each alternative will be scored on a relative basis against each criterion, the weights will be applied, and a total score will be calculated. Sensitivity analysis will be utilized to determine the affects of the weighting scheme on the outcomes. Finally the agents with the greatest

number of points will be selected for advanced testing.

## **CONCLUSIONS**

The decision analysis matrix system described in this report is a new approach to generating weights for a wide variety of applications. The application used to test this method is the selection of a Halon 1301 replacement agent. However the main outcome is that the general principles described herein can be used for any case that would benefit from the inputs of multiple experts in the generation of criteria weights.



A SIMPLIFIED MODEL FOR PREDICTING  
JET IMPINGEMENT HEAT TRANSFER

MARK E. KITHCART

FINAL REPORT  
SEPTEMBER 1992

AFOSR GRADUATE STUDENT SUMMER RESEARCH PROGRAM  
TYNDALL AFB, FLORIDA

## ABSTRACT

The effects of high temperature ( $\cong 1000^{\circ}\text{F}$ ) jet blast on runway surfaces has become a significant concern, particularly with the increasing prominence of V/STOVL (vertical/short take-off and landing) aircraft. In an attempt to model vertical jet impingement heat transfer, a computer code has been developed based on the Hiemenz solution of the Navier-Stokes equations. The primary use of the code would be to provide values of heat flux and wall temperature for use as input to finite element solid mechanics modeling codes, which are currently being used by the Jet Blast Research Group at Tyndall AFB Florida, to predict stresses in pavement materials as a result of high heat flux. Preliminary results show the code to be in good agreement with experimental data and analytical calculations. A research project is being proposed which would continue development of the computer program.

## BACKGROUND

In recent years, significant effort has been directed towards the problem of concrete runway degradation as a result of periodic, intense, heat output from military jet engines. With the increasing prominence of V/STOVL technology, the problems associated with this phenomenon have become more acute.

As with most research-oriented engineering endeavors, the solution to this problem has been sought using both experimental and analytical approaches. Experiments have focused on testing concrete pavement (both on-site and in the lab) in order to determine the mechanisms of material breakdown as a result of thermal input. Full-scale high heat (approximately 1000 °F) conditions have been produced using actual aircraft for experimental purposes.

Analytically, the focus has been on modeling the mechanisms which lead to concrete failure due to thermal stresses, with the more complex models considering the inhomogenous nature of concrete and the cosequential differential thermal stresses created by heating. Finite element codes are used mostly in these efforts. In terms of modeling the actual thermal (convective) output of jet engines, and the resultant temperature and heat flux generated when directed towards a surface, many of the codes of this type (Bose [1], and Aelhoff *et al* [2], for example) are Navier-Stokes solvers. Navier-Stokes codes, however, are inherently complex and require expensive computer hardware (supercomputers mainly) in order to obtain accurate solutions in a short time period.

## THE CODE

Due in part to the considerations expressed above, a short, easy to use jet impingement heat transfer code has been written to predict temperature and heat flux when modeling normal jet impingement on a solid surface. The code is based on the Hiemenz stagnation region solution of the Navier-Stokes equations as presented by White [3]. The governing differential equation is solved in an iterative manner using a fourth-order Runge-Kutta numerical integration algorithm coupled with an interpolation scheme based on the half-interval method. Surface temperatures are calculated using an equation derived by Abelhoff *et al* based on steady-state conditions.

The primary function of the code will be to provide heat flux and temperature data which could be used as input for codes which model thermal-induced stresses in concrete. Another possible use would be as a means of calculating the minimum thickness of runway protective coatings. At this time, materials are being tested and evaluated for use as coatings for concrete pavement, and a method for determining the minimum, or critical thickness of the material(s) would be beneficial from an economic point of view.

Preliminary results obtained from the code are encouraging, in that agreement has been achieved with both experimental (Table 1) and analytical results [4]. Particularly significant is the fact that the free jet itself is not modeled; known values of the jet exit temperature, exit velocity, along with the nozzle diameter and height are all that are required as input. With these values, the jet velocity and temperature near a surface some distance from the nozzle can be calculated using the general equation [5]

$$P = C\sqrt{\frac{D}{Z}}$$

where P represents the desired parameter to be calculated, C is a constant being equal to 0.9 when calculating velocity, and 0.85 for calculating temperature. The values of the constant were derived using results from calculations based on the method of [4] as a guide. The variables D and Z are the nozzle velocity and height, respectively.

At this time, the code predicts steady-state values of heat flux and surface temperature. Future efforts aimed at refining the code will include modifications to allow calculation of transient values of the parameters mentioned above. Also, an attempt will be made to model oblique-jet heat transfer as well. Finally, the model will be extended to the wall jet region of an impinging flow in order to predict heat transfer away from the stagnation point. A Research Initiation Proposal is being prepared at this time, and subject to approval by AFOSR, these objectives will be the focus of the research effort.

## SUMMARY

A computer code has been developed to model jet impingement heat transfer, in order to provide thermal input conditions for finite element codes used to predict the effects of thermal stresses on runway surfaces. Initial runs have resulted in data which is in good agreement with experimental data and calculations using analytical methods. Research is proposed which would continue development and refinement of the code.

TABLE 1

Measured versus predicted temperatures  
from F-18 Auxiliary Power Unit impingement tests (Ref. 6)

Mode*	Measured Surface Temp.	Predicted Temp.	Error
MES (Sch. I)	322 °F	323.2 °F	0.4%
ECS (Sch. I)	328 °F	320.6 °F	2.3%
ECS (Sch. II)	345 °F	320.6 °F	7.1%

\*Note: Data from production nozzle tests.

#### REFERENCES

1. Bose, T. K., "Laminar Impingement Jet Mach Number and Temperature Effects on Heat Transfer," *Journal of Thermophysics and Heat Transfer*. Vol. 6, No. 2, April-June 1992, pp. 308-313.
2. Abelhoff, P. A., Van Dalsem, W. R., Dougherty, F. D. "Thermal Interaction Between an Impinging Jet and a Conducting Surface," Abstract of a Proposed Paper for the AIAA 5th Aerodynamics Conference, August 20-22, 1990, Portland, Oregon.
3. White, F. M., *Viscous Fluid Flow*, McGraw-Hill Co., NY, 1974, pp. 172-184.
4. Burniester, L. C., *Convective Heat Transfer*, John Wiley and Sons, Inc., NY, 1983, pp 312-319.
5. Ranjaratnam, N., *Turbulent Jets*, Elsevier Scientific Publishing Co., NY, 1976.
6. Houck, M. L., "F-18 Auxiliary Power Unit Exhaust Gas Footprint Evaluation", Naval Air Propulsion Center NAPC-LR-90-18, November 1990.



**FRANK J. SEILER RESEARCH LABORATORY**

**VELOCITY AND VORTICITY MEASUREMENTS  
IN  
TRANSIENT OSCILLATORY SEPARATING BOUNDARY LAYER FLOWS**

**B. Terry Beck  
Associate Professor  
Department of Mechanical Engineering**

**Paul K. Berg  
Graduate Student  
Department of Mechanical Engineering**

**Kansas State University  
Durland Hall  
Manhattan, KS 66506**

**Final Report for:  
Summer Faculty Research Program/  
Graduate Student Research Program  
Frank J. Seiler Research Laboratory  
US Air Force Academy**

**Sponsored by:  
Air Force Office of Scientific Research  
Bolling Air Force Base, Washington, D.C.**

**September 1992**

**VORTICITY AND VELOCITY MEASUREMENTS  
IN  
TRANSIENT OSCILLATORY SEPARATING BOUNDARY LAYER FLOWS**

B. Terry Beck  
Associate Professor

Paul K. Berg  
Graduate Student

Department of Mechanical Engineering  
Kansas State University

**Abstract**

The velocity and vorticity distribution within a transient oscillatory separating boundary layer was investigated using a single-component Laser Doppler Velocimeter System. The flow was initiated above a flat plate test model by means of a computer-controlled rotating spoiler (flap), mounted above the model surface. The tests were conducted in a water tunnel test facility, and dye injection was also utilized for visualization of the flow separation phenomena. The rotating spoiler subjected the plate below to a time-dependent spatial pressure gradient, inducing periodic flow separation and vortex shedding from the region near the plate and downstream of the spoiler. Measurements of both horizontal and vertical velocity components were made by rotating the optics of the LDV system. These profile measurements were obtained for discrete angular flap positions, thus mapping out the spatial and time-dependent flow field downstream of the flap. From the separate velocity component profiles, a computerized scanning algorithm was implemented to obtain both scan-averaged velocity and velocity gradient fields. Using this technique resulted in remarkably smooth results, in spite of the limited spatial resolution of the transient measurements. Clear evidence of reverse flows and flow bifurcation is indicated from the measurements near the region of boundary layer separation. The effect of flap frequency on the separation phenomena was also investigated.

THIS PAGE INTENTIONALLY LEFT BLANK

# MULIVARIABLE TRANSFER FUNCTIONS AND OPTIMAL PASSIVE DAMPING FOR A SLEWING PIEZOELECTRIC LAMINATE BEAM

Thomas E. Alberts  
Associate Professor

and

Travis DuBois  
Graduate Student

Department of Mechanical Engineering and Mechanics  
Old Dominion University  
Norfolk, Virginia 23529-0247

Final Report for:  
Summer Research Program  
Frank J. Seiler Research Laboratory

Sponsored by:  
Air Force Office of Scientific Research  
Bolling Air Force Base, Washington, D.C.

July 31, 1992

# MULTIVARIABLE TRANSFER FUNCTIONS AND OPTIMAL PASSIVE DAMPING FOR A SLEWING PIEZOELECTRIC LAMINATE BEAM <sup>1</sup>

Thomas E. Alberts & Travis V. DuBois  
Department of Mechanical Engineering and Mechanics  
Old Dominion University  
Norfolk, Virginia 23529-0247, USA  
Phone: (804) 683-3736  
Email: talberts@mem.odu.edu

## Abstract

This report presents the development and experimental verification of a distributed parameter model for a slewing beam system with piezoelectric actuators and sensors. The beam is pinned at the proximal end, an endpoint motion sensor is attached at the distal end, and patches of thin piezoelectric laminates attached to its surface. The differential equation of motion for this system is transformed to Laplace domain transfer functions after application of the appropriate boundary conditions. Transfer functions relating the various actuator/sensor pairs are developed. The transfer functions are rationalized using a Maclaurin series expansion so that there is no need to assume mode shapes. Experimental results, which verify the model, are presented using a beam experiment at the US Air Force Academy, Frank J. Seiler Research Laboratory. The existing clamped beam experiment was modified through the addition of a hinged joint and appropriate instrumentation to carry out this work.

The transfer functions are eventually to be used to develop and experimentally validate a simultaneously optimal active and passive damping design for the experimental system. A preliminary damping design is discussed and initial experimental results presented.

---

<sup>1</sup> This work performed in collaboration with Dr. H.R. Pota of the Australian Defence Force Academy.

# A NEURAL NETWORK MODEL OF THE UNSTEADY AERODYNAMICS ON A PITCHING WING

William E. Faller  
Research Associate  
BioServe Space Technologies  
University of Colorado, Boulder

## ABSTRACT

A straight wing having a NACA 0015 cross-section and rectangular planform was attached to a circular splitter plate. Starting at 0 degrees this configuration was pitched to an angle of 60 degrees which exceeded the static stall angle. During the pitch history surface pressure readings were obtained from 15 pressure transducers spaced between 0 and 90% chord. A total of 54 data records were obtained which covered 6 non-dimensional pitch rates ( $\alpha^+$ ) ranging between 0.0001 and 0.2 and 9 span locations ranging between 0% and 80% span. These unsteady, vortex dominated flows were used to develop an artificial neural network (ANN) model of the unsteady flow field. The ANN model was then used to mathematically quantify the three-dimensional, vortex dominated, unsteady aerodynamics of the phenomenon. A linear equation system (LES) was derived from the weight matrices of the ANN. The results indicated that the derived ANN/LES yielded a predicted pressure field over time which was within 1% of the experimental data for all the  $\alpha^+$  cases at all the span locations. Further, the results indicated that the ANN/LES could accurately extrapolate to any non-dimensional pitch rate between 0.0001 and 0.2 and to any span location from the wing root, 0%, to near the wing tip at 80% span. And, in all cases, the linear equation system yielded identical results to those obtained using the ANN. Thus, it was possible to mathematically quantify the unsteady flow fields obtained experimentally. The techniques described contribute significantly to the computational methods available for modeling three-dimensional unsteady flow fields.

# A NEURAL NETWORK MODEL OF THE UNSTEADY AERODYNAMICS ON A PITCHING WING

William E. Faller

## INTRODUCTION

A large number of studies have looked at the unsteady separated flows associated with sinusoidally or constant-rate pitched airfoils (Robinson and Luttges, 1983; Adler and Luttges, 1985; Ashworth et al., 1986; Ashworth and Luttges, 1986; Robinson and Luttges, 1986; Robinson et al., 1986; Helin et al., 1986; Robinson and Wissler, 1988; Schreck and Luttges, 1988; Ashworth et al., 1989; Schreck and Luttges, 1989; Huyer et al., 1990; Klinge et al., 1990; Horner et al., 1990; Klinge et al., 1991; Huyer and Luttges, 1991; Schreck et al., 1991; Schreck and Helin, 1992) These studies have characterized the unsteady aerodynamics using flow visualization techniques, hot-wire anemometry and surface pressure readings. Further, these studies have looked at both two- and three-dimensional unsteady flow fields.

Instances of very high lift have been correlated with the generation and existence of a leading-edge vortex on the upper surface of the airfoil. The time history during convection of the leading-edge vortex in turn determines the amount of lift and moments generated. Further, the surface pressure and lift distributions on the airfoil are not the same at the wing root and tip. The interaction between the leading-edge vortex and the wing tip vortex has been shown to be a highly three-dimensional phenomenon. While such time and space dependent changes in both the vortex dynamics and lift profile are desirable from an applications standpoint they pose significant difficulties in both the prediction and control of these transient factors.

One possibility to overcome these difficulties might be to learn the time and space dependencies of leading-edge vortex generation and convection using an artificial neural network (ANN). Neural networks could then be utilized as a model of the flow field which



would function effectively across a wide range of flight regimes. Then, depending on the effectiveness of the neural network in predicting the unsteady flow field it might be possible to attempt to control this phenomenon. However, before any type of control system can be attempted, it is first necessary to determine the efficacy of neural networks in describing and predicting three dimensional unsteady flow fields.

The use of neural networks for both system identification and as control systems is emerging as one possible technique for handling complex non-linear systems. The use of neural networks to serve as system models has been addressed by (Chu et al., 1990; Chen et al., 1990; Ljung, 1991; Parlos et al., 1991). These studies have shown that non-linear models of complex systems can be developed using ANNs. The use of neural networks in the design of control systems has also been addressed (Nguyen and Widrow, 1990; Narendra and Mukhopadhyay, 1992; Sartori and Antsaklis, 1992). Using a neural-network system model a second neural network is trained to control the emulator (model). In this fashion, a neural network can be trained to solve a highly non-linear control problem. More recently the use of neural networks in the design of aircraft control systems has been addressed (Ha, 1991; Troudet et al., 1991; Linse and Stengel, 1992; Steck and Rokhsaz, 1992). In these examples, neural networks were trained to correlate functions such as stick position with various aerodynamic coefficients. Thereby, providing the opportunity to implement parts of an aircraft control system using neural networks.

The work described herein addresses the difficulties associated with learning the complex time and space dependencies of leading-edge vortex generation and convection using a neural network architecture. As shown, in the results, a highly successful system model can be developed using ANNs. Further, as shown, a mathematical model of the pressure gradient field over the surface of the airfoil can be derived from the ANN weight matrices. This work makes a significant contribution to both the computational techniques available for modeling three-dimensional, vortex dominated, unsteady flow fields as well

as to techniques which should facilitate the control of this phenomenon.

## METHODS

The data acquisition system is shown schematically in Fig. 1. A straight wing having a NACA 0015 cross-section and rectangular planform was attached to a circular splitter plate. Starting at 0 degrees this configuration was dynamically pitched at a constant rate about the wing quarter chord to an angle of 60 degrees which exceeded the static stall angle. During the pitch history surface pressure readings, in the form of pressure coefficients, were obtained from 15 pressure transducers spaced between 0 and 90% chord. A total of 54 data records were obtained which covered 6 non-dimensional pitch rates ( $\alpha^+$ ) ranging between 0.0001 and 0.2 and 9 span locations ranging between 0%, the wing root at the splitter plate, and 80% span, near the wing tip. Each data record was comprised of a total of 200 points which covered the full duration of the pitch cycle. As shown in Fig. 1, for each data sample acquired, all 15 pressure ports readings were simultaneously stored as pressure coefficients. The recorded spatial and temporal histories of the unsteady, vortex dominated flows were then used to develop an artificial neural network (ANN) model of the unsteady flow field. The ANN model was then used to mathematically quantify the three-dimensional, vortex dominated, unsteady aerodynamics of a NACA 0015 airfoil pitched at constant rates beyond the static stall angle.

To model the unsteady flow field a paradigm based on the backpropagation learning algorithm was developed. This is schematically shown in Fig. 2. The objective, in this case, of the training paradigm was to model the pressure gradient field using an ANN. Thus, post-training this model (ANN) could be used to predict the pressure coefficients at time  $(t+\Delta)$  given the pressure coefficients at any time  $(t)$ . In general, aerodynamic parameters of interest which can be characterized in this fashion would include the time-

Figure 1

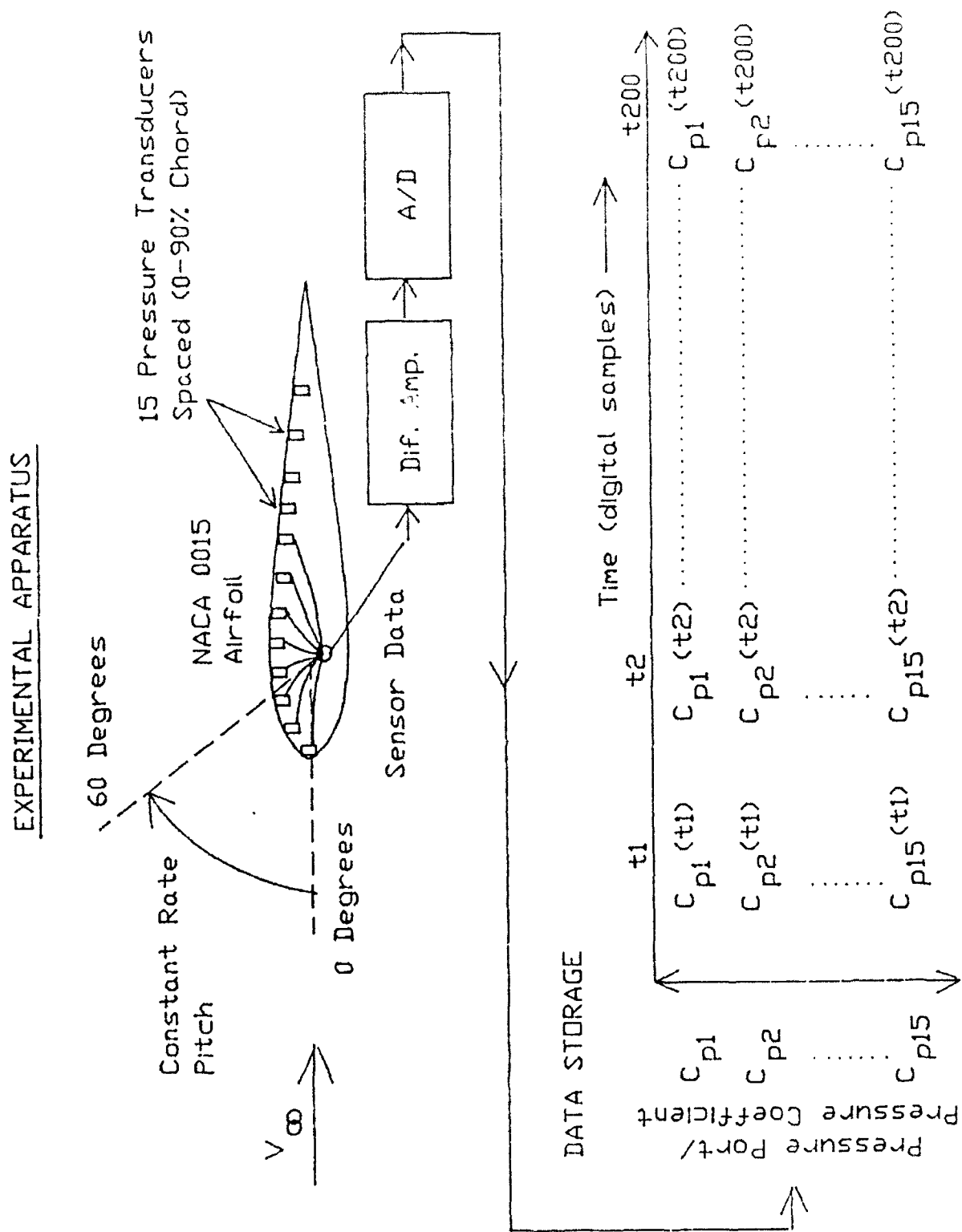
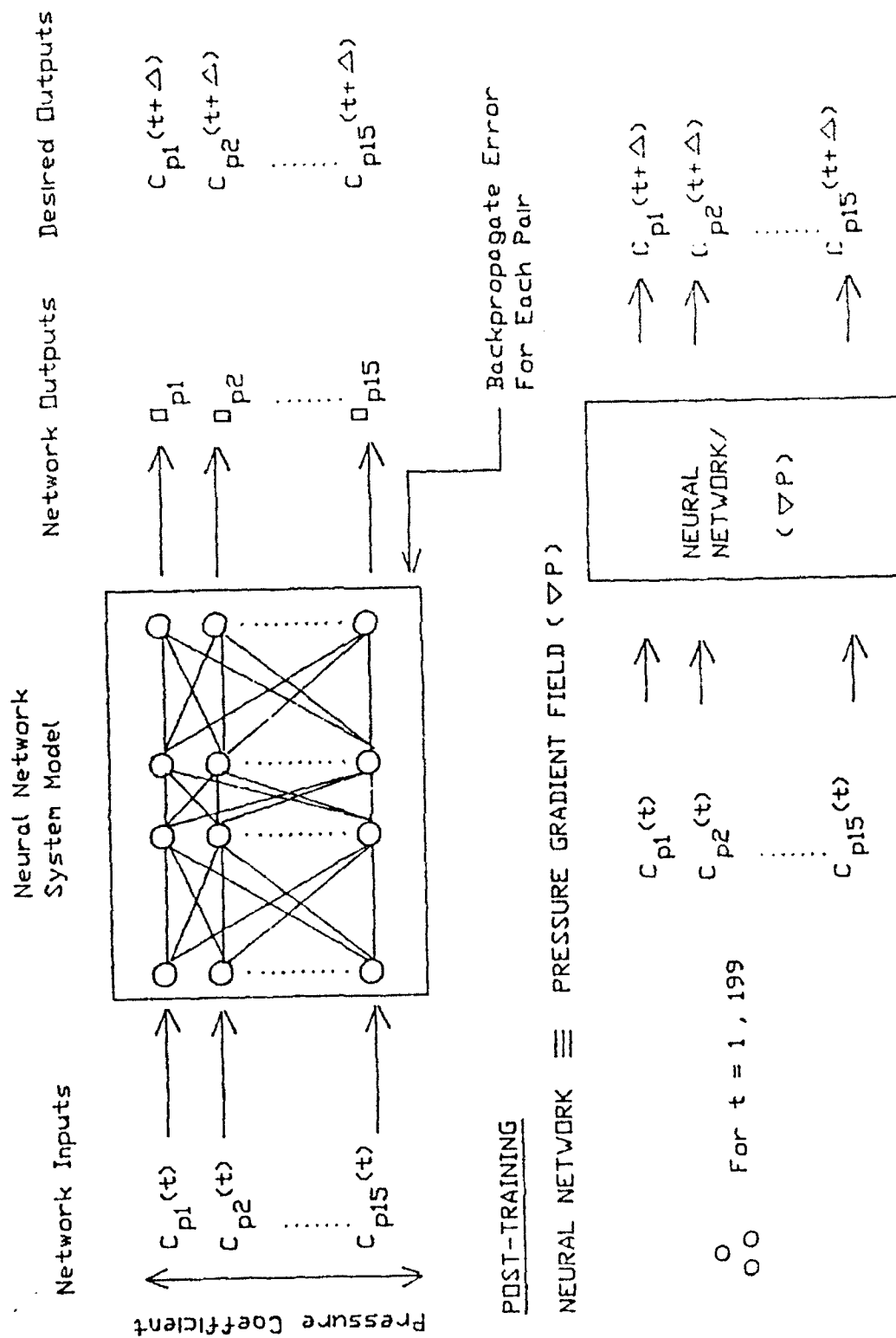


Figure 2

LEARNING THE PRESSURE GRADIENT FIELD USING BACKPROPAGATION



varying surface pressure profile (pressure coefficients), the integrated aerodynamic parameters (lift, drag & moments) as well as leading-edge vortex initiation, convection and shedding.

As shown schematically in Fig. 2 a feed-forward architecture with 2 hidden layers was used which had the following configuration. The ANN had 15 inputs for the pressure coefficients on the upper surface of the airfoil ( $C_{p1} - C_{p15}$ ). Each hidden layer was comprised of 32 units and the output layer was comprised of 15 units. Bias units were included for each of the two hidden layers. A "pattern association" paradigm was used where the input to the network at time ( $t$ ) was used to predict the output at time ( $t+\Delta$ ). In this case, the input was the 15 pressure coefficients at time ( $t$ ) and the targeted output was the 15 pressure coefficients at time ( $t+\Delta$ ). For each pitch history 199 consecutive pressure changes were required to be "learned" by the ANN over the full pitch cycle. Thus, the ANN had to "learn" the pressure gradient field necessary to generate the time-varying pressure profiles recorded experimentally. Training was based on a supervised gradient descent algorithm, backpropagation, where the training set was comprised of 5 data sets, (5 non-dimensional pitch rates at a location 40% span from the splitter plate). The learning rate was  $\eta=0.05$  for all layers, momentum was  $\alpha=0.2$  for both hidden layers and  $\alpha=0.0$  for the output layer. During training the 5 data sets were presented randomly with the stipulation that each data set be presented an equal number of times. The initial weights were set randomly between -0.25 and 0.25 and training was performed until the sum-squared error was less than 1% for all the training sets.

A novel approach was taken in defining the activation functions utilized in the network architecture. A modified quasi-linear function was used which had the following characteristics.

- (1)  $y = 0$  and  $W_{ij} = 0.5 * W_{ij}$  for  $x \leq -a$  ( $a = 4.0$ )
- (2)  $y = x/2a + 0.5$  for  $-a < x < a$  ( $a = 4.0$ )

$$(3) \quad y = 1 \quad \text{and} \quad W_{ij} = 0.5 * W_{ij} \quad \text{for } x \geq a \quad (a = 4.0)$$

As implied by the equations these units were not permitted to maintain a saturated,  $y=0$  or  $y=1$ , output during training. This was implemented by specifying that all weighted inputs ( $W_{ij}$ ) to a saturated unit were to be halved ( $W_{ij} = 0.5 * W_{ij}$ ). Thus, following training all activation values, for all units, were within the linear region of the activation function, Eqn. 2. Since the output of each unit was linear, the contribution of any input unit to any output unit remains linearly separable from all other inputs. Therefore, the contribution of each individual input unit to each individual output unit can be uniquely determined. Thus, post-training, it was possible to determine, from the weight matrices of the ANN, a single coefficient which described the contribution of each input unit to each output unit. In other words, the weight matrices could be compressed into a coefficient matrix  $[A]$  plus a constant vector  $[K]$ .

$$(4) \quad [A] [C_p(t)] + [k] = [C_p(t+\Delta)]$$

This in turn is nothing more than a linear equation system (LES) which acts upon the input vector, the pressure profile at time ( $t$ ), imposes the derived pressure gradient field  $[A]$  and yields the pressure profile at time ( $t+\Delta$ ). Thus, the ANN model facilitates the capability to mathematically quantify the unsteady aerodynamics of a NACA 0015 airfoil pitched at constant rates beyond the static stall angle. Since, based on the technique employed, the ANN and LES must yield absolutely identical solutions, during all further analyses the ANN/LES were used interchangeably to predict the time-varying pressure profiles.

Post-training to evaluate the performance of the ANN/LES each of the 54 data records was tested. Sum-squared errors were calculated for each individual unit. These values were then summed and averaged to yield a mean sum-squared error per unit. To determine the time-varying error, linear correlations between the predicted pressure profiles and the experimental data were calculated for each output unit. Again, a mean value was calculated for each unit yielding a mean correlation ( $r$ ). And, the performance of the

ANN/LES was verified graphically by co-plotting the recorded pressure profiles (raw data), the predicted pressure profiles and the difference between the two plots (raw data - predicted). Thus, post-training, it was possible to determine not only how well the ANN/LES predicted the training set data, but how well the ANN/LES could extrapolate (generalize) to both other non-dimensional pitch rates and to other span locations not used in constructing the model.

## RESULTS

Post-training the weight matrices of the ANN were used to derive a linear equation system (LES) of the type shown in Eqn. 4. The equation system is shown in Fig. 3. As shown the LES acts upon an input vector, the pressure profile at any time ( $t$ ), imposes the derived pressure gradient field  $[A]$  and yields the pressure profile at the corresponding time ( $t+\Delta$ ). An explicit relationship has been derived where the influence of the pressure gradient field on each pressure coefficient can be described by the constant coefficients in the  $[A]$  matrix. Thus, post-training either the ANN model or the LES model can be used to predict the pressure coefficients at time ( $t+\Delta$ ) given the pressure coefficients at any time ( $t$ ). Note: since the ANN and LES yield absolutely identical solutions in all cases, during all further analyses the ANN/LES were used interchangeably to predict the time-varying pressure profiles.

To test whether or not the artificial neural network (ANN)/linear equation system (LES) accurately described both the generation and convection of the leading-edge vortex as well as the highly three-dimension nature of the flow field, the equation system was tested against all the available data sets. The graphical analysis for predicting a non-dimensional pitch rate of 0.01 at the 40% span location are shown in Figs. 4,5 and 6. In each figure the upper left hand corner depicts the pitch history of the airfoil. The instantaneous angle of attack, in degrees, is shown along the ordinate and non-dimensional

Figure 3

A														
0.9880	0.1193	0.0082	-0.0634	-0.0760	-0.0026	-0.0671	-0.0481	0.0373	0.0105	-0.0192	0.1096	-0.0114	-0.0247	-0.0063
-0.0417	0.7074	0.4161	0.0716	-0.1287	-0.0879	0.0161	-0.0301	-0.0164	-0.0233	-0.0130	0.1167	-0.0055	0.0149	-0.0448
0.0393	0.5085	0.3233	0.0673	-0.0386	-0.0511	-0.0021	-0.0301	0.0051	0.0029	0.0051	0.1085	-0.0111	-0.0043	-0.0607
0.0471	0.2649	0.2785	0.1130	0.2222	0.0174	-0.0697	-0.0829	0.0252	0.0442	0.0430	0.1237	-0.0123	-0.0195	-0.1048
0.0303	-0.1631	0.2057	0.1886	0.6812	0.1821	-0.1413	-0.1868	0.0277	0.0726	0.0734	0.1289	-0.0059	-0.0215	-0.1546
0.0073	-0.2627	0.1336	0.1415	0.6127	0.3151	0.0782	-0.1052	-0.0021	0.0092	0.0166	0.0831	0.0078	0.0120	-0.0983
-0.0038	-0.1178	0.0599	0.0155	0.1661	0.3543	0.4336	0.1264	-0.0070	-0.0537	-0.0503	0.0304	0.0128	0.0334	-0.0092
0.0235	0.0258	-0.0089	-0.0597	-0.1989	0.1780	0.4971	0.3452	0.1140	0.0721	0.0382	0.0633	-0.0191	-0.0492	-0.0503
0.0308	-0.0111	-0.0167	-0.0118	-0.0948	0.0020	0.2189	0.2985	0.1984	0.2171	0.1728	0.1390	-0.0255	-0.1035	-0.1264
0.0199	-0.0501	-0.0084	0.0305	0.0344	-0.0829	0.0113	0.2067	0.2096	0.2743	0.2501	0.1986	0.0092	-0.0803	-0.1223
0.0052	-0.0556	-0.0014	0.0422	0.0931	-0.0918	-0.0859	0.1080	0.1507	0.2393	0.2647	0.2358	0.0860	0.0217	-0.0212
-0.0077	-0.0243	0.0028	0.0261	0.0659	-0.0534	-0.0712	0.0440	0.0670	0.1506	0.2202	0.2294	0.1494	0.1250	0.0962
-0.0094	0.0030	-0.0020	0.0019	0.0169	-0.0065	-0.0266	0.0009	-0.0105	0.0607	0.1663	0.2116	0.2009	0.2143	0.2036
0.0314	0.0042	-0.0236	-0.0267	-0.0323	0.0374	0.0189	-0.0280	-0.0704	-0.0175	0.1061	0.1780	0.2260	0.2682	0.2779
0.0579	0.0023	-0.0383	-0.0448	-0.0638	0.0666	0.0514	-0.0438	-0.1058	-0.0681	0.0608	0.1463	0.2305	0.2894	0.3123
K														
$C_{p1}(t+\Delta)$	$C_{p1}(t)$	-0.0849												
$C_{p2}(t+\Delta)$	$C_{p2}(t)$	-0.1743												
$C_{p3}(t+\Delta)$	$C_{p3}(t)$	-0.1166												
$C_{p4}(t+\Delta)$	$C_{p4}(t)$	-0.0998												
$C_{p5}(t+\Delta)$	$C_{p5}(t)$	-0.1126												
$C_{p6}(t+\Delta)$	$C_{p6}(t)$	-0.0648												
$C_{p7}(t+\Delta)$	$C_{p7}(t)$	-0.0238												
$C_{p8}(t+\Delta)$	$C_{p8}(t)$	-0.0666												
$C_{p9}(t+\Delta)$	$C_{p9}(t)$	-0.0583												
$C_{p10}(t+\Delta)$	$C_{p10}(t)$	-0.0637												
$C_{p11}(t+\Delta)$	$C_{p11}(t)$	-0.0268												
$C_{p12}(t+\Delta)$	$C_{p12}(t)$	0.0080												
$C_{p13}(t+\Delta)$	$C_{p13}(t)$	-0.0082												
$C_{p14}(t+\Delta)$	$C_{p14}(t)$	-0.0083												
$C_{p15}(t+\Delta)$	$C_{p15}(t)$	-0.0877												

$$[A] [C_p(t)] + [k] = [C_p(t+\Delta)]$$



Figure 4

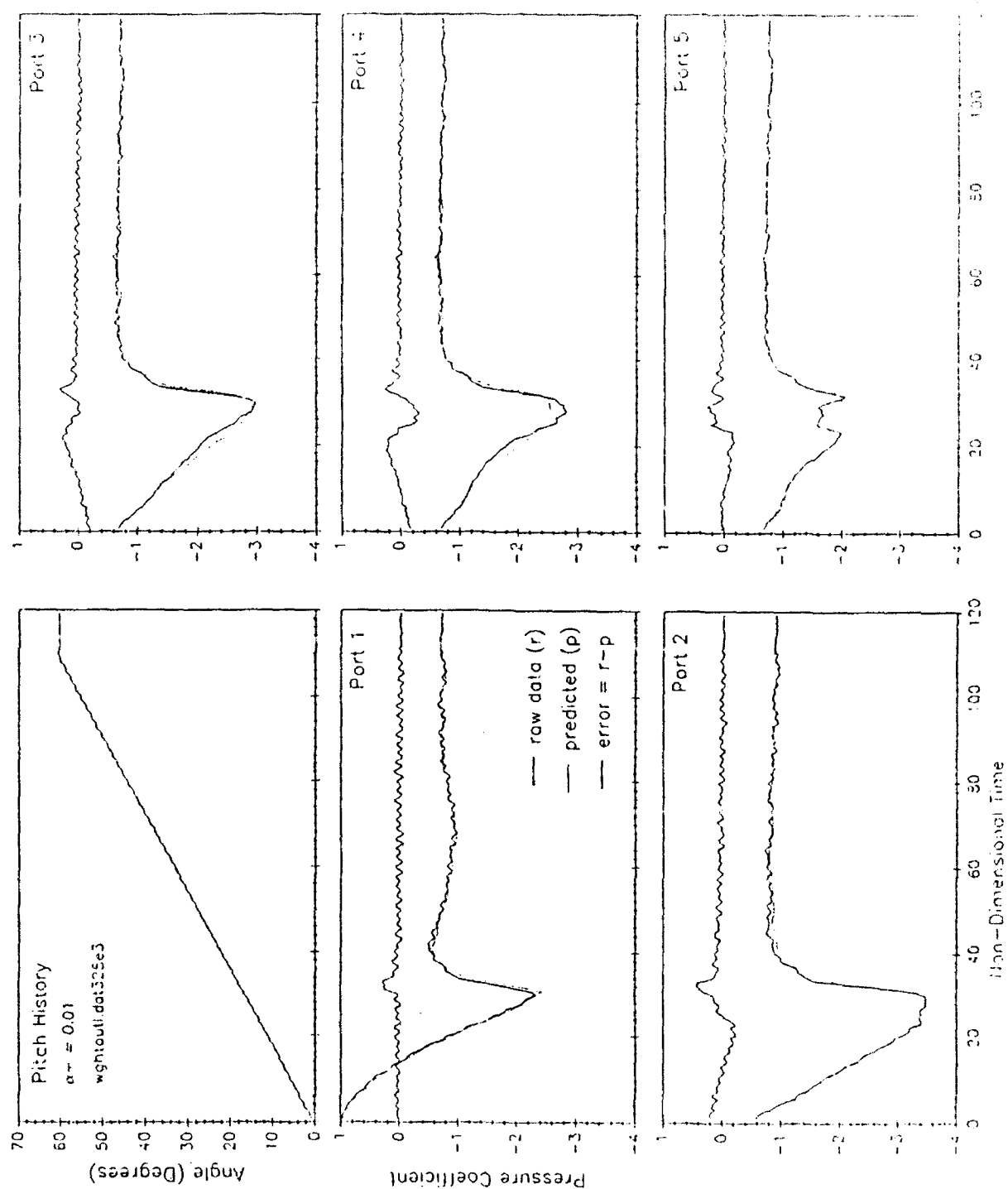


Figure 5

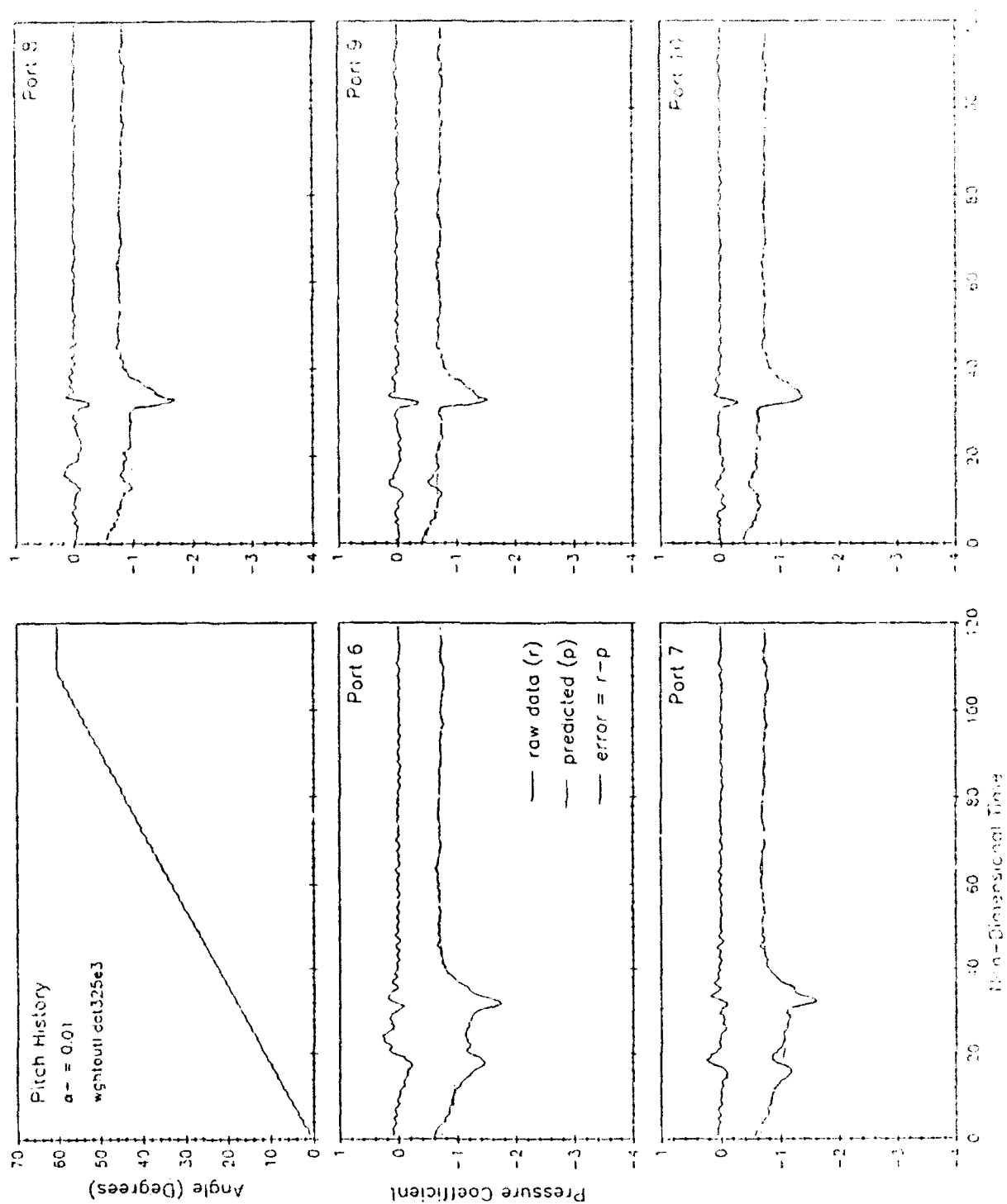
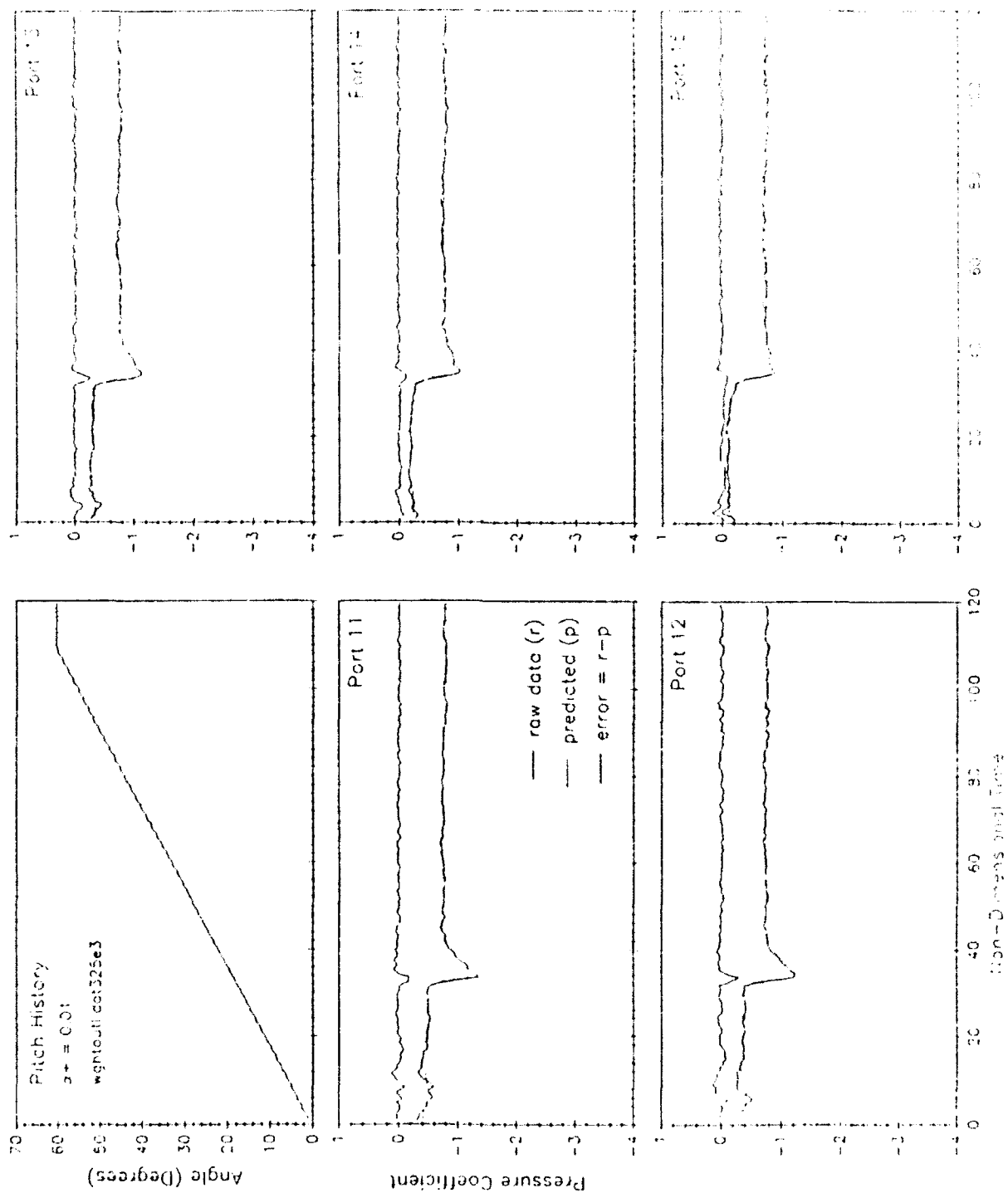


Figure 6



time is along the abscissa. Each figure is labeled with the pressure port number from which the data was obtained. Port 1 is at the leading edge of the airfoil and port 15 is at 90% chord, near the trailing edge of the airfoil. In each figure the ordinate is the pressure coefficient and the abscissa is non-dimensional time. In all figures the experimental (raw) data is shown as a solid line, the predicted data as a dotted line and the error (raw - predicted) as a solid line. Figure 4 shows the results for the prediction of the pressure coefficients obtained from ports 1-5. Figure 5 shows the results for the prediction of the pressure coefficients obtained from ports 6-10. And, figure 6 shows the results for the prediction of the pressure coefficients obtained from ports 11-15. In all cases, based on the sum-squared error, the equation system yielded a predicted pressure field over time which was within 1% of the experimental data, Table 1.

Table 1. Shown is the sum-squared error for the predicted pressure coefficients at each pressure port as well as the correlational coefficient (r) for a linear correlation between the experimental and predicted pressure profiles.

port	ssq	correlation (r)	port	ssq	correlation (r)
1	1.91E-03	0.996	2	5.19E-03	0.993
3	3.53E-03	0.994	4	4.03E-03	0.988
5	2.33E-03	0.983	6	2.63E-03	0.962
7	1.03E-03	0.970	8	1.31E-03	0.940
9	1.24E-03	0.939	10	7.53E-04	0.965
11	6.64E-04	0.978	12	1.01E-03	0.975
13	7.28E-04	0.986	14	3.59E-04	0.995
15	6.56E-04	0.993			

The average correlation (r) was  $0.977 \pm 1.87E-02$  and the average sum-squared error for each unit was  $1.82E-03 \pm 1.44E-03$ . Clearly, the model can accurately predict the time varying pressure profiles.

Moreover, even though the ANN had only been trained on a subset of the available  $\alpha^+$  cases at one span location, the results indicated that the ANN/LES was accurate for all the  $\alpha^+$  cases at all the span locations. Further, the results indicated that the equation system could accurately extrapolate to any non-dimensional pitch rate between 0.0001 and 0.2 and

to any span location from the wing root, 0%, to near the wing tip at 80% span. Consistent results were obtained for ANNs trained at different span locations. In addition, to further quantify these results a 4-layer non-linear ANN, based on a standard sigmoidal activation function, was trained in an identical fashion. The results from the non-linear model were then compared with those of the linear equation system. While increased performance was noted using a non-linear network, overall the performance as measured by the sum-squared error increased by roughly 0.5%. Thus, the linear equation system (LES)/ ANN was shown to provide a model which was highly accurate and showed no appreciable difference in performance as compared to a non-linear model of the unsteady flow field.

## DISCUSSION

A novel technique was developed and tested for computationally modeling three dimensional, vortex dominated, unsteady flow fields using artificial neural networks (ANN). Using backpropagation and a modified quasi-linear activation function an ANN model of the unsteady flow field for a NACA 0015 airfoil pitched at constant rate was derived. The ANN model was trained to "learn" the pressure gradient field underlying the time-varying pressure profiles recorded experimentally. The ANN model was then used to mathematically quantify the three-dimensional, vortex dominated, unsteady aerodynamics of the phenomenon. A linear equation system (LES) which yielded identical results to the ANN model was derived from the weight matrices of the ANN. Thus, post-training either the ANN model or the LES model could be used to predict the pressure coefficients at time  $(t+\Delta)$  given the pressure coefficients at any time  $(t)$ .

The method was tested on a total of 54 data records which covered 6 non-dimensional pitch rates ( $\alpha^+$ ) ranging between 0.0001 and 0.2 and 9 span locations ranging between 0%, the wing root at the splitter plate, and 80% span, near the wing tip. The results indicated that the derived ANN yielded a predicted pressure field over time which

was within 1% of the experimental data for all the  $\alpha^+$  cases at all the span locations. Further, the results indicated that the ANN could accurately extrapolate to any non-dimensional pitch rate between 0.0001 and 0.2 and to any span location from the wing root, 0%, to near the wing tip at 80% span. Further, in all cases the results indicated that the LES yielded identical results to those obtained using the ANN. Based on these results, it is reasonable to believe that not only can neural networks be used to model unsteady flow fields, but that they can provide new insights into the underlying physics of three-dimensional unsteady aerodynamics.

Based on these results it is hypothesized that the underlying physics of the problem must be contained in both the ANN and linear equation system. Thus, the modified quasi-linear ANNs described herein provide an analytical tool with which to mathematically identify the physics of three-dimensional, vortex dominated, unsteady flow fields. Further, since explicit equation systems, which are unattainable by other means, can be derived using the paradigm described, the development of system models and control systems targeted at controlling the behavior of the leading-edge vortex on a pitching wing should now be possible. In addition, this approach should be equally applicable to other types of data as well as a large number of control problems where it is either very difficult or impossible to derive a set of linear-control laws for the system being modeled. And, this technique should make it possible to derive a linear equation system which approximates the output of any non-linear artificial neural network.

## REFERENCES

- Adler, J.N. and Luttges, M.W. (1985) Three-Dimensionality in Unsteady Flow About a Wing, AIAA Paper #85-0132.
- Ashworth, J. and Luttges, M.W. (1986) Comparisons in Three-Dimensionality in the Unsteady Flows Elicited by Straight and Swept Wings, AIAA Paper #86-2280-CP, pp 446-455.
- Ashworth, J., Waltrip, M. and Luttges, M.W. (1986) Three-Dimensional Unsteady Flow Fields Elicited by a Pitching Forward Swept Wing, AIAA Paper #86-1104, pp 1-9.
- Ashworth, J., Crisler, W. and Luttges, M.W. (1989) Vortex Flows Created by Sinusoidal Oscillation of Three-Dimensional Wings, AIAA Paper #89-2227.
- Chen, S., Billings, S.A. and Grant, P.M. (1990) Non-linear System Identification Using Neural Networks, *Int. J. Control*, 51:1191-1214.
- Chu, S.R., Shoureshi R. and Tenorio, M. (1990) Neural Networks for System Identification, *IEEE Control Systems Magazine*, April, pp 31-34.
- Ha, C.M. (1991) Neural Networks Approach To AIAA Aircraft Control Design Challenge, AIAA Paper #91-2672-CP, pp 653-663.
- Horner, M.B., Addington, G.A., Young III, J.W. and Luttges, M.W. (1990) Controlled Three-Dimensionality in Unsteady Separated Flows About a Sinusoidally Oscillating Flat Plate, AIAA Paper #90-0689, pp 1-12.
- Huyer, S., Robinson, M. and Luttges, M. (1990) Unsteady Aerodynamic Loading Produced by a Sinusoidally Oscillating Delta Wing, AIAA Paper #90-1536.
- Huyer, S.A. and Luttges, M.W. (1991) The Vortex Kinematics Associated with an Oscillating Delta Wing, AIAA Paper #91-1797, pp 1-15.
- Klinge, J.D., Schreck, S.J. and Luttges, M.W. (1990) Dynamic Effects on High Frequency Unsteady Flow Structures, AIAA Paper #90-0690.
- Klinge, J., Schreck, S., Robinson, M. and Luttges, M. (1991) Three-Dimensional Flow Field Kinematics near the Root of an Oscillating Wing, AIAA Paper #91-3264, pp 1-14.
- Linse, D.J. and Stengel, R.F. (1992) Identification of Aerodynamic Coefficients Using Computational Neural Networks, AIAA Paper #92-0172, pp 1-11.
- Ljung, L. (1991) Issues in System Identification, *IEEE Control Systems Magazine*, January, pp 25-29.
- Narendra, K.S. and Mukhopadhyay, S. (1992) Intelligent Control Using Neural Networks, *IEEE Control Systems Magazine*, April, pp 11-18.
- Nguyen, D.H. and Widrow, B. (1990) Neural Networks for Self-Learning Control Systems, *IEEE Control Systems Magazine*, April, pp 18-23.

Parlos, A.G., Atiya, A.F. and Sunkel, J.W. (1991) Parameter Estimation in Space Systems Using Recurrent Neural Networks, AIAA Paper #91-2716-CP, pp 1010-1022.

Robinson, M.C. and Luttges, M.W. (1983) Unsteady Separated Flow: Forced and Common Vorticity About Oscillating Airfoils, Workshop on Unsteady Separated Flow, USAFA, August 10-11, 1983, pp 117-126.

Robinson, M.C. and Wissler, J.B. (1988) Unsteady Surface Pressure Measurements on a Pitching Rectangular Wing, AIAA Paper #88-0328.

Sartori, M.A. and Antsaklis, P.J. (1992) Implementations of Learning Control Systems Using Neural Networks, IEEE Control Systems Magazine, April, pp 49-57.

Schreck, S.J. and Luttges, M.W. (1988) Unsteady Separated Flow Structure: Extended K Range and Oscillations Through Zero Pitch Angle, AIAA Paper #88-0325, pp 1-14.

Schreck, S.J. and Luttges, M.W. (1989) Occurrence and Characteristics of Flow Reversal During the Genesis of Unsteady Separated Flows, AIAA Paper #89-0142.

Schreck, S.J., Addington, G.A. and Luttges, M.W. (1991) Flow Field Structure and Development Near the Root of a Straight Wing Pitching at Constant Rate, AIAA Paper #91-1793, pp 1-13.

Schreck, S.J. and Helin, H.E. (Accepted) Unsteady Vortex Dynamics and Surface Pressure Topologies on a Pitching Wing, AIAA Reno Conference.

Steck, J.E. and Rokhsaz, K. (1992) Use of Neural Networks in Control of High Alpha Maneuvers, AIAA Paper #92-0048, pp 1-7.

Troudet, T., Garg, S. and Merrill, W.C. (1991) Neural Network Application to Aircraft Control System Design, AIAA Paper #91-2715-CP, pp 993-1009.



NMR RELAXATION STUDIES OF MICRODYNAMICS IN  
CHLOROALUMINATE MELTS

Pamela A. Shaw  
Graduate Student  
Department of Chemistry

Wichita State University  
Wichita, Kansas 67208

Final Report for:  
Summer Research Program  
Frank J. Seiler Research Laboratory,  
USAF Academy, CO 80840-6528

Sponsored by:  
Air Force Office of Scientific Research  
Bolling Air Force Base, Washington, D.C.

August 1992

NMR Relaxation Studies of Microdynamics in  
Chloroaluminate Melts

Pamela A. Shaw  
Graduate Student  
Department of Chemistry  
Wichita State University

Abstract

The microdynamics of  $\text{EtAlCl}_2$  containing melts are examined by  $^{13}\text{C}$  NMR relaxation methods as a function of melt composition and temperature. Application of the Dual Spin Probe (DSP) method to these systems reveals interaction between (1) the  $\text{MEI}^+$  methyl group, (2) the terminal  $\text{CH}_3$  of the  $\text{MEI}^+$  ethyl group, and various  $\text{EtAlCl}_2$  containing species. Unlike  $\text{MEICl-AlCl}_3$  room temperature melts, there is no indication of interaction between the  $\text{MEI}^+$  ring  $\text{CH}'\text{s}$  and  $\text{EtAlCl}_2$ .

## INTRODUCTION

Room temperature molten salts consisting of mixtures of  $\text{AlCl}_3$  and 1-ethyl-3-methylimidazolium chloride ( $\text{MEICl}$ ), are of interest as aprotic solvents for studying a wide range of both organic and inorganic compounds [1-7]. These chloroaluminate molten salts possess considerable potential as battery electrolytes and various types of electrochemical agents [8-10].

The composition of a chloroaluminate melt has a considerable effect on its physical properties. The variations in physical properties of the melt are due to a combination of factors including ion-ion interactions [4], and Lewis acid-base properties. Chloroaluminate melts with  $\text{AlCl}_3$  present in excess (mole fraction,  $N$ , of  $\text{AlCl}_3 > 0.5$ ) are termed acidic with  $\text{AlCl}_4^-$  and  $\text{Al}_2\text{Cl}_7^-$  the predominant anions.

The use of NMR relaxation methods provides useful information about the dynamics and structure of various chemical systems and chloroaluminate systems in particular. In a previous work [11],  $^{13}\text{C}$  NMR relaxation measurements were used to investigate the motion and interactions of the MEI cation. The results indicate that  $\text{AlCl}_4^-$  in a  $\text{Na}^+_{0.2}\text{MEI}^+_{0.8}\text{AlCl}_4^-$  melt forms a complex by interacting with the C-2, C-4 and C-5 hydrogens on the  $\text{MEI}^+$  ring. This investigation was followed by studies [12,13] in which the Dual Spin Probe method [14] supported the existence of  $\text{MEI}(\text{AlCl}_4)_n^{(n-1)+}$  complexes in neutral ( $\text{AlCl}_3 = \text{MEICl}$ ) and  $\text{NaCl}$ -buffered melts.  $^{27}\text{Al}$ ,  $^{23}\text{Na}$  and  $^{13}\text{C}$  NMR relaxation results confirmed the presence of the chloroaluminate- $\text{MEI}^+$  complexes and yielded  $^{27}\text{Al}$  and  $^{23}\text{Na}$  liquid state quadrupole coupling constants [12,13].

Application of the Dual Spin Probe (DSP) relaxation method typically requires knowledge of  $^{13}\text{C}$  dipolar relaxation rates which are defined by (1), the basic equation in which the  $^{13}\text{C}$  nucleus is relaxed by  $^1\text{H}$  [15]:

$$R_1^{dd} = N_H (\hbar \gamma_C \gamma_H)^2 r_{CH}^{-6} \tau_{eff} \quad (1)$$

where  $R_1^{dd}$  ( $= 1/T_1^{dd}$ ) is the dipolar relaxation rate,  $N_H$  is the number of

hydrogens attached directly to the carbon atom,  $\gamma_C$  and  $\gamma_H$  are gyromagnetic ratios and  $r_{CH} = 1.09 \text{ \AA}$ .  $\tau_{eff}$  is the effective correlation time and varies exponentially with temperature. Equation (1) is operative while under the "extreme narrowing condition" ( $\omega\tau_{eff} \ll 1$ ) which is usually applicable for small molecules including the chloroaluminate melts[11].

$R_1^{di}$  is obtained by measuring  $T_1$ , the Nuclear Overhauser Enhancement factor,  $\eta$  ( $\eta_{max} = \gamma_H/2\gamma_C$ ) and using eqn (2) [16]:

$$R_1^{di} = \eta R_1 / 1.988 \quad (2)$$

The other part of the DSP method requires knowledge of quadrupolar relaxation rates for nuclei such as  $^{27}\text{Al}$  and  $^{23}\text{Na}$ . If there is a distortion from tetrahedral or cubic symmetry, nuclei such as  $^{27}\text{Al}$  and  $^{23}\text{Na}$  will be under the influence of an electric field gradient which produces the quadrupole interaction. The quadrupolar relaxation rate in the "extreme narrowing region" is given by(3) [15,17]:

$$R_1 = [3\pi^2(2I+3)/10I^2(2I-1)][1+(z^2/3)][e^2Qq/h]^2\tau_c \quad (3)$$

where  $I = 3/2$  for  $^{23}\text{Na}$  and  $5/2$  for  $^{27}\text{Al}$ ,  $eQ$  is the nuclear quadrupole moment,  $eq$  is the maximum component of the electric field gradient tensor, and  $z$  is the asymmetry parameter of the electric field gradient tensor ( $z = 0$  for  $\text{AlCl}_3$ ).

The quadrupole coupling constant, QCC, is given by:

$$\text{QCC} = [e^2Qq/h] \quad (4)$$

The DSP method has been applied to chloroaluminate melts[12,13] and has provided evidence that the ring hydrogens of  $\text{MEI}^+$  interact with the tetrachloroaluminate anion. The existence of these complexes has been supported by linear plots of  $^{13}\text{C}$  dipolar relaxation rates( $R_1^{di}$ ) vs. quadrupolar  $^{27}\text{Al}$

relaxation rates( $R_1$ ) that pass through the origin as predicted by equation (5):

$$R_1(^{13}\text{C})/N_{\text{H}}(\hbar\gamma_{\text{C}}\gamma_{\text{H}})^2r_{\text{CH}}^6 = R_1(^{27}\text{Al})/\alpha\chi^2 \quad (5)$$

where  $\alpha = [3\pi^2/10]\{(2I + 3)/I^2(2I - 1)\}[1 + (z^2/3)]$ , and  $QCC = \chi$ .

During this summer research program, the DSP method was applied to melts containing  $\text{MEICl}$ ,  $\text{AlCl}_3$ , and  $\text{EtAlCl}_2$ . The inclusion of  $\text{EtAlCl}_2$  provided a "baseline" as there is a covalent bond between the ethyl group and aluminum in  $\text{EtAlCl}_2$ . The existence of covalent bonding(or complexation) between quadrupolar and dipolar nuclei in a molecule results in a linear plot of eqn. (5) that passes through the origin. In the  $\text{MEICl-EtAlCl}_2$  melts reported herein, we observed a linear plot of eqn (5) that passed through the origin when applied to the terminal  $\text{CH}_3$  carbon in  $\text{EtAlCl}_2$  and one of the peaks in the  $^{27}\text{Al}$  NMR of the melts.

## EXPERIMENTAL

### Materials

The 1-ethyl-3-methylimidazolium chloride ( $\text{MEICl}$ ) and chloro-aluminate molten salts were prepared as described previously [1]. Ethylaluminum dichloride ( $\text{EtAlCl}_2$ ) was obtained from Aldrich. All materials were stored under anhydrous helium gas atmosphere in a dry box. All molten salt preparations and manipulations were performed in the dry box. Samples were loaded into 5 mm sample tubes, capped in the dry box, removed, and sealed immediately with a torch.

### NMR Measurements

$^{13}\text{C}$  NMR spin-lattice relaxation times were recorded this summer on a Varian Gemini-300 spectrometer at 75.43 MHz and  $^{27}\text{Al}$  NMR spin-lattice relaxation times were recorded previously on a Varian XL-300 spectrometer operating at 78.15 MHz. Temperature measurements were calibrated against methanol or ethylene glycol and

are accurate to within 0.5°C. Pulse widths(90°) were typically 8.6 (75.43 MHz) and 7.6(78.15 MHz)  $\mu$ s. Longitudinal relaxation times were measured by the the inversion-recovery method (180°- $\tau$ -90°-T) with T>10T<sub>1</sub>. At least 12 delay times( $\tau$ ) were used and the results fitted to a three parameter exponential. <sup>13</sup>C NOE measurements were made using the gated decoupler method[18]. It is likely that the error in the NOE measurements is in the 5-10% range[18].

## RESULTS AND DISCUSSION

The ability of both AlCl<sub>3</sub> and EtAlCl<sub>2</sub> to form C<sub>2u</sub> dimers[19,20] led us to examine the <sup>27</sup>Al spectra of: (1) neat EtAlCl<sub>2</sub>, (2) MEICl-EtAlCl<sub>2</sub> and (3) ternary melts (N = AlCl<sub>3</sub>/MEICl/EtAlCl<sub>2</sub>)[21]. The neat EtAlCl<sub>2</sub> <sup>27</sup>Al NMR spectrum contains two peaks [21]. Peak 1 is a broad downfield peak that dominates the spectrum. The second peak (upfield) overlaps peak 1 and is only a fraction of peak 1 in total peak area. Peak 2 collapses into peak 1 as the temperature is lowered from 60 to 25°C. These two aluminum sites are consistent with the extent of monomer-dimer formation in liquid EtAlCl<sub>2</sub>[21].

The MEICl-EtAlCl<sub>2</sub> (N = 0.5/0.5) melt <sup>27</sup>Al NMR spectrum also has two peaks. In this case, peak 1(downfield) is very broad while peak 2 is very sharp, and has a low peak area. Peak 2 increases slightly in area and peak 1 broadens as the temperature is lowered from 70 to 0°C. We have previously[21] made the tentative assignments of EtAlCl<sub>2</sub> for peak 1(downfield) and Et<sub>2</sub>Al<sub>2</sub>Cl<sub>3</sub> for peak 2.

In this study, we first apply the DSP method to the CH<sub>3</sub> carbon in EtAlCl<sub>2</sub> and <sup>27</sup>Al NMR peaks 1 and 2 from several melt combinations and neat EtAlCl<sub>2</sub>. Fig. 1 contains the results for <sup>27</sup>Al peak 1(downfield) and Fig. 2 contains the results for <sup>27</sup>Al peak 2. The fact that both plots are linear and pass through the origin, indicate that: (1) the DSP method is appropriate for these systems and (2) the species associated with each peak contains EtAlCl<sub>2</sub>. Furthermore, the slopes of these lines can be used to calculate the relative quadrupole coupling constants for the EtAlCl<sub>2</sub>-containing species in solution.

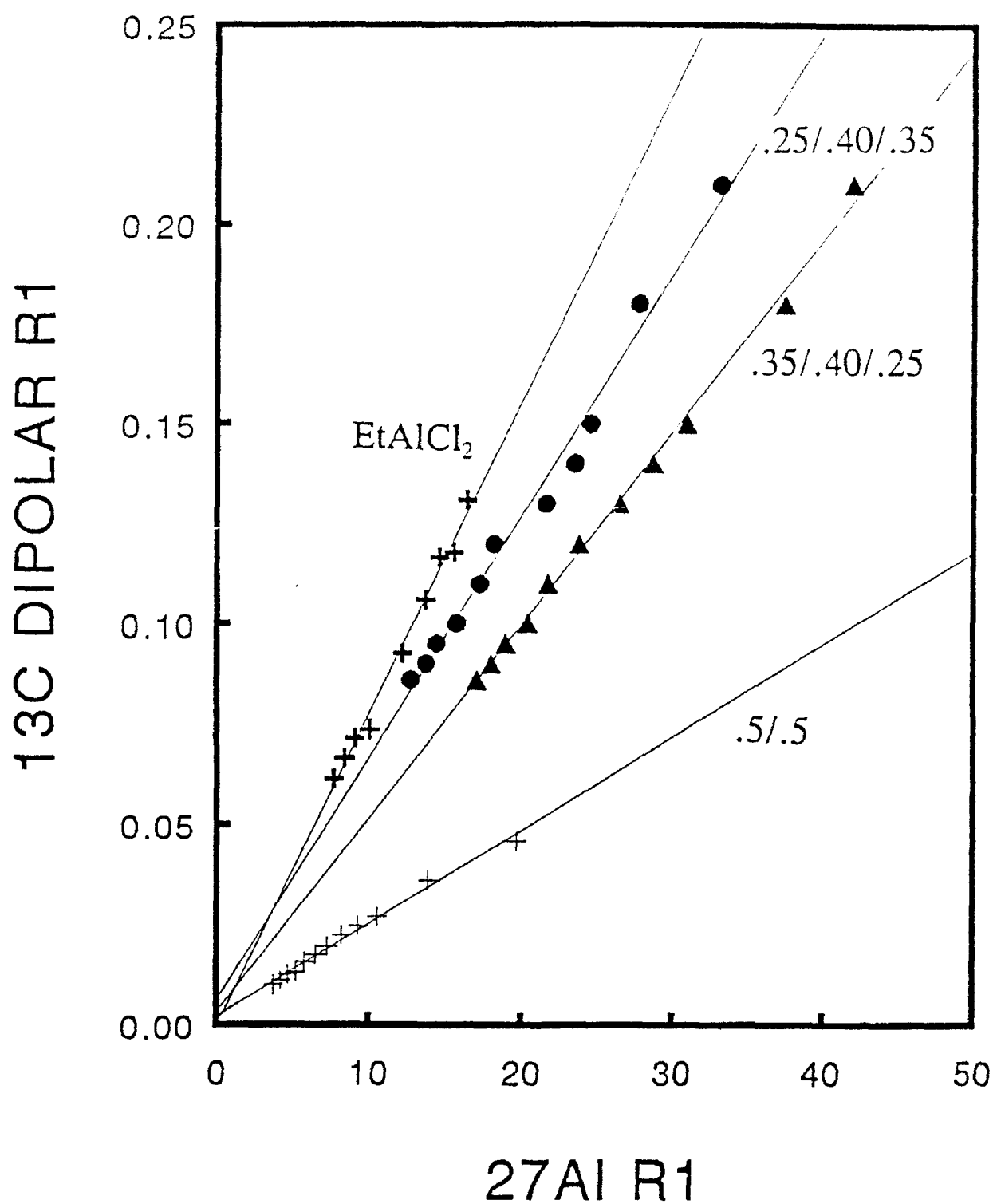


Fig. 1. <sup>13</sup>C Dipolar R1's vs <sup>27</sup>Al R1's (25 to 70°C) for Al peak 1 (127-131 ppm from Al(H<sub>2</sub>O)<sub>6</sub><sup>3+</sup>).

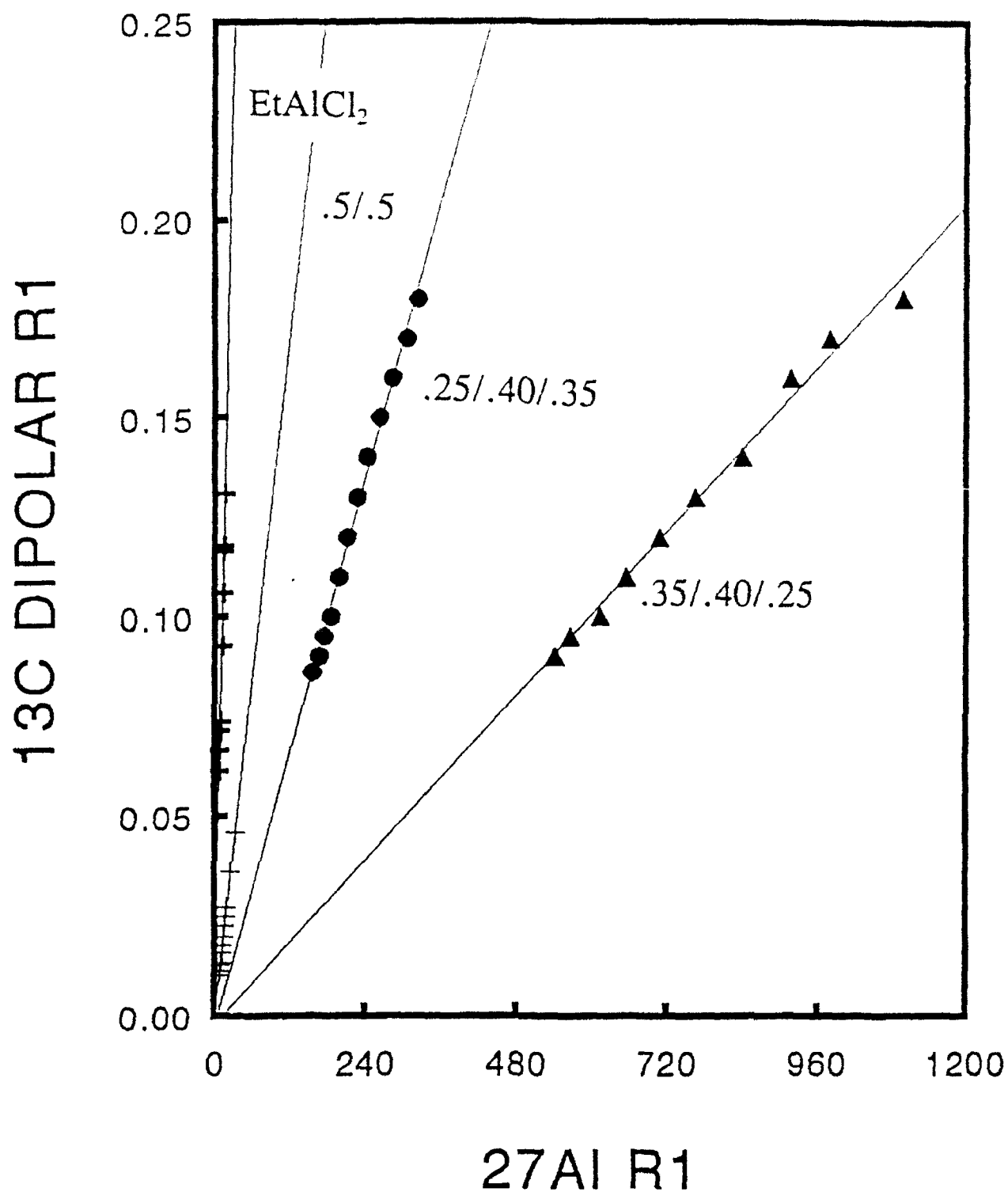


Fig. 2. <sup>13</sup>C Dipolar R1's vs <sup>27</sup>Al R1's (25 to 70°C) for Al peak 2 (102.5-103.0 ppm from Al(H<sub>2</sub>O)<sub>6</sub><sup>3+</sup>).



The QCC values obtained from Fig. 1(Al peak 1) are 171, 119, 106 and 93 MHz for the (.5/.5), (.35/.40/.25), (.25/.40/.35) melts and neat EtAlCl<sub>2</sub>, respectively. The QCC values obtained from Fig. 2(Al peak 2) are 6.9, 20, 11 and 93 MHz for the (.5/.5), (.35/.40/.25), (.25/.40/.35) melts and neat EtAlCl<sub>2</sub>(repeated).

Results of the Dual Spin Probe method (eqn. [5]) applied to the (.5/.5), (.35/.40/.25) and (.25/.40/.35) melts indicate interactions between the Al-containing species in peak 2(102.5-103.0 ppm relative to Al(H<sub>2</sub>O)<sub>6</sub><sup>3+</sup>) and both the NCH<sub>3</sub> and ethyl terminal CH<sub>3</sub> groups of MEI<sup>+</sup>. Fig. 3 contains the plots for the NCH<sub>3</sub> group in each melt and Fig. 4 contains data for the terminal CH<sub>3</sub> on the MEI ethyl group.

The QCC's obtained from the slopes in Fig. 3(MEI NCH<sub>3</sub>) are 1.7, 2.3 and 4.4 MHz for the (.5/.5), (.35/.40/.25) and (.25/.40/.35) melts. The QCC's from Fig. 4(terminal CH<sub>3</sub> on the MEI ethyl group) are 1.6, 6.9 and 1.3 MHz for the (.5/.5), (.35/.40/.25) and (.25/.40/.35) melts.

Finally, there is no correlation between the ring hydrogen dipolar R1's and any of the <sup>27</sup>Al peak R1's. This result is directly opposite to that found in MEICl-AlCl<sub>3</sub> systems [11,12].

## CONCLUSIONS

Application of the DSP method to these mixed melt systems indicates a lack of complexation between the ring hydrogens of MEI<sup>+</sup> and any of these aluminum containing species. These and previous results[21] suggest that the formation of various charged dimers containing EtAlCl<sub>2</sub> takes precedence over the formation of complexes between EtAlCl<sub>2</sub> and the MEI<sup>+</sup> ring hydrogens. However, there is evidence of interaction between the various Al-containing species and the CH<sub>3</sub> groups(NCH<sub>3</sub> and terminal CH<sub>3</sub> in the ethyl group) of MEI<sup>+</sup> in these melts.

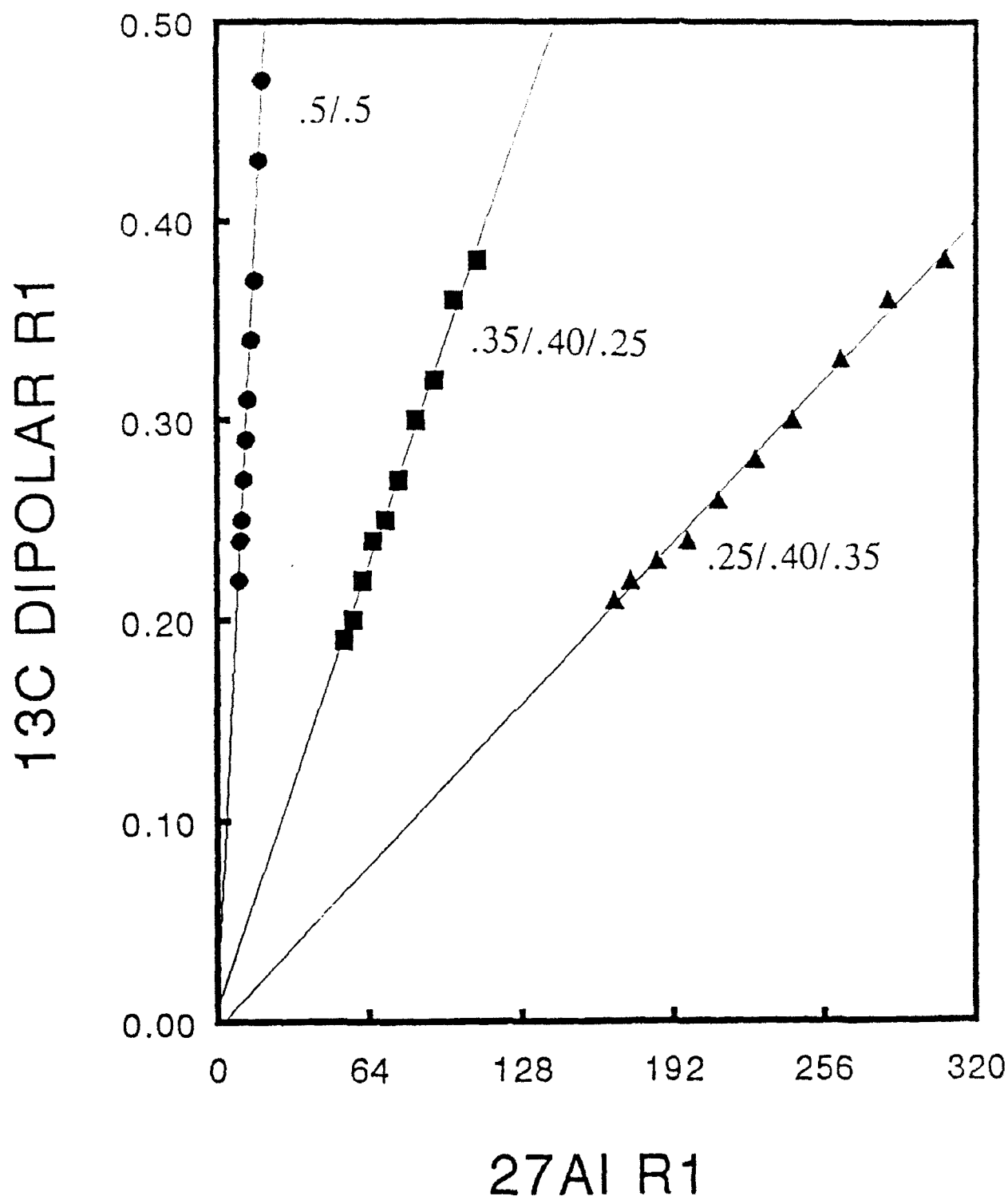


Fig. 3.  $^{13}\text{C}$  Dipolar R1's vs.  $^{27}\text{Al}$  R1's (25 - 70 C) for NCH, carbon vs Al peak 2 (25 - 70°C).

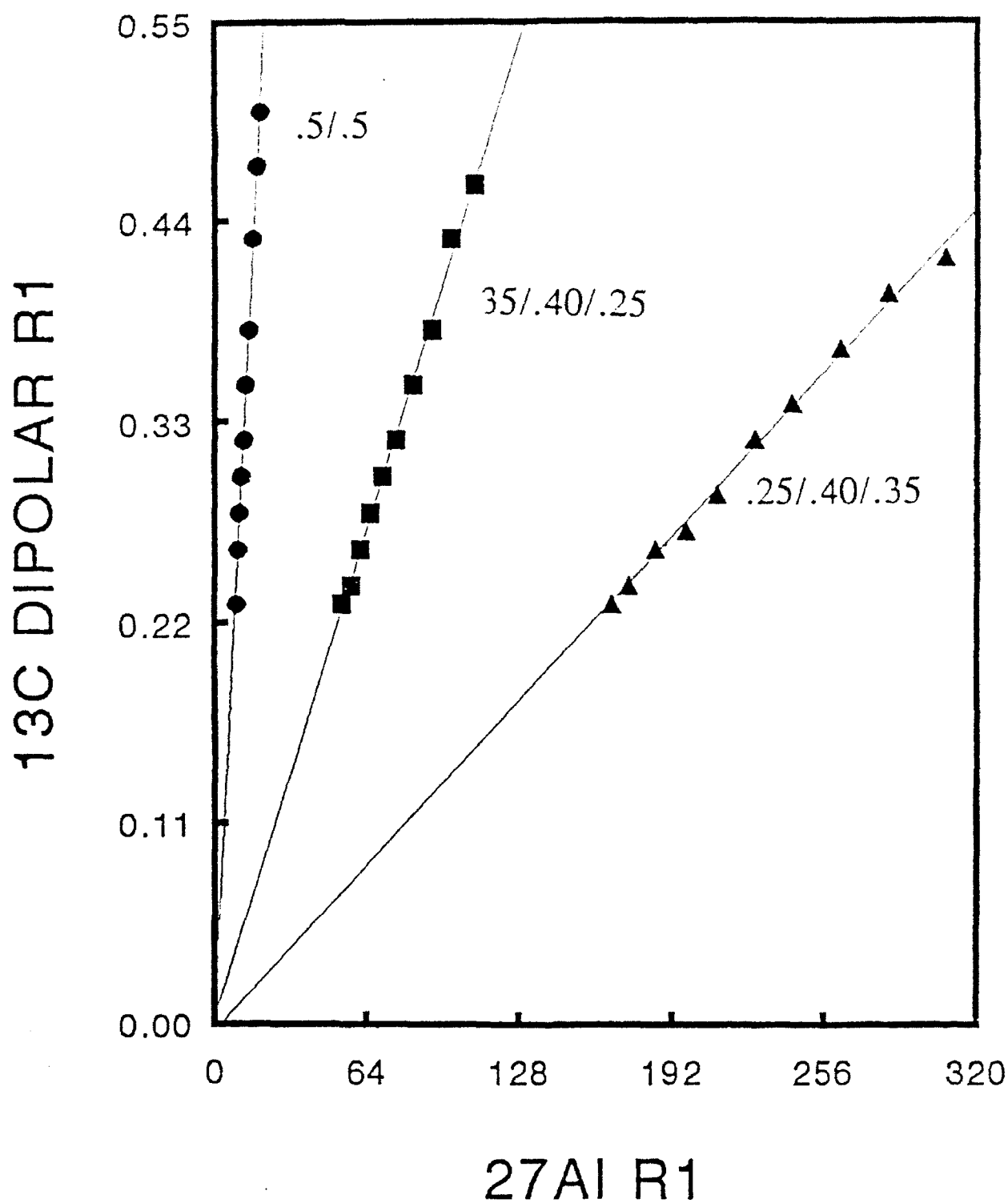


Fig. 4.  $^{13}\text{C}$  Dipolar R1's for ethyl  $\text{CH}_3$  carbon vs  $^{27}\text{Al}$  R1's (25 - 70°C) for Al peak 2.

## REFERENCES

- [1] J. S. Wilkes, J. A. Levisky, R. A. Wilson and C. L. Hussey, *Inorg. Chem.*, **21** 1263 (1982).
- [2] J. S. Wilkes, J. S. Frye and G. F. Reynolds, *Inorg. Chem.*, **22** (1983) 3870.
- [3] A. A. Fannin, L. A. King, J. A. Levisky and J. S. Wilkes, *J. Phys. Chem.*, **88** (1984) 2609.
- [4] A. A. Fannin, D. A. Floreani, L. A. King, J. S. Landers, B. J. Piersma, D. J. Stech, R. L. Vaughn, J. S. Wilkes and J. L. Williams, *J. Phys. Chem.*, **88** (1984) 2614.
- [5] K. M. Dieter, C. J. Dymek, N. E. Heimer, J. W. Rovang and J. S. Wilkes, *J. Amer. Chem. Soc.*, **110** (1988) 2722.
- [6] C. J. Dymek and J. J. P. Stewart, *Inorg. Chem.*, **28** (1989) 1472.
- [7] J. A. Boon, J. A. Levisky, J. L. Pflug and J. S. Wilkes, *J. Org. Chem.*, **51** (1986) 480.
- [8] C. J. Dymek, J. L. Williams, D. J. Groeger and J. J. Auborn, *J. Electrochem. Soc.*, **131** (1989) 2887.
- [9] C. J. Dymek and L. A. King, *J. Electrochem. Soc.*, **132** (1985) 1375.
- [10] C. L. Hussey, T. B. Scheffler, J. S. Wilkes and A. A. Fannin, *J. Electrochem. Soc.*, **133** (1986) 1389.
- [11] W. R. Carper, J. L. Pflug, A. M. Elias and J. S. Wilkes, *J. Phys. Chem.* **96** (1992) 3828.
- [12] W. R. Carper, J. L. Pflug and J. S. Wilkes, *Inorganica Chimica Acta* **193** (1992) 201.
- [13] W. R. Carper, J. L. Pflug and J. S. Wilkes, *Inorganica Chimica Acta* (in press).
- [14] J. J. Dechter and U. Henriksson, *J. Magn. Res.*, **48** (1982) 503.
- [15] A. Abragam, "Principles of Nuclear Magnetism", Oxford University Press, Oxford (1961).
- [16] K. F. Kuhlmann and D. M. Grant, *J. Amer. Chem. Soc.*, **90** (1968) 7355.

- [17] B. Lindman and S. Forsen, in "NMR Basic Principles and Progress," P. Diehl, E. Fluck and R. Kosfeld, Editors, Vol. 12, p. 22, Springer-Verlag, New York (1976).
- [18] D. Neuhaus and M. Williamson, "The Nuclear Overhauser Effect in Structural and Conformational Analysis", VCH Publishers, New York (1989).
- [19] J. Weidlein, *J. Organomet. Chem.*, 17 (1969) 213.
- [20] B. Gilbert, Y. Chauvin and I. Guibard, *Vib. Spectros.*, 1 (1991) 299.
- [21] W. R. Carper, C. E. Keller, P. A. Shaw, M. P. and J. S. Wilkes, in "Eighth International Symposium on Molten Salts", Electrochem. Soc., New York (in press).

THIS PAGE INTENTIONALLY LEFT BLANK

**WILFORD HALL MEDICAL CENTER**

**ENHANCED PHYSIOLOGIC MONITORING OF CLOSED HEAD-INJURY**

Michael L. Daley  
Associate Professor  
and  
Brian Carter  
Graduate Student  
Department of Electrical Engineering

Memphis State University  
Memphis, TN 38152

Final Report for:  
Summer Research Program  
Wilford Hall Medical Center  
Lackland AFB, TX

Sponsored by:  
Air Force Office of Scientific Research  
Bolling Air Force Base, Washington, D.C.

September, 1992



## ENHANCED PHYSIOLOGIC MONITORING OF CLOSED HEAD-INJURY

Michael L. Daley  
Associate Professor  
and  
Brian Carter  
Graduate Student  
Department of Electrical Engineering  
Memphis State University

### Abstract

The aim of this study was to develop both a laboratory model of closed head-injury and an analytical model of venous blood flow from the brain to test the *hypothesis that variations in venous pressure associated with the respiratory cycle can have a dominant influence on venous flow from the brain during elevated intracranial pressure.* A young adult pig with an implanted intracranial balloon designed to manipulate intracranial volume was used as a laboratory model. An analog electrical circuit model was used to provide a theoretical analytical description of cerebral venous blood flow during elevated intracranial pressure. Both experimental and theoretical results indicate that during intact autoregulation of cerebral blood flow, respiratory induced venous pressure changes systematically influence intracranial blood volume. Specifically, intracranial blood volume increases during inhalation and decreases during expiration. Furthermore, the difference in change of intracranial volume between the two phases of ventilation, inhalation and expiration, increases with increasing mean intracranial pressure. However, during loss of regulation of cerebral blood flow, venous blood flow and the resulting changes of intracranial blood volume are not systematically influenced by respiratory induced venous pressure changes.